Understanding extracellular vesicle biology for the development of bioinspired nanotechnology platforms

Scott Edward Bonner

Wolfson College

University of Oxford

A thesis submitted for the degree of

Doctor of Philosophy in Interdisciplinary Biosciences

Trinity 2022

Declaration

The work presented in this thesis was undertaken in Professor Matthew Wood's Laboratory, Department of Paediatrics, University of Oxford, Oxford, United Kingdom, between 2018 and 2022. All work presented is my own with the following exceptions: (1) Electron microscopy for the analysis of extracellular vesicle morphology, Chapter 3, 4 and 5 Erinn Johnson, Electron Microscopy Facility, Sir William Dunn School of Pathology, University of Oxford, Oxford, United Kingdom, OX1 3RE. (2) NanoView ExoView R100 operation and analysis of tetraspanin expression on extracellular vesicles, Chapter 5, Alexandra Shephard, NanoView Biosciences, Malvern Hills Science Park, Geraldine Road, Malvern, United Kingdom, WR14 3SZ (3) LC MS/MS to obtain raw proteomics data, Chapter 5, Sarah Flannery, Professor Benedikt Kesslerr's Laboratory, Target Discovery Institute, Nuffield Department of Medicine, University of Oxford, Oxford, United Kingdom, OX3 7FZ. (4) Proteomics analysis, Chapter 5 (section 5.3.4 only), Imre Mäger, Professor Matthew Wood's Laboratory, Department of Paediatrics, University of Oxford, Oxford, United Kingdom, OX3 7TY. (5) Operation of the BD FACSAria-II for single cell sorting of mesenchymal stem cells, Robert Hedley, Flow Cytometry Facility, Sir William Dunn School of Pathology, University of Oxford, UK, OX1 3RE.

The experimental findings have not been submitted for any other degree at the University of Oxford or any other institution. This thesis contains modified excerpts and figures of first-author manuscripts which have been published throughout the period of my DPhil in Open Access journals. Where required, permission from individual journals was obtained.

Word count: 49,692

Acknowledgements

The work presented within this would not have been possible without the contribution and support of numerous colleagues, departments and organisations.

Firstly, I would like to thank my funders, the United Kingdom Research and Innovation Biotechnology and Biological Sciences Research Council (UKRI BBSRC) and Evox Therapeutics Ltd for providing the necessary funds to support myself and my research over the last four years. Thank you also to the University of Oxford Doctoral Training Centre for the support and professional development provided throughout my DPhil and to the Department of Paediatrics and Wolfson College.

I want to thank my supervisor, Prof Matthew Wood, for his help and guidance throughout my DPhil and for liaising with Evox to support my DPhil. Thank you for providing me with the environment to complete my research project. I would also like to thank my co-supervisor from 2018 to 2020, Imre Mäger, for supporting me and frequently helping to develop my research project. Thank you also for dedicating your time to help produce a comprehensive research plan that was invaluable following your departure, especially considering the turmoil caused by the COVID-19 pandemic. Additionally, I would like to thank my co-supervisor from 2020 to 2022, Dave Carter, for kindly offering to step into a supervisory role following Imre's departure and providing invaluable support and feedback in the later half of my DPhil.

I thank Evox Therapeutics Ltd., particularly Tony de Fugerolles, Per Lundin, Dave Carter and Justin Hean. Thank you for introducing me to the field of extracellular vesicles and nurturing my passion for the subject in my employment as a research assistant before my DPhil, and for graciously accepting to help facilitate my DPhil project with the Wood lab. Thank you also for your guidance throughout my DPhil and for providing a 12-week internship project to develop my skills.

To Hans Friedrichsen, thank you for taking on a temporary supervisory role at short notice in 2020, providing advice and critique on my project throughout the last four years and being an endless source of stories and laughs. Likewise, to Antonio Garcia Guerra, thank you for your support in the lab, your advice and critique, for being a listening ear at times and for all the laughs. Thank you to the rest of the Wood lab EV team, past and present, including Mariana, Ghulzar, Carla, Ambra, Claire, Ioulia, Ashwin, Besarte and Nina. Additionally, I would like to thank all my colleagues within the Wood lab for making the lab such a welcoming and enjoyable place to work. Special thanks to Amarjit Bhomra for doing an outstanding job as lab manager; our runaway political chats over coffee have also been a pleasant respite. Many thanks to all my undergraduate and postgraduate project students, including Vince, Charlotte, Sofie, Taylor, Willemijn and Harriet. I'm grateful for your assistance both in and out of the lab.

Special thanks to Eduard Willms, who has been a constant source of professional support, advice and information despite moving to the other side of the planet. I'm very grateful to have been involved in the work subsequent to your DPhil project and for the opportunities offered to us as a result of this work. I hope we can continue working on our shared passion for EVs in the future.

To Denis Noble, thank you for your interest in my research and the advocacy you provided for my and Eduard's work. Thank you also for the honour of presenting and publishing alongside some of the most prestigious researchers in cancer and evolutionary biology. By extension, my thanks go out to Richard Jacobs and the Finding Genius Podcast team.

I would also like to acknowledge the contribution and assistance of everyone that collaborated on this project, including Laura Zanetti Domingues and Marisa Martin-Fernandez (Central Laser Facility, Harwell), Errin Johnson (Electron Microscopy Facility, University of Oxford), Alexandra Shephard and Ben Owen (NanoView Biosciences), Roman Fischer, Svenja Hester, and Sarah Flannery (Kesslerr Laboratory, University of Oxford), Robert Hedley (Flow Cytometry Facility, University of Oxford), Deborah Goberdhan and John Mason (Goberdhan Laboratory, University of Oxford). Thank you all for your technical assistance during this project.

To my friends, thank you for the unending support, encouragement, interest and joy you bring to my life; I could not have completed this DPhil without you. To all my family, to my brothers Tim and Luke, and my parents, Martin and Nickie, thank you for your support in everything I have done that has helped me to get to where I am today, and for the unconditional love you show, words cannot express my gratitude.

To my cat, Emerald, I could not have made it through the last four years without the joy you bring to every day, your affection, and the instant relief you provide under challenging times.

Finally, to my fianceé, Verity. I will never be able to express how truly grateful I am for everything you have done for me in the last nine years that has helped me get here. Your support, advice, encouragement, interest, companionship and love during my DPhil has been invaluable. I could not have done this without you. I love you with all my heart.

Abstract

Extracellular vesicles (EVs) are membranous nanoparticles released by cells that are important mediators of intercellular communication via transfer of their cargoes to recipient cells. For this reason, EVs have been harnessed as a novel targeted therapeutic delivery platform. However, EV research faces numerous challenges that need to be addressed if their potential as therapeutic devices is to be fully realised.

EV heterogeneity is arguably the most crucial challenge to be addressed. EVs differ in size, biogenesis, and composition, and these characteristic differences have been linked to functional differences which may impact EV therapeutic activity. Here, functionally heterogeneous EV populations were identified among size-based and subclonal EV populations. EVs were characterised revealing differences in marker and functional protein expression, including integrins, cell adhesion proteins and EV marker proteins. These differences may explain functional differences between EV subpopulations and could aid selective purification of therapeutically advantageous EVs. Furthermore, the subclonal nature of the analysed EV populations also indicated that EV heterogeneity might be linked to cellular heterogeneity. Separately, changes in EV protein expression were documented among EVs harvested at different time points, highlighting another critical consideration for EV therapeutic development.

Advancement of *in vivo* EV biodistribution and purification techniques was also sought to improve EV therapeutic development and characterisation. While requiring further experimentation, EV DNA barcoding, a technique that labels EVs with synthetic DNA identifiers, showed potential as a novel EV biodistribution and therapeutic siRNA delivery tool. Additionally, Capto Core binding chromatography showed significant improvement over size exclusion chromatography for purification of high concentrations of EVs from high cell density cultures.

Overall, this research offers insights into EV heterogeneity and novel techniques to aid therapeutics EV production. It also highlights the importance of understanding EV biology and overcoming the challenges associated with EV research to improve EV therapeutic development.

List of abbreviations

ANOVA	Analysis of variance
APC	Allophycocyanin
BCA	Bicinchoninic acid
CC400	Capto Core 400 kDa
CC700	Capto Core 700 kDa
CD	Cluster of differentiation
CMOS	Complementary metal-oxide-semiconductor
DAPI	4',6-diamidino-2-phenylindole
DGC	Density gradient centrifugation
DMEM	Dulbecco's Modified Eagle's Media
DPhil	Doctor of Philosophy
dUC	Differential ultracentrifugation
EC50	Half maximal effective concentration
ECM	Extracellular matrix
ECS	Extracapillary space
EMT	Epithelial mesenchymal transition
ESCRT	Endosomal sorting complex required for transport
EV	Extracellular vesicle
EXO	Exosome
FBS	Fetal bovine serum
FCM	Flow cytometry
FITC	Fluorescein isothiocyanate
g	Gravitational force
GFP	Green fluorescent protein
GO	Gene ontology
GOBP	Gene ontology biological process
HEK	Human embryonic kidney
HIV	Human immunodeficiency virus
hTERT	Human telomerase reverse transcriptase
ILV	Intra-luminal vesicles
kDa	Kilodalton
LC	Liquid chtromatography
LDL	Low density lipoprotein
MDA	MDA-MB-231
µg	Microgram
µL	Microlitre
µM	Micromolar
miRNA	MicroRNA
MISEV	Minimal information for the study of extracellular vesicles
mL	Mililitre
mRNA	Messenger RNA
Mal	Maleimide

MSC	Meschymal stem cells
MV	Microvesicle
MVB	Multi-vesicular body
MWCO	Molecular weight cut-off
NHS	N-Hydroxysuccinimide
nm	Nanometer
NTA	Nanoparticle tracking analysis
PAGE	Poly-acrylamide gel electrophoresis
PANTHER	Protein analysis through evolutionary relationships
PBS	Phosphate buffered saline
PC	Principal component
PE	Phycoerythrin
PEG	Polyethlene glycol
PVDF	Polyvinylidene fluoride
qPCR	Quantitative polymerase chain reaction
RFP	Red fluorecent protein
RIPA	Radioimmunoprecipitation assay buffer
RPM	Revolutions per minute
RT	Room temperature
RVG	Rabies virus glycoprotein
SD	Standard deviation
SDS	Sodium dodecyl sulphate
SEC	Size exclusion chromatography
SIM	Structutred illumination microscopy
siRNA	Short interfering RNA
TCEP	Tris(2-chloroethyl)phosphate
TE	Tris-ethylenediaminetetraacetic acid
TEM	Transmission electron microscopy
TFF	Tangential flow filtration
UC	Ultracentifugation
UV	Ultraviolet
VLDL	Very low density lipoprotin
WCL	Whole cell lysate
WT	Wild type

Table of Contents

Figures and Tables

1.0 Introduction

1.1 Intercellular communication

1.1.1 Fundamentals of intercellular communication

Cell-to-cell communication is a vital role of multicellular organisms that allows the coordination of cell functions. Historically, it has been accepted that cells facilitate intercellular communication by direct contact or release of soluble factors, including cytokines, chemokines, neurotransmitters, and growth factors, into the extracellular environment, which interact with specific receptors on recipient cells. However, in the last few decades, membrane-bound nanoparticles called extracellular vesicles (EVs) have also been identified as mediators of intercellular communication (EVs). EVs contain proteins, lipids and nucleic acids and have been shown to play an important role in intercellular communication by delivering their bioactive cargoes[1–3].

1.1.2 Extracellular vesicles

Extracellular vesicles (EVs) are membrane-bound nanoparticles released from eukaryotic and prokaryotic cells[1–3]. EVs have been identified in nearly all biological materials and fluids, such as blood, urine, breast milk, synovial, ascites, and even seminal fluids[4]. EVs are released naturally by cells under normal physiological conditions and pathophysiological conditions. However, their release can be upregulated in response to various stimuli such as changes in pH, hypoxia, injury, or complement activation[5–8].

EVs were first identified by Chargaff and West in 1946 during an investigation of procoagulants in the blood, wherein procoagulant platelet-derived particles in plasma

that sedimented at 31,000 x *g* after centrifugation were observed[9]. Wolf (1967) later coined the term "platelet dust" to describe these particles[10]. During the 1970s and 80s, various studies observed membranous particles in various biological fluids and in *in vitro* cell culture preparations, and in 1983, EVs were first documented to be released by the fusion of multivesicular bodies (MVBs) with the cell membrane[11]. However, throughout this period, EVs were regarded as a mechanism for waste disposal from cells[12]. It was not until 1996 when a landmark study by Raposo *et al.* reported that EVs derived from B cells could induce antigen-specific responses in recipient T cells, that EVs were considered an important mediator of intercellular communication in health and disease[13]. Subsequently, this led to a plethora of studies that reported the involvement of EVs in intercellular communication through the transfer of their proteins, lipids and nucleic acids cargoes to recipient cells[14–17]. In the previous decade, the number of researchers studying EVs has grown substantially, resulting in the formation of the International Society for Extracellular Vesicles (ISEV) in 2011 to unify the international EV research community and establish guidelines for the research and publication of EV based research[18,19].

1.2 Extracellular vesicle biogenesis and subpopulations

In the simplest of terms, EVs are membranous nanoparticles that are derived from cells. However, "extracellular vesicles" is a collective term that encompasses various vesicle subpopulations mainly based on their biogenesis and physical characteristics. The most extensively studied subtypes are exosomes and microvesicles (MVs). Figure 1.1 provides an overview of the differences between exosomes and MVs, including their formation and size range.

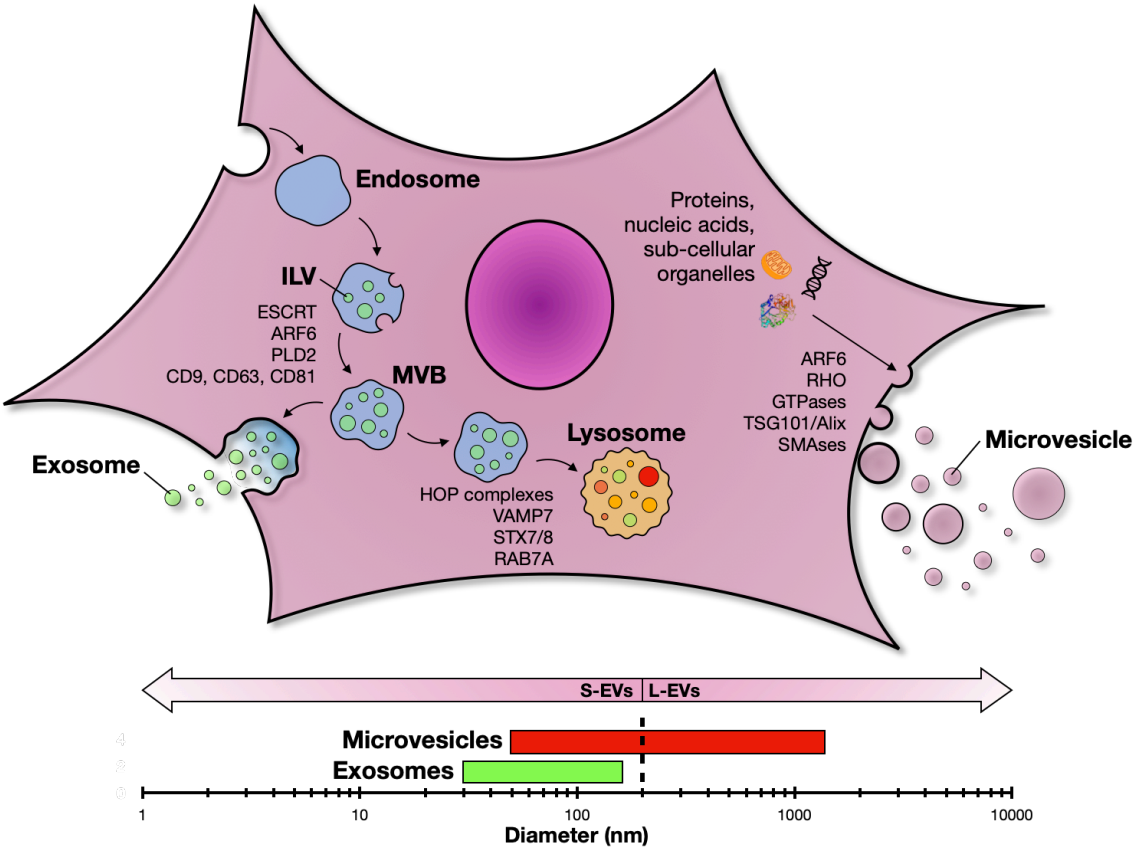

Figure 1.1 Extracellular vesicle biogenesis and subpopulations. Extracellular vesicles can be divided into two main subpopulations according to their route of biogenesis; exosomes (green) and microvesicles (pink). Exosomes are formed within the endolysosomal system. Multiple inward budding events fill endosomes with intraluminal vesicles (ILVs). Once filled with ILVs, these endosomes are termed multivesicular bodies (MVBs). MVBs can be trafficked to the cell membrane where they fuse and release exosomes. Exosome formation occurs dependently or independently of ESCRTs. ESCRT independent formation involves various other proteins for cargo sorting and release, including ADP-ribosylation factor 6 (ARF6), phospholipase D2 (PLD2) and tetraspanins CD9/63/81. MVBs displaying specific surface proteins, including HOP complexes, HSP70/90 organising (HOP) complexes, vesicle-associated membrane proteins 7

(VAMP7), syntaxin (STX) 7/8 and RAB7A, are trafficked to lysosomes for degradation[20,21]. Alternatively, Microvesicles bud directly from the cell membrane. Various proteins are involved in MV biogenesis and cargo sorting, including ARF6, Ras homology (RHO) gene family members, GTPases, tumour susceptibility gene 101 (TSG101) protein, ALG-2-interacting protein X (Alix) and sphingomyelinases (SMAses). Exosomes have a size range of 30 to 150 nm, while MVs have a size range of 50 to 1,300 nm. Due to the significant overlap in size and the difficulty of selectively purifying EV subtypes, EVs less than 200 nm are termed small EVs (S-EVs), while EVs larger than 200 nm are termed large EVs (L-EVs)[18]. Figure adapted from Bonner & Willms (2021)[22].

1.2.1 Exosomes

Exosomes are subpopulations of small EVs that range in size from 30 nm to 150 nm in diameter[23,24] and are formed via the endolysosomal pathway. During exosome formation, invaginations of the cell membrane form intracellular vacuoles known as endosomes. Subsequent invaginations of endosomal membranes form membranous vesicles within endosomes called intra-luminal vesicles (ILVs), which themselves are early exosomes. Multiple invaginations of endosomal membranes fill endosomes with ILVs; endosomes then become referred to as multivesicular bodies (MVBs)[25]. In the endolysosomal pathway, MVBs displaying specific surface proteins fuse with lysosomes to degrade their contents. These proteins include HSP70–HSP90 organising protein (HOP) complexes, Ras-related protein Rab-7A (RAB7A), vesicle-associated membrane protein 7 (VAMP7), and syntaxin 7 and 8 (STX7/8). Alternatively, MVBs required to release their ILV contents extracellularly are trafficked to and fuse with the cell membrane, releasing their ILVs which are then termed exosomes[20,21].

Exosomal formation in MVBs occurs dependently or independently of endosomal sorting complexes required for transport (ESCRT-0–III)[26,27]. ESCRT-dependent exosomal formation involves ubiquitylation of proteins for selective packaging into ILVs. Ubiquitiylated membrane-associated proteins and lipids are clustered into microdomains on the limiting membrane of MVBs by ESCRT-0 and ESCRT-I subunits. These microdomains also recruit soluble components, including cytosolic proteins and RNAs destined for packing as cargoes into exosomes. Subsequently, ESCRT-0 and -I subunits recruit ESCRT-II and -III, which aid in the budding and fission of exosomes[28].

In contrast, ESCRT-independent exosomal formation begins with hydrolysis of sphingomyelin by neutral sphingomyelinase (N-SMase) to form ceramide[29]. Ceramide allows the generation of MVB membrane subdomains which causes membrane curvature and elicits sorting of cargoes into ILVs[30,31]. The tetraspanins CD9, CD63 and CD81 aid ILV biogenesis by forming into microdomains with other tetraspanins, transmembrane proteins and cytosolic proteins that bud from the MVB surface[32], or via formation of CD81-rich domains which induce inward budding[33]. Syntenin-1 and ADP ribosylation factor 6 (ARF6) are also involved in endosomal sorting by targeting exosomal cargoes to endosomal membranes for packaging into ILVs[34]. ARF6 is also involved in ILV budding in a phospholipase D2 (PLD2) dependent manner[35].

1.2.2 Microvesicles

In comparison to exosomes, microvesicles are a subpopulation of larger EVs that range in size from roughly 50 nm to 1,300 nm in diameter[23,36]. MV formation occurs via direct budding of vesicles from cell membranes. This process is mediated by ARF6 and RHO family GTPase-dependent rearrangement of the actin cytoskeleton[24,37]. ARF6-positive

recycling vesicles involved in trafficking cargo to the cell surface for incorporation in MVs do, however, continue to take advantage of ESCRT-associated proteins for cargo sorting. The ESCRT-I component, tumour susceptibility gene 101 protein (TSG101), traffics to the plasma membrane and interacts with accessory proteins ALG-2-interacting protein X (ALIX) for subsequent cargo sorting and MV release[38]. Sphingomyelinases are also essential modulators of MV formation; neutral (N-SMase) and acid sphingomyelinase (A-SMase) are involved in downstream activation of receptors that trigger the release of MVs[29,39]. MV formation has also been shown to be mediated by increases in cytosolic calcium concentrations, which modulates the activity of membrane transporter proteins and leads to changes in lipid distribution and membrane blebbing[40,41].

Other examples of nanoparticles formed in a similar cell membrane-derived manner to MVs have also been documented. Most prominently, apoptotic cells release membranous nanoparticles termed apoptotic bodies by blebbing and fragmentation of the cell membrane [42]. Apoptotic bodies have a broader size range than MVs of between 50 and 2,000 nm in diameter[43]. Additionally, cancer cells release populations of cell membrane-derived nanoparticles termed large oncosomes due to their large sizes relative to other EV populations of 1,000 nm to 10,000 nm in diameter and their ability to transfer oncogenic material to recipient cells[44]. Large oncosome formation is associated with overexpression and activation of Akt1, epidermal growth factor (EGF) and EGF receptor (EGFR), and caveolin-1 (CAV1)[44–46].

1.2.3 Correct use of EV nomenclature

Despite their differences in biogenesis, exosomes and MVs share similar physical properties, including overlapping size ranges. As explained graphically in Figure 1.1, their overlapping size ranges make them difficult to distinguish from one another once released extracellularly. Many conventional EV purification techniques rely on physical properties such as size or density to separate EVs from other constituents of the medium into which they are secreted. Therefore, the selective purification of different EV subpopulations, such as exosomes and MVs, remains a challenge for the field to address the potential distinct functions of these subpopulations[47]. So far, heterogeneity in EV proteomes, transcriptomes and biological function have been observed in sub-150 nm populations which include both exosomes and MVs[23,48–51]. Consequently, in 2018 the International Society for Extracellular Vesicles published guidelines that recommended that in non-selective studies or studies where specific markers of subcellular origin cannot be reliably identified, heterogenous EV populations should simply be classified according to physical characteristics. For example, EVs can be classified by size as "small EVs" (sEVs) for particles smaller than 200 nm, and "large EVs" (lEVs) for particles larger than 200 nm. Alternatively, density (low, middle, high, with each range defined) or biochemical composition (i.e. CD63+ or CD81+ EVs) can also be used[18].

1.3 Biological function of EVs

1.3.1 EV interaction with cells

Once released into the extracellular space, EVs travel to recipient cells and evoke physiological and pathophysiological changes by transferring their bioactive cargoes. For this to occur, EVs must first interact with the plasma membrane to initiate their internalisation or fusion via various signalling pathways. Alternatively, surface moieties

on EVs may interact with the plasma membrane to initiate signalling and affect cellular physiology and phenotype without internalisation[52]. How EVs interact with cells seems to depend on the cell types that EVs are derived from, EV biogenesis, recipient cell phenotype and the physiological effects of EVs[53]. However, this is yet to be fully understood as various studies have documented functionally heterogeneous EV subpopulations derived from the same parent cell population[54–58].

Protein ligands enriched on the EV surface determine target cell specificity based on the expression of corresponding receptors on recipient cells. Integrins play a prominent role in these interactions by interacting with intercellular adhesion molecules (ICAMs)[59], fibronectin and laminin on recipient cells[60–62]. Differential expression of integrin subunits has been shown to target EVs to different recipient cells[63]. Conversely, integrins within recipient cell membranes interact with exosomal tetraspanins to facilitate binding and uptake. Differential tetraspanin expression on EV surfaces has also influenced EV targeting[64–66]. Aside from these proteins, lectins, heparan sulphate proteoglycans, and lipid binding proteins present on EVs and plasma membranes also aid the binding of EVs[67–70].

Once bound, EVs must be internalised or fused with recipient cells to facilitate cargo delivery. Feng *et al.* (2010) identified phagocytosis as a non-selective method of EV uptake via PI3-kinases mediated inhibition of phagocytosis in macrophages, significantly reducing EV internalisation in a dose-dependent manner[71]. Similarly, macropinocytosis, a process by which a large volume of extracellular fluid is engulfed by a cell, is also involved in EV uptake. Macropinocytosis of EVs occurs by stimulations of EGFR on recipient cells with EGF in EV preparations[72]. EGFR activation signals for

macropinocytosis via activation of the Rho family of small GTPase, Rac, which leads to rearrangement of the actin cytoskeletal and eventual engulfment[73,74].

Clathrin-mediated endocytosis (CME) is another well-documented mechanism of EV uptake. In CME, clathrin triskelions assemble into lattices which help shape the plasma membrane into clathrin-coated pits. Assembly protein complexes are then targeted to the plasma membrane and interact with various adaptin subunits to sort cargo into the pits. Dynamin, a multidomain GTPase, is then recruited to the necks of coated pits to assist invagination, fission, and release of endocytic vesicles[75]. Inhibition of CME has been shown to cause reduced uptake of EVs purified from bone marrow-derived mesenchymal stem cells (MSC)[76]. Finally, EV uptake can also be mediated by clathrin-independent endocytosis (CIE). CIE encompasses a variety of mechanisms, including caveolae-, ARF-6, flotillin-1-, CDC42- and RhoA-dependent endocytosis[77].

1.3.2 EVs in health and disease

Since Raposo *et al.* (1996) discovered that B cell and dendritic cell EVs stimulate immune responses in recipient T cells via major histocompatibility complex (MHC) class II activation[13], many studies have documented the important physiological and pathophysiological role of EVs. Table 1.1 summarises the various roles of EVs in normal physiology that have been identified over the last few decades. In addition, many other functions of EVs in normal physiology have also been proposed. However, due to the heterogeneous nature of tissues, the complexity of biological systems, and a lack of sensitive techniques, there is an absence of studies that can confirm the healthy physiological roles of EVs[78,79].

EV source	Function	Reference
Neutrophils	– Guiding leukocytes to sites of inflammation	Lim *et al.*, 2015[80] Nolan *et al.*, 2008[81]
	– Increase secretion of IL-8 from parent neutrophils – Increase E-selectin and vascular cell adhesion molecule-1 in recipient endothelial cells	Kolonics *et al.*, 2021[82]
	– Form aggregates with bacteria and reduces their growth rate	Timár *et al.*, 2013[83]
Natural killer cells	– Cytotoxic activity against activated PBMCs to mediate immunosuppression	Lugini *et al.*, 2012[84]
HEK293T cells stably expressing angiotensin II type I receptor (AT1R)	– Maintenance of normal blood pressure in response to hypotonicity	Pironti *et al.*, 2015[85]
Murine kidney collecting duct (mCCDC11)	– Transfer of aquaporin 2 (AQP2) to AQP2 deficient mCCDC11 cells to increase water flow across cells	Street *et al.*, 2011[86]
Prostate gland acinar epithelial cells (prostasomes)	– Transfer CD38 into sperm cells, inducing cyclic ADP-ribose (cADPR) production, which increases motility in a calcium-dependent manner	Park *et al.*, 2011[87]
	– Transfers of CD59 to sperm inhibit the membrane attack complex and protect sperm from complement-mediated lysis	Rooney *et al.*, 1993[88]
Murine reproductive luminal fluids	– Transfer of plasma membrane calcium ATPase 4 (PMCA4) to sperm to increase motility	Al-Dossary *et al.*, 2013[89]
Human skeletal myoblasts	– Myogenic differentiation of stem cells and muscle regeneration	Choi *et al.*, 2016[90]

Table 1.1 The various roles of EVs in normal physiology in different systems.

However, research has also implicated EVs in various pathological processes. Most notably, the role of EVs in cancer development and progression has been extensively studied. Firstly, tumour-derived EVs play an extensive role in immunomodulation, including modulation of macrophage activity by transfer of miRNA cargoes[91,92], inhibition of activated CD8+ T cell proliferation and signalling and expansion of suppressor CD4+ Treg cells[93,94]. Tumour EVs also interact with vascular cells surrounding tumours to promote angiogenesis[95], and can transfer oncogenic cargoes to healthy recipient cells leading to oncogenic transformation of healthy cells or aiding tumour cell metastasis[96].

Tumour-derived EVs can also aid metastasis by eliciting phenotypic changes in distant tissue microenvironments to establish a pre-metastatic niche that supports tumour establishment and growth, including initiating cancer-associated fibroblast transition and extracellular matrix remodelling[97–99]. EVs also seem to be involved in facilitating metastatic tumour cell adhesion, acting as scaffolds to anchor tumour cells at new sites prior to proliferation[60,100,101]. An example of the role of EVs in each of these processes was recently reviewed in the context of ovarian cancer, where EVs travel to the abdominal cavity, establishing a pre-metastatic niche, prior to ovarian cancer cell dissemination via the peritoneal fluid and subsequent metastatic tumour formation[102]. EVs also appear to be involved in chemotherapeutic resistance and removal of chemotherapeutics from cancer cells[103,104]. Human epidermal growth factor receptor 2 (HER2) on cancer-derived EVs has been shown to act as a decoy against Trastuzumab, an anti-HER2 antibody therapeutic[105].

Aside from cancer, the role of EVs in neurodegenerative disorders has also been extensively documented. The pathological activity of EVs in most major neurodegenerative disorders, including Alzheimer's disease, Parkinson's disease, and amyotrophic lateral sclerosis (ALS), seems to involve the transport of pathogenic proteins, thereby exacerbating disease pathology. For example, in Alzheimer's disease, EVs have been shown to spread amyloid beta (Aβ) proteins and amyloid precursor proteins (APPs), stimulate Aβ42 peptide aggregation and inhibit Aβ42 clearance by microglia cells[106–108]. Similarly, in Parkinson's disease, EVs have been shown to spread aggregated α-synuclein (α-syn)[109], causing degeneration of dopaminergic neurons. Additionally, in ALS, TAR DNA-binding protein 43 (TDP-43) has been detected in EVs isolated from ALS patient cerebrospinal fluid (CSF), which may support ALS propagation[110]. Furthermore, superoxide dismutase 1 (SOD1) may also be propagated via exosomes in TDP-43

negative cases of ALS from *in vitro* ALS models[111,112]. In contrast, in multiple sclerosis, as opposed to pathogenic protein dissemination, EVs seem to be involved in autoreactive leukocyte activation, causing demyelination, diffuse neurodegeneration, and inflammation[113,114].

Elsewhere, EVs have also been shown to be involved in disease pathology associated with many other organ systems. The role of EVs in disease pathology associated with different organ systems has been reviewed elsewhere, including cardiovascular diseases[115], musculoskeletal pathology[116], renal diseases[117], reproductive disorders[118], gastrointestinal diseases[119,120], and immunological conditions[121,122]. EVs have also been shown to be involved in infectious disease pathology[1,123,124].

1.3.3 EVs as therapeutics

As demonstrated, in most cases, EVs elicit their biological functions through uptake and transfer of their cargoes to recipient cells. The ability of EVs to shield cargoes and facilitate targeted delivery to different sites presents EVs as attractive candidates for development into therapeutic devices. Additionally, EVs are biocompatible, can be personalised by deriving EVs from autologous patient cells, and have been shown to cross biological barriers, including the blood-brain barrier[125–127]. Therefore, over the last few decades, copious research has been conducted to utilise EVs for therapeutic delivery and establish EVs as viable targeted therapeutic delivery vehicles.

In many cases, EVs are engineered to elicit therapeutic effects. EVs can be modified exogenously or via endogenous modification of parent cell lines to display motifs on their surface that may be therapeutically active, aid in EV targeting, uptake, or endosomal

escape, or can be loaded with therapeutic proteins or RNA[125,128,129]. However, some EVs possess innate therapeutic potential. Mesenchymal stem cell (MSC)-derived EVs have been extensively explored for their innate therapeutic benefits. MSCs have regenerative and immunomodulatory effects that have been harnessed to treat osteoarthritis, cardiomyopathies, pneumopathies, and autoimmune diseases[130]. Wiklander *et al.* (2019) recently reviewed various preclinical and clinical studies that have utilised MSC EVs for their innate regenerative properties to treat various diseases[131]. Of these studies, the most successful use of MSC EV has been in treating chronic kidney disease (CKD). In a randomised, placebo-controlled, phase III clinical trial, 40 CKD patients were divided into two groups; group A, 20 CKD patients treated with two intra-arterial doses of MSC-EVs, and a control group B of 20 CKD patients as a matching placebo group treated with intravenous saline injections. Significant improvement in estimated glomerular filtration rate, serum creatinine level, blood urea and urinary albumin creatinine ratio was observed among group A participants, as well as significant increases in plasma concentrations of TGF-β1 and IL-10 that exert immunosuppressive effects and a significant decrease in plasma levels of the inflammatory mediator TNF-α[132].

Elsewhere, some of the most prominent uses of therapeutic EVs have been to treat cancer. Ohno *et al.* (2013) endogenously engineered human embryonic kidney 293 (HEK293) cell-derived EVs to express GE11 on their surfaces, a strong EGFR targeting ligand, and carry the tumour suppressive miRNA, let-7a. Together these EVs delivered let-7a to EGFR expressing xenograft breast cancer cells in recombination activating gene two protein$^{-/-}$ (RAG2$^{-/-}$) immune-deficient mice, causing a significant ($P < 0.05$) ~60% reduction in tumour size following weekly administration of GE11^{+}, let-7a^{+} EVs for four weeks[133]. Similarly, Tian *et al.* (2014) engineered EVs derived from immature dendritic

cells to express lysosome-associated membrane glycoprotein 2b (Lamp2b) fused with iRGD, an integrin α-V targeting peptide. EVs were then loaded with doxorubicin by electroporation and administered to female BALB/c nude mice transplanted with MDA-MB-231 breast cancer cells, causing significant inhibition of tumour growth ($P < 0.01$) in a targeted manner that resulted in significantly less cytotoxicity than free doxorubicin ($P < 0.05$)[134]. Moreover, in a more recent study that investigated the benefits of EVs derived from T cells expressing chimeric antigen receptors (CARs), which themselves have recently been explored as a novel treatment for a wide range of cancers[135], Fu *et al.* (2019) observed that CAR-containing EV have anti-tumour activity both *in vitro* and in a severe combined immunodeficient (SCID) mouse model. CAR-containing EVs highly expressed cytotoxic perforin and granzyme B and did not express PD1; therefore, their anti-tumour activity was not weakened by recombinant PD-L1 treatment[136]. Each of these examples utilises different EV cargoes with differing anti-tumour activities, highlighting the versatility of EVs as targeted therapeutic devices. Thus, many other studies have also explored EVs in cancer treatment. Further significant contributions to this area have been reviewed elsewhere[131,137].

Independent of the use of EVs in cancer therapy, the use of EVs in neurodegenerative disorders represents some of the most significant contributions to developing EVs for targeted therapeutic delivery. Alvarez-Erviti *et al.* (2011) harvested EVs from mouse dendritic cells transfected with a rabies virus glycoprotein (RVG)-Lamp2b fusion protein to target EVs to the central nervous system. Electroporation was then used to load EVs with siRNA against beta-secretase 1 (BACE1), a protease responsible for Alzheimer's disease pathogenesis via N-terminal cleavage of the APP, which produced Aβ. This resulted in a significant 62% knockdown of BACE1 protein expression ($P < 0.01$) and

61% reduction in total BACE1 mRNA expression ($P < 0.01$) in mouse cortical tissue, as well as a significant 55% decrease in total Aβ42 levels ($P < 0.05$)[125]. Similarly, Tian *et al.* (2018) conjugated a brain lesion targeting peptide (c(RGDyK)) to EVs derived from bone marrow-derived MSCs by click chemistry and administered them to transient middle cerebral artery occlusion (MCAO) mice to treat ischaemic stroke brain lesions. c(RGDyK)-conjugated EVs loaded with curcumin targeted the lesion region of the ischemic brain and caused suppression of inflammation and apoptosis[138].

Aside from these major contributions to the therapeutic development of EVs, many other studies have engineered EVs with therapeutic potential and exploited their inherent therapeutic benefits. The use of EVs in the treatment of various diseases, including type 2 diabetes, myocardial infarction, inflammation, arthritis, hepatitis and even bone fractures, to name but a few, have been investigated and reviewed extensively elsewhere[131,139].

1.4 Current challenges in EV research

Despite considerable progress over the last few decades to understand EV biology and harness EVs for their therapeutic potential, EV research is faced with many technical challenges and unknowns that hamper further elucidation of EV characteristics, function, and therapeutic development[79].

1.4.1 Determining EV biodistribution

Following *in vitro* development of EV therapeutics, EVs often progress into *in vivo* studies using model organisms and, if successful, may progress into clinical trials. In *in vitro* phases of development, the focus is often placed on the efficacy, dosing, and toxicity of EV therapeutics. However, as EVs progress into *in vivo* studies, elucidation of EV biodistribution is also necessary to ensure that EVs efficiently target their intended sites within an organism. Additionally, EV biodistribution studies may also be meaningful in studies of EV heterogeneity to determine, for example, how EVs with different sizes, compositions, biogenesis, cellular origins, or functions distribute within organisms and, in return, may aid future therapeutic EV development.

Current methods of determining EV biodistribution involve labelling EVs with fluorescent, luminescent, or radioactive isotopes[140]. However, these commonly used methods lack sensitivity and specificity, producing false positives and negatives in EV biodistribution studies[140–144]. Chapter 3 of this thesis describes the various methods of determining EV biodistribution and their associated pros and cons. The use of a novel EV biodistribution tool that utilises short synthetic DNA sequences termed “barcodes” to determine EV biodistribution more sensitively and specifically was also explored.

1.4.2 EV purification

Since Chargaff and West first identified EVs in 1946[9], various methods of purifying EVs from biological materials, fluids, and cell culture supernatant have been developed, including various precipitation, ultracentrifugation, affinity, and chromatographic techniques, among other methods that continue to emerge. These purification techniques were developed to improve EV purity, integrity, and yield, improve purification speed and, in some cases, isolate specific EV subpopulations for downstream

applications[145,146]. However, access to appropriate equipment may present a barrier to some researchers in using the most appropriate purification technique to suit their downstream EV application, resulting in suboptimal EV purification quality and may impact EV analysis. Additionally, a lack of standardisation of the multitude of EV purification techniques has resulted in variations in the same techniques being performed, creating variability in results reported between similar studies. This has prompted ISEV to publish various studies and guidelines regarding the appropriate purification of EVs by various techniques and the steps necessary to characterise EVs before publication[18,19,147,148].

Additionally, as EV research and therapeutic development progress, upscaling cell culture to attain high or clinically relevant EV concentrations is essential, and this is often achieved using high-density cell culture techniques such as bioreactor or suspension culture[149–151]. However, with high EV yields comes high concentrations of contaminants such as host cell proteins and nucleic material, which popular EV purification techniques struggle to overcome to produce pure EV preparations. Therefore, this highlights the need to optimise a high throughput EV purification technique to purify EVs from high cell density culture preparations. In chapter 4 of this thesis, various methods of EV purification are described in detail, and the use of novel Capto Core binding chromatography is compared to size exclusion chromatography to validate its use in the purification of EVs from high cell density cultures.

1.4.3 EV heterogeneity

As previously described in section 1.2, “extracellular vesicles” is a collective term for many different subpopulations of cell-derived membranous nanoparticles that are often

further categorised as exosomes or MVs according to their route of biogenesis. Due to their extensive crossover in size (demonstrated in Figure 1.1), exosomes and MVs form a heterogenous assortment of EVs once released from cells. Furthermore, while identifying specific markers of exosomes and MVs has proven to be complex, exosomes and MV have also been shown to differ in protein expression and function[48,152]. Additionally, other degrees of EV heterogeneity have been shown to exist linked to EV size, cell type, cell state, protein expression and differentiation, and epigenetic factors[49,51,54,55,57,58,153].

Identifying heterogeneity within EV populations is essential to determine the different physiological and pathophysiological roles that EV subpopulations play. It may also reveal novel EV targets in treating various diseases or identify optimal subpopulations for therapeutic development. Furthermore, identification of the source or factors that affect EV heterogeneity and the impact that EV heterogeneity has on EV function is also important for therapeutic development[154]. Therefore, chapter 5 of this thesis describes various sources of EV heterogeneity previously identified in further detail. Additionally, size-based heterogeneity is scrutinised to identify marker proteins and proteins responsible for differential functions observed among EV subpopulations, and temporal change as a source of EV heterogeneity is investigated. Finally, functional heterogeneity among EVs derived from subclonal cell populations is also investigated to identify markers and functional proteins and determine whether EV heterogeneity is linked to cellular heterogeneity.

1.5 Thesis aims

In summary, extracellular vesicles are membranous cell-derived nanoparticles that play important roles in intercellular communication. EVs evoke functional activity in recipient cells via transfer of their bioactive cargoes. However, notable heterogeneity exists within secreted EV populations, which may impact EV function and therapeutic development. Furthermore, the field faces numerous technical challenges that need to be addressed to improve EV therapeutic development.

The following aims were addressed to confront some of these challenges:

1. Develop EV DNA-barcoding technology to provide a more sensitive and specific toolset for determining EV biodistribution *in vivo*. In addition to its potential benefits for therapeutic EV development, EV DNA barcoding may also be beneficial for investigating the effects of heterogenous EV populations *in vivo*, such as differences in EV uptake, targeting and cargo delivery.

2. Optimise the use of Capto Core binding chromatography as a novel alternative to purify EVs from high cell density cultures from host cell proteins and nucleic acids. Additionally, the efficiency of Capto Core binding chromatography will be compared to size exclusion chromatography to determine whether Capto Core is a valid and beneficial alternative.

3. Identify functional heterogeneity between different EV subpopulations and scrutinise their protein expression to identify patterns in functional protein expression that may

explain functional differences between EVs. Additionally, characterisation will be performed to discover markers of functional EV subpopulations that may be used to help purify therapeutically beneficial EV subpopulations. Finally, EVs derived from single cell sorted subclonal EV populations will be analysed to determine whether the source of heterogeneity within EV populations is linked to the heterogeneity of single cell precursors.

2.0 Materials and Methods

In this chapter, materials and methods that were employed throughout chapters 3, 4 and 5 of this thesis are described. Subsequent chapters also contain descriptions of materials and methods specific to or significantly different from the universal materials and methods described here.

2.1 Cell culture

Throughout investigations within this thesis, various cells were cultured *in vitro*. Some cell populations were expanded, and EVs were purified for use in further experiments. Other cell populations were grown to use in various *in vitro* assays to test EV function. Table 2.1 presents the various cell lines cultured, their source, and the mediums used for each.

Cells	Cell source	Culture medium
hTERT immortalised bone marrow derived mesenchymal stem cells (MSCs)	Kindly provided by Samir El Andaloussi (Karolinska Institutet, Stockholm, Sweden)	RPMI-1640 (Gibco, Waltham, MA, USA), +10% foetal bovine serum (FBS), + 1% 100x antibiotic/ antimycotic solution (A/A) (Sigma Aldrich, MO, USA).
Human embryonic kidney (HEK) 293T	ATCC, Manassas, VA, USA	DMEM (Gibco, Waltham, MA, USA) +10% FBS, + 1% A/A
Neuro2a	ATCC	DMEM +10% FBS, + 1% A/A
SKOV3	ATCC	DMEM +10% FBS, + 1% A/A
M.D. Anderson - Metastatic Breast 231 (MDA-MB-231)	ATCC	DMEM +10% FBS, + 1% A/A
ASC52telo, hTERT immortalised adipose derived MSCs (SCRC-4000, ATCC)	ATCC	MSC Basal Medium for Adipose, Umbilical and Bone Marrow-derived MSCs (ATCC) supplemented with Mesenchymal Stem Cell Growth Kit for Adipose and Umbilical-derived MSCs – Low Serum (ATCC) supplements and 1% A/A (Gibco). OptiMEM (Gibco) supplemented with 2% FBS (Gibco), 1% A/A (Gibco), 5 ng/mL recombinant human (rh) epidermal growth factor (EGF) (Novus Biologicals, Littleton, CO, USA), 5 ng/ mL rh- fibroblast growth factor (FGF) acidic (Novus Biologicals) and 5 ng/mL rhFGF basic (Novus Biologicals).
Human microvascular endothelial cells (HMEC-1)	CDC, Atlanta, GA, USA	MCDB131 medium with L-glutamine (Sigma Aldrich) supplemented with 1.18g of $NaHCO_3$ (Sigma Aldrich) and 1% A/A. The solution was divided in two and 10% FBS and 10 ng/mL rhEGF (Novus Biologicals)

Table 2.1 Cell lines and their culture medium. hTERT immortalised bone marrow-derived MSCs were isolated from human bone marrow and immortalised by Mihara *et al.* 2003[155].

All cell lines were grown in tissue culture vessels (Star Lab, Brussels, Belgium) and expanded to cell densities appropriate to their downstream applications. Cells were incubated at 37°C in a humidified environment of 5% CO_2. Cell cultures were checked

for mycoplasma contamination fortnightly using a PCR Mycoplasma Test Kit I/C (Promokine, Heidelberg, Germany).

2.2 Bioreactor cell culture

hTERT immortalised bone marrow-derived MSCs (used in chapter 3) and HEK293T cells (used in chapter 4) were expanded to 5 x 10^8 cells in 15 cm dishes (Star Lab, Brussels, Belgium) and seeded into the extra-capillary space (ECS) of FiberCell Systems C2011 20kD MWCO hollow-fibre bioreactor (FiberCell Systems, New Market, MD, USA). Once seeded, the glucose concentration of the complete culture medium in the reservoir was checked daily using a Bayer Contour XT Glucometer (Bayer, Leverkusen, Germany). The medium was renewed when 50% of the starting glucose was depleted.

2.3 Conditioned medium collection and concentration by tangential flow filtration

In preparation for harvesting conditioned medium from plate-based cell cultures, routine culture medium was removed and replaced with serum and supplement-free medium. In most cases, OptiMEM +1% A/A was used. However, in the case of HMEC-1 cells, serum and supplement-free MCDB-131 medium +1% A/A was used. Cells were incubated for 48 hours prior to harvest.

DMEM +1% A/A was flushed through the extra-capillary space (ECS) via the side ports and re-collected to harvest conditioned medium from the bioreactor. 22 mL of medium from the reservoir bottle was then drawn through the hollow fibres into new syringes on each side port and flushed among the syringes four times to dislodge material within the ECS. This was repeated three times.

Resulting harvests were pooled, centrifuged at 700 x *g* for five minutes, then 4000 x *g* for 20 minutes. Subsequently, medium was concentrated to ~5 mL by TFF with a 100 kDa MWCO Sartorius Vivaflow 50R hydrosart filtration system (Sartorius, Göttingen, Germany).

2.4 Size exclusion chromatography

Following TFF, concentrated conditioned medium intended for EV purification was further concentrated to <2 mL with Amicon Ultra 100 kDa MWCO centrifugal filters (Merck Millipore, Burlington, MA, USA) at 4000 x *g*. Subsequently, EV purification by size exclusion chromatography (SEC) was performed on an ÄKTA Pure chromatography system (Cytiva, Marlborough, MA, United States) with a Tricorn 10/300 column packed with Sepharose Fast Flow 4 resin (Cytiva) to separate EVs from host cell protein. Elution was performed in PBS at a flow rate of 0.5 mL/min and monitored through absorbance at 280 nm.

2.5 Capto Core binding chromatography

Following TFF, concentrated condition medium intended for EV purification by Capto Core binding chromatography was passed through a 5 mL HiScreen 700 Capto Core (CC700) column (Cytiva) using an ÄKTA Pure chromatography system at 0.5 mL/minute. Flow through containing purified particles was collected. Chromatography was performed in PBS and monitored using absorbance at 280 nm. CC700 was cleaned between runs using 0.5 mL/minute reverse flow of 1M NaOH in 30% isopropanol.

2.6 Nanoparticle tracking analysis

Particle size and concentration were determined with a Nanosight NS500 (Malvern Panalytical, Malvern, UK) using NanoSight NTA 3.3 software. Three 30-second videos were recorded for each sample with a delay of 5 seconds between each video. For all the recordings, the camera level was set at 13-14 with a well-adjusted camera focus for maximum sharpness. Detection threshold was set at 5, screen gain at 1.0, while other functions were set to automatic. Samples were diluted in 0.22μm filtered PBS.

2.7 Nanoflow cytometry

EVs were incubated with fluorescent antibodies, each of which is detailed in Table 2.2. Samples were incubated for two hours at room temperature at 500RPM on a Thermo Fisher Scientific Isotemp microtube shaker. After two hours, samples were made up to 100 μL with 0.22 μm filtered PBS to dilute unbound antibodies below interfering levels of background fluorescence.

Antibody	Source	Final Dilution
Mouse anti-CD81-PE	BD, Franklin Lakes, NJ, USA, 555676	1:100
Mouse anti-CD63-PE	BD, 556020	1:100
Mouse anti-CD9-PE	BD, 341647	1:100
Mouse anti-CD63-FITC	Miltenyi Biotech, Bergisch Gladbach, North Rhine-Westphalia, Germany 130-123-921	1:100
Mouse anti-CD29-FITC	Miltenyi Biotec, 130-123-935	1:100
Mouse anti-CD107a (LAMP-1)-FITC	Miltenyi Biotec, 130-119-957	1:100
Mouse anti-CD26-PE	Miltenyi Biotec, 130-126-411	1:1000
Recombinant human anti-HLA-A3-FITC	Miltenyi Biotec, 130-115-793	1:100
Recombinant human IgG1 anti-CD59-VioBright-FITC	Miltenyi Biotec, 130-118-501	1:100
Mouse anti-mIgG 1 isotype control-PE	BD, 555749	1:100

Table 2.2 Nanoflow cytometry antibodies. Primary antibody conjugated to fluorophores (PE or FITC) used in nanoflow cytometry analysis, their source and final dilution.

Labelling was assessed by nanoflow cytometry (NFC) using the NanoFCM Flow NanoAnalyzer and NF Profession 1.15. System alignment was performed using 0.25 μm Fluorescent Silica Microsphere (NanoFCM, Nottingham, UK), and sampling pressure was set to 1 kPa. Side scatter and 488 nm (FITC) channel intensity were between 1,000 and 1,500 with ≥30 events. The 638 nm (PE) channel intensity was calibrated to between 500 and 1,000 with ≥30 events. Events were recorded for one minute for use as a concentration standard. Size standard acquisition was performed using the 68-155 nm S16M-Exo Silica Nanosphere Cocktail (NanoFCM). Events were recorded for one minute, and a size standard curve was constructed.

Samples were diluted with PBS to between $1x10^8$ and $1x10^9$ particles/mL, and between 2,000 and 12,000 events were sought after. A PBS-only sample was used as a blank.

2.8 Western blotting

For SDS PAGE (sodium dodecyl sulphate polyacrylamide gel electrophoresis), samples were diluted with lithium dodecyl sulphate sample buffer (Thermo Fisher Scientific) and sample reducing agent (Thermo Fisher Scientific), heated ten minutes at 70°C and separated on a 4-12% Bis-Tris polyacrylamide gel (Thermo Fisher Scientific) accompanied by a Bio-Rad Dual Colour protein standard ladder (Bio-Rad). Proteins were blotted onto a PVDF membrane and membranes and blocked for 1 hour in Intercept Blocking Buffer (LI-COR Biosciences, Lincoln, NE, USA) at room temperature (RT). Immune-labelling with primary antibodies was performed in Intercept Blocking Buffer overnight at 4 °C or for 1 hour at RT. Details of primary antibodies can be seen in Table 2.3. Secondary antibodies included IRDye 800CW anti-mouse antibody (LI-COR Biosciences, 926-32210, 1:10,000 dilution) and IRDye 800CW anti-rabbit antibody (LI-COR Biosciences, 926-32211, 1:10,000 dilution). Imaging was performed on an Odyssey Infrared Imager (LI-COR Biosciences) at 700 nm and 800 nm or on a Bio-Rad ChemiDoc MP (Bio-Rad, Hercules, CA, USA) using IRDye 680RD and 800CW settings.

Antibody	Source	Final Dilution
Rabbit anti-ALIX	Abcam, Cambridge, UK, ab186429	1:1000
Mouse anti-syntenin	Origene, Rockville, MD, US, TA504796	1:1000
Mouse anti-CD81	Santa Cruz, Dallas, TX, USA, SC-166029	1:1000
Rabbit anti-annexin A1	Abcam, ab214486	1:1000
Rabbit anti-calnexin	GeneTex, Irvine, CA, USA, GTX 101676	1:1000
Rabbit anti-b-actin	Sigma Aldrich, A1978	1:1000
Rabbit anti-TSG101	Abcam, ab125011	1:500
Rabbit anti-fibronectin FN1	Sigma Aldrich, F3648	1:2000
Mouse anti-CD44	BioLegend, 858802	1:500
Rabbit anti-annexin A2	Cell Signalling Technology, 8235S	1:1000
Mouse anti-CD151	Santa Cruz, sc-271216, 1:500	1:500
Rabbit anti-CD29	Cell Signalling Technology, Danvers, MA, USA, 9699S	1:1000
Mouse anti-caveolin-1	Novus Biologicals, NB100-615	1:1000

Table 2.3 Western blotting primary antibodies. Primary antibodies used in western blotting, their source and dilution.

2.9 Transmission electron microscopy

If required, the EV solution was diluted with water to a protein concentration of 100-200 µg/ml. Next, carbon coated 300 mesh copper grids were glow discharged and inverted carbon side face down onto a 10 µl droplet of an EV suspension for 2 minutes. Subsequently, the grid was blotted with filter paper and stained for 10 seconds with 2% uranyl acetate, followed by blotting and air drying. Finally, grids were imaged in an FEI Tecnai 12 transmission electron microscope (FEI Company, Hillsboro, OR, USA) at 120 kV using a Gatan OneView CMOS camera (Gatan, Pleasanton, CA, USA).

3.0 Exploring EV DNA barcoding as a potential enhanced EV biodistribution tool

3.1 Introduction

3.1.1 EV biodistribution and uptake

Following administration of EVs to a recipient, often systemically[156], EVs perfuse throughout the circulation and distribute to different sites within the body. Subsequently, EVs can reach recipient cells and deliver their cargo to elicit physiological changes. For this to occur, either ligands or receptors in the membrane of EVs must interact with their counterparts on the cell membrane, evoking a signalling cascade that results in physiological change. Otherwise, EVs must interact with cells and be internalised to release their cargo and elicit change in cellular function[157].

While EV transportation and distribution mechanisms are yet to be precisely defined, protein enrichment on the EV surfaces and receptor expression on recipient cells is the most likely determinant of EV target cell specificity. Numerous examples of this phenomenon have been recorded, including phosphatidylserine, CD11a, intercellular adhesion molecule 1, and the tetraspanins CD9 and CD81 on EVs associating with integrins and cell adhesion molecules on recipient dendritic cells to facilitate their uptake[59], Tspan8 on EVs interacting with integrins on recipient cells[64], and EVs engineered to express rabies viral glycoprotein (RVG) specifically interacting with acetylcholine receptors on recipient neuronal cells in the brain[125].

Likely due to heterogeneous expression profiles of EV surface proteins, EVs from different sources and with different modifications present heterogeneous distribution profiles. However, EV dose and route of administration have also been shown to affect EV biodistribution[158]. Therefore, identifying the different distribution profiles of EVs is a critical step in developing EV therapeutics to discern their potential efficacy and safety. Additionally, it is important to determine the impact that heterogeneity within EV populations may have on EV biodistribution. With further understanding of how EVs distribute within the body down to a single vesicle level, it may be possible to harness or mitigate EV heterogeneity to improve the efficacy of EV therapeutics.

In addition to EV biodistribution, determining EV circulation half-life and factors affecting EV clearance or uptake into recipient cells and tissues are also important factors to determine during EV therapeutic development. In a systematic review of biodistribution studies in animal models, Kang *et al.* (2021) presented that while EVs derived from different sources may have different biodistributions, EVs accumulate in major organs of clearance; liver, lungs, kidneys and spleen[144]. Furthermore, numerous markers on the surface of EVs have been suggested to promote or inhibit EV clearance. For example, naturally present CD47 and the addition of polyethylene glycol have been shown to increase EV circulation time and inhibit uptake and clearance by macrophages[129,159], while phosphatidylserine is recognised by macrophages leading to EV clearance[160].

Furthermore, Kang *et al.* (2021) also argued that while most biodistribution studies aim to understand where EVs target and therefore where the EVs are most likely to elicit biological effects, experimental restraints are responsible for the clearance of most administered EVs from circulation. Such constraints include the administration of the EVs

via a single bolus, resulting in excessive EV concentrations that do not reflect physiological EV concentrations achieved by continuous release[144]. Wiklander *et al.* (2015) demonstrated this as while engineering EVs to express RVG resulted in increased accumulation in the brain, a high quantity of EVs continued to localise to the liver, spleen, lungs, and kidneys[158].

3.1.2 Detecting biodistribution

As interest in the potential of EVs as a biotherapeutic delivery platform has increased, numerous methods have emerged to analyse EV biodistribution and clearance *in vivo*. Many of these methods involve directly labelling EVs or their parent cells with moieties that can be detected using various techniques and equipment[140].

The most prominent category of EV labelling for biodistribution analysis is fluorescent labelling. Here EVs are labelled with fluorophores which emit a fluorescent signal when excited by specific electromagnetic wavelengths. Emitted fluorescent signals can then be either visualised with a microscope fitted with appropriate fluorescent filters or measured using a fluorometer or flow cytometer with appropriate filters and detectors. Fluorescent labelling includes direct incubation of fluorescent lipophilic dyes or membrane crosslinkers, intraluminal loading of fluorescent molecules and transfection or modification of parent cell lines to include fluorescent proteins[140].

Various lipophilic fluorescent dyes have been employed for biodistribution analysis, including PKH dyes (PKH26, PKH67) and carbocyanine dyes (DiD, DiL DiO, DiR) which embed themselves in EV membranes. This method of EV labelling for biodistribution analysis has been widely employed. It is simple to perform with direct incubation of dyes

with EVs and provides a consistent signal for EV uptake and biodistribution studies[161–164]. Despite this, there are numerous pitfalls associated with lipophilic dye labelling. Firstly, low fluorescence intensity and limited tissue penetration make biodistribution analysis difficult. Furthermore, signal loss is experienced in cases where imaging techniques are employed to assess distribution, and transfer of dyes to non-EV membranes can produce false positives and background fluorescence in *in vivo* imaging, thus requiring organs to be imaged *ex vivo* to mitigate background signals[165,166]. False positives have also been reported due to lipophilic dyes labelling lipoprotein particles that can copurify with EVs and the presence of aggregated dye molecules that form nanoparticles of a similar size to EVs[141,167].

While less popular, covalent labelling of EV membranes is also employed to assess EV biodistribution. NHS and maleimide are the most common covalent crosslinker used for EV labelling, however various methods of click chemistry have also been employed[168–170]. Much like lipophilic dyes, labelling EVs with covalent fluorophores is a simple process that requires direct incubation. The method is intended to universally label EV membranes while ensuring EV size is not affected and does not impact the function of EVs on recipient cells[171,172]. However, covalent methods also present numerous issues, including substantial non-specific labelling creating high background signal, including labelling lipoprotein particles, and incomplete labelling of EV populations[141,142].

EVs can also be labelled with fluorescent protein reporters by transfection of parent cell lines with plasmids encoding fluorescent proteins fused with EV membrane proteins, i.e. CD63-GFP[158,173] or -RFP[174]. This method can circumvent false positive detection through non-specific labelling and aggregation observed in direct labelling techniques. Fusion

proteins have also been modified to be pH-sensitive, enabling monitoring of their release, transfer, uptake, and function over time. However, in some cases, weak fluorescence limited quantitative analysis and analysis of *in vivo* interactions[174–176]. In other cases, only low proportions of secreted EV populations contain the fluorescent protein[158], and overexpression of modified EV surface proteins has had undesirable biological effects[177].

Aside from fluorescence, bioluminescence is another frequently used method of assessing biodistribution[178–182]. Here, cells are transduced with protein reporter genes which emit luminescent signals. Released EVs express the protein internally or on the membrane. Light is emitted from an enzymatic reaction wherein a substrate is added that is converted by the luciferase enzyme to luciferin, which luminesces and signals are quantified or imaged in a similar manner to fluorescence techniques. Bioluminescent imaging has a high signal-to-noise ratio suitable for tracking EV biodistribution. Furthermore, the visualisation of EVs using bioluminescent imaging is highly specific and reliable. However, like fluorescence-based techniques, bioluminescence imaging also suffers from low intensity, low tissue penetration and short half-life signals, and is more time-consuming and resource-intensive to perform than most fluorescence-based techniques[140,177,178].

Nuclear imaging has also been employed to assess EV biodistribution. EVs are labelled with a radioactive isotope, and emitted radiation signals are detected by gamma cameras, positron emission tomography/computed tomography (ET/CT)[183–186], or even magnetic resonance imaging (MRI) for better localisation of EVs. Nuclear imaging can be applied to trace EVs or achieve high-sensitivity images with deep tissue penetration. The major drawback of this issue is its safety and accessibility, as radioactive isotopes can

harm human health, and training is required to handle these substances. Facilities in which nuclear research is performed also need to be appropriately outfitted for general health and safety[140].

Similarly, there are a small number of studies that have explored tomography for assessing EV biodistribution. To perform tomography, EVs are labelled with nanoparticle tracers and biodistribution determined by CT or MRI. Like nuclear imaging, tomography enables deep penetration. Furthermore, tomography enables long-term observation of EVs and presents high image resolution, enabling sites of EV accumulation to be precisely determined[184,187,188]. However, tomography suffers from low sensitivity as a high number of nanoparticles must accumulate in one place to be detected, and like fluorescent labelling, nanoparticles labelled on or in EVs may release during circulation, yielding possible false positives as they may accumulate in different places to EVs. Access to specialist equipment may also be a barrier to using this technique[140,143].

Overall, various methods have been investigated and employed to assess EV biodistribution and uptake. Each method has various advantages and may suit different applications, but each also presents numerous drawbacks. Synonymous with the observations of Kang *et al.* (2021), most methods referred to suffer from sensitivity issues. Therefore, it is unlikely that many of these methods will be able to quantify EV biodistribution using EV concentrations closer to physiological norms[144]. As the development of the therapeutic EV platform continues, sensitive and specific EV biodistribution tools are required to understand the physiology and biodistribution of therapeutic EVs *in vivo* and to understand how EV heterogeneity may impact therapeutic efficacy.

3.1.3 EV DNA barcoding

Until now, there have been few examples of the use of nucleic acid quantification as a method of identifying or quantifying EVs. Various studies have investigated the microRNA content of EVs, which seems to change depending on the cell source and its physiological state[189]. However, likely due to inconsistent expression of EV microRNA, it has not been employed for EV biodistribution analysis. Other studies have developed techniques similar to DNA-assisted immunoassays, where amplifiable oligonucleotides are conjugated to antibodies or affinity probes and incubated with EVs. Specific proteins on EV surfaces associate with specific DNA sequences, and by identification of these sequences, EV surface proteomes can be quantified on a single-EV basis[190]. However, while these techniques have been used for EV detection and characterisation, they have not been developed for biodistribution analysis[191–193].

In this chapter, the aim was to develop a new EV biodistribution tool in the form of EV DNA barcoding. In this technique, EVs are first incubated with DNA capture probes, short synthetic single-stranded DNA sequences functionalised with a covalent crosslinker. Capture probes can crosslink with EV membranes and then hybridise with a barcode, a complimentary short synthetic single-stranded DNA sequence. Labelling EVs with a precise, reliably reproducible quantity of DNA barcodes would allow for indirect quantification of EVs by qPCR. If successful, EV DNA barcoding could overcome some of the sensitivity and specificity issues encountered in other biodistribution analysis methods, as qPCR has a theoretical lower limit of detection at 95% confidence of between two and four target molecules[194]. Additionally, as the barcode sequences are synthetic, there is no risk of amplifying naturally occurring genomic DNA sequences.

Therefore, EV DNA barcoding offers the potential to identify accumulation of single EVs in organs and tissues following administration.

3.2 Materials and Methods

3.2.1 EV DNA barcoding and EV labelling

EV DNA barcoding involves the decoration of EV surfaces with crosslinker functionalised single-stranded DNA sequences and the subsequent hybridisation of a complementary DNA barcode to the capture probe. Barcodes are then detected and quantified by qPCR. Figure 3.1 describes the process in further detail.

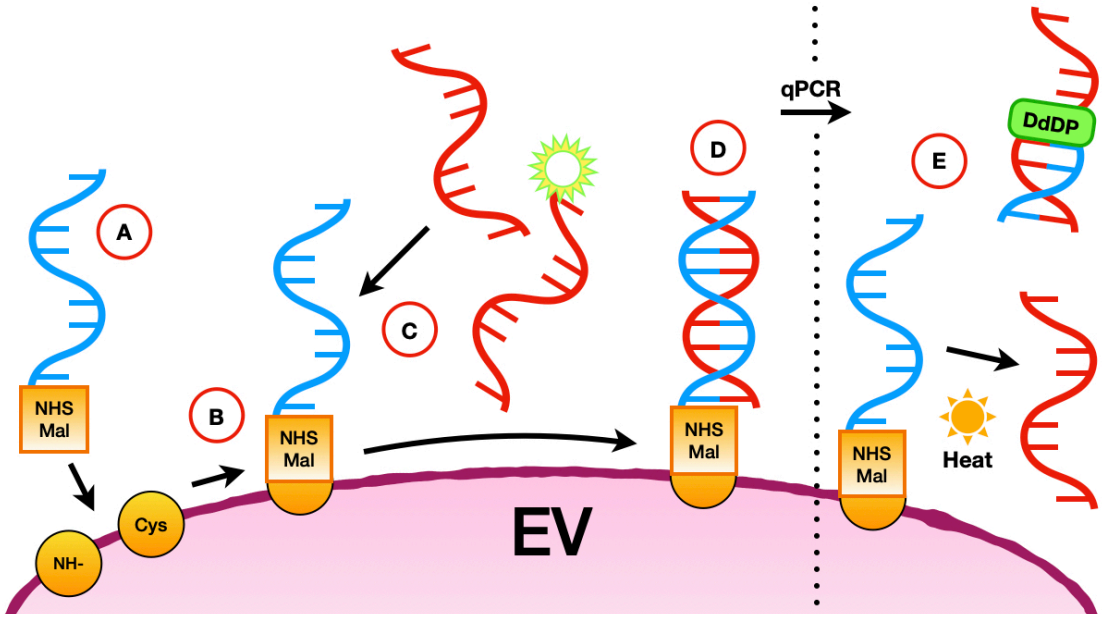

Figure 3.1 EV DNA barcoding. (A) Capture probes are single-stranded DNA sequences conjugated to N-Hydroxysuccinimide (NHS) or maleimide (Mal) (Integrated DNA Technologies, Coralville, IA, United States). (B) EVs were incubated with an excess of capture probes to 10^{11} EVs to first allow binding of capture probes to free amine (NH-) or cystine (Cys) residues on the EV surface. (C) Following SEC to remove excess capture probes, single-stranded DNA barcodes, with or without fluorophore conjugation depending on final quantification technique, were added in 10x excess to capture probes. Samples were topped up to 500 µL with PBS, and 50 µM Tris(2-

carboxyethyl)phosphine (TCEP-HCl) (Fisher Scientific, Waltham, MA, United States) was added. (D) Samples were incubated for two hours at room temperature on a tube rotator to allow hybridisation of the single-stranded DNA barcode to capture probe sequences on the EV surface. EVs were purified from unbound excesses by SEC using an ÄKTA Start chromatography system (Cytiva) with a Tricorn 10/200 column packed with Sepharose Fast Flow 4 resin (Cytiva). Elution was performed in PBS at a flow rate of 0.5 mL/min and monitored through absorbance at 280 nm. EV fractions were collected, and EVs were re-quantified using the Nanosight. (E) qPCR using a master mix containing a DNA directed DNA polymerase (DdDP) was performed as described in section 3.2.2 to quantify the number of barcode copies in each sample. Barcode copies per EV were calculated using NTA. Capture probe and barcode sequences are outlined in Supplementary Table S3.1.

3.2.2 Quantitative polymerase chain reaction (qPCR)

Labelling efficiency in experiments that used unlabelled barcodes was evaluated by qPCR. A standard curve of barcodes was calculated using a known concentration range and used to calculate copies of barcodes per EV using NanoSight data following clean-up.

qPCR reaction mixtures were prepared using 6 µL KiCqStart® SYBR® Green qPCR ReadyMix™ (Sigma Aldrich) and 5 nM forward and reverse primers (Integrated DNA Technologies). EV samples were diluted by up to 10,000x with nuclease-free water (Ambion, Austin, TX, USA) to ensure they were in the range of barcode standards, and 1.5 µL was added to each reaction mixture. Each reaction mixture was made up to 10 µL with nuclease-free water to achieve the quoted concentrations primers. Primer

sequences can be seen in Supplementary Table S3.1. Barcode copies in EV samples were quantified using the Step One Plus Real-Time PCR system (Applied Biosystems, Waltham, MA, USA).

3.2.3 Fluorescent assay

Labelling efficiency in experiments that used barcodes conjugated to fluorescein (Integrated DNA Technologies) were evaluated by a fluorescent assay. The assay was performed in 96-well F-bottom Black FluoTrac microplates (Greiner Bio-One, Kremsmünster, Austria) and quantified in a Clariostar Plus Microplate Reader (BMG Labtech, Aylesbury, UK).

A standard curve of fluorescent barcodes was calculated using a known concentration range to calculate copies of fluorescent barcodes per EV using Nanosight data following clean-up.

3.2.4 siRNA delivery

For siRNA delivery experiments, EVs were labelled in the same manner described in section 3.2.4, but with the addition of a sense DNA strand (Integrated DNA Technologies) and an antisense anti-luciferase siRNA strand (Integrated DNA Technologies) that adhered to the sense DNA in the incubation process. siRNA sense and antisense siRNA strands hybridised with sense strands which in turn hybridised to capture probe strands. Sequences for each are outlined in Supplementary Table S3.1.

siRNA delivery using barcoding capture probes was assessed by incubating ~5 x 10^8 EVs with 50,000 Neuro2a cells seeded 96 well plates that stably expressed firefly and renilla

luciferase. The resulting luminescent signal was measured to determine the extent of luciferase knockdown achieved by siRNA delivery. In addition to EVs labelled with siRNA, PBS, EV only negative controls, and 1 and 50 nM siRNA transfection controls were used. RNAiMAX (Thermo Fisher Scientific, Waltham, MA, USA) was used to transfect siRNA following the manufacturer's protocol.

Following 24-hour incubation at 37°C in a humidified atmosphere of 5% CO_2, a Dual Glo Luciferase assay (Promega, Madison, WI, USA) was performed following the manufacturer's protocol. Relative percentage change of renilla and firefly luciferase expression was calculated as outlined in the manufacturer's protocol, where the positive control was the 50 nM siRNA transfection, and the negative control was the EV-only sample.

3.3 Results

3.3.1 Optimisation of EV DNA Barcoding

MSC EVs purified from bioreactor harvests were characterised prior to the commencement of DNA barcoding optimisation. Figure 3.2A presents NTA size distribution analysis of particles derived from the bioreactor. Particles demonstrated a typical EV size distribution of between 50 and 200 nm with a modal size of 125 nm, as presented by the peak in the size distribution profile. Furthermore, as seen in Figure 3.2B, TEM images displayed numerous cup-shaped particles typical of EVs in this format. In addition, minimal other structures and dark staining material were visualised, presenting EVs to be well purified. Finally, western blots shown in Figure 3.2C presented high expression of typical EV markers of β-actin, annexin A1, syntenin and CD81, and low to no expression of co-isolate markers, fibronectin and calnexin, demonstrating high representation of EVs in purified MSC bioreactor harvests. Overall, particles isolated from the MSC bioreactor presented a typical EV morphology and proteome and were therefore viable for use in barcoding optimisation experiments.

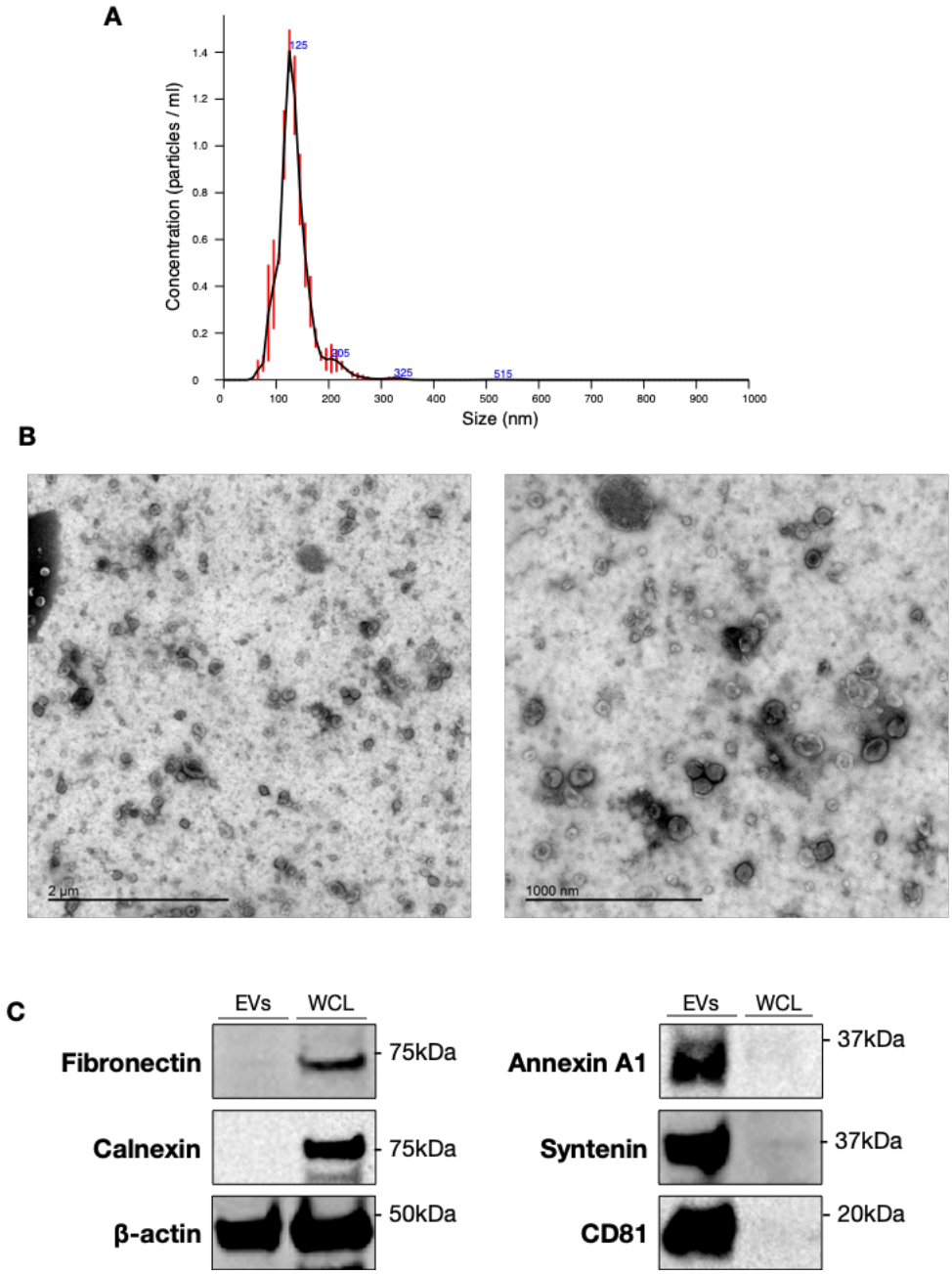

Figure 3.2 Bioreactor-derived MSC EV characterisation. (A) EV size distribution from purified MSC bioreactor harvests, identified using the NS500 NanoSight. (B) TEM images of EVs purified from MSC bioreactor harvests at 2 µm and 1 µm scale, respectively. (C) Western blot characterisation of purified MSC bioreactor harvests presenting the

expression of EV markers (β-actin, annexin a1, syntenin and CD81) and non-EV markers (fibronectin and calnexin).

Following confirmation of successful MSC EV purification from bioreactors, optimisation of the EV DNA barcoding protocol was commenced, beginning with investigating a one-step incubation process instead of a two-step incubation process, as described in sections 3.2.4 and Figure 3.1. In the first phase, EVs were incubated with DNA capture probes to decorate EV surfaces prior to purification of decorated EVs by SEC to remove excess capture probes. In the second phase, EVs were incubated with DNA barcodes which hybridised with DNA capture probes, prior to purification of decorated EVs by SEC to remove excess capture probes.

Firstly, the efficiency of decorating EVs with a one-phase protocol that included incubation of EVs with both capture probes and barcodes as opposed to separate incubations was compared to attempt to speed up the EV DNA barcoding protocol and eliminate the need for a second purification step. Following EV purification and Nanosight determination of EV concentration, the EV prep was divided into two sets of samples; the first for a one-phase reaction and the second for a two-phase reaction. In both cases, MSC-derived EVs were incubated with a 1,000x or 10,000x excess of maleimide-functionalised capture probes to EVs and a 10x excess of barcode to capture probe. A barcoding control was also prepared by omitting capture probes and incubating EVs with a 10,000x excess of barcode to EVs (same quantity as 1,000x sample). As seen in Figure 3.3A, the two-phase reaction yielded more barcode copies per EV for both 1,000x and 10,000x excesses compared to the one-phase reaction. However, the two-phase 1,000x sample yielded extremely high barcode concentrations that likely indicated

contamination or sample preparation errors due to the number of barcodes per EV being far greater than all other samples. Additionally, compared to the control, the one-phase reactions yielded a surprisingly low number of copies per EV. However, Figure 3.3B presents the EV concentration data of each sample. EV concentrations in the two-phase reactions were roughly three to ten times lower than the one-phase reactions and close to the limit of detection of the Nanosight. Together these results indicated that while the two-phase protocol elicited a higher number of barcode copies per EV than the one-phase protocol, substantial EV losses were seen, likely due to performing two purification steps. This could create the illusion of a higher number of barcode copies per EV by having fewer EVs after the two-phase protocol. Therefore, the one-phase reaction was selected for further study.

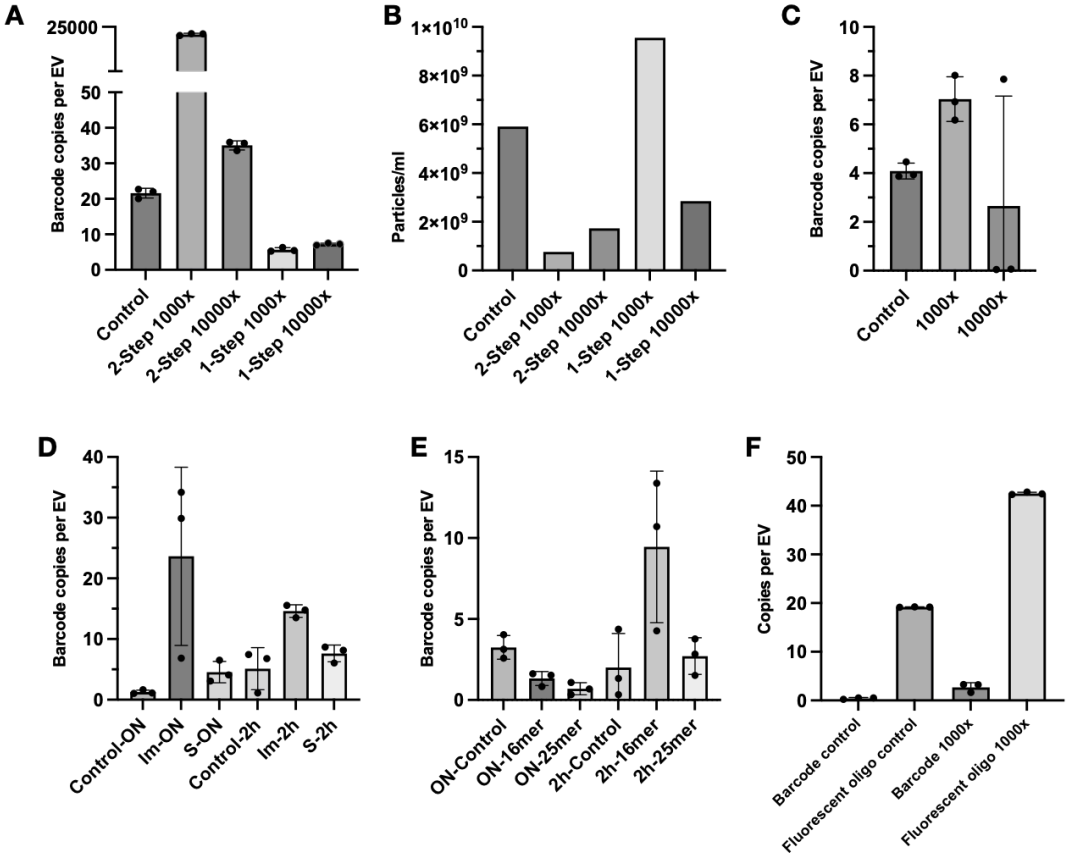

Figure 3.3 Optimisation of EV DNA barcoding. (A) MSC EVs incubated with capture probes followed by barcodes (2-Step) or incubated with both simultaneously (1-Step). 1,000x and 10,000x excesses of capture probes to EVs were used. (B) EV concentrations determined by Nanosight of purified 2-Step and 1-Step samples. (C) EVs incubated with 1,000x and 10,000x excesses of capture probes to EVs in pH 8.0 TE buffer. (D) EVs incubated with immobilised TCEP (Im) prior to capture probe addition or soluble TCEP (S) overnight at 4°C (ON) or for two hours at room temperature (2h). 1,000x excess of capture probes to EVs was used. (E) EVs incubated overnight at 4°C (ON) or for two hours at room temperature (2h) with a 16-nucleotide or 25-nucleotide capture probe. 1,000x excess of capture probes to EVs was used. (F) EVs incubated with a 1,000x excess of capture probes to EVs and either DNA barcodes or fluorescent DNA barcodes. A 10x excess of barcodes or fluorescent barcodes to capture probes was used in all cases. Controls represent EV incubations with DNA barcodes but without capture probes. Values are means of technical replicates ±SD; n=1.

Next, to investigate whether pH was the cause of low labelling efficiency in the one-phase reactions, the reaction was conducted in pH 8.0 TE buffer (Sigma Aldrich). A 1,000x and a 10,000x excess of maleimide capture probes to MSC EVs were used, along with a 10x excess of barcodes to capture probes. As shown in Figure 3.3C, the inclusion of TE buffer made little to no difference to labelling efficiency compared to the efficiency seen in 3.2A. The 10,000x excess of barcodes to EVs also yielded no improvement in EV labelling.

Subsequently, as there is much debate as to whether TCEP helps or hinders membrane crosslinking efficiency[195–198], it was investigated whether the cause of poor EV labelling could be due to the inclusion of TCEP during the labelling process. Samples were

prepared using 25 µL of Piece Immobilised TCEP (Thermo Fisher Scientific) as opposed to soluble TCEP so that following reduction of disulphide bonds to expose free thiol groups on EV surfaces, TCEP could be removed from the samples prior to the addition of barcodes. Incubation time was also explored to improve labelling efficiency. In all cases, a 1,000x excess of maleimide-functionalised capture probes to MSC-derived EVs was used. EVs were incubated either overnight at 4°C with immobilised or soluble TCEP prior to capture probe addition or soluble TCEP, or for two hours at room temperature with immobilised or soluble TCEP prior to capture probe addition or soluble TCEP. Prior to SEC, samples with immobilised TCEP were centrifuged at 1,000 x *g* for one minute to remove immobilised TCEP. Barcoding controls were also prepared by omitting capture probes and incubating EVs with a 10,000x excess of barcodes to EVs either overnight at 4°C or for two hours at room temperature. As seen in Figure 3.3D, immobilised TCEP before capture probe addition seemed to continue producing the greatest labelling efficiency with both overnight and two-hour incubation. However, labelling success was very low compared to controls, and there was a wide variation among replicates. Overnight incubation improved labelling efficiency when using immobilised TCEP but reduced labelling efficiency with soluble TCEP. Overall, incubation of EVs with immobilised TCEP followed by its removal prior to labelling reactions caused superior labelling efficiency compared to soluble TCEP included within reactions. However, immobilised TCEP could not continue to be used due to residual beads blocking the liquid chromatography apparatus, thus soluble TCEP was used in further experiments.

Next, the use of a longer 25-nucleotide (25-mer) capture probe (Integrated DNA Technologies) sequence was compared with the original 16-nucleotide (16-mer) long capture probe with and without overnight incubation to explore whether an extended

capture probe sequence could improve EV labelling efficiency. In all cases, a 1,000x excess of maleimide-functionalised capture probes to MSC-derived EVs was used. EVs were incubated either overnight at 4°C or for two hours at room temperature. Barcoding controls were also prepared by omitting capture probes and incubating EVs with a 10,000x excess of barcodes to EVs either overnight at 4°C or for two hours at room temperature. As shown in Figure 3.3E, two-hour incubation with the 16-mer capture probe produced the greatest labelling efficiency but was highly varied among replicates. All other samples did not deviate far from the controls, and overall labelling efficiency remained very low. Therefore, the original 16-mer capture probe continued to be used with two-hour incubations at room temperature.

After numerous changes to the labelling protocol with little to no improvements in labelling efficiency, to explore the possibility that barcode contamination or problems with the qPCR method of quantification caused poor labelling efficiency, barcodes conjugated to fluorescein (Integrated DNA Technologies) were instead used to quantify labelling efficiency using a fluorescent assay and associated standard curve. Two sets of samples were made up, one using unconjugated DNA barcodes, the others using fluorescein-conjugated barcodes. A 1,000x excess of maleimide-functionalised 16-mer capture probes to MSC EVs was used in all cases. EVs were incubated for two hours at room temperature. A 10x excess of barcode or fluorescein-conjugated barcode to capture probes was used. Barcoding controls were also prepared by omitting capture probes and incubating EVs with a 10,000x excess of barcodes or fluorescein-conjugated barcodes. As presented in Figure 3.3F, a far greater number of fluorescent oligos per EV were calculated using the fluorescent assay rather than the qPCR-based system, though the number of fluorescein-conjugated barcodes in the control also increased

substantially. Due to the much higher labelling efficiency reported using fluorescent oligos, the unknown reason for low labelling efficiency reported in the qPCR system, and speculated barcode contamination in the qPCR-based system, we switched to using fluorescent oligos until noticeable improvements were achieved.

The use of NHS functionalised barcodes instead of maleimide-functionalised barcodes was explored using fluorescent oligos to improve EV labelling efficiency. MSC-derived EVs were incubated with a 1,000x excess of NHS-functionalised capture probes and a 10x excess of fluorescent barcodes. As shown in Figure 3.4A, NHS capture probes enabled EVs to be labelled with approximately 40 fluorescent oligo copies per EV. Copies per EV were over double that of the control. As shown in Figure 3.4B, maleimide and NHS capture probes were compared, and capture probe excesses were increased to 2,500x. NHS-functionalised capture probes prevailed as the better of the two capture probes for labelling EVs, yielding roughly 136 fluorescent oligo copies per EV, while maleimide probes labelled EVs with approximately 90 copies per EV. Therefore NHS-functionalised capture probes were deemed the better of the two capture probes and were used as the benchmark in further optimisation experiments.

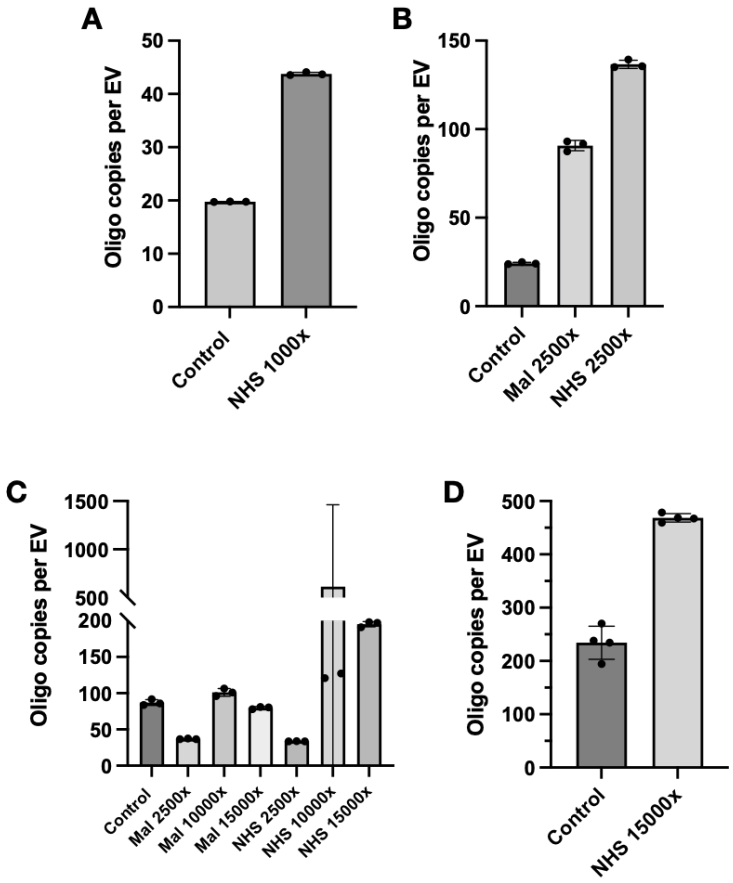

Figure 3.4 Optimisation of DNA barcoding using fluorescent oligo barcodes. (A) MSC EVs incubated with a 1,000x excess of NHS-functionalised capture probes to EVs. (B) EVs labelled with a 2,500x excess of maleimide or NHS-functionalised capture probes. (C) EVs labelled with a 2,500x, 10,000x or 15,000x excess of maleimide or NHS-functionalised capture probes. (D) EVs incubated with a 15,000x excess of NHS probes to EVs and a no-capture-probe control incubated with a 150,000x excess of fluorescent oligos to EVs to check for non-specific binding. A 10x excess of barcodes or fluorescent barcodes to capture probes was used in all cases. Controls represent EV incubations with DNA barcodes but without capture probes. Values are mean of technical replicates ±SD; n=1.

Subsequently, increasing the excess of capture probes and barcodes to EVs was explored to improve labelling efficiencies. EVs were incubated with a 2,500x, 10,000x or 15,000x excess of NHS or maleimide-functionalised capture probes and a 10x excess of fluorescent barcodes. As shown in Figure 3.4C for both maleimide and NHS probes, the 10,000x excess of capture probes to EVs produced the greatest number of barcodes per EV. NHS probes could capture and label EVs with a far greater quantity of fluorescent barcodes than maleimide probes. However, a notable deviation in the sample replicates was seen from the NHS 10,000x sample, with two points clustered around the 150 oligo copies per EV mark rather than the ~500 copies average. Overall, the highest number of copies per EV was achieved using the NHS capture probe with a 15,000x excess of capture probes to EVs.

Finally, contamination of excess fluorescent barcodes was investigated due to concerns that higher barcodes copies detected in samples incubated with high oligo concentrations were due to non-specific binding or inefficient clean-up rather than hybridisation with capture probes. A 15,000x NHS sample was prepared along with a control of 150,000x excess of fluorescent oligos to EVs (ten times greater than 15,000x) with no NHS capture probes. Results shown in Figure 3.4D revealed an unexpectedly high concentration of fluorescent oligos per EV in the control sample, even though no capture probes were incubated with EVs or barcodes in this sample. While the concentration of fluorescent oligos per EV in the NHS 15,000x sample was double that of the control, the high presence of barcodes in the negative control indicated that over half of these oligos were not associated with capture probes. In conclusion, the high number of barcodes in the control and a lower-than-expected increase in barcode

decoration in the NHS capture probe sample suggested incomplete purification, non-specific binding of fluorescent oligos to EVs or contamination of fluorescent oligos.

Altogether, the qPCR and fluorescent-based barcoding experiments to indirectly quantify EVs revealed poor labelling efficiencies, inconsistencies in labelling success and problems accurately and reliably determining the number of barcodes per EV.

3.3.2 N-Hydroxysuccinimide (NHS) universal protein labelling is insufficient to label entire EV populations

Due to the low labelling efficiencies of EVs seen in the barcoding optimisation process, the NFC Flow NanoAnalyzer was employed to assess the proportion of particles labelled with NHS-functionalised capture probes and barcodes. This was performed to investigate whether the low number of barcode copies calculated per EV was being diminished by a proportion of the EV population not being labelled with barcodes. MSC EVs were labelled with a 2,500x excess of NHS capture probes to EVs with a further 10x excess of fluorescent barcodes to capture probes and a 1:500 dilution of anti-CD81-PE antibody. Following labelling, EVs were purified using a Tricorn 10/200 column packed with Sepharose 4 Fast Flow resin at 0.5 mL/min with a Cytiva Aktä Start liquid chromatographer, and labelling quantified using the 488 nm and 638 nm lasers. Figure 3.5A presents the particle size distribution of the fluorescent barcoded sample. Particles are distributed between ~45 nm and ~160 nm, with a peak at ~75 nm and a mean particle size of 85.55 nm. This was typical of EVs, which adopt sizes between 30 and 1,300 nm in diameter, and more so of small EVs that range in size from 30 to 150 nm. Furthermore, Figure 3.5B displays the number of particles in the sample and PBS blank that were excited in the FITC channel in which fluorescein is excited. 6,694 particles were counted

in a one-minute period, of which 1,688 particles (27.1%) were fluorescein positive after PBS blank correction. This was surprising as NHS is a universal protein label that binds to free amine residue and should bind to all EV surfaces. However, despite incubation with a high excess of capture probes to EVs, only a minority of particles were successfully labelled. Therefore, this could substantially impact accurately calculating the number of barcodes per EV. Additionally, Figure 3.5C shows the number of particles in the sample and PBS blank that were excited in the PE channel and were therefore CD81-positive. 4,778 particles were counted in a one-minute period, of which 417 particles (10.1%) were CD81 positive after PBS blank correction. As CD81 is an EV-associated protein, this raised further concerns that not all the particles within purified barcoding samples were EVs, creating further difficulties for accurately determining the number of barcodes per EV, therefore the reliability of the barcoding protocol for *in vivo* biodistribution studies. Altogether the results support the hypothesis that NHS cannot label all particles within purified EV populations; however, CD81 labelling also suggested that a large proportion of the particles may not have been EVs, therefore offering an explanation for the low labelling efficiency seen here and in the barcoding optimisation experiments.

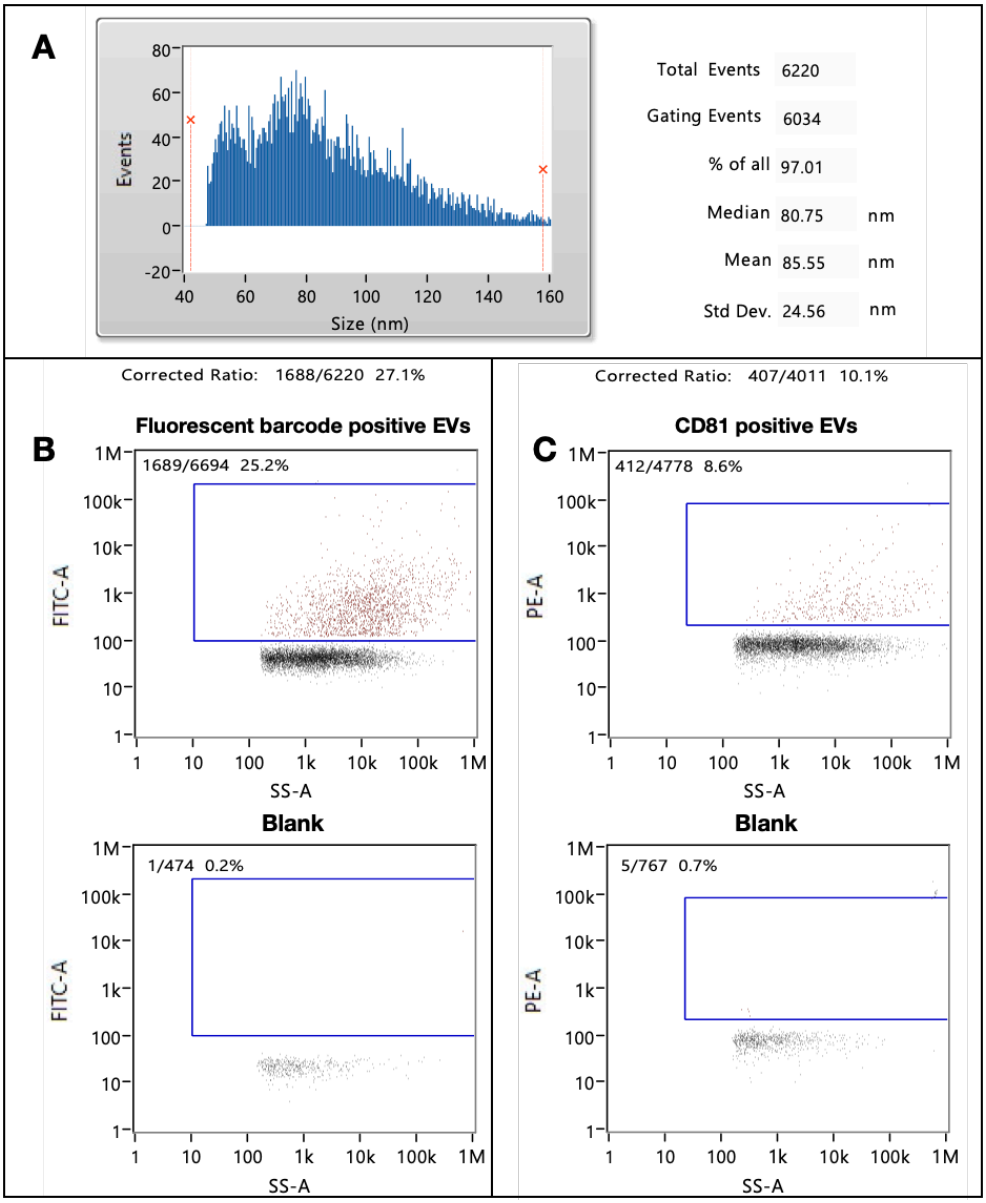

Figure 3.5 Particle sizing and profiling of fluorescein barcoded and anti-CD81 labelled EVs. Nanoparticle flow cytometry of NHS fluorescein barcoded and anti-CD81-PE labelled EVs. (A) Size distribution of particles in fluorescein barcoded and anti-CD81 PE labelled MSC EVs. (B) Profiling of fluorescein positive particles in MSC EV sample and PBS control in FITC channel. (C) Profiling of CD81 positive particles in MSC EV sample and PBS control in PE channel. SS = Side scatter.

3.3.3 NHS-functionalised DNA capture probes can deliver siRNA to recipient cells in vitro

The problems experienced during the barcoding optimisation process indicated that significant changes were required for the barcoding tools and, in their current form, would likely be insufficient for determining EV biodistribution. Therefore, the barcoding reagents were repurposed to test whether they could be used to deliver siRNA to recipient cells. HEK293T-derived EVs were incubated with a 2,500x and 10,000x excess of NHS capture probes to EVs and a 10x excess of sense and antisense siRNA. To test siRNA delivery *in vitro*, EVs labelled with anti-luciferase siRNA were incubated with luciferase-positive Neuro2a cells. EV-only negative controls and 1 and 50 nM siRNA transfection positive controls were used. 1 nM siRNA was roughly equivalent to the quantity of siRNA used to label EVs in the 10,000x samples. Following 24-hour incubation, luciferase knockdown versus positive and negative controls was measured using Promega Luciferase Assays, and relative percentage change of renilla and firefly luciferase expression was calculated as outlined in 3.2.7 siRNA delivery. As seen in Figure 3.6, no significant differences were seen between the NHS 2,500x sample and the PBS and barcoding control. Additionally, while the NHS 10,000x sample elicited ~25% knockdown in luciferase expression on average, this was also not statistically significant versus the PBS or barcode control. Approximately the same amount of siRNA transfected into Neuro2a cells (1 nM) elicited a roughly 50% knockdown in luciferase expression. However, no significant difference was detected between the NHS 10,000x labelled EVs and the 1 nM transfection despite a significant difference between the 1 nM transfection and the barcoding control. Together this suggested that the trend in luciferase expression following incubation of Neuro2a cells with the NHS 10,000x sample was consistent with the hypothesis that EVs labelled with siRNA can elicit knockdown of luciferase expression in recipient cells.

However, to confirm this hypothesis, further repetitions should be conducted until concordance in the results is reached. 50 nM transfections produced highly significant reductions in luciferase expression versus all samples and controls. Overall, while the differences between siRNA labelled samples and negative controls were insignificant, the trend in luciferase expression after incubation of Neuro2a cells with NHS 10,000x labelled EVs indicated that with further development, the barcoding tools could be used for delivery of siRNA to recipient cells.

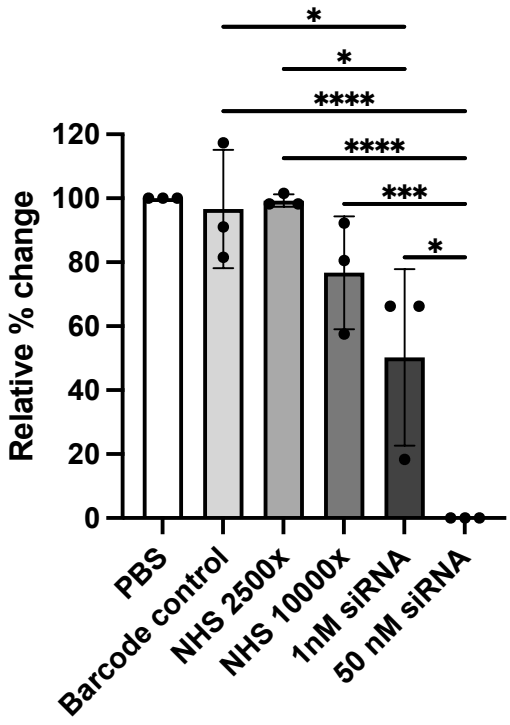

Figure 3.6 Anti-luciferase siRNA barcoded EVs knockdown luciferase expression in modified Neuro2a cells *in vitro*. HEK293T EVs were incubated with 2,500x or 10,000x excess of capture probes to EVs and a 10x excess of sense and antisense anti-luciferase siRNA to capture probes. Barcode control represents EV incubations without capture probes with sense and antisense siRNA equivalent to the amount used in the NHS 2,500x

sample. 1 nM and 50 nM siRNA samples were transfected with RNAiMAX into recipient Neuro2a cells. 50,000 Neuro2a cells per well. 24-hour incubation with EV samples. Values are mean percentage change relative to positive (50 nM siRNA) and negative (PBS) controls ±SD; n=3.

3.4 Discussion

Over the last few decades, the development and exploration of EVs as biotherapeutic delivery vehicles or as therapeutics themselves has increased substantially[131]. An important stage in this development process is determining EV biodistribution following administration, whether natural or influenced by other factors such as targeting motifs. Additionally, it is important to determine the impact of EV heterogeneity on their biodistribution to discern how EV heterogeneity can be harnessed or mitigated to improve the efficacy of EV therapeutics. Despite this, current techniques used to assess EV biodistribution have various sensitivity and specificity limitations and temporal and financial drawbacks[167,177,183,184,199]. Therefore, EV-DNA barcoding was explored and attempted to be optimized as a new tool for assessing EV biodistribution. EV DNA barcoding has the potential to overcome sensitivity limitations imposed on other methods due to the qPCR quantification method, which has a theoretical lower limit at 95% confidence between two and four target molecules, offering a highly sensitive tool for biodistribution[194].

The most comparable previously published example of DNA barcoding is DNA-assisted immunoassays wherein antibodies or affinity probes are conjugated to amplifiable oligonucleotides and incubated with protein-based samples to associate protein with specific DNA sequences and allow protein detection and quantification on a single molecule basis[190,200,201]. With respect to EVs, DNA-assisted immunoassays have been developed to detect prostate-derived exosomes[191], fluorescent detection of individual EVs by flow cytometry using rolling circle amplification (RCA) of conjugated DNAs to amplify the fluorescent signal[192], and simultaneous profiling of 38 surface proteins by

RCA of DNAs and subsequent next-generation sequencing to identify surface protein composition on a single EV basis[193].

The most apparent difference between DNA-assisted immunoassays and EV DNA barcoding is the coupling agent that conjugates DNA to EV surfaces. Immunoassays utilized antibodies chemically conjugated to oligonucleotides[190,193], whereas in DNA barcoding, amine-reactive NHS or cystine-reactive maleimide crosslinkers were chemically conjugated to oligonucleotides. Although, in contrast, labelling efficiency using the antibody-functionalized oligos reported by Wu *et al.* (2019) (in a method dubbed a proximity barcoding assay; PBA) was far more successful than the reactive chemical groups used here, with a vast majority of EVs being successfully labelled with immunoassay probes. Incubation of EV samples with no less than a 1,000-fold excess of capture probes and a further 10-fold excess of barcodes resulted in less than 5% of the barcodes associated with EVs reported by either qPCR or fluorescent assay (Figure 3.2 and 3.3). Investigating alternative EV crosslinking strategies could improve labelling efficiency, although an immunoaffinity labelling strategy could result in the clearance of EVs from circulation. Nanobodies may instead be better to mitigate potential EV clearance issues[202,203].

However, it is noteworthy that comparisons between this investigation, Wu *et al.* (2019) and most other EV labelling or biodistribution optimization studies are imperfect as in all other cases, the measure of labelling success is mostly binary, i.e., EVs are or are not labelled with fluorescent probes regardless of labelling efficiency or quantity. Comparatively, EV DNA barcoding aimed to reliably label EVs with a precise quantity of barcodes per EV to ensure the accurate and sensitive determination of EV biodistribution.

In hindsight, the excesses used to attempt to label EVs may have been too high. Due to a lack of sensitive techniques, the extent to which a single EV can be labelled has yet to be determined. As was suggested by the results of the NFC experiments, a lack of free amine or cysteine residues on EV surfaces or even steric hindrance of DNA barcodes and capture probes could limit EV labelling[204].

Turning next to barcoding optimization experiments seen in Figure 3.3, overall, the results of these experiments suggested that in all cases, EVs were labelled with at least one barcode copy. However, the NFC experiments shown in Figure 3.5, which assessed the efficiency of NHS-functionalised capture probes to label EVs, revealed that after incubating EVs with a high excess of NHS capture probes and fluorescent barcodes, only 27.1% of the particle population was fluorescein positive. This was surprising as NHS is a universal amine-reactive crosslinker that should be capable of labelling all EVs. Low labelling could have been due to a high proportion of non-EV particles within the preparation, such as lipoprotein particles, chylomicrons, or aggregates[205], which may be suggested by the low identification of the EV marker protein, CD81, seen in Figure 3.5C. However, the expression of CD81 is not homogenous within EV populations[206]. Therefore the 10.1% of particles that were CD81-positive likely do not represent the entirety of the EV population. On the other hand, Melling *et al.* (2022) stained mEmerald-CD81 positive MCF7 EVs with C5-Maleimide-Alexa633 and checked for colocalization of the mEmerald signal with Alexa633 and also noted that only a proportion of the population was stained with the universal maleimide label. Only a strikingly low 5.4%±1.8 of the EVs were positive for C5-Maleimide-Alexa633[141]. Not only does this corroborate the evidence shown here that universal crosslinkers produce poor EV labelling efficiency, but it also supports evidence shown in Figure 3.4 that NHS, while poor, is better for labelling EVs

than maleimide as 27.1% of the EV population was reported as fluoresceine positive by NFC while Melling *et al.* (2022) reported only 5.4%. Additionally, Melling *et al.* (2022) reported poor labelling efficiency of the PKH26 lipid intercalating dye (4.6%±1.6) and the formation of PKH26 dye aggregates[141].

Numerous challenges were encountered during the barcoding optimization process, the first of which was apparent particle losses following two EV purifications rather than one, as seen in Figure 3.3A and B. Particle losses following SEC have also been noted in other labelling studies. For example, Hwang *et al.* (2015) reported low EV yields following clean-up of EV radiolabelling reactions by SEC[183]. Viveiros *et al.* (2022) also reported an 80-89% loss of particle yield following SEC, compared to 2,000 x *g* centrifuged conditioned medium from cells stained with DiI (with prior measures to remove excess stain). However, it should be noted that EV concentration was determined using fluorescent-based particle detection (NTA with 405 nm laser and imaging flow cytometry)[207]; thus, it is plausible that losses detected could be due to free dye or dye aggregates reported elsewhere[141]. Furthermore, by modifying CHO cells to stably express a CD81-GFP fusion protein, Carrillo Sanchez *et al.* (2022) reported a 97% recovery of EVs following SEC[208]. Therefore, particles present in EV preparations before each purification step could instead be contaminants such as aggregates or co-eluting particles falsely identified as EVs.

Furthermore, throughout the barcoding optimization process, a high barcode signal was seen in negative controls in both qPCR and fluorescent barcoding, although the issue was exacerbated when using fluorescent barcodes. This may suggest a greater propensity for fluorescent oligos to non-specifically bind to EVs or be removed from

labelled EV preps and was supported by an apparent proportional increase in the number of barcodes per EV in subsequent controls incubated with higher barcode excesses. However, as opposed to more non-specific binding, the higher number of copies per EV in controls compared to qPCR controls may highlight the lower sensitivity of the fluorescence oligo system, or background fluorescence/autofluorescence producing false positives[167,177,199]. Alternatively, if the non-specific binding was not the cause of high barcode presence in controls, contamination of controls with barcodes could be responsible. The source of contamination could be environmental, or a by-product of experimental set-up caused by carry-over contamination[209].

Another problem encountered during EV DNA barcoding optimization was using TCEP to break disulphide bonds and allow for easier access to protein residues for crosslinking[195]. There is much debate about whether TCEP helps or hinders labelling efficiencies[195–198]. However, as shown in Figure 3.3, when immobilised-TCEP was employed instead of soluble TCEP, in both overnight and two-hour incubations, immobilized TCEP produced a higher number of copies per EV than soluble TCEP remaining in the reaction mixture, and this has been mooted as an excellent alternative to soluble TCEP within the literature[196].

Finally, despite being unable to achieve optimal labelling efficiency or quantification of EV DNA barcoding, the barcoding tools showed potential as a therapeutic siRNA delivery tool. As shown in Figure 3.6, following incubation of EVs with a 10,000x excess of capture probes to EVs and a further 10x excess of anti-luciferase siRNA, labelled EVs elicited a 20% reduction in luminescence signal. However, transfection with an equivalent amount of siRNA resulted in a 50% reduction in luminescence, presenting room for improvement.

Comparatively, other studies utilizing novel EV-mediated siRNA delivery techniques reported greater target gene knockdown but used much higher siRNA concentrations. For example, O'Loughlin *et al.* (2017) used cholesterol conjugation to load siRNA into EVs endogenously and reported that target gene expression reduced by 36% following 24-hour EV incubation with 400 nM siRNA[210]. Furthermore, Dar *et al.* (2020) used a GAPDH-derived G58 peptide conjugated to dsRNA-binding motifs to load siRNA onto EV surfaces. They reported ~70% knockdown of target gene expression following treatment with 50 nM HTT siRNA bound to G58TF EVs for 48 hours[211]. While capture probe-mediated siRNA delivery could only elicit a ~20% knockdown, it used 50-400x less siRNA when incubated for the same length of time or less. These insights reveal an excellent potential for barcoding technology for siRNA delivery.

3.5 Limitations, future work, and conclusions

3.5.1 Limitations

The main limitation of the EV DNA barcoding optimization data is the lack of biological replicates. While three technical replicates using the same purified EV preparation were obtained for each optimization experiment, applying the same optimization steps to separate EV purifications would have been beneficial to understand whether the observed results were consequential of factors associated with individual EV preparations opposed to the labelling protocol or mechanism itself. For example, high amounts of non-EV particles, such as lipoprotein particles or protein aggregates, may impact EV labelling efficiency[142,153,167,212]. Nonetheless, variation between technical replicates in some samples and labelling efficiencies below that of negative controls highlighted the technical challenges discussed in section 3.4 that must be overcome to make EV DNA barcoding a viable EV biodistribution tool.

Furthermore, assumptions were made regarding the level of labelling that could be achieved by EV DNA barcoding. A goal of 1,000 barcode copies per EV was set based on preliminary investigations conducted by a previous researcher (data not shown). However, as discussed in section 3.4, this figure was not based on previously published evidence regarding the extent to which a single EV can be labelled. Advancement of single-vesicle analysis tools will help establish realistic expectations of EV labelling efficiency based on the biological limitations of single EVs regarding spatial and resource availability[213].

3.5.2 Future work

Despite the challenges faced in developing EV DNA barcoding, other studies have demonstrated success using oligo-based EV labelling techniques for EV characterisation[193]. The evolution of capture probes to include immunoaffinity crosslinkers instead of NHS and maleimide may improve labelling efficiency[202,203]. Furthermore, changes to the readout method may improve the sensitivity and reliability of EV DNA barcoding. Technology such as RCA could be employed as RCA offers ultrasensitive detection of specific DNA or RNA sequences at a single nucleotide level. Therefore, RCA may enable labelling to be performed with lower excesses. Furthermore, barcodes could be utilized as a "padlock probe" to join ends of a circularizable DNA oligonucleotide prior to RCA, providing high selectivity of amplification and detection of barcodes after biodistribution, as perfect hybridization of padlock probes is necessary for RCA[214]. Additionally, further development of single-vesicle analysis technologies is necessary to understand the limits of engineering, such as the extent to which an EV can be labelled due to the availability of free protein or due to steric hindrance blocking further labelling[213].

Using the EV DNA barcoding toolset to deliver siRNA to recipient cells *in vitro* resulted in the knockdown of luciferase expression. However, variability between biological replicates resulted in no significant difference in knockdown between negative controls and siRNA-labelled EVs. Therefore, additional biological replicates should be performed to obtain concordance in results and investigate whether differences in knockdown between labelled EVs and negative controls are significant. If successful, the EV DNA barcoding toolset could be investigated for therapeutic RNA delivery *in vivo* to discover whether siRNA delivery can be replicated in a complex biological system. EV uptake

experiments may also be beneficial in understanding how siRNA-labelled EVs interact with recipient cells. Furthermore, due to the overhangs created by siRNA sequences following hybridization to capture probes, therapeutic RNA could also be multiplexed with a synthetic barcode sequence for simultaneous determination of biodistribution *in vivo* to improve therapeutic efficacy.

3.5.3 Conclusion

Overall, the optimization of the EV DNA barcoding toolset for use as a novel biodistribution tool was fraught with challenges, including suboptimal labelling efficiency, loss of EVs, high background contamination signals and potential non-specific binding. Ways of improving labelling efficiency were encountered, such as removing TCEP from labelling reactions, reducing incubation steps, and changing crosslinkers. NFC experiments revealed that NHS capture probes and fluorescent barcodes were only able to label, at most, 27.1% of particles in EV samples. This suggested that NHS is an inefficient method of labelling EV populations, synonymous with findings seen elsewhere[141]. Further biological repeats across barcoding optimization experiments are necessary to understand the extent of biological variation within labelling reactions and produce reproducibility within results. While success using oligo-based EV labelling techniques has been previously seen within the literature[193], if future developments do not improve EV labelling efficiency or EV quantification, the toolset showed potential as a siRNA delivery platform.

3.6 Supplementary Figures

Name	Sequence (5' - 3')
Capture probe	/Maleimide/ or /NHS Ester/AGTTTAGAGTTTACCAT
Barcode	G*C*T*CAGGTCATGCGTAGAAGGCGTGTTACCCGCCGCAGGGTATGGTAAACTCTAA*A*
Barcode forward primer	GCTCAGCTCATGCGTAGAAGG
Barcode reverse primer	AGTTTAAGATTACCATACCCTGCGG
Fluorescent barcode	/56-FAM/ATGGTAAACTCTAAACT
siRNA sense	rGrGrArCrGrArGrGrUrGrCrCrUrArArArGrGrACArUrGrGrUrArArArCrUrCrUrArArAr
siRNA antisense	rUrCrCrUrUrUrArGrGrCrArCrCrUrCrGrUrCrCCG

Supplementary Table S3.1 DNA barcode, capture-probe, siRNA and primer sequences. * = phosphorothioate protected ends. /56-FAM/ = fluorescein fluorescent modification.

4.0 Improved EV purification from high-density cultures with novel binding chromatography

4.1 Introduction

4.1.1 General principles of EV purification

When cultured *in vitro*, EVs are released into cell culture medium. To accurately observe, characterise, manipulate, or utilise EVs in an experimental or clinical setting, EVs must first be purified from other contaminants such as cells, proteins, lipids, and nucleic acid that are also present within the aforementioned fluids into which EVs are released. Historically EVs have been purified from cell culture supernatant and biofluids using a variety of different techniques, including various precipitation, ultracentrifugation, affinity, and chromatographic techniques. These techniques were developed and optimised for EV purification due to the various advantages and disadvantages associated with each, including differences in EV purity and downstream applications of EVs[145,146].

4.1.2 Ultracentrifugation

The most common method of EV purification in the last few decades has been ultracentrifugation[148,215]. Ultracentrifugation can purify components of a solution due to differences in centrifugal forces applied to different components based on the size, shape and density of the components and the viscosity of the medium. The greater the difference in density of elements of a solution, the faster and greater the separation. The most common ultracentrifugation-based techniques employed for EV purification are differential ultracentrifugation (dUC) and density gradient centrifugation (DGC)[148,216].

dUC exploits the size and density of particles to sequentially separate components of a solution in a series of centrifugation steps at different speeds and for different lengths of time[217]. Firstly, several slower centrifugation steps are performed in a benchtop centrifuge at up to 1,000 x *g*, 2,000 x *g,* then 10,000 x *g* for 10 minutes each to remove preparations of cells, cellular debris and large EVs such as apoptotic bodies and some microvesicles. Next, the supernatant is ultracentrifuged at between 100,000 and 120,000 x *g* for approximately 70 minutes to sediment EVs. EVs are then resuspended following the discard of the supernatant[218,219]. While dUC is easy to perform, fluctuations in centrifugation time, temperature, and sample dilution are important factors in dUC separation efficiency, and the various long centrifugation steps make it time intensive[216,218,220,221]. Additionally, EV samples purified by dUC can be contaminated with protein aggregates, lipoprotein, and lipoprotein particles and can be damaged, malformed, and aggregated[220,222].

Alternatively, DGC separates exosomes based on their size, mass and density using a pre-constructed density gradient medium. Particles distribute to the position within the medium that matches their density; low-density particles distribute to the top, and the high-density particles distribute to the bottom[223]. Numerous mediums are available, although sucrose and iodixanol are commonly used for EV isolation[222]. An advantage of DGC over dUC is that the gradient, in addition to differential speeds, aids the separation of small EVs and large EVs[18], which can improve EV purity and enable separation from contaminating small particles such as virus particles[224]. However, DGC has longer cycle times, produces lower EV yields, requires larger sample volumes and has presented high levels of lipoprotein particles in processed samples[225,226].

4.1.3 Precipitation

Precipitation of EVs is another common method of EV purification[148]. Precipitation is often performed using polyethylene glycol (PEG), a polymer that encircles water molecules and causes other solution components to precipitate. Precipitated EVs can then be collected by low-speed benchtop centrifugation[227]. PEG precipitation is fast, easy to perform and has a wide range of scalability[223]. However, a major disadvantage of PEG precipitation is its lack of selectivity. Following PEG addition, protein, protein aggregates, lipoprotein, lipoprotein particles and other particulate constituents of EV preparations also precipitate out of solution along with EVs[225,228,229]. Numerous studies that have compared various common EV purification techniques have concluded that PEG precipitation produces EV samples more highly contaminated with protein and lipoprotein than most other techniques[225,226]. Numerous PEG precipitation commercial kits are also used for EV isolation, including exoEasy (Qiagen), ExoPrep (HansaBioMed), Exosome Purification Kit (Norgen Biotek), ExoQuick (System Biosciences), miRCURY Exosome Isolation Kit (Exiqon) and Total Exosome Isolation Reagent (Invitrogen). These kits also suffer from the same disadvantages as standard PEG precipitation[230].

As an alternative to PEG, lectins such as Concanavalin A or Phytohemagglutinin can be used to precipitate EV. Lectins bind carbohydrate moieties on EV surfaces, changing their solubility and causing them to precipitate out of solution. As biological samples or conditioned medium is rich in carbohydrate-containing components, often the sample is pre-treated to remove these contaminants. Samples are incubated with lectins overnight, and EVs are precipitated the following day by benchtop centrifugation. The lectin

precipitation methods are straightforward, requiring little time and expertise, and other soluble components are usually only co-precipitated if they are highly glycosylated[231].

4.1.4 Immunoaffinity capture

Immunoaffinity capture-based techniques use antibodies against antigens expressed on EV surfaces. Antibodies are attached to inert media such as gold nanoparticles or magnetic beads[232–235], and EVs are then removed from suspension following capture. Arguably, the greatest benefit of immunoaffinity techniques is their selectivity which allows for specific subsets of EVs to be isolated from a preparation. Furthermore, immunoaffinity methods result in a lower yield of isolated EVs but with higher purity than other common purification techniques[232,236]. Despite this, immunoaffinity capture also has various disadvantages. Firstly, the specificity of purification is limited by the specificity of the antibody used, therefore, other non-EV components may also be co-isolated[233]. For this reason, immunoaffinity techniques are often used following ultracentrifugation or ultrafiltration to reduce contamination[237]. Furthermore, antibodies that can be used for immunoaffinity capture are limited to antigens present on EV surfaces as antibodies will not be able to capture antigens within the EV lumen. Furthermore, the technique is also expensive due to using antibodies and has low scalability[216]. Finally, the separation of EVs from antibodies used during immunoaffinity capture purification when required for functional studies, for example, requires harsh conditions such as high temperature or low pH, which can damage EVs. However, recent advances in this area have shown that 0.5M NaCl incubation may be sufficient to facilitate intact release[238].

4.1.5 Microfluidics

A more recent addition to the roster of techniques that has gained popularity for EV isolation is the use of microfluidic devices[148]. Microfluidic devices purify EVs in various ways, including filtration through membranes with different pore sizes[239], subjection to inertial lift force to distribute and separate EVs from contaminants[240], particle migration caused by size-dependent elastic lift forces in a viscoelastic medium[241], size-based separation by lateral deflection in an acoustic field[242], separation of EVs based on their dielectric properties[243], and sorting using deterministic lateral displacement arrays[244]. These microfluidic techniques benefit from high surface-to-volume ratios, low analysis time, laminar flow, ease of use and high yields and purity[245–247]. Furthermore, microfluidic devices have high selectivity for EVs in various sample types and have low processing times and costs compared with other more common purification techniques[248]. The previously described variations of microfluidic purification can be classified as either passive or active. Passive methods of particle sorting, such as filtration or deterministic lateral displacement, do not require any external fields for particle sorting, while active methods require external actuators, such as electric fields and acoustic waves[249]. This presents a potential drawback of these systems as it increases the complexity and cost of the system. Furthermore, besides filtration, microfluidic purification can only operate with micro-scale volumes of sample, and many devices can also suffer from clogging issues[239–244].

4.1.6 Ultrafiltration

Ultrafiltration is another popular method of EV purification that purifies EVs based on their size[148]. During filtration, EV preparations are exposed to a membrane containing pores which extrude larger particles while smaller particles can pass through. In some cases,

pores are intended to be smaller than EVs, causing EV retention and removal of smaller contaminants, or conversely, pores are larger, allowing EVs to pass through membranes and leave behind larger contaminants. A drawback of this method is that EVs may experience high pressure while passing through the membrane pores, which can damage EVs, cause aggregation and even change their morphology which could impact EV function or analysis following purification[233]. Furthermore, smaller particles can become trapped in the membrane, causing clogging, resulting in EV losses, and may cause an increase in pressure[250,251]. Additionally, the purity of EVs obtained using this method is relatively low as particles of a similar size, such as protein aggregates or lipoprotein particles are not excluded by the membrane. The filter material itself can also impact EV purification by ultrafiltration[251].

Sequential ultrafiltration has been used to improve EV purification efficiency and preserve EV integrity instead of attempting to purify EVs in a single step. Here EVs are exposed to membranes with different pore sizes in sequence. First, larger constituents such as cells and cell debris are excluded while EVs pass through, followed by exposure to membranes containing smaller-sized pores until purer EVs are obtained. This method applies lower pressures to EVs therefore preserving their shape and integrity[223,252]

Alternatively, EV preparations can be filtered by tangential flow filtration (TFF) to circumvent clogging and high-pressure issues observed in many ultrafiltration methods. In TFF, instead of applying the sample perpendicular to the filter membrane, a pump mechanism creates a flow of samples along a membrane surface. This way, pressures are lower, and clogging is less frequent[253–256]. Furthermore, the membrane pores are large enough to allow passage of free protein and even very small particles, but EVs are

retained. TFF has high scalability and can be used to concentrate EVs following harvest. EV purity can also be improved by diafiltering EV preparations with PBS, for example[253,254,256].

4.1.7 Size exclusion chromatography

Between 2015 and 2019, there was a highly significant ~2.5x increase in the use of size exclusion chromatography (SEC) for EV purification. This and an increase in a variety of other methods has coincided with a decrease in the use of ultracentrifugation and made SEC the second most popular EV purification method[148,215]. SEC employs columns packed with inert, porous, beaded resin that can be perfused with a liquid sample to separate its components based on size. Components larger than the resin pores flow around the beads and elute first. Smaller components can enter the beads, have a longer path through the column and are eluted last. Components can be separated to varying degrees depending on the resolving capabilities of the resin[257–259]. Traditionally, SEC is performed using a liquid chromatography system that uses buffers, pumps, and capillary tubes to transport a sample through a SEC column and separate constituents at a constant flow rate[260]. This method has been used with EV preparations[220,261,262], although purchase of or access to a chromatography system presents a barrier to some researchers. Therefore, some manufacturers have developed cheaper, more accessible, gravity-fed SEC columns for EV purification that operate independently of chromatography systems[263].

For conventional EV purification from cell culture preparations or low contaminant density biofluids, SEC yields clean EV preparation that are intact and functional[220,261,264,265]. Furthermore, the purity of EVs isolated by SEC has shown to be superior to the purity of

EVs isolated by other techniques[226,264,266,267]. Processing times vary, but in comparison to other techniques such as ultracentrifugation, SEC purification is relatively short, ranging from 20 minutes to one hour[220,258,261,265]. Additionally, unlike all other techniques, as different sizes of column and resin with different fractionation ranges and resolutive properties can be used, SEC has shown the potential to enable size-based fractionation with EV populations. This can aid the study of EV heterogeneity, as shown by Willms (2018)[51]. The superior purity, integrity, and functionality of EVs present SEC as an ideal EV purification technique for therapeutic development and biomarker identification, as well as accurate determination of EV characteristics and function.

However, SEC is not devoid of disadvantages. Firstly, SEC has been shown to cause dilution of EV samples, which can negatively impact their use in downstream applications such as functional assays or characterisation as the EV concentration may not be high enough. The extent of dilution depends on the input volume, fraction size, column parameters and the number of fractions, although dilution factors of between two- and five-fold have been reported[263,268]. Furthermore, as SEC isolates EVs from preparation based on their size, unfortunately, without prior processing, SEC can also co-isolate similarly sized non-EV components such as cell debris, protein aggregates, low-density lipoproteins, lipoprotein particles and chylomicrons[153,226,263,266,267].

Finally, while many studies have reported that SEC yields high concentrations of pure EVs, every SEC column has limits to its resolutive capabilities and pressure limits. These limits create difficulties for the purification of EVs by SEC from preparations with high EV concentrations or high densities of contaminants such as protein, DNA, or lipoprotein[269]. Therefore, as the need to upscale EV production arises, such as for attaining clinically

relevant EV concentrations, SEC no longer presents as a viable purification technique. To attain complete purity, repeated runs or multiple techniques may need to be employed, which are highly time-consuming and resource intensive and may result in lower EV yields, defeating the purpose of upscaling.

4.1.8 Binding chromatography

Binding chromatography (also known as bind-elute chromatography or multimodal chromatography) is an emerging method of EV purification that has risen to prominence due to a lack of stringent purification techniques in the field and numerous drawbacks associated with commonly used techniques[256]. Numerous studies for large biomolecule purification have reported binding chromatography as a time-efficient and scalable method that yields intact product and consistently high yields[256,270–272]. Like SEC, binding chromatography uses columns packed with resin, although the modality of the resin is different to SEC. Resin particles with an inert shell are permeated with size-selective pores surrounding an absorptive core. Pores allow entry of contaminating proteins and small molecules into the resin beads, wherein they bind to the core. Pores are small enough to exclude large biomolecules and nanoparticles such as EVs allowing purified particles to be collected in the flow-through. Columns are then washed to remove bound contaminants and can be reused.

Capto™ Core (CC) is a range of binding chromatography resins produced by Cytiva Life Sciences that have previously been explored in conjunction with other methods for EV purification[256,270,271,273,274]. Figure 4.1 provides a visual description of the functionality of Capto Core binding chromatography resin. Resin particles are composed of an inert crosslinked agarose shell permeated with either 700kDa (CC700) or 400kDa (CC400)

molecular weight cut-off pores. Inside each particle is an octylamine ($CH_3(CH_2)_7NH$-) ligand functionalised core. Due to its ionic capacity and high hydrophobicity, the core can bind a broad range of proteins and small molecules with high salt tolerance. Furthermore, CC700 has demonstrated a high binding capacity for bovine serum albumin (Mr ~65 kDa) and thyroglobulin (Mr ~660 kDa) (55 and 105 mg/mL of total resin volume, respectively)[275]. This suggests that binding chromatography may be useful for EV purification from biological preparations with high protein densities, or in instances where upscale of EVs or biomolecule production is necessary. Furthermore, as binding chromatography columns also utilise chromatography systems, this method may be an accessible alternative for SEC users when purifying EVs from high EV or contaminant density samples.

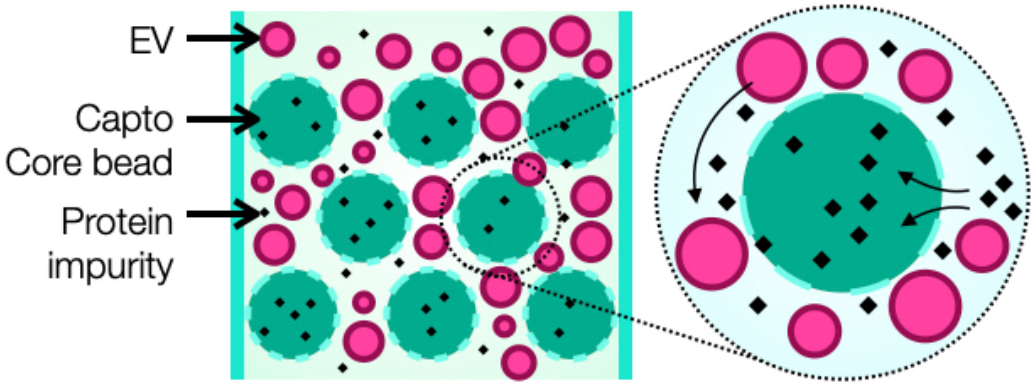

Figure 4.1 Capto Core binding chromatography functionality. Capto Core beads are composed of an inactive shell with pores of a defined size and a ligand activated core. Large molecules such as EVs pass around the beads and elute from the column, while smaller contaminants enter the beads and are bound by the hydrophobic, positively charged octylamine core, producing pure EV preparations.

Various groups have begun to explore the use of binding chromatography for EV purification, in most cases in conjunction with other methods[256,270,273,274,276]. Corso *et al.*

(2017) recently performed minimal essential comparisons of the use of SEC and CC700 for the purification of EVs from TFF concentrated cell culture medium[270]. However, Corso *et al.* (2017) did not compare other commercially available Capto Core columns, focused analysis on EV purification from lower EV and contaminant density cell culture preparations, and did not include some of the minimal information required for the study of extracellular vesicles when making comparisons between SEC and CC700[18]. A step-by-step analysis of purification was also lacking.

This chapter provides a more comprehensive comparison of SEC and CC700 for the purification of EVs from bioreactor-derived high cell density culture preparations, which produce high EV and contaminant densities. In addition, the best commercially available Capto Core column for EV purification from protein and nucleic acids was also identified. Similarly, Capto Q anion exchange chromatography was also explored to further purify EVs from nucleic acids. Resolving the issue of efficient EV purification from high cell density cultures when scaling up EV production was essential to later investigations conducted within this thesis, as high concentrations of EVs were necessary to investigate EV functional heterogeneity presented in chapter five.

4.2 Materials and methods

4.2.1 Capto Core binding chromatography

Following TFF, samples destined for Capto Core binding chromatography were purified by Capto Core binding chromatography as described previously in chapter 2. In cases where nucleic acid removal was explored, TFF concentrates were incubated with 150 units/mL of benzonase (Merck Millipore) for one hour at 37°C.

In addition to standard Capto Core binding chromatography, various commercial Capto Core columns were also used to assess their purification efficiency. Using an ÄKTA Pure chromatography system, concentrate was passed through either a 1 mL HiTrap 400, 1 mL HiTrap 700 or 5 mL HiScreen 700 Capto Core (CC700) column (Cytiva) at 0.5 mL/minute and flow through containing purified particles was collected. Chromatography was performed in PBS and monitored using absorbance at 280 nm. Columns were cleaned between runs using a 0.5 mL/minute reverse flow of 1M NaOH in 30% isopropanol.

4.2.2 Anion exchange

Samples destined for Capto Q anion exchange were subjected to binding chromatography with prior incubation of 150 units/ml of benzonase (Merck Millipore) for 1 hour at 37 °C. The 1 mL Capto Q column (Cytiva) was primed with five column volumes of Tris HCl pH 8.0. Once purified by CC700, a 5 mL sample from the CC700 peak was taken and passed through a Capto Q column with Tris HCl pH 8.0 as the mobile phase. The elution step was conducted using NaCl as the mobile phase and following the manufacturer's instructions. Chromatography was performed at 0.5 mL/min and

monitored using absorbance at 280 nm. Samples from the flow-through and elution phases were collected and pooled separately.

4.2.3 Protein quantification

Protein concentrations were determined using Pierce Micro Bicinchoninic Acid (BCA) protein assay kits (Thermo Fisher Scientific) following the manufacturer's protocol.

4.2.4 Silver staining

Silver staining was performed to visualise total protein in differently purified samples. Gels were fixed for one hour at room temperature in 50% ethanol (Fisher Scientific), 5% acetic acid (Fisher Scientific) in double distilled water, followed by a 30-minute wash at room temperature in 50% ethanol. Subsequently, the gel was sensitised for one minute in 0.02% sodium thiosulphate (Sigma Aldrich) solution, followed by washing in two changes of double distilled water. Next, the gel was stained for 30 minutes in 0.1% silver nitrate (Sigma Aldrich) solution and then washed in two changes of double distilled water. Silver nitrate stain was developed in 250 mL of a 2% sodium carbonate (Sigma Aldrich), 0.04% paraformaldehyde (Sigma Aldrich) solution until the desired staining was achieved. Development was stopped in 5% acetic acid solution for 15 minutes before rinsing in 2 changes of double distilled water for 5 minutes each.

For preparation of whole cell lysates (WCL), cells were removed from culture vessels with trypsin and centrifuged at 700 x *g* for 5 minutes. Next, cells were washed with PBS and resuspended in RIPA buffer (Merck Millipore). After incubation on ice for 15 minutes with frequent vortexing, the solution was centrifuged for 10 minutes at 14,000 x *g* at 4 °C. Supernatant was removed and stored at -20 °C until required.

4.2.5 Nucleic acid quantification

DNA+RNA concentrations were determined using the Quant-iT RiboGreen RNA assay kit (Thermo Fisher Scientific) following the manufacturer's protocol. DNAse included in the kit to quantify RNA only was omitted from the protocol to ensure all nucleic acids were quantified.

4.3 Results

4.3.1 Size exclusion chromatography is insufficient to purify EVs from high protein density cultures

Firstly, to investigate the efficiency of SEC to purify EVs from high cell density culture preparations, conditioned medium from HEK293T bioreactor harvests were concentrated by 100 kDa MWCO TFF to ~5 mL and further concentrated to ~2 mL with Amicon Ultra 100 kDa MWCO spin filters. The concentrate was passed through a Tricorn 10/300 column packed with Sepharose 4 Fast Flow resin using a Cytiva Äkta Pure at 0.5 mL/min. Figure 4.2A displays a UV chromatogram produced following an EV purification from a concentrated low cell density culture preparation harvested from 15x 15 cm dishes of HEK293T cells. In most SEC-based EV purifications, “peak a” represents the EV/particle peak, while “peak b” represents soluble protein and other impurities[220,261]. This is due to the general principles of SEC, where larger material elutes first due to having a shorter path through the column by moving around resin beads, while smaller material takes a longer path through the column by moving through the beads, eluting later. In contrast, run 1 in Figure 4.2B presents the result of passing a concentrated high cell density bioreactor preparation through the Tricorn 10/300 column (SECx1). Extensive crossover in both peaks was seen compared to low-density purification in Figure 4.2A, indicating incomplete separation of the constituents of both peaks. After running 1, “peak a” fractions were pooled, concentrated to ~2 mL using 100 kDa MWCO spin filters and reapplied to the SEC column, resulting in the run 2 chromatogram, although crossover between “peak a” and “peak b” was still present. Finally, concentration and SEC were repeated a third time, resulting in the run 3 chromatogram to achieve complete separation of “peak a” and “peak b”. However, a marked reduction in mAU in “peak a”

was also seen, indicating potential reductions in EV yield. In summary, while SEC could efficiently separate EVs from contaminants after a single run from a low cell density culture preparation, three consecutive SEC runs were necessary to achieve complete separation between EVs and contaminants (SECx3).

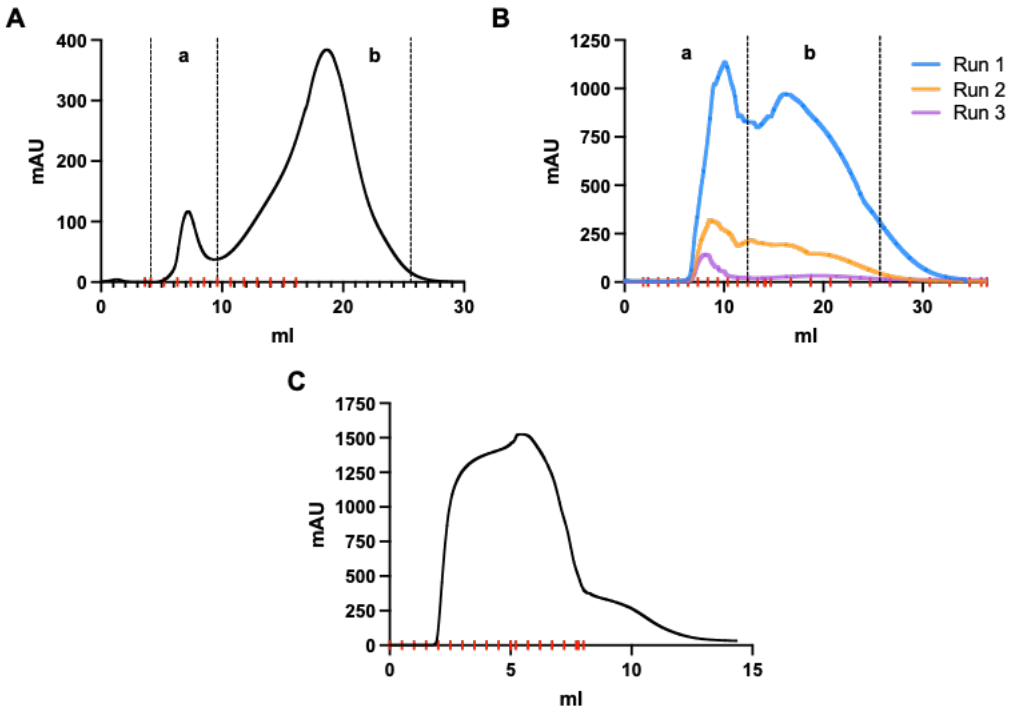

Figure 4.2 Comparison of UV chromatograms from SEC and Capto Core EV purification from low protein density plate-based culture and high protein of bioreactor culture. (A) Chromatogram from EVs purified by SEC from 15x 15 cm dishes where “a” represents the EV/particle peak, and “b” represents soluble protein and other impurities. (B) Chromatograms from three consecutive SEC purifications of the same high cell density bioreactor culture are required to attain complete separation of particle (a) and protein peaks (b). (C) Representative Capto Core purification chromatogram from a

bioreactor harvest applied to a HiScreen Capto Core 700 column. In all chromatograms, red lines on x-axis denote fractions collected.

Following the investigation of SEC to purify EVs from concentrated high cell density bioreactor preparations, Capto Core binding chromatography was investigated as a more efficient and potentially preservative method of EV purification. TFF concentrated HEK293T bioreactor harvests were passed through Cytiva Capto Core binding chromatography columns using a Cytiva Akta Pure system at 0.5 mL/min. Figure 4.2C presents a chromatogram acquired by passing the media through a HiScreen Capto Core 700 (5 mL) column (CC700). The broad peak represents the entirety of the purified product due to the inert, size-exclusive shell of the Capto Core beads that excludes EVs and the hydrophobic and electrostatic binding functionality of the core, which binds smaller impurities such as protein. In addition, a shoulder on the right side of the chromatogram demonstrated minor size separation effects. Overall, due to the differing functionality of the CC700 column, the resulting chromatogram presented differently from the SEC chromatograms, however it was hypothesised that CC700 was successfully able to purify EVs in a single run.

Following analysis of chromatograms, further investigation was necessary to investigate the purification efficiency of these techniques and characterise the obtained EVs. TEM imaging and silver staining were performed to provide initial assessments of EV purification efficiency. Figure 4.3A and B show TEM images from SECx1 and SECx3 samples. Spherical, membranous particles with cup-shaped morphology were observed that were characteristic of EVs. However, some EVs appeared warped, and many dark-stained contaminants were seen in both samples, though with arguably more in SECx1.

SECx3 samples appeared cleaner, although similar dark staining contaminants were also observed, as well as extensive EV aggregation. In comparison, Figure 4.3C presents CC700 TEM images. EV purifications appeared far less muddied by contaminants such as protein aggregates, and EVs were more clearly visible. Moreover, markedly less EV aggregation was present, and EVs appeared less warped than in SEC samples. Figure 4.3D presents a silver stain of differently purified HEK293T bioreactor samples, including TFF, SECx1, SECx3 and CC700. Silver staining provided a visual representation of the remaining protein in the samples. TFF concentrated conditioned medium, and SECx1 samples were saturated in proteins greater than 55 kDa, while SECx3 removed most of the contaminating proteins between 55 and 171 kDa. However, a high concentration of proteins greater than 171 kDa were co-purified with EVs in SECx3 samples. In contrast, CC700 removed nearly all darkly stained contaminating proteins greater than 55 kDa seen in the TFF, SECx1 and SECx3 samples. Together, both TEM images and silver staining showed CC700 as more efficient than SEC in removing contaminating protein and producing intact, non-aggregated EVs.

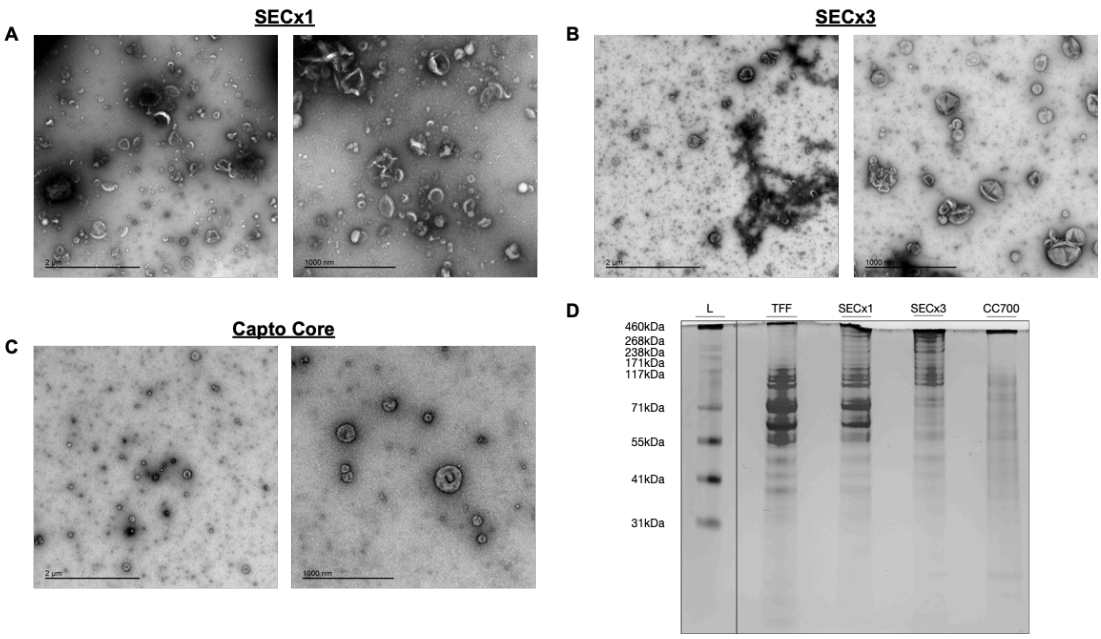

Figure 4.3 TEM and silver stain characterisation of SEC and Capto Core purified samples. (A) TEM images from SECx1 and (B) SECx3 purifications presented typical "cup-shaped" EV particles amidst other *darkly stained* contaminants. *Some* EVs appeared warped *and* aggregated. (C) TEM images from Capto Core purifications presented typical "cup-shaped" EV particles with far less *darkly stained* contamination and aggregation. (D) Silver stain of TFF concentrated conditioned medium, SECx1, SECx3 and Capto Core samples. 10 µg was loaded per well.

4.3.2 Capto Core binding chromatography is an attractive alternative to SEC to purify EVs from high protein density cultures

Following initial comparisons of SEC to CC700, other commercially available Capto Core columns were compared to identify the most efficient binding chromatography EV purification method. Fractions from the Capto Core peak (shown in Figure 4.2C) were pooled, creating a ~2 mL sample to identify and analyse whether binding chromatography was better at purifying EVs from free protein. This sample was then subjected to SEC using a Tricorn 10/300 column packed with Sepharose 4 Fast Flow resin to separate any remaining free proteins co-purified with EVs following Capto Core binding chromatography. As shown in Figure 4.4A, the resulting chromatogram presented a characteristic EV peak (a), free protein/contaminant region (b) and a "right-peak" (c), later attributed to components of DMEM +1% A/A (Supplementary Figure S4.1). Following SEC, fractions from the free protein/contaminant region (b) were analysed by BCA assay to determine the free protein concentration remaining following EV purification using different commercial Capto Core columns. Figure 4.4B shows that the 5 mL HiScreen Capto Core 700 column was superior to the 1 mL HiTrap 400 and 1 mL HiTrap 700 columns, leaving just 21.74 µg/mL of free protein remaining in solution, roughly 5x lower than the next best alternative, the HiTrap 400 with 111.4 µg/mL remaining. Overall, EVs purified from high cell density culture preparations by the 5 mL HiScreen Capto Core 700 column (CC700) were the purest from contaminating host cell protein, and this column was selected as the best Capto Core option for further comparison to SEC.

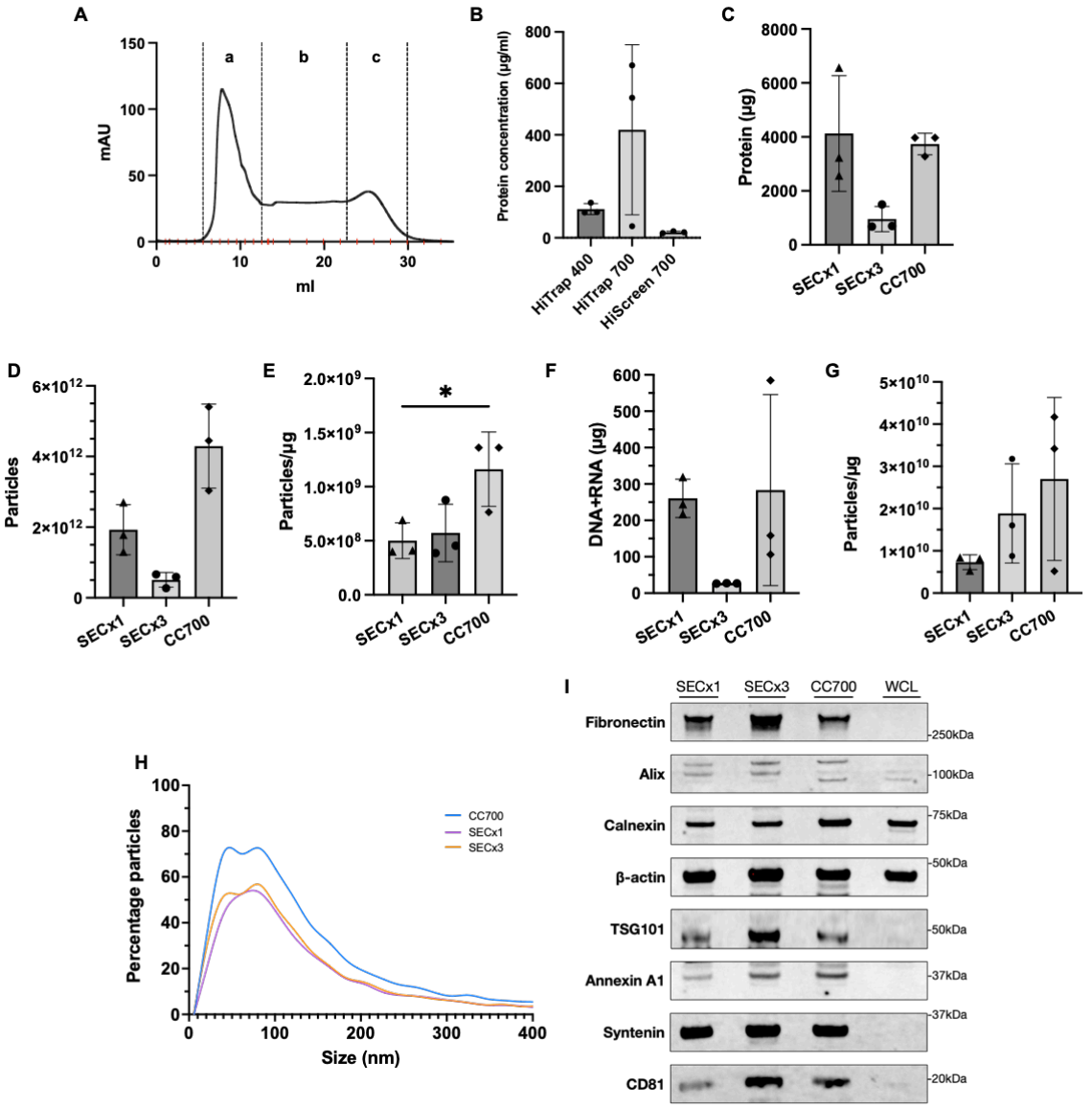

Figure 4.4 CC700 binding chromatography presents significantly improved EV purity compared to SEC. (A) 2 mL samples from the top of the Capto Core peaks were subjected to SEC to separate any remaining free protein or contaminants from the EV peak, presenting the displayed representative chromatogram where “a” represents the EV peak, “b” the contaminant peak and “c” the DMEM constituent peak, as demonstrated in Supplementary Figure S4.1. Red lines on x-axis denote fractions collected. (B) Concentration of soluble protein remaining in Capto Core purified bioreactor samples obtain for “b” peaks following SEC separation. (C) Total protein

content of bioreactor harvests following SECx1, SECx3 and CC700 purification. (D) Total particle counts of bioreactor harvests following SEC and CC700 purification. (E) Particle/protein ratios of bioreactor harvests following SEC and CC700 purification. (F) DNA and RNA content of purified harvests assessed by Quant-iT RiboGreen RNA Assay following SEC and CC700 purification. (G) Particle/μg of DNA and RNA in SEC and CC700 purified samples. (H) NTA size distribution of particles from SEC and CC700 purifications. Smoothed best-fit splines with 50 knots generated with Prism 9 GraphPad Software. (I) Western blot of SEC and CC700 purified samples for expression of EV proteins (ALIX, beta-actin, syntenin, CD81, annexin A1 and TSG101) and non-EV proteins (fibronectin and calnexin). WCL = whole cell lysate. Values are mean concentrations ±SD; n=3. One-way ANOVA with Tukey's multiple comparisons tests (* = $P < 0.05$).

Next, total protein, particle yield and particle-protein ratios from CC700 and SEC purified bioreactor preparations were determined and compared. TFF concentrated bioreactor preparations were purified by CC700 or SEC and analysed by BCA assay and NTA. Interestingly, as presented in Figure 4.4C, the total protein that remained after CC700 purification was approximately 4,000 μg, similar to the total protein in SECx1 samples. In contrast, SECx3 total protein was over 4x lower. On the other hand, Figure 4.4D presents the number of particles yielded following CC700 purification was roughly 8x higher than the total particles yielded after SECx3 and roughly 2x higher than SECx1. Consequently, particle/protein data shown in Figure 4.4E demonstrated a significantly higher purity of CC700 purified EVs than SECx1, followed by SECx3, which presented only slightly higher purity than SECx1. Altogether, CC700 samples presented far greater total protein than SECx3 samples, but this was concurrent with a much higher amount of particles in

CC700 than SECx1 and SECx3, resulting in a significant difference between the purity of EVs purified by SECx1 compared to CC700 and a comparable improvement over SECx3.

Following analysis of the ability of the CC700 columns to purify EVs from free protein, the ability of the CC700 columns to deplete DNA and RNA in high cell density harvests was investigated. Quant-iT RiboGreen assays were performed to determine the amount of DNA and RNA remaining in each sample, and the same NTA values as previous were used to calculate particle-DNA+RNA ratios. As shown in Figure 4.4F, SECx3 was the best method of depleting DNA and RNA from high cell density harvests. CC700 yielded the highest amount of remaining DNA and RNA, although with a high standard deviation. CC700 was closely followed by SECx1, which also presented DNA and RNA quantities of over 250 µg. However, in a similar manner to particle-protein ratio data presented in Figure 4.4E, despite apparently high nucleic acid levels seen in CC700 samples, particles-DNA+RNA ratios displayed in Figure 4.4G show that EVs purified by CC700 produced 2x purer EV preparations than SECx3. In summary, while higher amounts of DNA+RNA were present within CC700 samples, CC700 produced preparations that were purer per particle from DNA and RNA.

Finally, EVs purified by SEC and CC700 were characterised. NTA and western blotting were performed to obtain size distributions and EV protein expression profiles from differently purified samples. Figure 4.4H displays the size distributions of differentially purified particles obtained by Nanosight. Results are presented as an average percentage of the greatest number of particles that occupy a single size in each dataset. Most particles in both SECx1 and SECx3 were less than 200 nm, typical of small EVs[18], with pronounced peaks at 50 and 80 nm. Furthermore, CC700 purified particles also

presented a size distribution conducive to EVs, though a greater percentage of particles occupied sizes less than 200 nm, potentially suggesting a higher proportion of small EVs in CC700 samples than SEC samples. Western blotting showed high expression of CD81, ALIX, TSG101, syntenin and annexin A1 in both SEC and CC700 samples versus low to no detectable expression of these markers in HEK whole cell lysate was characteristic of EVs. SECx1 samples appeared to present a noticeable increase in purity due to reduced intensity of CD81, annexin a1 and TSG101 EV marker expression in SECx1 samples compared to SECx3. SECx3 and CC700 protein expression was very similar, suggesting that CC700 was able to purify EVs at least to the same extent as SECx3. However, a higher expression of the extracellular matrix protein, fibronectin, was seen in SECx3 samples compared to CC700, suggesting that SEC remained unable to fully purify EVs from contaminating protein. Although interestingly, the expression of the secretory pathway-associated protein, calnexin, appeared to be potentially higher in CC700 samples than in SECx3 samples. Overall, EVs purified by SEC and CC700 presented typical EV size distribution profiles with peaks around 80 nm, and western blot data revealed high expression of typical EV markers for both SEC and CC700 EVs though it did not provide further conclusions regarding EV purity.

4.3.3 Capto Q anion exchange further reduces DNA and RNA concentrations following Capto Core EV purification

As previously shown, despite the higher particle/µg data seen in CC700 samples, a high amount of DNA and RNA remained in CC700 samples compared to SEC; therefore, further reducing DNA and RNA in CC700 EV purifications was explored. Firstly, TFF concentrated bioreactor harvests were incubated with 150 units/mL of benzonase for 1 hour at 37°C before CC700 purification. Furthermore, following benzonase incubation and CC700 purification, some EV samples were passed through a Capto Q anion exchange column to explore whether this method could further increase EV purity from DNA and RNA. Quant-iT RiboGreen assays were performed on purified EV samples to determine free DNA and RNA levels. Figure 4.5A presents the consecutive steps taken to reduce DNA and RNA concentration, beginning with TFF concentration of bioreactor harvests, followed by CC700 with prior benzonase incubation and ending with Capto Q anion exchange. CC700, with prior benzonase incubation (CC benzonase), lowered DNA and RNA levels from 763.8 µg to 165.8 µg; a ~64% depletion of total DNA and RNA compared to TFF levels (shown in Figure 4.5B). Moreover, subsequent Capto Q lowered DNA and RNA levels further to 21.0 µg, a ~96% depletion of total DNA and RNA compared to TFF levels (shown in Figure 4.5B). However, interestingly, as seen in Figure 4.5C, both CC benzonase and Capto Q anion exchange caused a marked reduction in particle yield, reducing particle counts near those seen following SECx3 purification. Although, particles-DNA+RNA ratios shown in Figure 4.5D presented that EVs yielded from Capto Q were over 3x purer from nucleic acids than those obtained by SECx3. CC benzonase also remained purer from DNA and RNA than SECx3, despite the reduction in particles. CC700 without benzonase treatment had a higher number of particles/µg of DNA and RNA than bezonase treatment, though with a large standard deviation.

Altogether, the data showed that while benzonase and Capto Q treatment were able to reduce DNA and RNA levels in CC700 samples and yield high-purity EVs, particle yields were far lower than if benzonase or Capto Q were used at all.

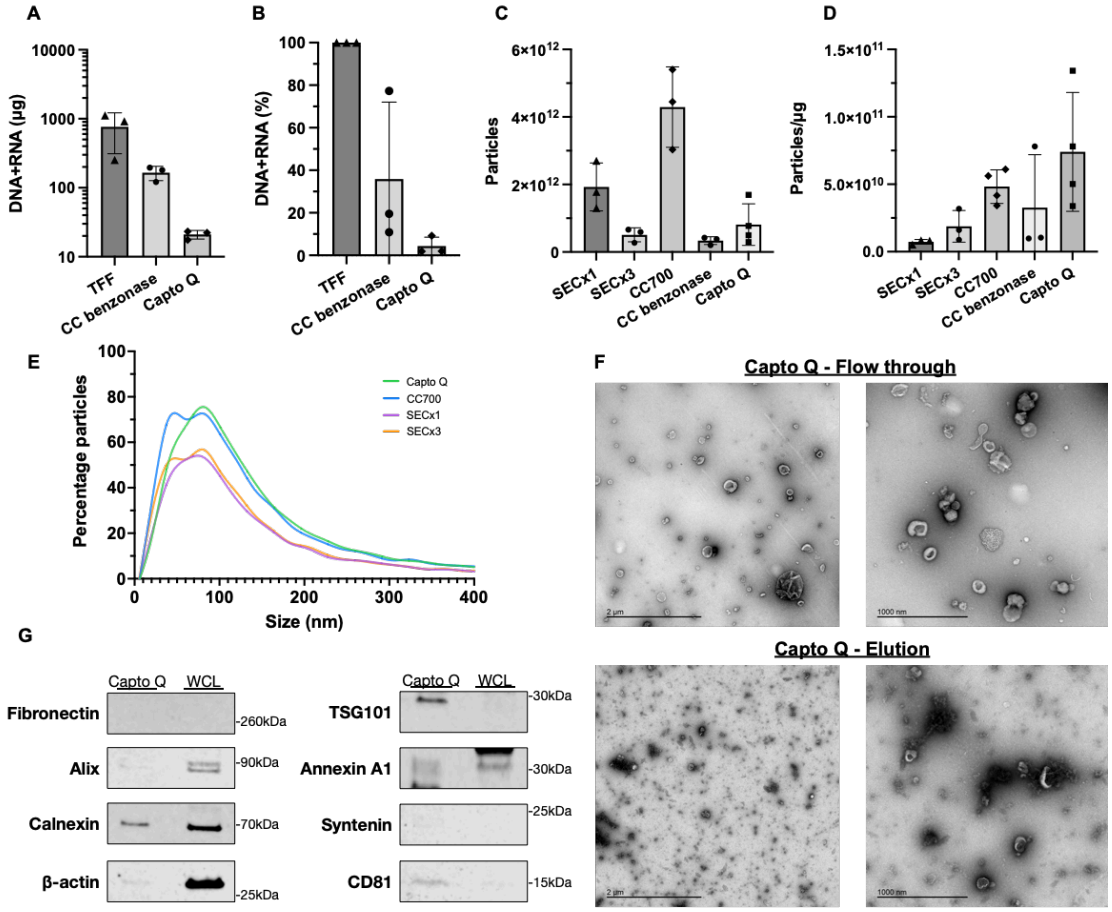

Figure 4.5 Capto Core with benzonase treatment (CC benzonase) and Capto Q purification are superior to SEC for EV purification from DNA and RNA. Following TFF, to further deplete nucleic acids in some Capto Core destined preps, 150 U/ml of benzonase were incubated EV preps at 37°C for one hour (CC benzonase). Following Capto Core purification, some preps were subjected to Capto Q anion exchange. The flow through and elution phases were collected and assessed for nucleic acid content. (A) Total micrograms and (B) percentage of DNA and RNA at each phase of EV

purification, including after TFF, CC benzonase and Capto Q. (C) Total particle counts following each purification method. (D) Particle/µg of DNA and RNA following each purification method. (E) NTA size distribution of particles from Capto Q purification. Smoothed best-fit splines with 50 knots generated with Prism 9 GraphPad Software. (H) TEM images from Capto Q flow through and elution phases of Capto Q purification. (G) Western blot using 10 µg of each loaded sample to detect EV proteins (ALIX, beta-actin, syntenin, CD81, annexin A1 and TSG101) and non-EV proteins (calnexin and fibronectin).

Finally, EVs purified by Capto Q were characterised by NTA, TEM imaging, and western blotting. As seen in Figure 4.5E, the size distribution profiles of particles purified by Capto Q were consistent with EVs. Like Capto Core purification alone, a much greater percentage of particles purified by Capto Core occupied sizes less than 200 nm than SEC purified particles. Although interestingly, Capto Q purification eliminated a peak at ~40 nm seen in all other assessed purification methods. TEM images displayed in Figure 3F presented characteristic cup-shaped EVs in Capto Q flow-through fractions. However, once again, EV purity was visibly seen to have further improved compared to SEC and CC700. Images were remarkably less soiled by dark stained contaminants enabling EVs to be very clearly visualised. Capto Q purification also presented less EV aggregation than SEC purified samples, although notably more aggregation than in CC700 samples seen previously. Despite the negative charge of EVs, only a small minority were recovered in the elution phase of the Capto Q protocol compared to the flow-through stage. A large amount of dark-stained contaminants were also eluted in this phase. Western blot characterisation of Capto Q purified EVs shown in Figure 4.5G presented expression of typical EV markers: CD81, ALIX, TSG101, syntenin and annexin A1, versus low to no detectable expression in HEK whole cell lysate samples, aside from

ALIX that was more highly expressed in the whole cell lysate. The band intensities of every protein marker in the Capto Q samples were heavily diminished compared to samples from SEC and Capto Core. This may reflect the lower EV yields in Capto Q samples, although similar EV yields were seen in SECx3 samples with higher EV marker expression. Altogether, EVs purified by Capto Q presented typical EV size distribution profiles, TEM images revealed clear images of typically cup-shaped EVs and western blot data revealed expression of typical EV markers despite diminished expression compared to SEC and CC700.

4.4 Discussion

Upscaling EV production is often necessary to attain high or clinically relevant EV concentrations. This can be achieved using high-density cell culture techniques such as bioreactor or suspension culture. However, these techniques come at the cost of high concentrations of host cell proteins and nucleic acids within harvests. Consequently, conventional EV purification methods such as size exclusion chromatography (SEC) struggle to purify EVs harvested from these cultures. Here SEC was compared to novel Capto Core binding chromatography, with additional benzonase pre-treatment and Capto Q anion exchange, as an alternative to purify EVs derived from high-density bioreactor culture. This was particularly important to the research conducted within this thesis as upscaling EV production was necessary to attain high concentrations of EVs to investigate EV heterogeneity, as described in chapter 5.

We first assessed the ability of SEC to purify EVs from high cell density culture preparations by comparing UV chromatograms obtained from both low and high-cell density cultures. The low cell density culture preparation produced two resolved peaks, whereas the high cell density culture preparations produced two much larger unresolved peaks (Figure 4.2A). Nordin *et al.* (2015) also reported and analysed the same observation; SEC of pre-filtered EV preparations produced two resolved peaks, with the first eluted peak containing almost all particles, while most of the protein from the preparation was detected in the second peak[261]. The extensive crossover of the UV chromatogram peaks from the first SEC run (SECx1) of the high cell density culture preparations was initially assumed to have resulted in extensive crossover of contaminant protein into the EV peak. This was later confirmed as shown in the silver stain (Figure 4.3D) and BCA total protein quantification (Figure 4.4C), where high protein

signals were seen in SECx1 samples, and successive SEC runs of high-density cell culture preparations (SECx3) resulted in complete resolution between UV chromatogram peaks and lower protein signals.

In contrast, the UV chromatograms obtained using Capto Core columns to purify EVs from high cell density culture preparations were compared to those produced by SEC. As seen in Figure 4.2A, a single large peak was produced, which was expected, as the primary method of function of Capto Core columns is the retention of small impurities that can pass into Capto Core beads and bind to the core. Some size exclusion effects were seen as indicated by the shoulder on the right of the chromatogram, although the columns used were not large enough to elicit complete separation of preparation constituents that remained unbound. Similarly, Corso *et al.* (2017) also report the production of a single large peak corresponding to purified EVs following Capto Core purification of pre-filtered cell culture preparations[270]. This supported initial assumptions that the Capto Core columns were functioning correctly to purify EVs from high cell density cultures.

TEM imaging and silver staining of SEC and CC700 purifications were performed to make initial comparisons of EV purity prior to further investigation by BCA, NTA and RiboGreen DNA/RNA assays. In all TEM images in Figure 4.3, numerous cup-shaped, globular particles of varying sizes were observed. This morphology is typical of EVs in TEM imaging and is highly represented[219,277–280]. EVs are believed to present this way due to their adsorption onto hard surfaces and drying[280]. Aside from EVs, there was a high amount of small <50 nm light staining non-EV particles also present in SEC samples, with considerably more in SECx1 samples than in SECx3. The size and presentation of these

particles are synonymous with other reports of lipoprotein particles in EV preparations[281]. In contrast, little to none of these particles were seen in the Capto Core samples. These findings support previous studies that report the co-isolation of lipoprotein particles by SEC[153,212,282]. Furthermore, EVs in SEC images appeared aggregated and warped, whereas EVs from Capto Core were not aggregated and appeared spherical. This was interesting as previous studies utilising SEC to purify EVs have not reported EV aggregation or changes in morphology[226,261,264,266]. This phenomenon is more typical of differential ultracentrifugation, where high shear forces cause aggregation and rupture of EVs[222,283]. As opposed to a feature of SEC, it is possible that due to the high EV and contaminant concentrations of the cell culture preparations used in this study, high pressure may be exerted on EVs when attempted to be purified by SEC due to exceeding the maximum load of the column, therefore causing aggregation. Altogether, along with the observations of notably more dark stained non-EV constituents and high background in SEC images compared to the clear and detailed images of spherical EVs in the Capto Core images, TEM analysis provided strong initial evidence that Capto Core was superior to SEC for the purification of EVs from high cell density culture preparations. Silver staining of SECx1, SECx3 and Capto Core samples also supported TEM observations. Successive SEC runs saw a marked reduction of contaminant protein in TFF and SECx1 samples between 117 and 55 kDa, though the CC700 sample was further cleared of contaminant protein. This supported the suggestion that CC700 was superior to SEC for the purification of EVs from high cell density cultures.

Following initial comparisons, host cell protein that remained within preparations purified by different Capto Core columns was compared to select the best column for purifying EVs. This was conducted using the same analysis method as Corso *et al.* (2017). Pre-

filtered high cell density culture preparations passed through different Capto Core columns were separated from their remaining constituents by SEC[270]. Here BCA protein assay quantification was used on pooled fractions from the contaminant peak from SEC purifications to assess remaining contaminant protein. Corso *et al.* (2017) used this method to evaluate contaminant protein and RNA that remained when using the HiScreen Capto Core 700 only[270]. However, this investigation represents the first instance where the purification efficiency of different commercially available Capto Core columns has also been assessed. HiScreen Capto Core 700 (CC700) columns elicited the greatest reduction in total contaminant protein (Figure 4.4B); therefore, this was selected as the best column to use for the remainder of the investigation. In the context of other studies that have investigated Capto Core columns for the purification of EVs, this was significant as most other studies also employed HiScreen columns, therefore validating their findings as the best possible representation of EV purification using commercially available Capto Core columns[256,270,273,274]. McNamara *et al.* (2018) were the only group to use a HiTrap Capto Core 700 column. Interestingly, McNamara *et al.* reported a particle/μg value of approximately 2.5 x 10^9 particles/μg, which was slightly higher than the 1.16 x 10^9 value reported here for CC700 presented in Figure 4.4E[276]. This may be due to the prior purification steps performed by McNamara *et al.,* including ultrafiltration and PEGylation that removed high amounts of contaminant proteins prior to Capto Core.

Other studies that have compared the efficiency of different EV purification methods such as precipitation, ultracentrifugation and immunoaffinity binding have reported that SEC yields EVs of the highest purity with respect to protein. These studies have compared the ability of these techniques to purify EVs from serum which offers further similarity to this investigation due to the high protein density of serum[205,226,266]. Here, as seen in Figure

4.4E, CC700 was reported as superior to SEC for the purification of EVs from high cell density culture preparations. Similarly, Veerman *et al*. (2021) also compared the efficiency of common EV purification methods to deplete DNA and RNA from EV preparations and reported that SEC yielded among the purest EVs per microgram of RNA for both conditioned medium and plasma purifications[205]. However, as shown here, while the deviation between biological repeats was high, CC700 produced higher purity EVs per microgram of DNA and RNA than SECx3 (Figure 4.4G). Additionally, as shown in Figure 4.4F, total DNA and RNA amounts were much higher than presented by Veerman *et al.* (2021) due to working with high cell density culture preparations[205], presenting the high dynamic range of CC700. Furthermore, CC700 is an inexpensive and accessible technique, particularly for researchers that routinely utilise SEC due to its similarity and utilisation of the same equipment. CC700 is also far more time efficient than all other common techniques[216,268]. Here the scalability of CC700 for EV purification from high cell density culture preparations and large volumes is demonstrated, and its ability to yield high-quality, clinically applicable EVs. Altogether, CC700 binding chromatography presents a marked improvement over SEC for EV purification from free protein, although further investigations should simultaneously compare CC700 binding chromatography to other common methods of EV purification.

While CC700 presented as the better of SEC and CC700 for the purification of EVs from DNA and RNA in high cell density culture, total DNA and RNA remained as high as in SECx1 samples, as shown in Figure 4.4F. On the other hand, a far greater particle yield was obtained by CC700 than SECx3, which had a far lower total remaining DNA and RNA. This may suggest that remaining DNA and RNA were directly associated with EVs, either as cargoes or associated with RNA binding proteins on EV surfaces[284].

Nonetheless, solutions were explored to further reduce total DNA and RNA levels and increase EV purity. Interestingly, treatment with benzonase saw both a reduction in DNA and RNA (Figure 4.5A, B) and total particles (Figure 4.5C). Total particle losses may have been due to damage to EVs following digestion of EV-associated DNA and RNA or to degradation of some EVs after incubating TFF concentrates for one hour at 37°C. However, other studies investigating this hypothesis did not report a loss of EVs or a change in EV integrity[285,286]. As seen in Figure 4.5A and B, Capto Q anion exchange caused a marked reduction in EV DNA and RNA levels and, as seen in Figure 4.5D, yielded the highest purity EVs per microgram of DNA and RNA. However, this was also accompanied by low total particle yields. Other studies investigating anion exchange for EV purification have reported improved particle purity and EV yield versus ultracentrifugation[255,287,288]. Although, when investigating particle retention, Rautaniemi *et al.* (2021) reported between a 35.3% and 54% loss of EVs by anion exchange[288]. Additionally, these studies only examined particles from the elution of phase of anion exchange and did not include EVs from the flow-through phase. A possible explanation for EV losses seen in this investigation and elsewhere following anion exchange could be due to the overall negative charge of EVs, causing them to be bound to anion exchange resin[289]. However, as shown in Figure 4.5F, far fewer EVs were identified in the sodium chloride elution fractions than in the flow-through of Capto Q, suggesting that EVs did not bind to the Capto Q column. Together the data suggest that benzonase treatment of TFF filtered high cell density culture preparations followed by CC700 and Capto Q anion exchange produces the highest purity EVs from DNA and RNA; however, reductions in EV concentration present a notable trade-off to achieve this outcome.

Turning to the characterisation of EVs derived from CC700 and SEC, the high expression of the EV-associated proteins ALIX, β-actin, TSG101, annexin A1, syntenin and CD81 in both CC700 and SECx3 samples (Figure 4.4I), and a higher expression in these samples than in SECx1 and whole cell lysate provided further evidence for the presence of purified EV in both of CC700 and SEC samples[18]. Interestingly, a high expression of calnexin was seen in all samples. Calnexin has previously been reported as a non-EV marker[19], although more recently, it has been suggested as a marker of large EVs (larger than 150 nm)[18]. This may explain the slightly greater calnexin band intensity in the CC700 sample, as the CC700 size distribution profile presents a greater percentage of post 150 nm particles than in SECx1 and SECx3 samples (Figure 4.4H). Other studies have reported a low expression of calnexin from SEC and CC700 purification by western blotting[267,290]. However, as image contrast and brightness if often altered in western blotting to achieve a clear image, without densitometric analysis and comparison, it is difficult to compare expressions between studies. Additionally, the greater fibronectin band intensity in the SECx3 sample may indicate a greater purity of CC700 EVs than SECx3 EVs, as fibronectin is a secretory protein not typically associated with EVs and only associates with EVs by binding to promiscuous receptors on the EV surface[18,291]. In contrast, little to no detection of EV markers in Capto Q samples, as seen in Figure 4.5G, provided further evidence for the loss of EVs following this purification method.

Lastly, as seen in Figure 4.5E, a higher proportion of sub-200 nm particles were retained by CC700 and Capto Q purifications than by SECx1 and SECx3. Other studies have also reported differences in the size of particles yielded by different purification techniques. SEC tends to yield fewer particles with a smaller average size and a narrower size distribution than other techniques[226,264,266,290]. Corso *et al.* (2017) also showed that CC700

yields EVs with an average modal size of roughly 120 nm[270], while Brennan *et al.* (2020) report a modal size of roughly 60 nm for EVs isolated by SEC and a low relative yield of large EVs. Furthermore, Brennan *et al.* (2020) suggest the reason for the smaller modal particle size and narrower size distribution of EVs purified by SEC is the disproportional amount of protein aggregates or could indicate the presence of LDL and VLDL[226]. Altogether this corresponds with the observations in this investigation, including potentially a larger proportion of lipoprotein particles in SEC samples as discussed previously in association with the TEM images. Alternatively, differences in size distributions could be due to the much lower total particle counts in SECx3 compared to CC700. Finally, compared to CC700, a population of small particles seemed to be removed following Capto Q purification, as presented by the differences between the CC700 and Capto Q size distribution curves. This could correspond to the removal of aggregates or lipoprotein contaminants[255], particularly as Capto Q TEM images appeared the cleanest of all TEM images. On the other hand, this population could represent exomeres which average around 35 nm, although these particles are reported to have a weaker negative charge[50].

4.5 Limitations, future work, and conclusions

4.5.1 Limitations

Overall, compared to SEC, clear improvements in purity among EVs derived from high cell density cultures were seen in CC700 samples. However, notable variability among biological repeats was seen in almost all assays, causing differences to appear insignificant. The experiments seen here would benefit from further biological repeats to produce concordance in the data and any significant differences. Alternatively, comparisons of CC700 versus SEC or other techniques may benefit from performing paired analysis to observe any significant differences by dividing TFF concentrated EV preparations in two before performing subsequent purification techniques. However, this may not accurately represent the capability of any assessed techniques to purity EVs from high cell density cultures due to the reduction in contaminant and EV yield by dividing a preparation in two.

Certainly, particles/μg data, western blotting and TEM imaging provided strong evidence of improved EV purity following CC700. However, assessments of protein and nucleic acids remaining in purified EV preparations by BCA and RiboGreen assays, respectively, did not reveal reductions in soluble protein and nucleic acids exclusively. Further investigations into CC700 EV purification may benefit from purifying EVs from cells modified to release a fluorescent or traceable soluble protein. Alternatively, a fluorescent EV membrane protein to distinguish between proteins contaminants and EV protein could be used[158,174,292]. Fluorescent oligos could also be spiked into EV preparations and tested in the same manner. In this way, the efficiency of a technique to separate EVs from contaminating protein can be monitored through the reduction in fluorescence of purified

EV samples and may provide a more specific representation of CC700 purification efficiency.

Additionally, while the ability of CC700 and SEC to remove contaminating proteins and nucleic acids was assessed, the level of non-EV particles such as lipoprotein particles that remained in EV preparations was not specifically tested[153,212,273]. Identifying these co-isolates in EV preparations will strengthen purification efficiency analysis, as the presence of non-EV particles may skew particles/µg data towards higher values, giving the impression of purer EV preparations. If non-EV particles are confirmed to be a constituent of CC700 preparations, the CC700 purification protocol could be further developed to address the high unmet need for purification techniques that isolate EVs from non-EV particles, such as lipoproteins[273,282].

Finally, while the function of CC700 and SEC purified EVs was not compared within this chapter, functional assays in chapter 5 present CC700-derived EVs as functionally active *in vitro*. Future studies should perform this comparison to ensure that CC700 EVs are not only pure but retain their functional activity.

4.5.2 Future work

The data in this chapter describes the suitability of CC700 for the purification of EVs from high cell density culture. While other studies have demonstrated the suitability of CC700 to purify EVs from lower density cell culture preparations[256,270,273,274,276], it is likely that CC700 will also be suitable for EV purification from low cell density culture. This is particularly interesting as it suggests that CC700 could serve as a replacement for SEC, particularly given its accessibility, inexpensiveness and time efficiency. However, to

further validate the use of CC700, future studies should compare CC700 EV purification with other commonly used methods for the purification of EVs from low and high-cell density culture preparations. Additionally, comparing CC700 to other purification techniques for EV purification from biofluids such as serum and plasma will also be valuable due to the high protein and nucleic acid concentrations within these preparations and the few studies that have compared EV purification methods from biofluids. Furthermore, while SEC combined with ultracentrifugation has been shown to produce pure EVs from serum and plasma samples [226,266], CC700 could offer a much faster alternative.

Otherwise, while Capto Q anion exchange presented a promising addition to CC700 to reduce total DNA and RNA levels in EV preparations, significant reductions in total particle counts and EV marker expression highlight the need to optimise anion exchange to improve EV yield. As other studies have reported successful EV purification using anion exchange, adopting protocols used elsewhere may help improve Capto Q yields[255,287,288]. Furthermore, similar comparative and functional studies to those proposed for CC700 would also be beneficial in combination with anion exchange. Additionally, work should be done to categorise the particle population that was seemingly removed following Capto Q anion exchange, as seen in Figure 4.5.

Once optimised, CC700 presents a valuable tool for purifying high, clinically relevant EV concentrations for therapeutic delivery. Although, *in vivo* toxicity studies should be performed to ensure the safety of EVs purified by CC700.

4.5.3 Conclusion

Overall, CC700 binding chromatography was superior to SEC for the purification of EVs from high cell density culture preparations. During conventional SEC-based EV purification, SEC columns are exposed to EV and contaminant concentrations far beyond their separation capabilities, causing incomplete resolution of protein and nucleic acid contaminants from EVs. For high cell density cultures, SEC must be performed multiple times on the same preparation to achieve complete purification of EVs. However, this results in significant EV losses, defeating the purpose of utilising high cell density culture preparations.

CC700 offers an inexpensive and accessible alternative to SEC, with high scalability and yields high-quality, clinically applicable EVs over twice as pure from contaminating protein and nucleic acids as EVs purified by SEC. CC700 also offers high scalability. Although numerous studies comparing EV purification techniques conclude that SEC represents the current gold standard of commonly used EV purification techniques, this study presents CC700 as a new gold standard of EV purification.

4.6 Supplementary Figures

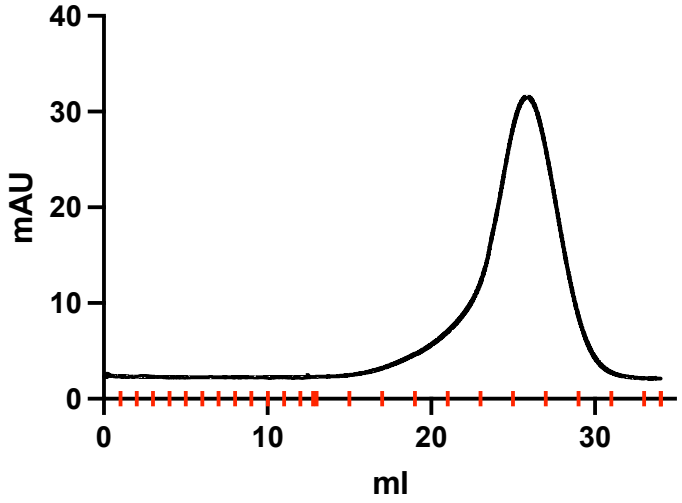

Supplementary Figure S4.1 Validation of "DMEM constituent peak" following SEC purification of DMEM + 1% A/A. 2 mL of DMEM + 1% A/A passed through a Tricorn 10/300 size exclusion chromatography column packed with Sepharose 4 Fast Flow resin producing the displayed chromatogram showing a ~30 mAU peak beginning after ~15 mL of elution. The resulting peak is close to identical to the "DMEM constituent peak" described in Figure 4.4A. Red lines on x-axis denote fractions collected.

5.0 Identifying EV heterogeneity to improve therapeutic potential

5.1 Introduction

5.1.1 EV heterogeneity

As previously described, “extracellular vesicles” is an umbrella term that encompasses many subtypes of cell-derived membranous nanoparticles that are often further categorised as exosomes or microvesicles according to their route of biogenesis. Exosomes are sized between 30 and 150 nm[23,36], whereas microvesicles are sized between 50 and 1,300 nm[23,24]. Once released from cells, the crossover in size ranges results in the formation of a heterogenous mix of EVs, which also differ in their respective proteomes and cargoes. However, aside from biogenesis, further degrees of EV heterogeneity have been shown to exist that are associated with EV size; cell type, state, protein expression and differentiation; and epigenetic factors[47,51,54,55,57,58,153], evoking questions regarding the true source and determinants of EV heterogeneity, or whether EV heterogeneity occurs more stochastically.

A study by Kowal *et al.* (2016) demonstrated these degrees of heterogeneity by first separating small EVs (sEVs), and large EVs (lEVs) derived from dendritic cells using both differential ultracentrifugation (dUC) and density gradient centrifugation (DGC) and performing LC-MS/MS proteomics analysis to assess differences in EV proteomes. sEVs with a majority size range of 50 to 150 nm were exclusively enriched in syntenin-1, TSG101, ADAM10, and EHD4, which are often associated with exosomes. However, both sEVs and lEVs with a majority size of over 150 nm were also enriched in other markers thought to be exclusive to exosomes, including MHC class II or class I, heat-

shock proteins 70, flotillins, and actin, despite the majority presence of EVs larger than the normal exosome size range. The universal expression of these markers demonstrates the mix of EVs secreted from cells and the challenge that EV researchers face to separate subtypes of EVs to understand or mitigate EV heterogeneity. Kowal *et al.* (2016) also isolated EVs based on their expression of CD9, CD63 and CD81 by immunoaffinity binding[48]. These tetraspanins have previously been shown to be exosome-associated[18,32,293–295], although the presence of CD63 and CD9 was also confirmed on lEVs. Proteomics analysis of EVs in each of these tetraspanin populations showed differential protein expression and some proteins that were exclusively associated with one tetraspanin than the others[48]. This further presents the extent of EV heterogeneity within EV subtypes and the complexity of distinguishing between different EVs within a heterogeneous population.

5.1.2 Size-based EV heterogeneity

Historically, in EV-based studies, researchers are often quick to categorise EVs as either exosomes or microvesicles to attempt to explain or attribute EV characteristics to a specific subtype of EVs. However, as explained previously, EVs are naturally heterogeneous in particle size, and crossover in size ranges makes isolation of exosomes or microvesicles challenging to isolate and study selectively. In addition to various proteins considered markers of EVs in general, various proteins have also been proposed as markers of exosomes or microvesicles[18,48,152]. However, various studies have shown that identifying these specific EV subsets is not so simplistic as heterogeneity has been observed among these assumed EV subsets themselves[48,152]. Instead, one of the most common methods of studying EV heterogeneity has been according to EV size, to

establish if size itself is a delineating factor in determining EV contents or functional roles as opposed to biogenesis.

Numerous studies have demonstrated significant differences in EV proteomes and transcriptomes that accompany differences in size. Xu *et al.* (2018) used sequential ultrafiltration to separate sEVs, and lEVs derived from LIM1863 colon cancer cells. LC-MS/MS Proteomics analysis revealed 354 differentially expressed proteins in sEV and 606 differentially expressed proteins in lEVs, with 256 proteins in common and 350 uniquely enriched proteins in lEVs. Unlike the study performed by Kowal *et al.* (2016), Xu *et al.* (2018) presented highly significant ($P < 0.0005$) functional differences between sEVs and lEVs; lEVs elicited a three-fold higher invasion of non-invasive recipient fibroblast cells than sEVs. These differences were attributed to differential enrichment of proteins involved in invasion, migration, and cell motility among the two EV populations[23]. Similarly, Willms *et al.* (2016) used density gradient centrifugation to isolate low- and high-density EVs that the authors termed “LD-EXO” and “HD-EXO”, respectively. These EV populations differed in size, with the majority of LD-EXOs ranging from 75 to 200 nm with a modal size of 117 nm, while the majority of HD-EXOs had a size range of 50 to 120 nm with a modal size of 66 nm. Once again, the authors present differences in function elicited by the two differently sized EV populations. HD-EXO altered the expression of 1116 genes, whereas LD-EXO altered the expression of only 257 genes, compared with PBS treatments. Subsequently, altered gene expression significantly impacted protein expression[49]. Lastly, Zhang *et al.* (2018) were able to optimise the use of asymmetric flow field-flow fractionation to fractionate EVs into different size-based subpopulations, including 90-120 nm (Exo-L), 60-80 nm (Exo-S). In addition, they were the first to characterise a sub-50 nm, non-membranous nanoparticle population termed

exomeres with a proteome substantially different from that of Exo-L and Exo-S. Exo-S were predominantly enriched in proteins associated with endosomes, multivesicular bodies, vacuoles and phagocytic vesicles, while Exo-L were specifically enriched in the plasma membrane, cellular contact/junctions, late-endosome and trans-Golgi network proteins[50,296].

The studies mentioned above have used different techniques to separate EVs into different size-based populations, including ultrafiltration density gradient centrifugation and asymmetric flow field fractionation. In most cases, a population of post-150 nm lEVs were produced, as were a population of sub-150 nm sEVs. However, size-based heterogeneity has been shown to exist among sub-150 nm EV populations, thus highlighting the need for higher resolution techniques to separate EVs into EV populations with narrower size ranges to explore the extent of size-based heterogeneity further. To explore this further, Willms (2018) used a Cytiva XK-16/70 column packed with Sephacryl S1000 resin to fractionate SKOV3 ovarian cancer EVs into four different populations. The four populations were selected according to the resulting UV chromatogram profile produced by the XK-16/70 corresponding to sample elution at different times following size separation. NTA analysis showed marked differences in size distribution profiles of each pool, with incrementally smaller EVs ranging from roughly 175 nm to 45 nm across all four pools. Willms (2018) later showed significant differences in the facilitation of SKOV3 cell adhesion by EVs from each of the four pools and unfractionated SKOV3 EVs, which was linked to CD29 expression on EVs[51].

Given the vast heterogeneity of secreted EVs, the numerous factors that can affect their composition, and the plethora of cell sources, it has been difficult to clearly attribute any

given function to a particular subset of EVs. Furthermore, currently available EV purification methods are arguably unable to distinguish EVs based on their subtype or biogenesis due to overlapping sizes of EVs subtypes and continued uncertainty surrounding biogenetic markers, resulting in heterogeneous EV populations of diverse origin[23,48]. Advances in EV purification methods and the use of novel high-resolution and single-particle characterisation techniques will enable significant advancements in understanding EV heterogeneity, and the precise role of EVs in physiological and pathophysiological processes such as cancer will aid the advancement of the therapeutic EV platform.

5.1.3 Composition-based EV heterogeneity

As previously described, aside from size, EV heterogeneity has also been associated with cell type and state, and differences in cellular protein expression. Therefore, as opposed to studying EV heterogeneity based on size, the composition of EVs has been used as a focus for studying EV heterogeneity. Immunoaffinity isolation techniques have been used to isolate EVs with heterogeneous protein compositions from different types of cells, cells in different states or cells exposed to different stimuli that may affect EV heterogeneity.

In a study that demonstrates the value of composition-based EV heterogeneity studies, Pietrowska *et al.* (2021) isolated EVs from the plasma of 15 melanoma patients and performed magnetic bead-based immunoaffinity purification to separate chondroitin sulfate peptidoglycan 4 (CSPG4)-positive EVs from CSPG4-negative EVs, as CSPG4 is overexpressed in melanoma cells. The authors identified 73 proteins upregulated in melanoma-associated CSPG4-positive EVs, including 13 proteins such as ALIX and heat shock protein 90-beta, whose levels discriminated patients with progressive metastatic

melanoma from those who had no evident or stable disease after therapy[297]. Identifying these differences in protein expression between EVs may help produce a melanoma liquid biopsy or serve as a prognostic marker. In a similar study, Mathivanan *et al.* (2010) isolated EVs positive for colon cancer-specific marker glycoprotein A33 (GPA33) from LIM1215 colorectal cancer cells by immunoaffinity binding, revealing 394 proteins that were unique to GPA33-positive EVs compared to EVs isolated by ultracentrifugation. Of these 394 proteins, more than 50% were categorised in at least one of the seven cancer hallmark attributes[237]. Therefore, these findings could serve as a basis for a potential anti-cancer therapy and highlights the impact that composition-based EV heterogeneity studies could have on therapeutic development. In a separate disease context, EVs expressing neural cell adhesion molecule L1 purified from the plasma and serum of Alzheimer's disease (AD) patients have shown to be enriched in p-T181-tau and p-T231-tau, which are highly involved in the development of AD[298]. This could provide a liquid biopsy to contribute to the diagnosis of AD, or a therapeutic strategy to slow the progression of AD.

Elsewhere, Herwitz *et al.* (2016) assessed the heterogeneity of EV populations derived from 60 cancer cell lines to identify common EV protein cargoes and biomarkers specific to different cancer types. 6071 proteins were identified in EVs by LC-MS/MS proteomics, of which 213 were common to all cell lines. Of EV-specific proteins, only CD81, ALIX, and heat shock protein 8 (HSPA8) were common to all samples, while many of the other EV proteins varied greatly in their expression between EVs derived from different cell lines. LC-MS/MS analysis also revealed similarities between EVs derived from cells with similar metastatic potentials[299]. Despite these differences, EVs were purified by PEG precipitation and ultracentrifugation, which may have included impurities within EV

preparations[220,228,229]; therefore, replications of these studies using more strenuous purification techniques may be beneficial. As with other examples, comparisons of EV heterogeneity between cell lines may provide novel diagnostic or therapeutic avenues. Various studies have also focused on EVs derived from cells exposed to differences in environmental factors such as heat stress, hypoxia, and nutrition, revealing differences in EV heterogeneity as a result[300–302].

5.1.4 Advancing understanding of EV heterogeneity

Considerable progress has been made in documenting, understanding and utilising EV heterogeneity. However, many questions remain regarding the factors that may impact EV heterogeneity, the source or determinants of EV heterogeneity, and the impact that EV heterogeneity may have on the function of EVs, particularly for therapeutic development. In this chapter, numerous findings that further present the extent of EV heterogeneity with respect to numerous factors and the impact of heterogeneity on EV functions are described.

Firstly, while Willms (2018) showed the high resolutive capability of XK-16/70 SEC for separating sub-150 nm EVs and demonstrated the functional heterogeneity of SKOV3 EVs in different size-based subpopulations, until now, the proteome of these EVs has not been extensively scrutinised[51]. In this chapter, the protocol of Willms (2018) was replicated to separate SKOV3 EVs into the same four size-based subpopulations and analyse their differences in protein expression. NanoView ExoView R100 was utilised to assess the tetraspanin profile of each EV subpopulation, structured illumination microscopy to assess colocalisation of CD81 and CD29 among each of the EV subpopulations, and performed LC-MS/MS proteomics analysis to gain detailed insights

into the differences in EV proteomes among each of the four pools. The analysis in this investigation provided further evidence of the heterogeneous nature of EVs, showed the association between EV size and protein expression at a higher resolution than seen elsewhere in the literature, and presented differences in the expression of functional proteins and protein classes that suggest different functions for different sized EVs.

Furthermore, while heterogeneity with respect to EV biogenesis, size, protein expression, cell type and external factors has been explored[303], whether temporal changes in EV protein expression occurs has yet to be explored. In addition to assessments of size-based EV heterogeneity, within this chapter conditioned medium was harvested from two different subclones of MDA-MB-231 breast cancer cells on a weekly basis for seven weeks, and changes in expression of EV surface proteins were determined by MACSPlex Exosome Flow Cytometry. This data presented an additional source of EV heterogeneity that had not previously been documented and further displays the complexity of EV heterogeneity due to its many sources.

Finally, in the study of EV heterogeneity, it is important to remember that once released from cells, EVs travel to recipient cells and deliver their cargoes to elicit biological effects. Due to the vast heterogeneity in EV cargoes and protein expression, these differences may translate into heterogeneous EV functions. Indeed, various studies have documented differences in function between different subsets of EVs derived from the same parent cell population, and these differences have been linked to EV size, biogenesis, and functional protein expression[54–58]. This highlights the differential function of EVs derived from the same cell type and suggests that some EVs within a total cell-derived EV population may not be involved in certain functions, potentially dampening or

even having an antagonistic effect on EV efficacy. Therefore, functional heterogeneity is an important factor to determine in the development of EV therapeutics, as the use and engineering of a total EV population may yield EV therapeutics that have an unintentionally lower efficacy. Characterising functionally heterogeneous EV subpopulations may aid industry therapeutic development strategies by providing the necessary data to selectively purify therapeutically advantageous EVs. Furthermore, whether heterogeneity in EV function is directly mirrored in parental cells and is a direct cause of EV heterogeneity is yet to be determined. While biologists habitually assume uniformity of the clonal cell populations grown *in vitro*, numerous studies have shown differences between single cells in clonal populations. This is suggested to arise due to genetic variability, somatic mutations, epigenetic factors, and stochastic fluctuations. Cellular heterogeneity has been shown to affect the function of a cell, its differentiation and even affect EV production and EV function[304–308]. Therefore, in the final investigation that took place in this chapter, subclonal populations of mesenchymal stem cells were generated by single-cell sorting, and EVs were harvested from each subclone. Subsequently, *in vitro* assays assessing various functions of isolated EVs were performed to identify functional heterogeneity. The proteome of EV populations was then assessed by LC-MS/MS proteomics analysis to provide possible explanations for the differences in function and identify markers that could be used to identify these functional EV subpopulations in other EV preparations in the future.

5.2 Materials and methods

5.2.1 EV fractionation by XK-16/70 size exclusion chromatography

To further separate particles according to size, EVs purified by Tricorn 10/300 SEC were pooled and were subjected to a higher resolution SEC protocol using an ÄKTA Pure chromatography system and an XK-16/70 SEC column (Cytiva) packed with Sephacryl® S-1000 Superfine SEC medium (Cytiva). Chromatography was performed in PBS at a flow rate of 0.5 mL/min and monitored using absorbance at 280 nm.

Thirty individual 4 mL fractions were collected and stored at 4˚C. Fractions were pooled together according to the positions of peaks on the UV chromatogram. Pooled fractions were concentrated using Amicon Ultra 10 kDa MWCO centrifugal filters (Merck Millipore).

5.2.2 Adhesion assay

The adhesion assay protocol was adapted from Willms (2018)[51]. 1 µg of each sample was coated, in triplicate, onto 96-well plates (Corning, NY, USA) overnight at 4°C. PBS alone was used as a negative control. After incubation, wells were washed with PBS to remove unbound sample. Cells were washed with PBS, trypsinised, and resuspended in supplement-free medium (the final concentration of SKOV3 cells was 200,000 cells/mL, whereas, for MSCs, it was 100,000 cells/mL). 100 µL of this cell suspension was added to each well and left to incubate and adhere for 30 minutes. Subsequently, each well was washed in three changes of PBS to remove unadhered cells. Images were taken on an EVOS FL Cell Imaging System (Thermo Fisher Scientific) to evaluate the level of adhesion; the number of adhered cells was quantified using ImageJ – Analyse Particles.

Alternatively, the IncuCyte ZOOM (Essen BioScience, Newark, UK) was used to take images of each well and count cells using built-in software after washing.

Raw results for each n-number were summed. Individual results were then divided by the sum and multiplied by 1000 to compensate for fluctuations in cell adhesion due to experimental error.

5.2.3 NanoView ExoView R100

Single particle characterisation of SKOV3 EV populations was performed using the ExoView R100 (NanoView Biosciences, MA, USA), operated by NanoView Biosciences personnel. EVs were diluted in Solution A (a proprietary formulation containing Tween-20) to a concentration of 1 x 10^8 EVs. 35 µL of each sample were incubated at room temperature on ExoView Tetraspanin chips (NanoView Biosciences) printed with anti-CD63 (clone H5C6), anti-CD81 (clone JS81), or anti-CD9 antibodies (clone H19a), or mouse IgG1κ isotype control antibodies.

Chips were washed in three changes of 1 mL Solution A for three minutes, followed by incubation for one hour at room temperature with a 1:5000 dilution of fluorophore-conjugated tetraspanin antibodies (anti-CD9-Alexa Fluor 488 [AF488], anti-CD81-AF555, and anti-CD63-AF647) in Solution A with 2% bovine serum albumin. Subsequently, chips were washed in Solution A, three changes of Solution B, then a wash in filtered deionised water and dried. Chips were then imaged with the ExoView R100 reader. Images were acquired and analysed using ExoViewer software.

Sizing was obtained by interferometry-based label-free particle measurements between 50 and 200 nm performed on each spot. Mean size was calculated from three spots for each capture antibody. Particle number was defined in terms of normalised particles (number of particles in a 150 μm area of the antibody capture spot).

5.2.4 LC-MS/MS proteomics analysis

Before LC-MS/MS analysis, EV samples needed to be digested and desalted and proteins needed to be purified. 10 μg of purified EVs were used for each sample and made up to 200 μL with PBS.

Firstly, to digest the EVs, dithiothreitol (Thermo Fisher Scientific) was added to each sample to a final concentration of 5mM, vortexed and incubated for one hour. Next, Iodoacetamide (Sigma Aldrich), an alkylating agent, was added to each sample to a final concentration of 20 mM and incubated for one hour.

Proteins were then precipitated by the methanol/chloroform extraction method. 600 μL of methanol (Fisher Scientific) and 150 μL of chloroform (Sigma Aldrich) were added to each sample and vortexed. 450 μL of Milli-Q water was added to samples, and they were vortexed again. Samples were centrifuged at 17,000 x *g* for one minute, separating the solution into phases. The upper phase was carefully pipetted, ensuring not to disrupt the interphase solution. 450 μL of methanol was added to each sample, and they were vortexed and centrifuged again at 17,000 x *g* for two minutes. The supernatant was discarded from each sample, and precipitated proteins were resuspended in 50 μL 6 M urea (Sigma Aldrich) buffer by vortexing. The urea concentration was reduced to a final concentration of less than 1 M by adding 250 μL of Milli-Q water and vortexing. 0.2 μg of

sequencing grade modified trypsin (Promega) was then added to achieve a 1:50 ratio of trypsin to protein and digest proteins into small peptides. This was performed overnight at 37°C.

Finally, peptides were purified and concentrated using Thermo Scientific Pierce C18 Spin Column (Thermo Fisher Scientific). Two solutions were made up: 0.1% trifluoroacetic acid in 2% acetonitrile (solution A), and 0.1% trifluoroacetic acid in 65% acetonitrile (solution B). 200 µL of solution B was added to each column. Columns were centrifuged at 1500 x *g* for one minute, and the flow-through was discarded. This was repeated a second time. 200 µL of solution A was added to each column, and columns were centrifuged at 1500 x *g*. The flow-through was discarded, and this was repeated a second time. Digested samples were then added to the columns, and columns were placed in new receiver tubes and centrifuged at 1500 x *g* for one minute. The flow-through was recovered, re-applied to the column, and centrifuged again at 1500 x *g* to ensure complete binding of the peptides to the column. 200 µL of solution A was added to each column, and columns were centrifuged at 1500 x *g* for one minute to wash the peptides bound to the columns. The flow-through was discarded, and the wash was repeated. Finally, columns were placed into new receiver tubes, and 20 µL of solution A was added to each column to elute the bound peptides. Columns were centrifuged at 1500 x *g* for 1 minute, and the elution with the same receiver tube.

Samples were dried using a ScanVac Scanspeed 40 vacuum centrifuge and submitted to the Target Discovery Institute, University of Oxford, for label-free mass spectrometry analysis. Before analysis on the Q Exactive (Thermo Fisher Scientific) or Fusion Lumos (Thermo Fisher Scientific), peptides were separated using an Ultimate 3000 RSLCnano

system (Thermo Fisher Scientific). The Q Exactive was operated in a data-dependent manner, selecting the top 10 precursors for fragmentation by HCD. The survey scan was performed at 70.000 resolution from 400-1600 m/z, with a max injection time of 100 ms and a target of 1 x 10^6 ions. For generation of high-energy collision dissociation fragmentation spectra, a max ion injection time of 140 ms and automatic gain control of 1 x 10^5 were used before fragmentation at 30% normalised collision energy, 35.000 resolution. Precursors were isolated with a width of 2 m/z and put on the exclusion list for 70 s. Single and unassigned charge states were rejected from precursor selection.

Analysis was performed using MaxQuant Perseus v2 (Max Planck Institute of Biochemistry, Munich, Germany), and graphs were constructed in Prism 9. Raw intensity-based absolute quantification (iBAQ) scores were filtered to remove protein duplicates, reverse variables, contaminants, and any protein hits included in only one of three n-numbers. Data was also transformed on a $\log_2$ scale, and width adjustment normalisation was performed. Gene Ontology (GO) term enrichment and overrepresentation analysis were performed using the Protein Analysis Through Evolutionary Relationships (PANTHER) software, as outlined in Sork *et al.* (2018)[309].

5.2.5 Structured illumination microscopy and colocalisation analysis

SKOV3 EV populations were incubated with recombinant rabbit anti-CD81 (Abcam, ab219209, 1:100) and mouse anti-CD29 antibodies (Genetex, GTX44230, 1:500) overnight at 4°C. Subsequently, EVs were incubated with donkey anti-rabbit IgG Alexa Fluor® 647 (Abcam, ab150075, 1:1000) and donkey anti-mouse IgG Atto-488 (Jackson ImmunoResearch Europe Ltd, Ely, Cambridgeshire, UK, 715-545-150, 1:500) for one hour at room temperature. After incubation, structured illumination microscopy (SIM) was

performed without needing further EV purification due to labelled EVs being identifiable above background levels. 200 µL of labelled EV samples were pipetted into separate wells of ibidi µ-Slide 8 Well Glass Bottom slides (ibidi GmbH, Gräfelfing, UK) and incubated at room temperature for 30 minutes. Samples were then aspirated, wells were washed with one change of PBS, and 200 µL of PBS was re-applied to each well. Samples were imaged with the Zeiss Elyra 7 with Lattice SIM² (Carl Zeiss, Oberkochen, Germany) using 532 nm and 642 nm lasers.

Colocalisation analysis of SIM images was performed using the EzColocalization plug-in for FiJi as described in Weston *et al.* (2018)[310]. Briefly, images from the 532 nm (CD29-positive) and 642 nm (CD81-positive) channels were loaded into ImageJ. The brightness and contrast were adjusted for both images to make positive particles more visible. A Gaussian blur was applied to both images to enable EzColocaliztion to identify crossover between colocalised signals in each channel. The 642 nm channel image was then duplicated, thresholded and converted to a binary format, and inverted. This image was then used as a mask for EzColocalization. Images from both channels were loaded into EzColocalization along with the mask, and threshold overlap scores were generated. 1.0 indicates complete colocalization between CD81 and CD29, 0.0 indicates no relationship between CD29 and CD81, and -1.0 indicates complete anti-colocalization between CD81 and CD29.

5.2.6 MACSPlex flow cytometry assay and temporal variation analysis

MACSPlex exosome flow cytometry was carried out as described by Wiklander *et al.* (2018)[311]. 120 µL of centrifuged conditioned medium from each MDA-231-MB (MDA) cell culture was incubated with 15 µL of MACSPlex capture beads (Miltenyi Biotech, Bergisch

Gladbach, North Rhine-Westphalia, Germany) overnight with gentle rotation. Beads were then washed in MACSPlex buffer and incubated with CD81-APC, CD63-APC and CD9-APC conjugated antibodies (Miltenyi Biotech) for one hour. Beads were then washed in two changes of and resuspended in MACSPlex Buffer. Fluorescence of the 39 bead populations was assessed using a CytoFlex S flow cytometer (Beckman Coulter, Brea, CA, USA). Bead populations were resolved in FITC (B525) and PE (B585) channels. Data was analysed by assessing the median fluorescence intensity (MFI) for APC (R660) for each gated bead population.

Background bead mean APC fluorescence intensities were subtracted from the respective sample mean APC fluorescence intensities. Values were relativised to the mean APC fluorescence intensities of CD63, CD81 and CD9 bead populations at week one of harvesting, respective of MDA cell subclone (lung or brain variant). Subsequently, the sum of fluorescence intensities for each sample was made equal to 1,000. The mean of each weekly set of samples for each MDA cell subclone was calculated, and this was used to display the most highly expressed proteins on a weekly basis and rank proteins in order of their expression in week one of harvesting. Finally, proteins were normalised to their expression in week one, and $\log_2$ was derived to show the change in protein expression on a weekly basis.

5.2.7 FACS single cell sorting

MSCs were removed from their culture vessels using trypsin and centrifuged at 700 x *g* to pellet the cells. Supernatant was discarded, and cells were resuspended in 4 mL of 0.22 μm filtered complete culture medium (MSC Basal Medium for Adipose, Umbilical, and Bone Marrow-derived MSCs supplemented with Mesenchymal Stem Cell Growth Kit

for Adipose and Umbilical-derived MSCs – Low Serum and 1% A/A) to wash cells and remove trypsin. Cells were again centrifuged at 700 x *g* to pellet cells. Cells were then resuspended in 1 mL of 0.22 µm filtered complete culture medium. 150 µL of complete culture medium was pipetted into each well of 96-well plates.

Dead cells were stained with 4',6-diamidino-2-phenylindole (DAPI) to distinguish live cells from dead cells. The BD FACSAria-II, operated by Robert Hedley, was used to gate for the live cells and sort a single live cell into each well of a 96-plate. Following single cell sorting, 96-well plates were re-incubated at 37°C in a humidified environment of 5% CO_2. Single-cell populations were monitored and expanded into larger vessels upon outgrowing 96-well plates. MSC single-cell subclonal populations were named according to the wells of 96-well plates they were derived from; for example, MSC subclone B4 cells were derived from well B4 of a 96-well plate.

5.2.8 T cell proliferation assay

As shown in Grist *et al.* (2018), T cell proliferation is proportional to extracellular lactate production[312]. Therefore, to indirectly measure the effects of MSC subclone-derived EVs on CD4+ and CD8+ T cell proliferation, the Promega Lactate-Glo Assay (Promega) was employed.

CD4+ and CD8+ T cells derived from healthy patient blood samples were identified by flow cytometry and kindly provided by Ashwin Jainarayanan. 50,000 cells of each type were seeded in triplicates in 96-well plates corresponding to the number of EV samples to be tested. A further two triplicates of each cell type were established to be used for

positive and negative controls. Once seeded, cells were incubated for 48 hours at 37°C in a humidified environment of 5% CO_2.

Following acclimatisation, 5 x 10^7 EVs were added per well for each condition in the 96-well plate generating a 1:1000 ratio of cells to EVs. Positive and negative controls were applied to designated wells. The positive control consisted of 2 µL of flow cytometry purified IL-2, provided by Ashwin Jainarayanan. The negative control consisted of 150 µL of serum-free OptiMEM. Wells were topped up to 200 µL with serum-free OptiMEM containing 1% A/A. 96-well plates were reincubated at 37°C until in a humidified environment of 5% CO_2.

After 48 hours, 96-well plates were removed from incubation and centrifuged at 1,000 x *g* to sediment the T cells. 1 µL of the suspension in each well was transferred to a new 96-well plate and diluted with 49 µL of PBS. Subsequently, T cell proliferation was assessed by measuring extracellular lactate using the Promega Lactate-Glo assay and following the manufacturer's protocol.

5.2.9 Migration assay

The migration assay protocol was adapted from Willms (2018)[51]. Briefly, a 10 µL sample of HMEC-1 or wild-type MSC cells were stained with trypan blue (Sigma Aldrich). The number of live and dead cells was counted using a LUNA-II Automated Cell Counter (Logos Biosystems, Gyeonggi-do, South Korea). 50,000 live HMEC-1 cells or 5,000 live MSC cells suspended in the serum-/supplement-free medium were seeded per well in 96-well IncuCyte® ImageLock Plates (Essen BioScience). Cells were incubated overnight at 37°C in a humidified environment of 5% CO_2 to form a confluent monolayer.

The next day scratches in confluent cell monolayers were made using a Woundmaker 96 (Essen BioScience), and detached cells were washed away with PBS. Subsequently, the cells were treated in triplicate with a 1,000x excess of EVs to cells. Migration of the cell monolayer was followed over time using IncuCyte ZOOM (Essen BioScience), which was set to take images every hour. Migration was quantified using a FiJi plug-in kindly written by Oliver Gerrit De Jong.

5.2.10 Dipeptidyl peptidase-4 (DPP4) activity assay

To assess dipeptidyl peptidase-4 (DPP4) activity in MSC subclone-derived EVs or cells, EVs or cells from each subclone and parental wild-type MSCs were added in triplicate to 96-well plates. The volume of each well was made up to 50 µL with PBS. Subsequently, a DPP4-Glo Protease Assay (Promega) was performed following the manufacturer's protocol. Briefly, a 1:500 dilution of DPP4-Glo substrate in Luciferin Detection Reagent dissolved in DPP4-Glo Buffer was made up. Then, 50 µL of this solution was added to each well of the 96-well plate containing EVs or cells diluted in PBS, as well as PBS negative control and 1 ng/mL purified recombinant human DPP4 protein (Enzo Life Sciences, Exeter, UK). The assay was then incubated for 30 minutes at room temperature, and DPP4 activity measured via luminescence using the Clariostar Plus Microplate Reader (BMG Labtech).

A standard curve of MSC subclone B10-derived EVs ranging from 1 x 10^5 EVs and 1 x 10^9 EVs were constructed in triplicate in a 96-well plate to approximate the appropriate amount of EVs to use for each sample without infringing the limit of detection of the

assay. A standard curve of MSC subclone B10 cells ranging from 25 to 2,500 cells were also constructed for the same purpose.

5.3 Results

5.3.1 SKOV3-derived EV subpopulations present differential effects on SKOV3 adhesion *in vitro*

As previously described in section 5.1.2, secreted EV populations are heterogeneous in terms of both their physical characteristics and their associated physiology. EV size is one such factor related to functional and physical EV heterogeneity. Numerous studies have documented EV heterogeneity, often with respect to EV biogenesis or EV populations with broad size ranges (i.e. sEVs and lEVs). However, whether size-based heterogeneity exists between narrower size ranges, and whether EV size is linked to EV heterogeneity irrespective of EV biogenesis is yet to be fully understood.

To test the link between EV size and heterogeneity, high-resolution size-based separation of SKOV3-derived EVs performed by Willms (2018) was replicated using an XK-16/70 SEC column packed with Sephacryl S1000 resin (XK-16/70)[51]. Following the same methodology for the fractionation of EVs according to the UV chromatogram, four EV subpopulation pools were identified and characterised. Figure 5.1A presents a UV chromatogram from a SEC XK-16/70 Sephacryl S1000 EV purification to separate SKOV3 EVs into four subpopulations. Fractions 1 to 8 formed Pool 1, 10 to 15 formed Pool 2, 17 to 20 formed Pool 3, and 22 to 30 formed Pool 4. Two fractions were skipped between each pool to reduce possible carryover of the constituents of one section of the elution profile into another. Pool 1 encompassed the large peak on the left side of the chromatogram. Pool 2 encompassed the second broad peak. Pool 3 included a small number of fractions on the decline of the second peak. Finally, Pool 4 included a small

peak on the right side of the chromatogram. Altogether, four EV pools were obtained by successfully replicating XK-16/70 fractionation of SKOV3 EVs.

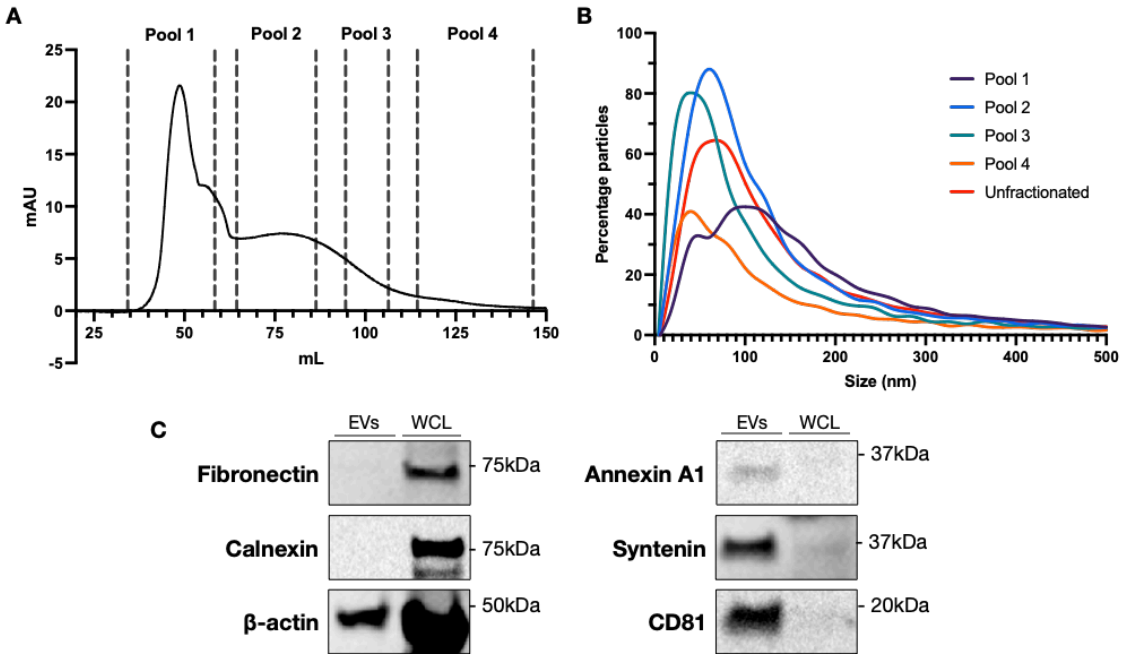

Figure 5.1 Fractionation and characterisation of fractionated and unfractionated SKOV3 EVs. (A) UV chromatogram of SKOV3 EVs separated using an XK-16/70 Sephacryl S1000 and the subsequent pools formed from resulting fractions. (B) Particle size distribution of fractionated and unfractionated SKOV3 EVs determined by NTA. (C) Western blot characterisation of unfractionated SKOV3 EVs demonstrating high representation of EV marker proteins (β-actin, annexin a1, syntenin and CD81) in EV samples and low to no expression of co-isolate proteins (fibronectin and calnexin).

Following this, the size distribution of particles in each population was determined by NTA to confirm that XK-16/70 was able to separate EVs of different sizes, and the expression of EV markers in SKOV3 purified preparations was determined by western blotting to confirm EV content and purity. Figure 5.1B shows the size distribution profiles

of each of the four SKOV3 EV subpopulations and SKOV3 EVs that were not fractionated by the XK-16/70 column (unfractionated). All populations presented particle size distributions typical of EVs with peaks at around 100 nm or less. However, the size distribution of each population varied. Broad size distribution was seen in pool 1 with a modal size of 110 nm, but in contrast, a much tighter size distribution was seen in pool 4 with a modal size of roughly 50 nm. Differing modal sizes were also observed in pools 2 and 3, although a higher proportion of particles was seen in these populations. As expected, the size distribution of unfractionated EVs was presented as an average of all four EV subpopulations. As shown in Figure 5.1C, the expression of typical EV markers β-actin, annexin A1, syntenin and CD81 was observed in SKOV3 EV samples, although a comparatively low expression of annexin A1 was reported. Fibronectin and calnexin expression were undetectable in EV samples presenting that EVs were successfully purified from non-EV contaminants. Overall, differences in size distributions and the average size of particles detected by NTA showed that XK-16/70 was successfully able to separate EVs in four different size-based populations, and the identity of SKOV3 EVs was synonymous with a purified EV population.

Following the characterisation of EVs by NTA and western blotting, TEM images of XK-16/70 fractionated and unfractionated SKOV3 EVs were taken to further confirm the identity of particles in each fraction in line with MISEV2018 guidelines. TEM images of EV populations shown in Figure 5.2A present particles in each population with an intact, spherical, cup-shaped morphology typical of EVs in this format. In all cases, preparations of particles appeared clean and devoid of dark stained contaminants or other unknown structures. Similar to NTA size distribution data, upon visual inspection, EV particles in each pool appeared to vary in size, with much larger particles seen in pool 1 and much

smaller in pool 4. To confirm whether the observed differences in size were measurable and significant, EVs in TEM images were measured in FiJi. Figure 5.2B shows violin plots of the sizes of EVs in each population. Highly significant ($P < 0.0001$) differences in EV sizes were observed between each population, except for unfractionated EVs and pool 3, where a less significant difference was seen ($P < 0.05$). No significant differences were seen between pool 4, the unfractionated EVs, and pool 3 EVs. Sizing data confirmed original observations of a decreasing trend in size from pool 1 to pool 4, with median sizes of 120.0 nm, 65.1 nm, 41.8 nm, and 39.2 nm from pool 1 to 4, respectively. The range and inter-quartile range of particle sizes also got noticeably smaller, with each particle size presenting clear separation of EVs of different sizes into different pools. Unfractionated SKOV3 EVs had a median size of 49.4 nm presenting EVs in this population as an assortment of sizes from all four subpopulations. Altogether, TEM images presented particles of typical EV morphology with significant differences in sizes between each EV pool, presenting the ability of XK-16/70 SEC to successfully separate EVs into size-based subpopulations.

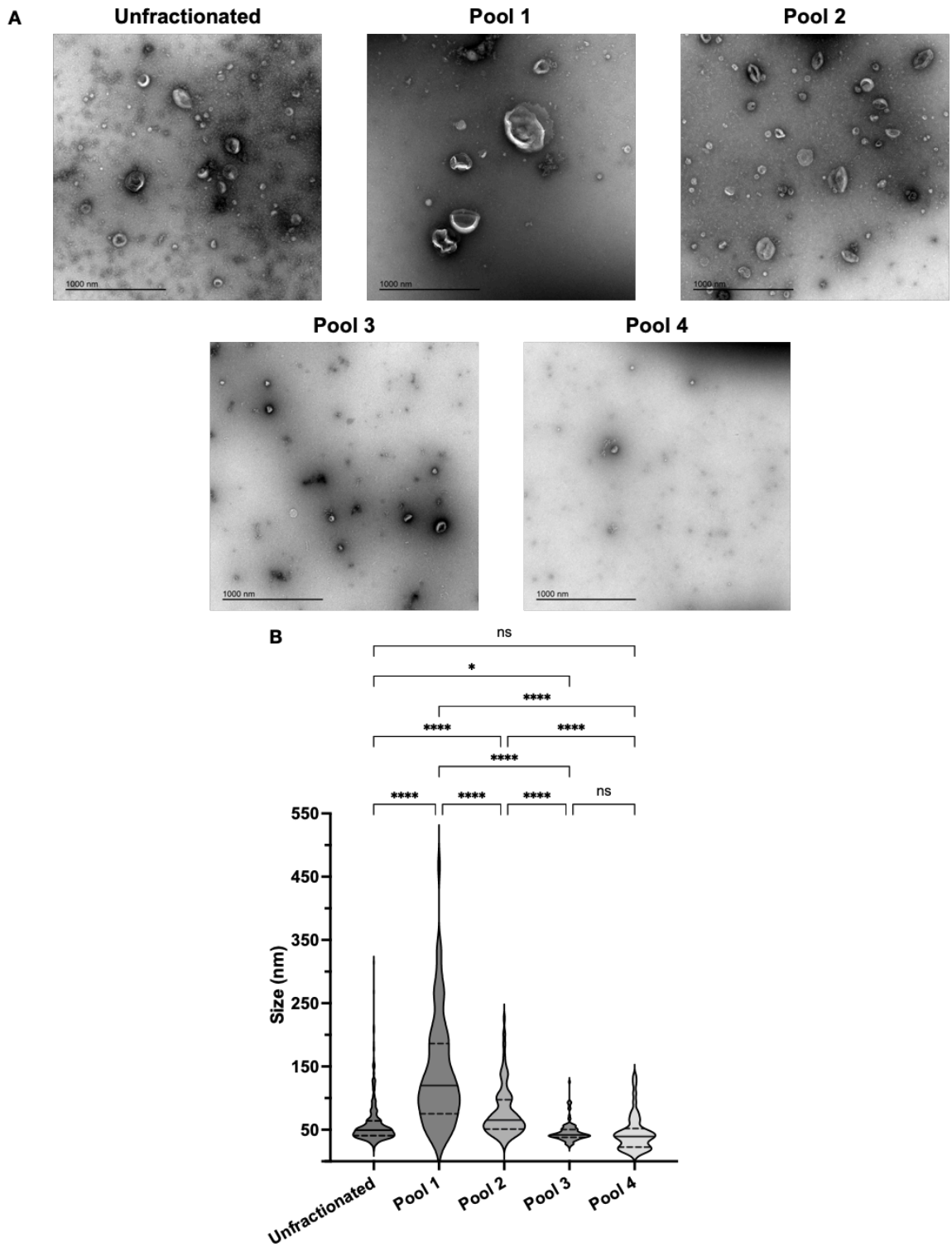

Figure 5.2 TEM analysis of unfractionated SKOV3 EVs and XK-16/70 SEC fractionated SKOV3 EV subpopulations. (A) TEM images of respective SKOV3 EV samples with a scale of 1,000 nm. (B) FiJi size analysis from TEM images of

unfractionated and fractionated SKOV3 EVs. Five representative images analysed per population. The total number of particles measured for each population was as follows: unfractionated = 432, pool 1 = 78, pool 2 = 222, pool 3 = 116, pool 4 = 45. Solid horizontal lines denote medians. Dashes lines denote upper and lower quartiles. One-way ANOVA with Tukey's multiple where significance is indicated by $P < 0.05$ (* = $P < 0.05$, **** = $P < 0.0001$, ns = non-significant).

Following the characterisation of EVs in SKOV3 EV pools, the differential function of these EV subpopulations was investigated. Due to the involvement of cancer-derived EVs in assisting cancer cell adhesion and establishing metastatic niches, an *in vitro* cell adhesion assay was conducted to assess differences in cell adhesion that may be elicited by both unfractionated and fractionated SKOV3 EVs. 1 µg per well of each sample was coated, in triplicate, onto 96-well plates. SKOV3 cells or soluble protein from Tricorn 10/300 SKOV3 EV purifications were added to each well and incubated for 30 minutes to adhere. After washing to remove unbound cells, images of each well were then captured and analysed using the IncuCyte ZOOM. Results were relativised as explained in section 5.2.2. As seen in Figure 5.3, unfractionated SKOV3 EVs (Unf) elicited the greatest SKOV3 cell adhesion. Surprisingly, unfractionated SKOV3 EVs evoked significantly greater cell adhesion than both pool 4 EVs ($P < 0.05$) and the soluble protein negative control ($P < 0.01$). No other significant differences were identified, although notable differences were seen among EVs from each of the four pools, with pool 3 EVs facilitating the greatest SKOV3 cell adhesion of the four subpopulation pools. EVs from pools 1, 2 and 4 all induced a similar level of SKOV3 cell adhesion. In summary, size-based SKOV3 EV subpopulations facilitated differences in cell adhesion, with

significantly greater cell adhesion observed between unfractionated EVs and pool 4 and soluble protein.

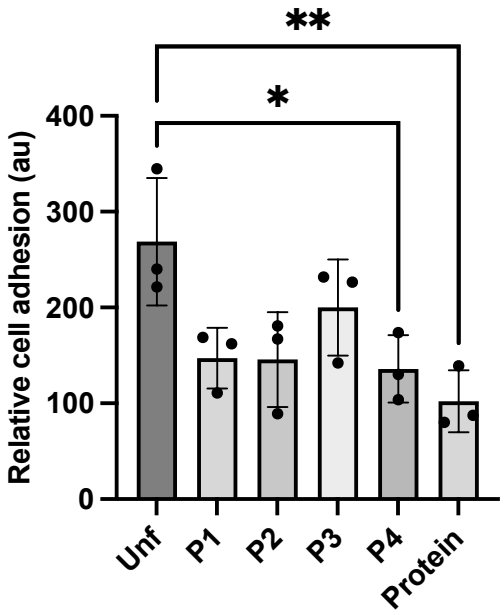

Figure 5.3 Size-based SKOV3-EV subpopulations present differential effects on SKOV3 cell adhesion in vitro. 1 µg of EVs from each pool and the unfractionated sample were coated in triplicate on to a 96-well plate, followed by incubation of SKOV3 cells and counting using the IncuCyte ZOOM. Raw results of each n-number and relativised to make results comparable. One-way ANOVA with Tukey's multiple comparisons versus the unfractionated EV sample where significance is indicated by $P < 0.05$ (* = $P < 0.05$, ** = $P < 0.01$). Values are mean relativised values ±SD; n=3.

5.3.2 SKOV3-derived EV subpopulations present differential expression of EV tetraspanins

After identifying functional heterogeneity between SKOV3 EV pools, differences in EV tetraspanin expression between subclone EVs were investigated to identify a potential marker of these EV populations. CD9, CD63 and CD81 were analysed on a single particle basis using the NanoView ExoView R100. SKOV3 EVs from each subpopulation were incubated with chips coated with anti-CD63, anti-CD8 and anti-CD9 antibodies or mouse IgG1κ isotype control antibodies. Chips were then imaged with the ExoView R100 reader and analysed using ExoViewer software.

Initially, unfractionated SKOV3 EVs were analysed for tetraspanin expression using the ExoView R100. Figure 5.4A presents the results of co-incubation of unfractionated SKOV3 EVs with ExoView tetraspanin chips and anti-tetraspanin antibodies. Each group category represents EVs bound to the respective tetraspanin capture spot on ExoView chips, and coloured bars represent the colocalisation of free anti-tetraspanin antibodies to EVs. CD81 was the most abundant tetraspanin to the extent that it was the highest expressed tetraspanin among EVs bound to all three tetraspanin capture spots. CD63 was the next most common tetraspanin among EVs that were CD63- and CD81-positive. However, among CD9-positive EVs, CD63 was the lowest expressed tetraspanin. CD9 was the lowest expressed tetraspanin among CD81- and CD63-positive EVs. However, overall, the number of EVs bound to the CD9 capture spot seemed to be higher than the number of EVs bound to the CD63 capture spot. Figure 5.4B displays a representative image of SKOV3 EVs bound to the ExoView anti-CD81 capture spot and co-localised with other anti-tetraspanin antibodies. Epitope fluorescence reflected the spread of tetraspanin expression seen in Figure 5.4A, with most EVs bound to the CD81 capture

spot also bound with anti-CD81 (green) antibodies. CD63 (red) and CD9 (blue) fluorescence were far less abundant to the extent that it was difficult to distinguish whether either was more abundant than the other. Colocalised fluorescence of CD81 with CD63 or CD9 was sparse, although several triple positive EVs were identified, appearing white due to crossover in green, red, and blue fluorescence. Overall, CD81 was the most abundant tetraspanin on unfractionated SKOV3 EVs and outcompeted CD63 and CD9 on their respective capture spots, causing CD63 and CD9 expression to be diminished in comparison to CD81.

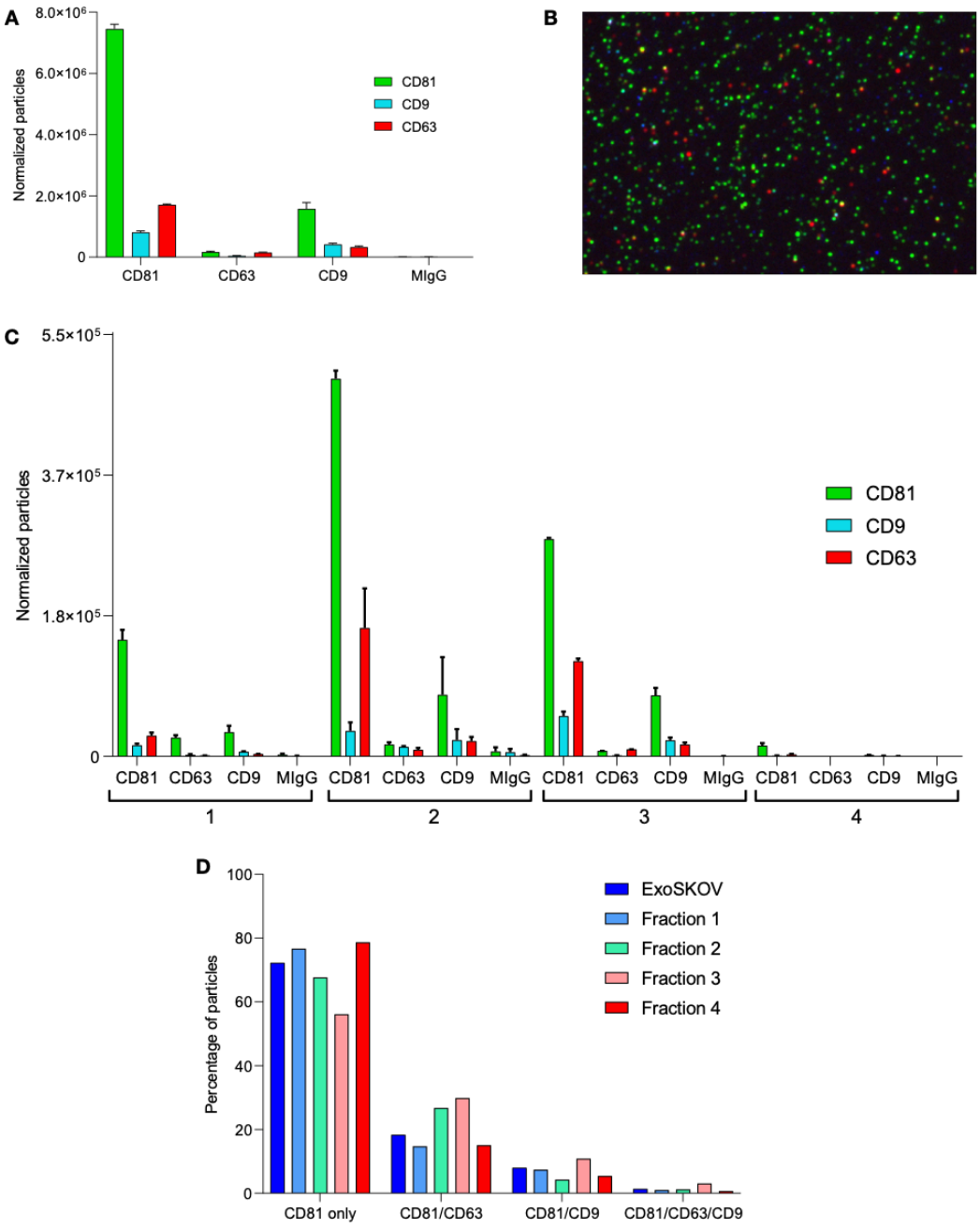

Figure 5.4 Pattern in EV tetraspanin expression is conserved across all four SKOV3 EV subpopulations, but the number of tetraspanin-positive particles differs. (A) Normalised total SKOV3 EVs bound to respective capture spots co-stained with CD81, CD63, CD9, or MIgG isotype control antibodies. (B) Representative image of SKOV3 EVs bound to ExoView anti-CD81 capture spots and co-stained withed anti-CD81 (green), anti-CD63 (red) and anti-CD9 (blue). (C) Number of fractionated SKOV3 EVs bound to

respective tetraspanin or MIgG isotype control capture spots and co-stained with CD81, CD63 or CD9 antibodies. (D) Percentage of SKOV3 EVs in unfractionated and fractionated samples bound to CD81 capture spots that either expressed CD81 alone or co-expressed CD63, CD9 or both. Normalised particle counts are defined as the number of particles in a 150 μm area of the antibody capture spot. Mean ±SD; n=1.

Following analysis of unfractionated SKOV3 EVs, tetraspanin expression across all four EV subpopulations was assessed. Figure 5.4C shows CD81 persisted as the most abundant tetraspanin across all four pools on every tetraspanin capture spot, including MIgG controls. The highest number of tetraspanin-stained EVs was present in pool 2, followed by pools 3, 1 and 4 in descending order. The same trend in tetraspanin identification seen in the unfractionated EV sample (Figure 5.4A) was seen across all four EV pools, demonstrating minimal heterogeneity in EV tetraspanin expression across the EV subpopulations. The main difference between subpopulations was the number of particles that expressed a particular tetraspanin, not a difference in expression pattern. Finally, Figure 5.4D presented that 70 to 80% of particles in each EV population captured with CD81 were not positive for other tetraspanins, except for pool 3, in which 56% of EV expressed CD81 alone. This trend is reflected in the representative image seen in Figure 5.4B. Interestingly a slightly higher colocalisation of CD81 with CD63 and CD9 was seen in pools 2 and 3 as the percentage of vesicles positive for CD81 alone reduced. Very few vesicles were positive for all three EV tetraspanins, and this trend is also visualised in Figure 5.4B. Altogether, ExoView analysis of SKOV3 EVs showed no differences in tetraspanin expression pattern between each subpopulation that could serve as a marker of a particular subpopulation, although CD81 was highly expressed across all subpopulations.

Due to some differences between TEM and NTA EV sizing analysis, SKOV3 EVs were also sized using the ExoView to provide more certainty regarding the size of EVs in each pool. Sizing was obtained by interferometry-based label-free measurements on each spot, and mean size was calculated from three spots for each capture antibody. As seen in Figure 5.5, for each tetraspanin in each population, peaks were seen between 50 and 60 nm, and the size distributions of tetraspanin-positive particles in each pool were roughly the same. Size distributions were dissimilar to those reported by both NTA and TEM. This may highlight the drawbacks of light scatter-based measurements to obtain particle sizing data. Alternatively, narrowing the data to only include particles positive for the EV tetraspanins may skew the data in favour of a specific particle size range, particularly as EV tetraspanin expression is usually associated with exosomes that have a smaller size range compared to other EV subtypes. Overall, particle sizes measured by ExoView did not agree with TEM and NTA data, which may have been due to exclusive exosome sizing rather than the previously employed non-selective sizing techniques.

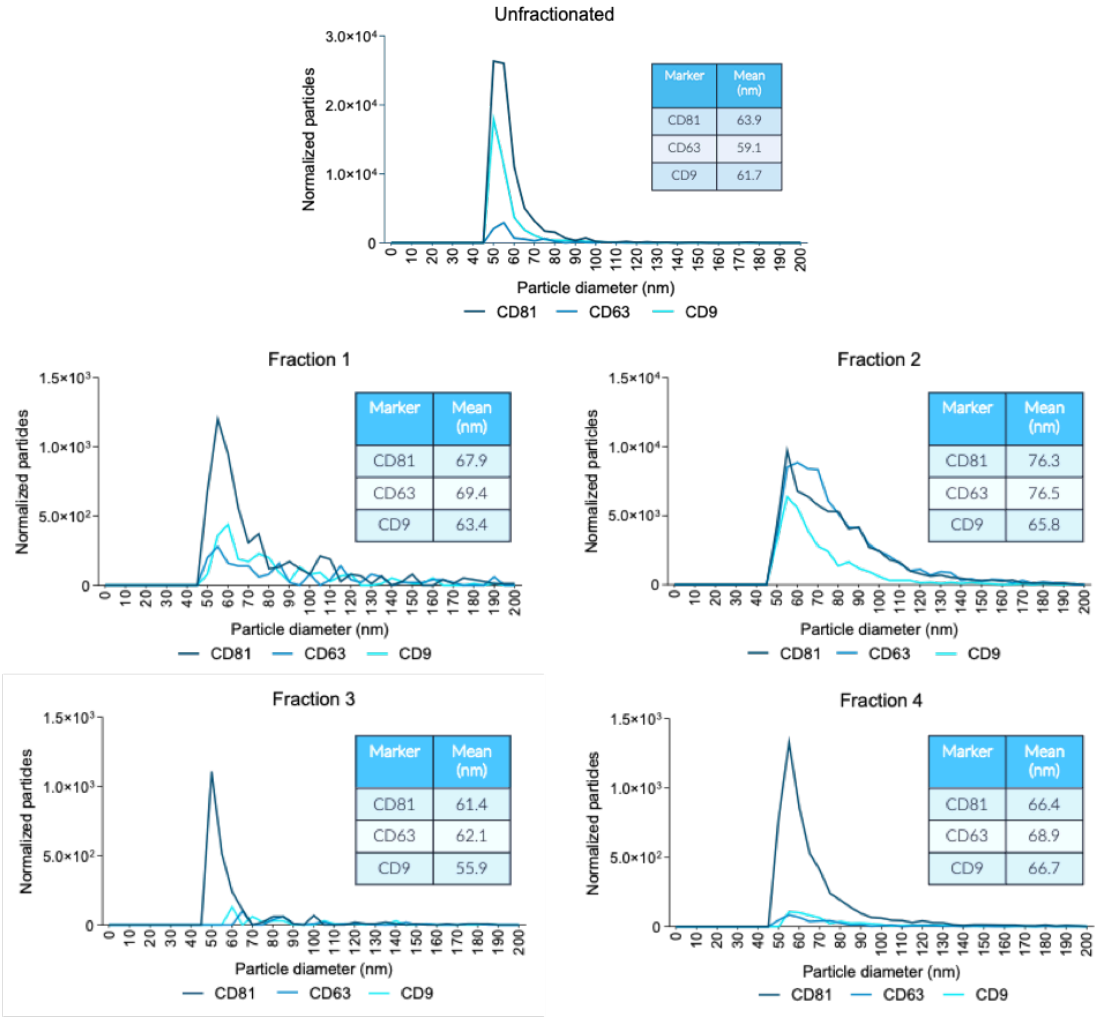

Figure 5.5 Tetraspanin positive particles possessed similar size distributions across unfractionated and fractionated SKOV3 EV samples. Size distributions of different tetraspanin positive particles determined by interferometry-based label-free measurements performed on each spot on ExoView chips. Mean size calculated from three spots for each capture antibody. Normalised particle counts are defined as the number of particles in a 150 μm area of the antibody capture spot. Mean ±SD; n=1.

5.3.3 CD81 and CD29 are anti-colocalised in unfractionated and fractionated SKOV3-derived EVs

In section 5.3.1, differential cell adhesion was facilitated among the SKOV3 EVs subpopulations. Cancer cell-derived EVs have previously been shown to be involved in cancer cell adhesion pre-metastatic niche establishment *in vivo*[60,100,101], and CD29, also known as integrin beta-1 (ITGB1), expressed on the surfaces of EVs, has been implicated in EV-mediated cell adhesion[102]. Willms (2018) also previously showed that blockade of CD29 on SKOV3 EVs inhibited SKOV3 mediated cell adhesion *in vitro*[51,313,314]. Moreover, as CD81 was identified in high abundance among SKOV3 EVs by ExoView analysis in section 5.3.2, CD81 was used as a marker of SKOV3 EVs to determine relative CD29 abundance in separate SKOV3 EV subpopulations and assess CD81/CD29 colocalisation by structured illumination microscopy (SIM). Data obtained would provide further comparisons to the study by Willms (2018) and assess the role of CD29 in differential EV-mediated SKOV3 cell adhesion.

SKOV3 EVs were labelled with anti-CD81 (Alexa647 secondary) and anti-CD29 (Atto-488 secondary) antibodies. EVs were imaged via SIM in 561 nm and 633 nm channels. Ten images from the unfractionated and each fractionated EV samples were captured by structured illumination microscopy, and colocalisation of CD81 and CD29 tagged EVs was analysed using the EzColocalization plug-in for FiJi[310]. Representative images, including control samples incubated without primary antibodies for each secondary antibody, can be seen in Supplementary Figure S5.1 and S5.2. Representative colocalisation heatmaps in Figure 5.6 present colocalisation in the form of red, white, and blue colouration; red denotes colocalisation, blue denotes anti-colocalisation, and white denotes neither colocalisation nor anti-colocalisation. Atto-488 and Alexa647

fluorescence intensity is grouped into categories of fluorescence intensity, where the highest percentage indicates the entirety of the fluorescent populations, and the lowest percentage indicates only the fluorescent particles with the strongest intensities. Across all four subpopulations and the unfractionated samples, the top 30% of all fluorescent signals corresponding to CD29 and CD81 were completely anti-colocalised with one another. Colocalisation was only observed among the top 30% of fluorescent signals in one channel and the top 70% of signals in the other, thus further denoting anti-colocalisation. This was surprising due to the abundance of CD81 identified in ExoView experiments and suggested that CD29 expression was far lower than CD81, and because of the association between CD29 and EV-mediated cell adhesion shown by Willms (2018)[51]. In summary, SIM microscopy presented complete anti-colocalisation between CD81 and CD29.

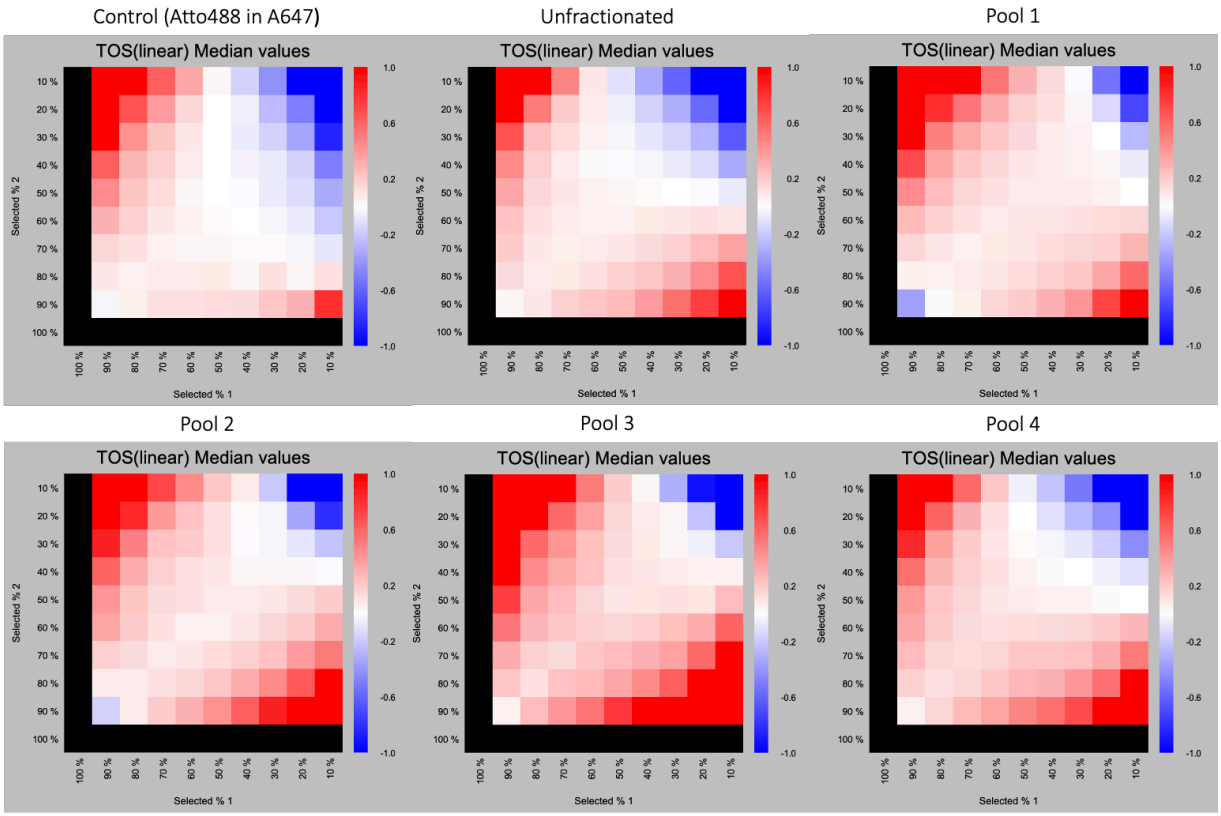

Figure 5.6 CD81 and CD29 are anti-colocalised across all SKOV3 EV subpopulations and unfractionated EVs. Fractionated and unfractionated SKOV3 EVs labelled with anti-CD81 (Atto-488) and anti-CD29 (Alexa647) were imaged by SIM. Ten images of each sample and control were taken, and colocalisation analysis was performed using FiJi with the EzColocalization plug-in. Heatmaps shown are representative of the ten images taken. The highest percentiles include all fluorescent signals, while the lowest percentiles filter out low-intensity fluorescent signals and include only the strongest signals. Red colouration denotes colocalisation between CD81 and CD29, blue colouration denotes anti-colocalisation, and white denotes no trend in colocalisation. Fluorescence intensity is grouped into percentiles. Heat maps are representative of ten technical replicates.

5.3.4 Heterogeneity in EV proteomes exists between SKOV3 size-based subpopulations

Having observed differences in size and function of fractionated SKOV3 EV subpopulations, LC-MS/MS proteomics was performed to analyse the association between EV size and protein expression. The proteomics analysis aimed to identify proteins that may explain differences in cell adhesion, identify protein markers that could identify SKOV3 subpopulations in the future, and identify other functions for different-sized EVs. To provide enough EVs in each pool to achieve the 3 x 10 ug necessary to perform LC-MS/MS proteomics with three technical replicates, three separate harvests of SKOV3 EVs were pooled and fractionated by XK-16/70 SEC. Therefore, the one biological replicate denoted in the data shown here consists of EVs from three biologically distinct harvests. Data was analysed using MaxQuant Perseus v2 and PANTHER pathway analysis.

Firstly, principal component analysis was performed to assess the overall protein expression differences between the SKOV3 EV populations. Results of principal component analysis shown in Figure 5.7A presented similarities between pool 2 and pool 3 EVs as populations clustered closely together. Pool 1 and the unfractionated sample also clustered closely together, presenting similarities in protein expression between these populations. In contrast, EVs in pool 4 clustered separately from the other populations presenting these EVs as phenotypically distinct from the other EV populations. Similarly, Figure 5.7B presents volcano plots of protein expression from each pool versus the unfractionated control. Again, some similarities can be drawn between pools 2 and 3, while not many proteins in pool 1 were significantly different to the unfractionated control, again emphasising the similarity between the two populations,

and pool 4 presented further differences in protein expression. In summary, principal component analysis and volcano plots revealed similarities in protein expression between unfractionated EVs and pool 1, and EVs in pools 2 and 3, while pool 4 EVs presented a distinct protein expression profile, further presenting the heterogeneity among the size-based SKOV3 EV subpopulations.

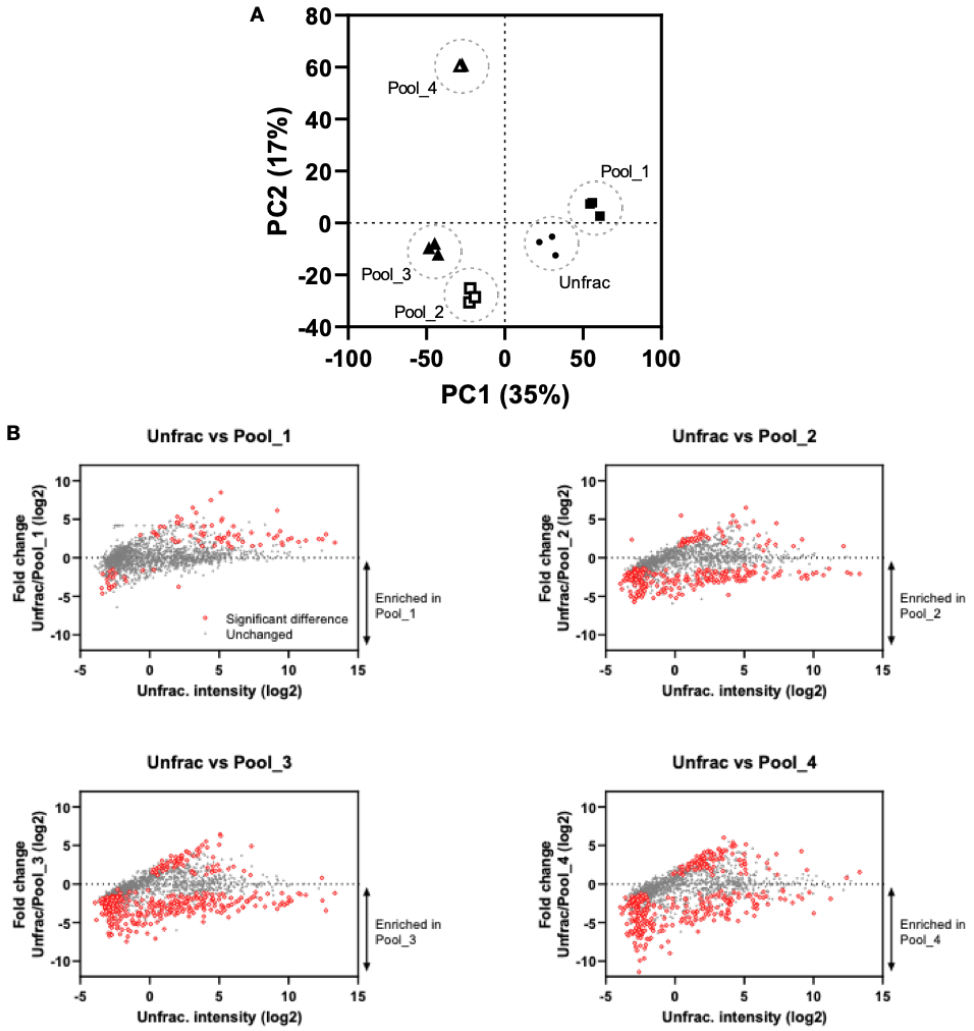

Figure 5.7 Principal component analysis and volcano plots reveal distinct differences in proteomes of fractionated EV pools. (A) Principal component analysis of SKOV3 EV subpopulations. Principal component 1 (PC1) and PC2 account for 35% and 17% of total variance, respectively. (B) Volcano plots presenting fold change in expression of all proteins in each fractionated EV sample vs unfractionated controls and

their associated intensities where red colouration indicates statistically significant deviation determined by t-test ($P < 0.05$). Mean, n = 1, three technical replicates.

Next, to observe differences between the different classes of protein that were enriched in each subpopulation, gene ontological analysis using PANTHER and selecting for protein classification was performed, showing protein classes that were overrepresented or underrepresented in each pool versus unfractionated EVs. As displayed in Table 5.1, upregulation of receptors, cell adhesion molecules and extracellular matrix linkers, and structural and glycoproteins were seen across all four pools, while all other protein classes were differentially expressed among all four pools. Given the high cell adhesion evoked by unfractionated SKOV3 EVs, it was surprising to see an upregulation of cell adhesion proteins in each EV pool. Additionally, various protein classes were upregulated in pool 4, which was synonymous with previous analysis showing pool 4 EVs to be phenotypically distinct. Differences in protein classes further display the heterogeneity among the size-based EV populations and suggest distinct functions for differently sized EVs.

PANTHER Protein Class	Pool1 vs Unfrac	Pool2 vs Unfrac	Pool3 vs Unfrac	Pool4 vs Unfrac
receptor	+	+	+	+
cell adhesion molecule	+	+	+	+
extracellular matrix linker, structural & glycoprotein	+	+	+	+
protease inhibitor	+	+	+	
annexin	+			
nucleic acid binding		+		
small GTPase		+	+	
ribosomal protein			+	
calcium-binding protein			+	+
chaperonin				+
glycosidase				+
vesicle coat protein				+
serine protease inhibitor				+
acyltransferase				+
protease				+

Table 5.1 PANTHER protein class analysis reveals differential upregulation of various functional protein classes across EV pools. PANTHER Overrepresentation Tests using Fisher's exact tests with Bonferroni corrections. Significance is indicated by $P < 0.05$. Enrichments differentially upregulated (+) in each EV subpopulation versus unfractionated EVs. Mean, n = 1, three technical replicates.

As cell adhesion proteins were equally upregulated across all four SKOV3 EV populations, the expression of the integrin family of cell adhesion proteins was scrutinised across all four EV pools to see if differential expression could be observed. Figure 5.8A first presents PCA with respect to integrins, presenting a very similar clustering pattern to that seen in Figure 5.7, therefore denoting little deviation in the overall differences between each EV population with respect to integrin expression. Figure 5.8B presents fold change in respective integrin expression in each pool versus

their intensity among unfractionated SKOV3 EVs. Significant increases in integrin expression were observed in pools 2 and 3, including integrin alpha 1, alpha 3, alpha 6, alpha V, beta 1 (CD29) and beta 6. Interestingly, while high integrin expression was seen in pool 2 EVs, this was not mirrored in cell adhesion function seen in Figure 5.2. In addition, CD29 (ITGB1) was significantly enriched in pools 2 and 3 and slightly de-enriched in pools 1 and 4. Integrin-alpha-3 (ITGA3) displayed the same expression pattern, though significantly de-enriched in pool 4. Integrin-alpha V (ITGAV) was the only protein significantly enriched in pools 2, 3 and 4. Altogether the data presents marked differences in integrin expression between each EV pool, presenting differential cell adhesion potential; this included high integrin expression in pool 3, which agreed with cell adhesion assay data.

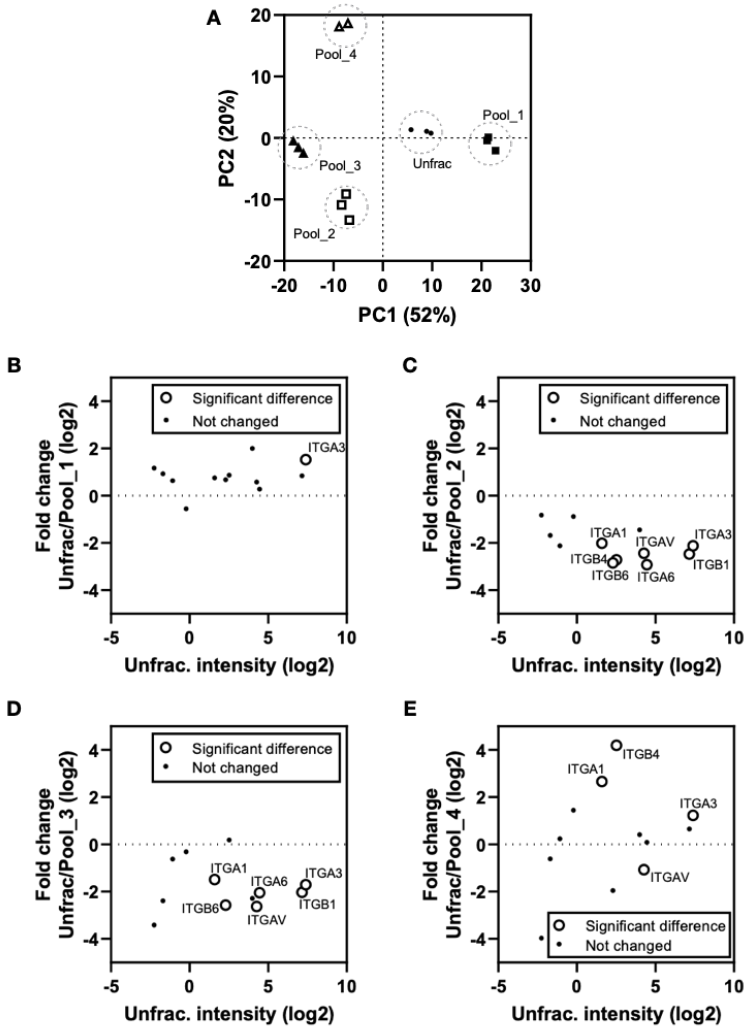

F

Integrin	Normalised expression in Unfrac sample (log2)	Fold enrichment/de-enrichment (+/-) over Unfrac sample			
		Pool 1	Pool 2	Pool 3	Pool 4
ITGA3	7.39	-2.88x	4.34x	3.26x	-2.34x
ITGB1	7.16		5.53x	4.07x	
ITGA6	4.45		7.58x	4.13x	
ITGAV	4.27		5.43x	6.19x	2.10x
ITGB5	4.00				
ITGB4	2.52		6.56x		-18.33x
ITGB6	2.29		7.19x	5.94x	
ITGA1	1.59		4.03x	2.80x	-6.35x
ITGA2	-0.22				
ITGA5	-1.08				
ITGA4	-1.69				
ITGB8	-2.25				

Figure 5.8 Differential integrin expression among EV subpopulations. (A) PCA with respect to integrins. Principal component 1 (PC1) and PC2 account for 52% and 20% of total variance, respectively. (B-E) Volcano plots showing fold change in integrin

expression versus their expression among unfractionated EV, where black circles and labels indicate significant differences determined by t-test ($P < 0.05$). (F) Fold enrichment/de-enrichment of integrins over their unfractionated expression. Mean, n = 1, three technical replicates.

Aside from integrin expression, the expression of all cell adhesion proteins detected by LC-MS/MS was further scrutinised to identify similarities between protein expression and cell adhesion activity. Table 5.2 displays enrichment of cell adhesion proteins identified by PANTHER protein class in each EV pool versus their fold change in enrichment in each EV pool. Interestingly integrins did not feature as the most abundantly expressed adhesion protein. Instead, the most abundant of all adhesion proteins was laminin subunit alpha 5 (LAMA5), followed by fibronectin 1 (FN1) and collagen alpha-1(XII) chain (COL12A1), all of which are extracellular matrix-associated proteins rather than EV membranes themselves. This argued the possibility that despite the inhibition of EV-mediated cell adhesion presented by Willms (2018) upon blockade of CD29, differential cell adhesion activity could instead be due to differential extracellular matrix proteins co-isolated with EVs.

		Fold change (log2)			
Gene name	Unfrac (normalised intensity, log2)	Pool1 vs Unfrac	Pool2 vs Unfrac	Pool3 vs Unfrac	Pool4 vs Unfrac
LAMA5	12.43	-2.39	1.89	2.12	
FN1	12.39			-0.81	-0.81
COL12A1	12.17	-2.44	-1.50		
LGALS3BP	11.24	-2.25		1.43	1.92
VCAN	11.12		1.41		
COL18A1	10.86			1.33	
NID2	10.72	-2.07	2.23	1.22	
LAMB1	10.20	-2.54	1.92	2.18	
LAMC1	9.98	-2.37	2.08	2.35	
MFGE8	9.91			2.44	
LAMB2	9.55	-1.72	2.70	2.40	
CLSTN1	9.18	-2.86	-2.36		
LAMA3	8.96	-2.55	1.83	2.48	
APP	8.56	-3.03	-1.52		
LOXL2	7.51		2.26	1.60	
ITGA3	7.39	-1.53	2.12	1.71	-1.23
MYH9	7.26		-1.72	-1.16	
ITGB1	7.16		2.47	2.03	
NPNT	6.79		-2.24	-1.70	-1.97
TINAGL1	6.63				-2.74
COL7A1	6.39	-3.00	0.99	2.15	1.01
COL5A1	6.09	-2.86	-1.48		
TNC	5.72			2.81	

		Fold change (log2)			
Gene name	Unfrac (normalised intensity, log2)	Pool1 vs Unfrac	Pool2 vs Unfrac	Pool3 vs Unfrac	Pool4 vs Unfrac
FBN1	5.67	-3.08	-4.70	-1.95	
NTN4	5.66		2.00		
FAT1	5.64	-1.97		2.84	2.07
BCAM	5.16	-4.79	1.54	3.73	3.71
CERCAM	5.13	-8.49	-6.52	-6.26	-5.15
FLOT2	4.66	-1.57	3.05	2.36	
IGFBP7	4.56			-2.30	
ITGA6	4.45		2.92	2.05	
HMCN1	4.41	-7.50	-4.69		
ITGAV	4.27		2.44	2.63	1.07
CRB2	4.18		-5.48		-4.88
RPSA	4.12				2.13
ACTN1	4.00			1.75	2.69
COL6A1	4.00			1.73	2.58
CD44	3.88			3.14	3.71
EDIL3	3.86			2.24	
DAG1	3.81				2.07
SRPX	3.80			-5.05	
NRP1	3.60		1.79		
PTPRS	3.58				1.47
CDH1	3.46		-2.83	-3.75	-1.70
CYR61	3.37		-3.41		
GPC4	3.33			3.03	3.97

Table 5.2 Fold change in cell adhesion protein expression among fractionated SKOV3 EVs versus unfractionated SKOV3 EVs. Cell adhesion proteins identified by PANTHER protein class. Unfractionated intensities and fold changes of the proteins in each fraction versus unfractionated EVs are presented. Mean, n = 1, three technical replicates.

5.3.5 Breast cancer-derived EVs present temporal-dependent differences in EV proteomes

In section 5.3.4, heterogeneity among size-based EV subpopulations was demonstrated and further presented the extent of EV heterogeneity in cell culture-derived EV preparations. However, little is known about the cause or source of this EV heterogeneity, and little work has been performed to understand whether EV heterogeneity is stable over time. In this section, three independent samples of two different metastatic subclones of MDA-MB-231 (MDA) breast cancer cells were cultured to assess whether the differences observed in EV heterogeneity are conserved over time or more dynamic for seven weeks, and EVs were harvested weekly. From work previously performed within the Wood lab, one MDA subclone had previously shown a propensity to metastasise to the lungs (L-MDA), while the other showed a propensity to metastasise to the brain (B-MDA). After harvesting, the EV surface proteome was analysed by MACSplex Exosome Flow Cytometry kit. A schematic representing this workflow is presented in Figure 5.9.

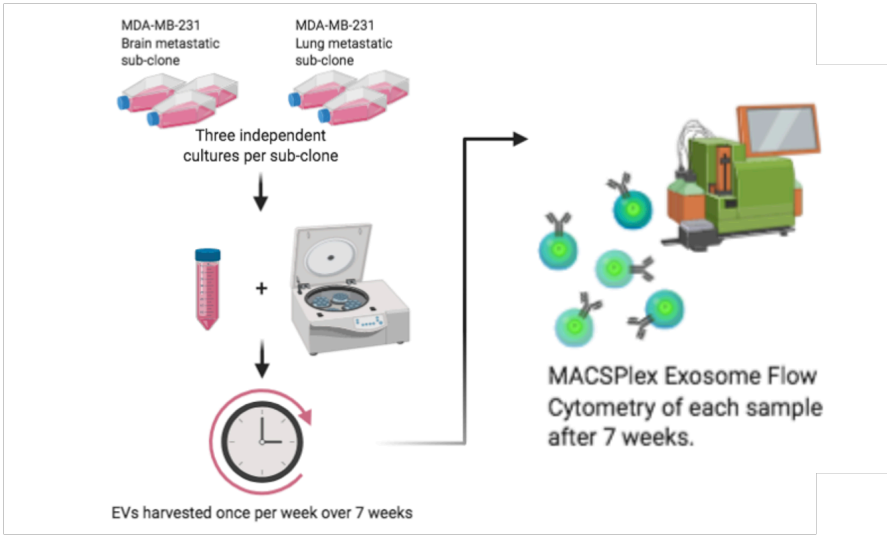

Figure 5.9 Workflow for EV isolation from MDA-MB-231 cells and MACSPlex analysis. EVs were derived from three independently cultured populations of two

metastatic breast cancer cell subclones (brain metastatic and lung metastatic). After 72-hour incubation in serum-free OptiMEM each week, the medium was harvested and centrifuged at 700 x *g* for 5 minutes, then 2000 x *g* for 15 minutes. Supernatant was then transferred to new conical tubes and frozen at -80°C until required for MACSPlex analysis

Firstly, the expression of EV surface proteins in EVs harvested during the first week of cell culture was determined for both lung and brain MDA EVs to establish the baseline expression of each protein, to which protein expression in subsequent weeks could be compared. As shown in Figure 5.10, CD81 was the most abundantly expressed protein in B-MDA EVs, whereas CD29 was the most abundantly expressed protein in L-MDA EVs. Furthermore, significant differences in protein expression were observed between the two MDA subclone EVs, the most significant of which were CD81 and CD63, which were significantly more highly represented in brain metastatic subclone MDA (B-MDA) EVs. Furthermore, chondroitin sulfate proteoglycan 4 (MCSP) was significantly more highly represented in B-MDA EVs. As for L-MDA EVs, human leukocyte antigen class II (HLA-DRDPDQ) and tyrosine-protein kinase transmembrane receptor (ROR1) were significantly more highly represented than in B-MDA EVs. Various other proteins also showed significant differences, including the EV tetraspanin CD9 and various cell adhesion proteins, including CD29, CD44 and CD146. Overall, significant differences in surface protein expression were seen between the two MDA subclone-derived EVs harvested during the first week of culture, and results serve as a baseline for comparison of temporal change.

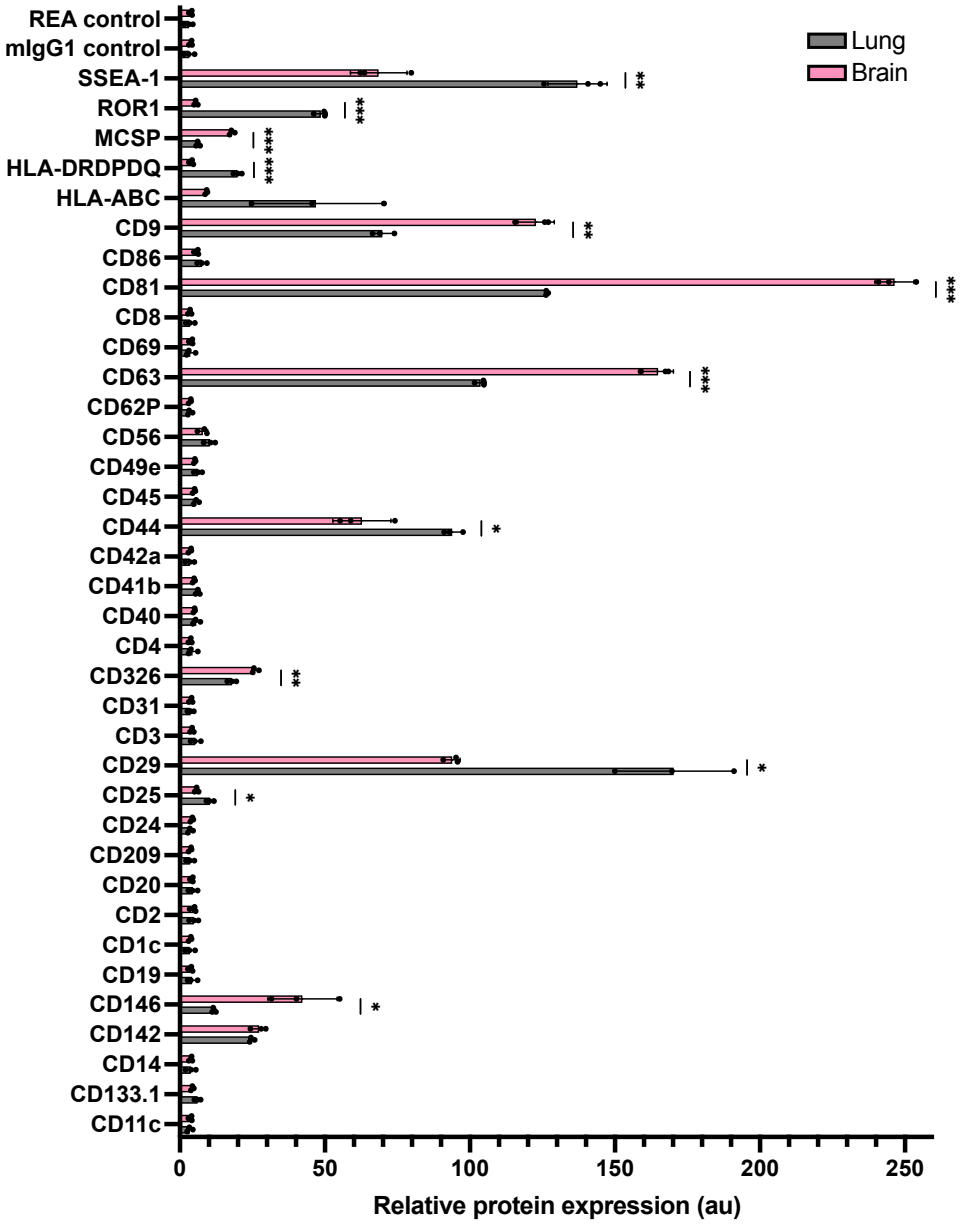

Figure 5.10 MACSPlex analysis of EV surface proteins derived from MDA-MB-231 cells cultured for one week. EV surface protein expression differences can be seen among EVs derived from lung and brain metastatic subclone-derived EVs. Recombinant human IgG1 (REA) and monoclonal human IgG1 (mIgG1) served as negative controls for non-specific antibody binding. Multiple unpaired t-tests with Benjamini, Krieger and Yekutieli false discovery rate corrections ($Q \leq 1\%$). Significance is indicated by $P < 0.05$

(* = $P < 0.05$, ** = $P < 0.01$, *** = $P < 0.001$). Mean, background corrected data expressed as a factor of 1000 for protein expression each week. N = 3.

Once the baseline protein expression had been determined, protein expression on a weekly basis was compared to protein expression in week one to monitor change in protein expression over time. Figure 5.11 presents the normalised, averaged expression of EV surface proteins on a weekly basis for both lung and brain metastatic MDA subclones, arranged from highest to lowest expressed protein at week one. Supplementary Figure S5.3 and S5.4 present EV surface protein expression for each MDA subclone culture. As seen in the supplementary material, few differences between each independent culture were presented; however, as shown in the averaged data in Figure 5.11, CD29 remained the most abundantly expressed protein in the L-MDA EVs, whereas CD29 and CD63 surpassed the expression of CD81 by week seven in B-MDA EVs. No marked increases in expression were observable in lower represented proteins, and changes in expression were more clearly seen in higher represented proteins. Stage-specific embryonic antigen-1 (SSEA-1) fluctuated in both subclones throughout the seven weeks, while the expression of both HLA proteins in L-MDA EVs was downregulated over seven weeks. A gradual increase in CD146 was also noted in L-MDA EVs. The greatest observable difference between the two subclones was that human leukocyte antigen class II (HLA-DRDPDQ) and tyrosine-protein kinase transmembrane receptor (ROR1) were consistently upregulated in L-MDA EVs as opposed to B-MDA EVs. In summary, the expression of highly represented proteins fluctuated weekly, while no observable changes could be seen in lower represented proteins.

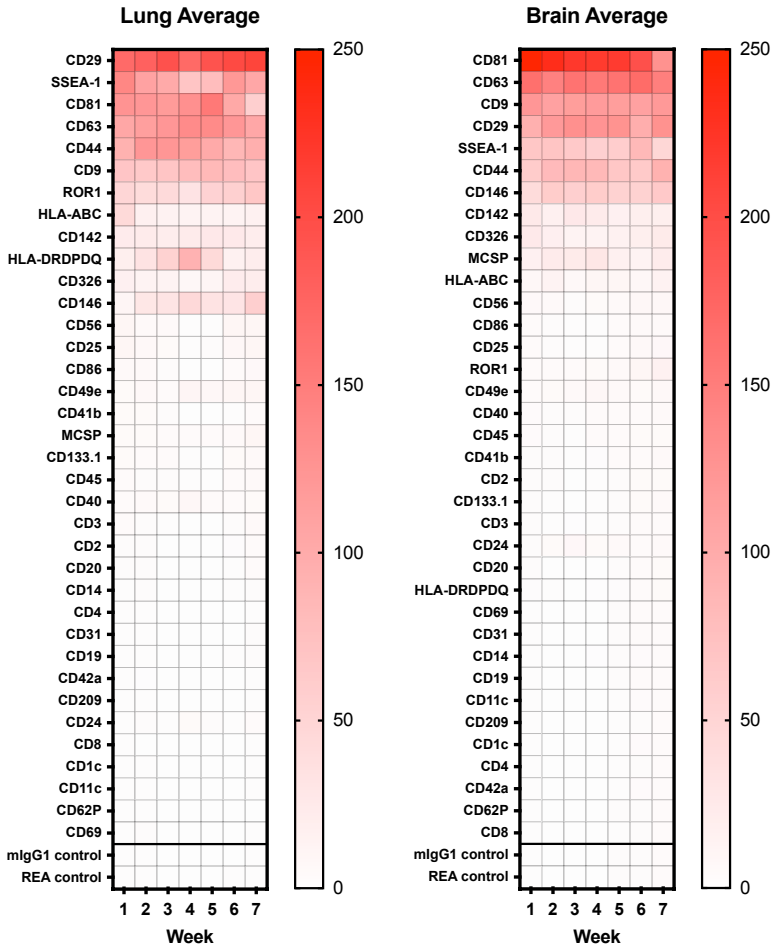

Figure 5.11 MACSPlex analysis of EV surface proteins over seven weeks. Red denotes high expression, and white denotes low expression. Recombinant human IgG1 (REA) and monoclonal human IgG1 (mIgG1) served as negative controls for non-specific antibody binding. Mean, background corrected data expressed as a factor of 1000 for protein expression each week. N = 3.

While fluctuations in protein expression were visualised among the more highly represented proteins seen in Figure 5.11, any change in protein expression in the lower expressed proteins was not observable. Therefore, averaged marker expression was normalised to their respective expression in week one and expressed on a Log2 scale, enabling visualisation of fold change versus week one over time. Protein was again

arranged from highest to lowest represented protein at week one. Supplementary Figure S5.5 and S5.6 present changes in EV surface protein expression for each MDA subclone culture. As shown in Figure 5.12 calculation of fold change in expression allowed lower expressed proteins to be visualised. Furthermore, marked changes in clonal phenotypic drift between independent cultures were far more easily observed than in Figure 5.11. The expression of lower represented proteins followed the expression pattern of REA and mIgG1 negative controls presenting a relatively unchanged expression over time. However, the expression of more highly represented proteins appeared to change over time. CD49a, ROR1, CD24 and CD29 in B-MDA EVs, and CD146, HLA and CD44 in L-MDA EVs appeared to be consistently upregulated over time. Some lower expressed proteins also varied in their expression in both populations, including CD24, CD49e and MCSP. CD40 variation was seen more extensively in L-MDA EVs than in B-MDA EVs. Overall, differences in marker expression were seen between the two subclones, and individual marker expression varied over time, particularly among more highly expressed proteins.

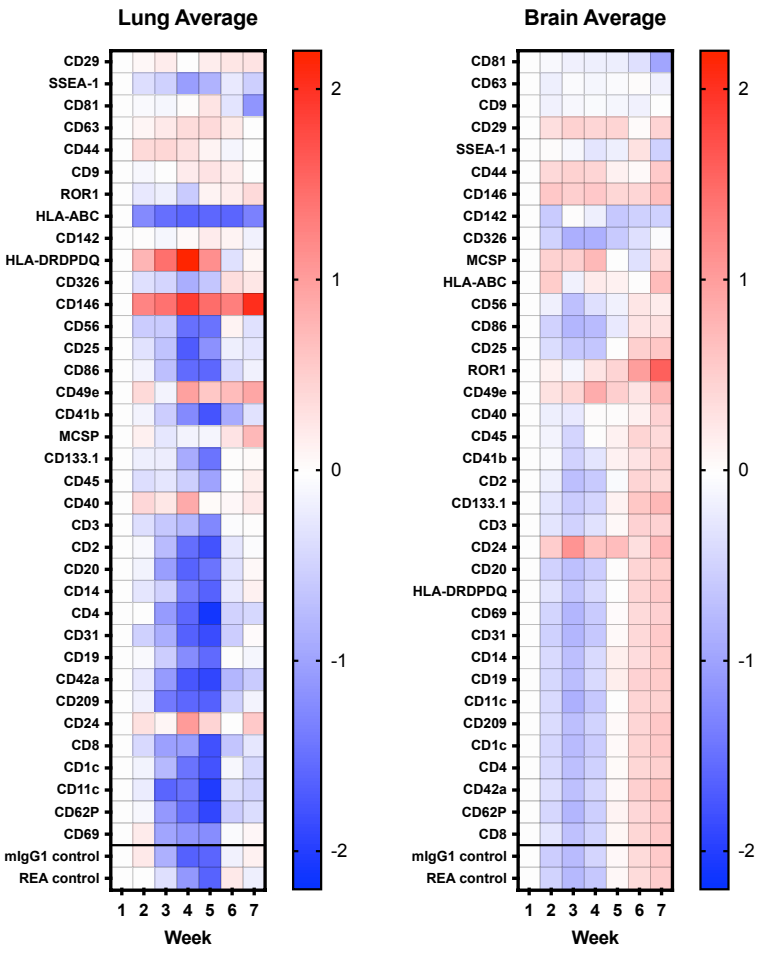

Figure 5.12 Temporal variation of EV surface proteins as shown by MACSPlex analysis. Blank corrected and scaled data normalised to respective expression in week one and expressed on a Log2 scale. Red denotes an increase in expression versus week, white indicates no change, and blue indicates a decrease in expression. Temporal variation can be seen among some of the most highly expressed proteins as indicated by a difference between the expression pattern of the negative controls (REA, mIgG1) and the expression pattern of the proteins. N = 3.

5.3.6 EVs derived from subclones of the same parent cell exhibit phenotypic differences

In the previous section, EV heterogeneity fluctuated over time among highly expressed EV surface proteins and appeared conserved among lower expressed EV surface proteins. Differences in protein expression between EVs derived from subclones of the same breast cancer cell line were also observed. So far, little to no work has taken place to investigate differences in EVs derived from subclonal cell populations. Investigation of differences between EVs derived from subclonal cell populations may aid in understanding the origins of EV heterogeneity, such as whether EV heterogeneity is linked to cellular heterogeneity or generated more stochastically. Due to the clinical potential of mesenchymal stem cells (MSCs) and MSC EVs, heterogeneity between EVs derived from subclones of MSCs generated by single-cell sorting was investigated to detect any functional and potentially therapeutically advantageous differences. Any differences observed could be due to heterogeneity of MSCs themselves, and functional differences between MSC EVs may aid selection of EVs with higher efficacy during EV therapeutic development.

To generate MSC subclones, live MSCs were kindly sorted into single cell isolates using a BD FACSAria II operated by Robert Hedley of the Flow Cytometry Facility, Sir William Dunn School of Pathology, University of Oxford, UK. Populations were named according to the well in which they originated in a 96-well plate. Following single cell sorting and expansion of 11 cell colonies, a supplement-free conditioned medium was collected, and screenings for functional differences were conducted via T cell activation assays. Patient-derived CD8+ and CD4+ resting T cells were first used to assess whether harvested cell conditioned medium containing EVs would elicit T cell activation. Activity was assessed

using the Promega Lactate-Glo assay to measure extracellular lactate concentrations, as lactate production by T cells is proportional to T cell proliferation[312]. Surprisingly, despite the innate immunosuppressive effects of MSCs and MSC EVs[130], as presented in Figure 5.13, varying lactate concentrations were observed in response to incubation of T cells with MSC subclone-derived conditioned medium. Standard deviation in both raw lactate concentration (A) and percentage change (B) graphs was very high for almost all samples. Lactate concentrations and percentage change were highly variable among each subclone in incubations with each cell type. However, the pattern in lactate levels was conserved for most subclones across each cell type. Of the 11 subclones produced, six were selected for further experimentation. Subclones B4, B10, C3, E5, F7 and G4 were selected due to the range of lactate levels observed in association with these subclones following incubation with T cells; low lactate levels from C3 and E5 EVs, high lactate levels from B10 and F7 EVs, and medium lactate levels from B4 and G4 EVs. Overall, surprisingly differential lactate concentrations were observed following incubation of MSC subclone cell condition medium with T cells, suggesting differential T cell activation, and subclones B4, B10, C3, E5, F7 and G4 were selected for further testing.

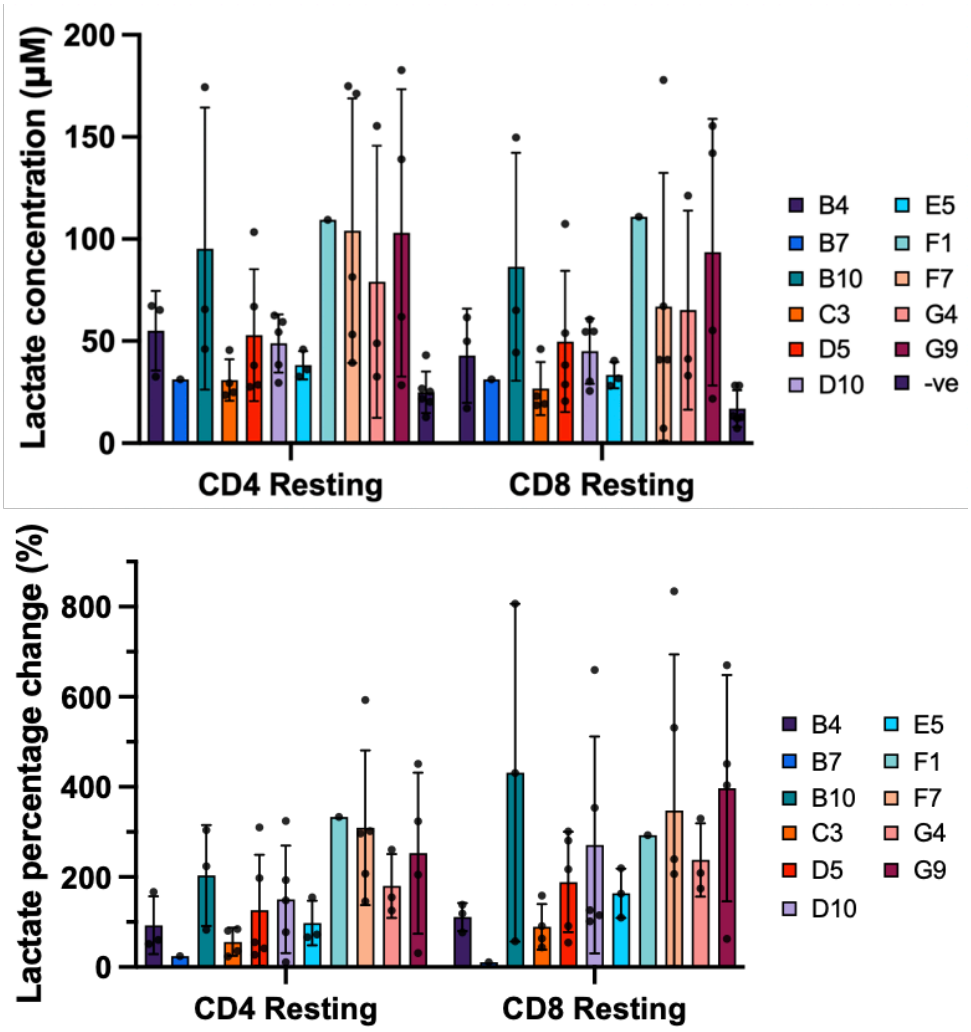

Figure 5.13 Lactate Glo assays reveal wide variation in lactate concentration in response to T cell incubation with MSC subclone conditioned medium. (A) Lactate concentration in µM following 48-hour incubation of CD4+ and CD8+ T cells with MSC subclone conditioned medium. (B) Percentage change in lactate concentration normalised to the negative control in which no condition medium was added. Lactate levels assessed in cell-cleared conditioned medium containing EVs. Mean ± SD, n ≥ 3 aside from B7 and F1 where n = 1.

After selecting six different MSC subclones based on differential lactate levels in T cell activation assays, EVs from each subclone were purified by TFF and Capto Core binding

chromatography and characterised. Nano flow cytometry (NFC), western blotting, and transmission electron microscopy were used to obtain data on EV size, protein expression and morphology. As shown in Figure 5.14A, EVs from each MSC subclone presented an almost identical size distribution, with peaks at roughly 70 nm and shouldering peaks at around 90 and 110 nm. The main difference between each subclone was the percentage of EVs that occupied given sizes. The distribution curves for subclone C3 and wild-type MSCs had smaller peaks, demonstrating a reduced number of particles within subclone datasets that occupied the most prominent sizes, reducing the average percentage. Figure 5.14B presents western blot characterisation of MSC subclone-derived EVs. All MSC subclone EVs expressed typical EV markers: CD81, ALIX, TSG101, syntenin and annexin A1, versus low to no detectable expression in HEK whole cell lysate samples. As expected, beta-actin was expressed across all samples, including the whole cell lysate. Fibronectin was also expressed across all samples, suggesting some secreted proteins were recovered with EVs. Lastly, Figure 5.14C displays TEM images of MSC subclone-derived EVs. In all cases, spherical particles of a wide range of sizes that bare a cup-shaped morphology, typical for EVs in this format, were observed. In most cases, preparations were mostly clear of any dark staining contaminants, although the subclone B10 preparation appeared somewhat muddied with contaminants. Furthermore, subclone E5 and WT preparations contained some large spherical salt crystals due to the buffer reacting with the TEM stain. Altogether, few differences in EV characteristics were observed between EVs derived from each MSC subclone; EVs presented typical sizes and EV marker expression and presented cup-shaped morphologies via TEM.

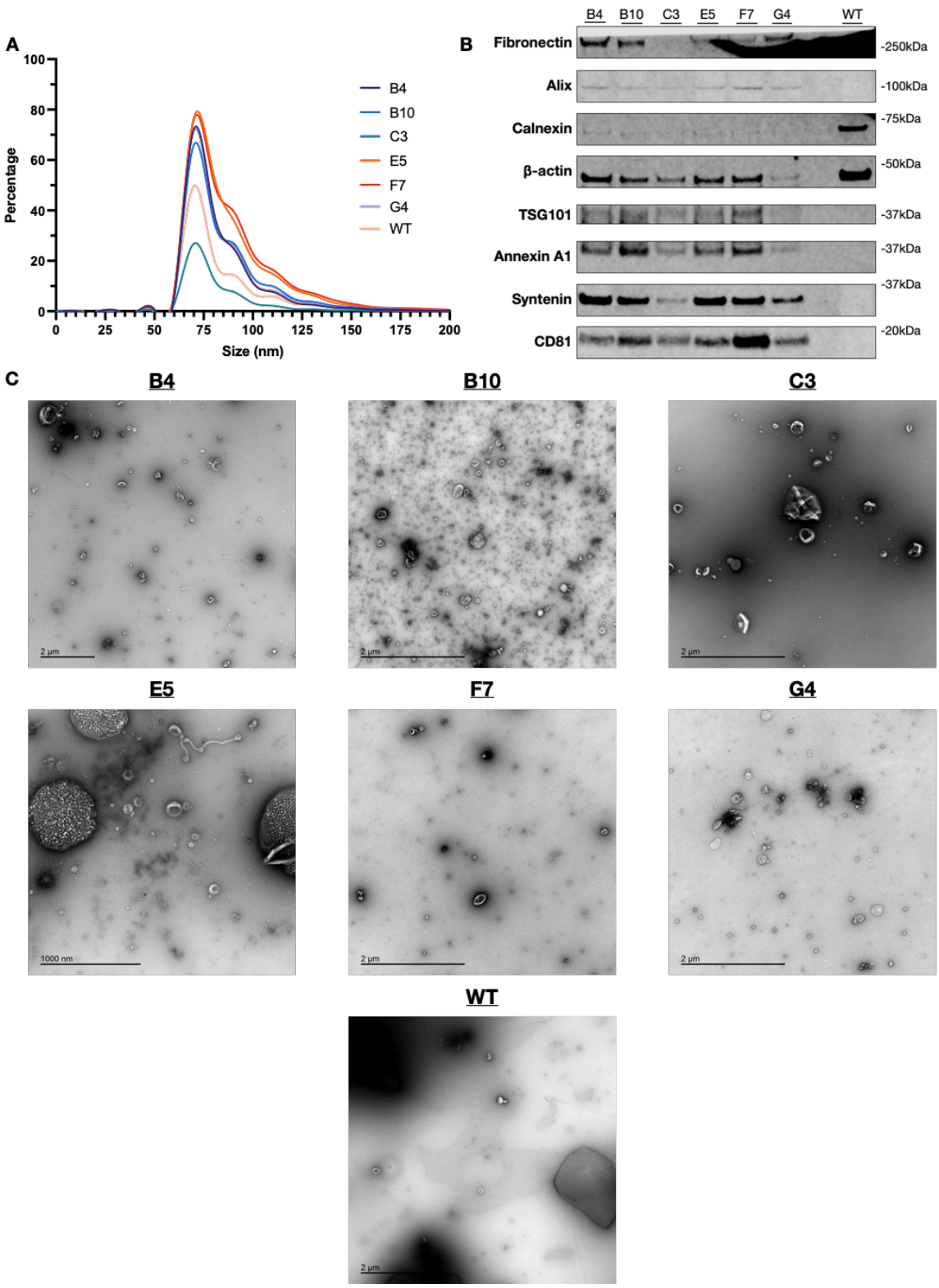

Figure 5.14 Characterisation of MSC subclone-derived EVs. (A) Size distribution of MSC subclone-derived EVs determined by NFC using the NanoFCM Flow NanoAnalyzer.

Average percentage of the greatest number of particles that occupy a single size in each subclone dataset. Smoothed best-fit splines with 100 knots generated with Prism 9 GraphPad Software. (B) Western blots for EV markers in MSC EV subclones. (C) Transmission electron microscopy images of MSC EV subclone samples.

After the presence and characteristics of purified MSC EVs was confirmed in each Capto Core purified MSC subclone preparation, T cell proliferation assays using resting T cells were repeated using purified EVs. This was performed to check whether high lactate concentrations observed in the previous assay that used conditioned medium were due to other factors that may have been present within the medium. 5 x 10^7 EVs purified from each of the six selected MSC subclones were incubated for 48 hours in triplicate with 50,000 CD4+ and CD8+ T cells. Extracellular lactate was measured using the Lactate Glo assay to assess T cell proliferation in response to incubation with purified MSC subclone EVs. Figure 5.15A presents lactate concentrations, and 5.15B presents percentage change in lactate concentration relative to the negative control. Surprisingly, lactate concentrations again varied widely, with significant differences seen between various subclone EVs in response to incubation with T cells. Notably higher lactate concentrations were present in response to incubation with subclone F7-derived EVs in both T cell variants. However, no significant differences were detected between CD4+ and CD8+ T cell datasets.

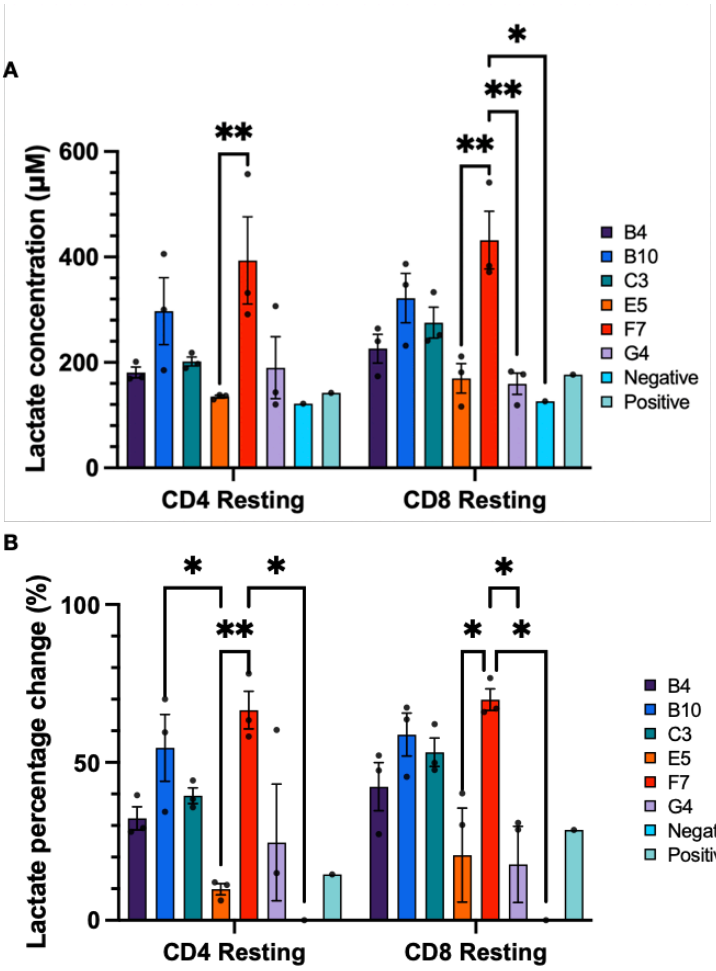

Figure 5.15 Significant differences in lactate concentration in response to incubation of T cells with MSC subclone-derived EVs. (A) Lactate concentration in µM following 48-hour incubation of CD4+ and CD8+ T cells with MSC subclone-derived EVs. (B) Percentage change in lactate concentration normalised to the negative control in which no condition medium was added. Positive controls are incubations with 2 µL of flow cytometry purified IL-2. Lactate levels assessed in cell-cleared conditioned medium containing EVs. Two-way ANOVA with Tukey's multiple comparisons test. Mean ± SD, n = 3.

High lactate concentrations and T cell activation were unexpected due to the immunosuppressive effects of MSCs and MSC EVs. Therefore, T cell activation assays

were repeated with the implementation of EV-only controls that did not include any T cells within respective wells to check whether the observed differences in extracellular lactate concentrations were from the EV preparations themselves or due to T cell proliferation. As displayed in Figure 5.16, in most cases, there was little to no difference between EV-only controls and EVs incubated with T cells. Therefore, any differences in lactate concentration observed previously could not be attributed to differences in EV function and instead were derived from EVs themselves.

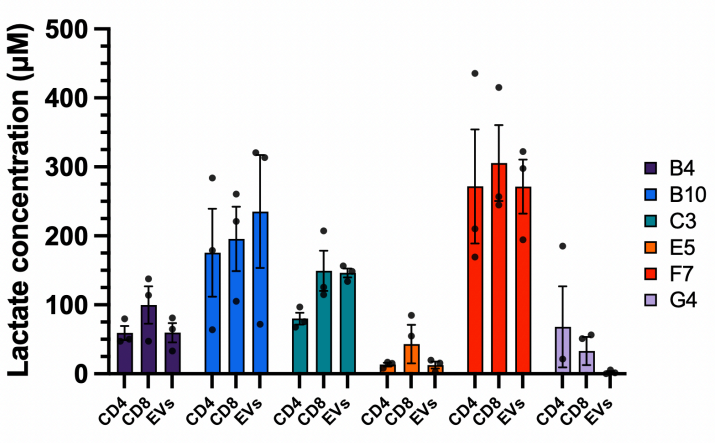

Figure 5.16 Differences in extracellular lactate in T cell activation assays are derived from EVs instead of T cell proliferation. T cell activation assay performed with CD4+ and CD8+ T cells with the implementation of EV-only controls. For CD4+ and CD8+ T cell samples lactate levels were assessed in cell-cleared conditioned medium containing EVs, while EV only samples were not incubated with T cells. Mean ± SD, n = 3.

5.3.7 EVs derived from MSC subclones exhibit functional differences *in vitro*

While no actual functional differences between MSC subclone-derived EVs were observed in T cell activation assays, EVs derived from the same six MSC EV subclones were screened for functional heterogeneity in other *in vitro* assays.

5.3.7.1 Cell migration assay

Firstly, MSC subclone EVs were screened for differences in evoking cell migration by performing *in vitro* scratch wound assays. Cell monolayers of either wild-type MSCs or HMEC-1 endothelial cells were established in 96-well plates by seeding 50,000 HMEC-1 cells or 5,000 MSCs in respective wells and incubating overnight and 37°C. Subsequently, uniform scratches were made in cell monolayers using a Woundmaker 96, monolayers were washed, a 1,000x excess of EVs to cells was added, and migration was followed over time using an IncuCyte ZOOM (Essen BioScience). Migration was quantified using a FiJi plug-in kindly written by Oliver Gerrit De Jong. As shown in Figure 5.17, MSC subclone-derived EVs exhibited differences in their capacity to elicit cell migration in both MSC and HMEC-1 monolayers. Figure 5.17A presents representative images of scratch wounds in MSC monolayers made with the Woundmaker 96 and taken over time with the IncuCyte. The area inside the green lines generated by the FiJi scratch analyser was calculated to assess migration over time. Over time cells were observed to fill void space until green outlines indicating free space disappeared. Figure 5.17B presents results of migration assays performed using MSC monolayers. Overall, only slight differences in cell migration were seen, with E5 EVs evoking the fastest closure, with close to complete wound closure on average after 24 hours. Subclone B10 and G4 EVs also evoked wound closure marginally faster than other subclones. The negative control containing supplement-free medium saw the slowest cell migration, with MSC

monolayers still not completely closed after 96 hours. Similarly, Figure 5.17C presents the results of a migration assay performed using HMEC-1 monolayers. The same trend in migration was observed, although at a slower rate, with E5 EVs evoking the fastest cell migration, followed by B10 and G4 EVs. B4, C3 and F7 EVs failed to evoke wound closure after 96 hours which was slower than the negative control, which may indicate an inhibitory effect of these EVs on cell migration. Interestingly, migration rate was generally greatest within the first 24 hours, then slowed substantially. In all cases, subclones healed less effectively than the FBS-supplemented positive control. However, in both assays, no statistically significant differences between each subclone or control were detected, likely due to the high variability between biological repeats. In summary, notable differences in cell migration were elicited by MSC subclone-derived EVs, particularly in HMEC-1 migration assays though high variability resulted in no significant differences being detected.

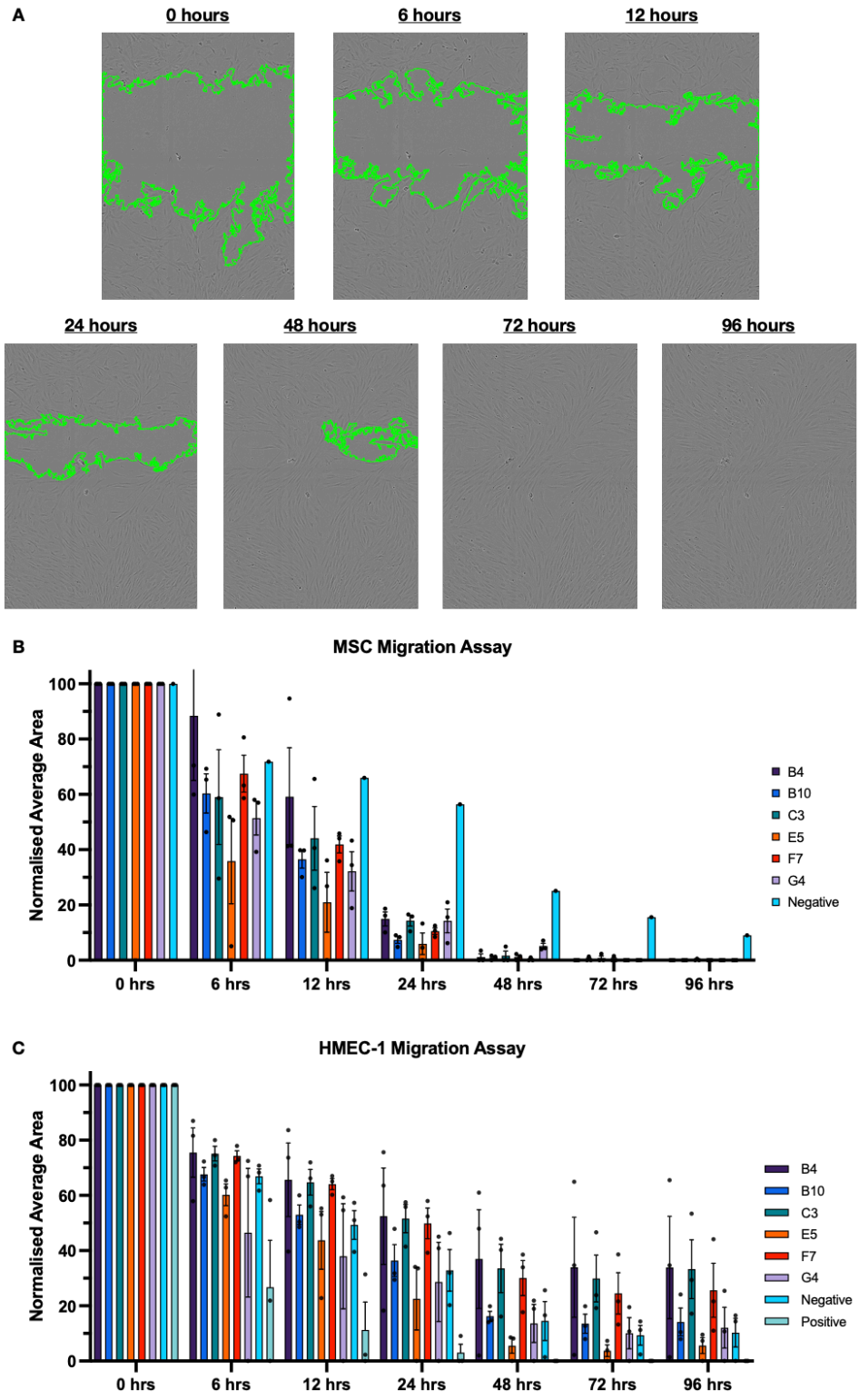

Figure 5.17 MSC subclone-derived EVs exhibit functionally heterogeneous effects on cell migration. (A) Representative images of MSC monolayers at given time intervals following scratch wound application with a Woundmaker 96 and analysis with the FiJi

scratch analyser plug-in. (B) MSC monolayer migration assay and (C) HMEC-1 monolayer migration assay. Data represent mean normalised percentage wound area, where 0% represents complete wound closure. Mean ± SD, n = 3.

5.3.7.2 Cell adhesion assay

Functional heterogeneity between MSC subclone-derived EVs was also assessed by *in vitro* cell adhesion assays. 1 µg of each MSC subclone EV sample was coated in triplicate onto 96-well plates. Following incubation, 10,000 MSCs were added to each well and left to incubate and adhere for 30 minutes. Wells were then washed and imaged to evaluate adhesion. The number of adhered cells was quantified using ImageJ – Analyze Particles. As shown in Figure 5.18A, differences in cell adhesion were visualised among representative images taken from each of the wells coated with different MSC subclone-derived EVs. Notably more adhered cells were seen in response to coating with subclone B4, B10 and F7 EVs than other subclones, wild-type MSC EVs and the negative control, with significant differences observed between the wild-type and subclones B10 and F7, respectively ($P < 0.05$). While B4 elicited high cell adhesion, high deviation resulted in no significant differences between this sample and the wild type. The functionality of B4 and F7-derived EVs contrasted their function in migration assays, as these two subclones did not appear to influence cell migration. B10 EVs exhibited a significant degree of influence over both cell migration and cell adhesion. Together this reinforced the idea that some subclones are better at performing specific functions than others. Cell adhesion assays were also performed by coating wells with 1 x 10^8 EVs instead of 1 ug of EVs to check whether any differences were observed when changing the normalising factor within the assays (Supplementary Figure S5.8). Aside from slight reductions in variability in some samples, little to no difference in cell adhesion was observed. Overall, significant

differences in cell adhesion were elicited by MSC subclone-derived EVs, and different MSC subclones were shown to be functionally active in cell migration assays, presenting further functional heterogeneity among MSC subclone EVs.

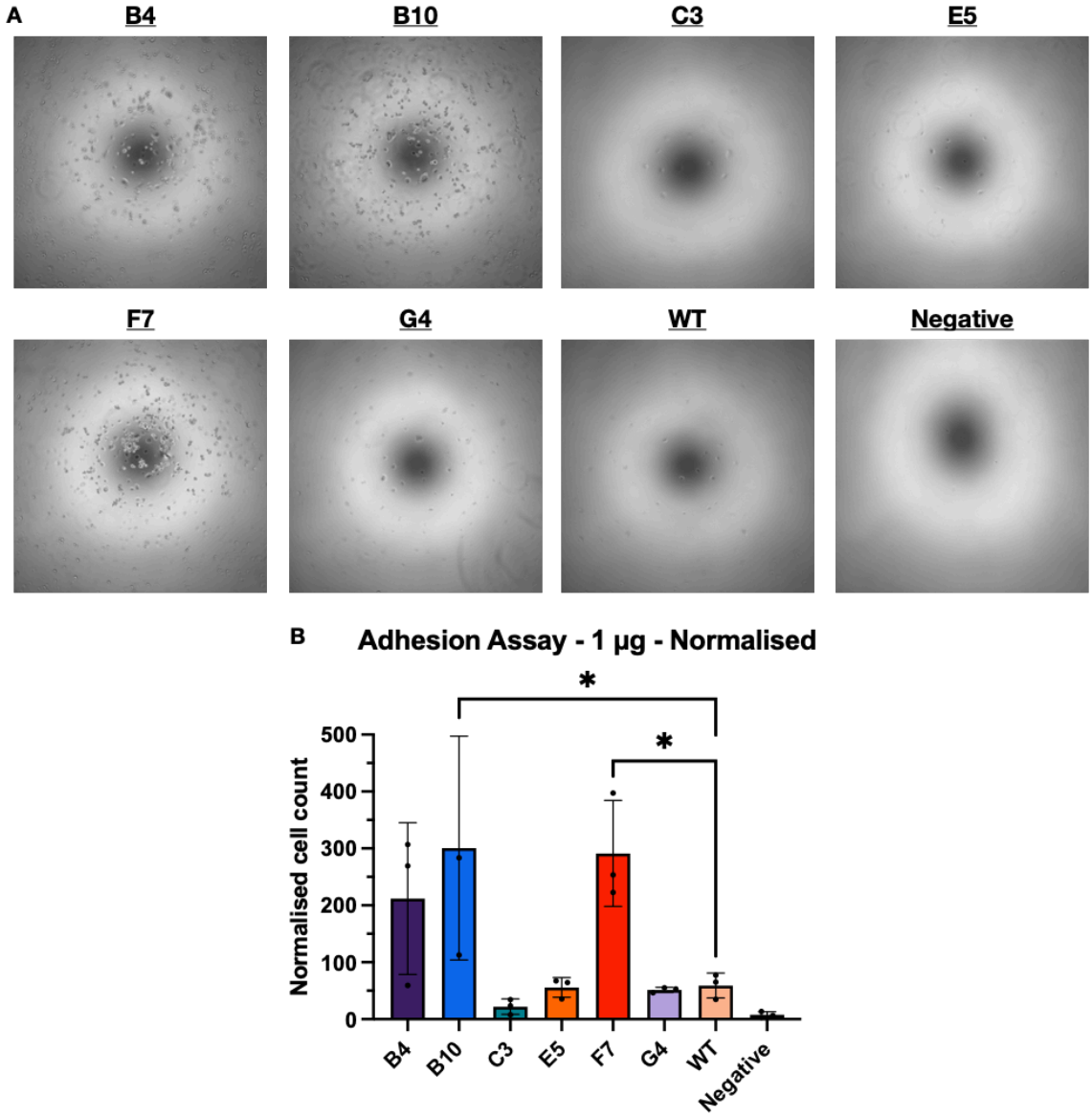

Figure 5.18 MSC subclone-derived EVs elicit heterogeneous effects of MSC cell adhesion. (A) Representative images of MSC cell adhesion in response to coating wells of 96-well plates with 1 µg of MSC subclone-derived EVs and wild-type EVs per well and

a PBS negative control. Images taken at 4x magnification on an EVOS FL Cell Imaging System. (B) MSC cell adhesion assay using 1 µg of MSC subclone-derived EVs. Images were analysed using FiJi – Analyze Particles. Raw results of each n-number were averaged and summed. Individual averages were divided by the sum and multiplied by 1000 to relativise results. One-way ANOVA with Tukey's multiple comparisons versus the wild-type (WT) sample where significance is indicated by $P < 0.05$ (* = $P < 0.05$). Values are mean relativised values ±SD; n=3.

The final way differences in MSC subclone EV function were assessed was via a dipeptidyl peptidase-4 (DPP4) activity assay. DPP4 is a transmembrane glycoprotein with proteolytic activity expressed in various tissues[315]. DPP4 cleaves N-terminal dipeptides from polypeptides with proline or alanine in the penultimate position[316], and is involved in numerous physiological processes, including migration, adhesion, invasion, apoptosis, and immunomodulation[315]. DPP4 is also essential for glucose metabolism by inactivating glucagon-like-peptide-1 (GLP) through N-terminal truncation and inactivating gastric inhibitory protein (GIP)[317]. DPP4 inhibitors have been used in clinical trials to treat cancer and approved for treatment of type 2 diabetes by causing an increase in insulin secretion via preservation of GLP-1 and GIP[316,318,319]. High DPP4 expression has also been reported in EVs derived from numerous cell lines and has also shown to be functionally active[320–324]. The Promega Lactate-Glo assay was used to measure DPP4 activity which measures the ability of DPP4 (embedded in EV membranes) to cleave Gly-Pro-aminoluciferin, a luminogenic DPP4 substrate.

Before beginning DPP4 activity assays, an EV dose-response assay was performed to determine the appropriate number of EVs to use within the assay to observe differences.

EVs derived from subclone B10 were selected for the assay as EVs from this subclone exhibited high functional activity in cell migration and adhesion assay, both of which DPP4 is involved in. A standard curve of B10-derived EVs was constructed ranging from 1×10^5 to 1×10^9 EVs, diluted up to 100 µL with PBS, and the Promega DPP4-Glo assay was performed. As shown in Figure 5.19A, plateaus of DPP4 activity were observed at both limits of the standard curve. The half maximum effective concentration (EC^{50}) of the DPP4 assay using subclone B10-derived EVs was 2.88×10^7 EVs; therefore, this quantity of EVs was selected for the DPP4 activity assays proper.

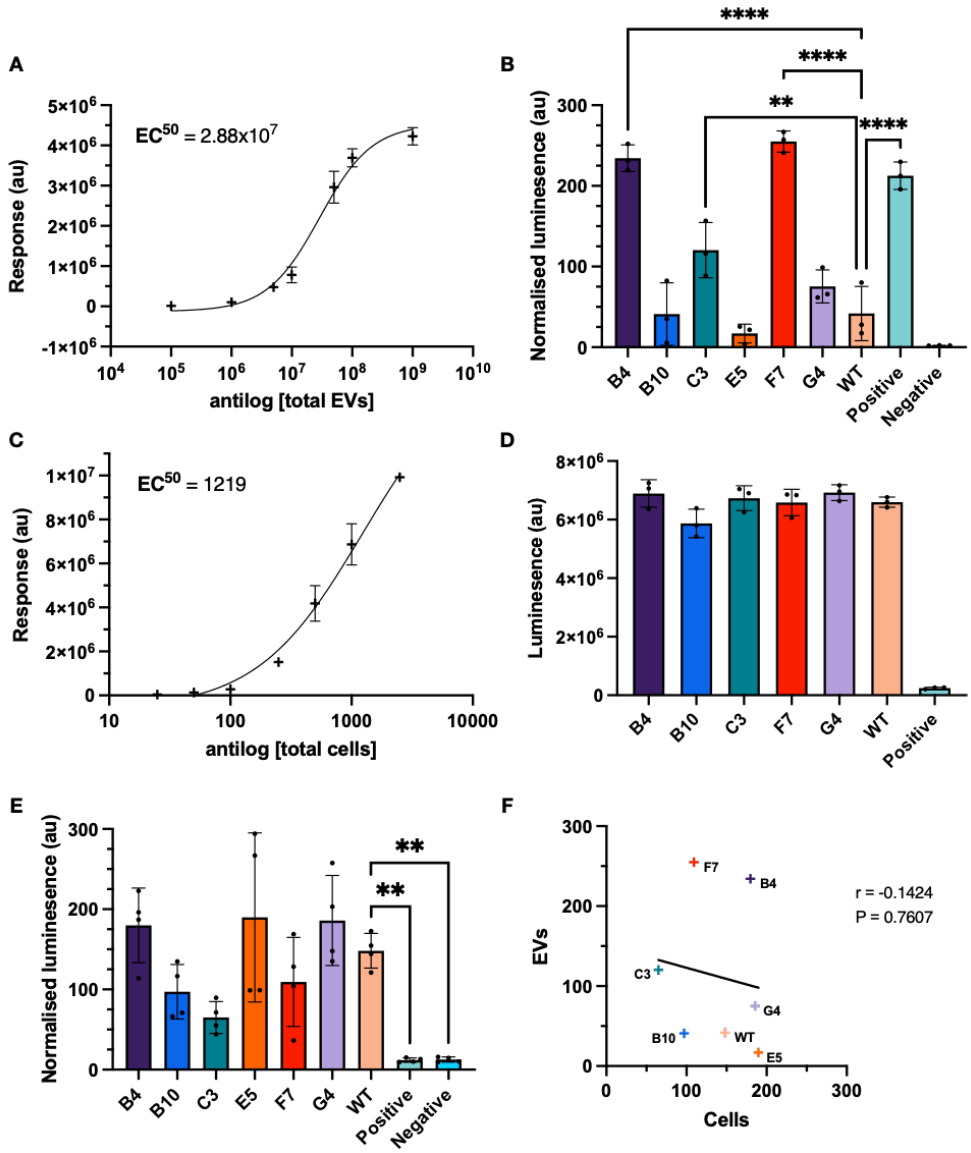

Figure 5.19 MSC subclone cells and their EVs exhibit heterogeneous DPP4 activity *in vitro*. (A) DPP4-Glo dose-response curve of MSC subclone B10-derived EVs ranging from 10^5 to 10^9 on a $\log_{10}$ scale. Best-fit curve and EC^{50} calculated by non-linear least squares regression in Prism 9.0. (B) DPP4-Glo assay of MSC subclone-derived EVs and wild-type MSC EVs, using 2.88 x 10^7 EVs in triplicate per sample. 1 ng/mL purified DPP4 positive control and PBS negative control. Raw results of each n-number averaged and summed. Individual averages divided by sum and multiplied by 1,000 to relativise results. Mean relativised values ±SD; n = 3. (C) DPP4-Glo dose-response curve of MSC subclone

B10 cells ranging from 25 to 2,500 cells on a log_{10} scale. Best-fit curve and EC^{50} calculated by non-linear least squares regression in Prism 9.0. (D) DPP4-Glo assay of MSC subclone cells and wild-type MSCs, using 1,219 cells in triplicate per sample. 1 ng/mL purified DPP4 positive control and PBS negative control. Mean luminescence signal ±SD; n = 1. (E) DPP4-Glo assay of MSC subclone cells and wild-type MSCs, using 100 cells in triplicate per sample. 1 ng/mL purified DPP4 positive control and PBS negative control. Raw results of each n-number averaged and summed. Individual averages divided by sum and multiplied by 1,000 to relativise results. Mean relativised values ±SD; n = 4. (F) Two-tailed Pearson's correlation analysis of relativised MSC subclone EV and cell DPP4 activity assays. r = Pearson's correlation coefficient ranges from 1, denoting strong positive correlation, to -1, denoting strong negative correlation. Significance is indicated by $P < 0.05$. No overall correlation was detected, and no significant differences were detected. In each DPP4 assay a one-way ANOVA with Tukey's multiple comparisons versus the wild type was performed sample where significance is indicated by $P < 0.05$ (* = $P < 0.05$, ** = $P < 0.01$, **** = $P < 0.0001$).

Subsequently, DPP4 activity assays were performed to assess functional differences in DPP4 activity between MSC subclone EVs. 2.88×10^7 MSC subclone EVs (identified by the dose-response assay as the EC^{50}) were used per sample. As shown in Figure 5.19B, clear function heterogeneity was observed among MSC subclone EVs with respect to DPP4 activity. Subclones B4 and F7-derived EVs elicited the highest DPP4 activity, while subclones B10, E5 and G4-derived EVs were among the lowest and slightly lower than wild-type (WT) MSC EVs. Subclone C3 showed medium DPP4 activity. Highly significant differences were seen between subclones B4 ($P < 0.0001$), C3 ($P < 0.05$) and F7-derived ($P < 0.0001$) EVs and WT EVs. Compared to prior functional assays, a different pattern in

EV activity was again observed, with subclones B4 and F7 eliciting the highest DPP4 activity, similarly to their function in adhesion assays. In contrast, subclone C3-derived EVs exhibited higher activity for the first time. Surprisingly, despite their high cell migration and adhesion activity, B10 EVs did not present high DPP4 activity, nullifying the previous hypothesis that B10 EVs would be more active than other subclone EVs. In summary, the data presented significantly different DPP4 activity among EVs derived from subclones of the same MSC parent cell line. Additionally, each subclone exhibited some high functional activity in at least one of the three *in vitro* assays, suggesting that certain EVs are better at performing certain functions than others, offering an argument for selective purification of EVs for improved efficacy.

Following assessment of EV activity, functional differences in DPP4 activity between the MSC subclone cells were also screened to determine whether there was any correlation between DPP4 activity in EVs and DPP4 activity in cells, providing insights into the origin of the EV functional heterogeneity observed. As with the EV activity assay, a dose-response curve was constructed before conducting the cell activity assay to ascertain the appropriate number of cells to use in the assay. For consistency, MSC subclone B10 was used again as the model cell line. Figure 5.19C presents the standard curve ranging from 25 to 2500 cells. Like the EV standard curve, plateaus of DPP4 activity were just about reached at both limits of the standard curve. The EC^{50} was 1219 cells; based on this, 1219 cells were to be used for the cell-based DPP4 activity assay. Although, as shown in Figure 5.19D, when 1219 cells were used per subclone, very high levels of luminescence signal were observed that were far above the levels of the positive controls (1 ng/mL purified DPP4 protein), which itself represents a recommended upper limit of

the Promega DPP4-Glo assay. Consequently, no differences were seen in DPP4 activity among the MSC subclones.

Subsequently, the number of subclone cells used in the DPP4 activity assay was reduced to 100 cells to attempt to see differences and the assay was repeated. Here luminescence was reduced, and differences in DPP4 activity were observable. Figure 5.19E presents notable differences in DPP4 activity among MSC subclone cells, although no significant differences between MSC subclones and wild-type MSC EVs were observed. Significant differences were only observed between wild-type MSC EVs and the positive ($P < 0.01$) and negative ($P < 0.0001$) control. Of note, the positive control signal was particularly low compared to the cell samples, which may further highlight the high DPP4 activity of the MSC subclone cells or suggest errors in the positive control. Some observable similarities between the cell activity assay and the EV activity assay were seen, including higher DPP4 activity of E5 and G4 subclones and lower activity of the C3 subclone. However, as seen in Figure 5.19F, upon conducting correlation analysis between MSC subclone EVs and cell DPP4 activity, no correlation was detected. This suggested that the functional heterogeneity observed among MSC subclone-derived EVs was not linked to parental cell heterogeneity. Overall, significant functional heterogeneity in DPP4 activity was observed among MSC subclone cells, though no correlation was detected between MSC subclone EV activity and cell activity, suggesting that the source of the differences seen in EVs was not a consequence of mirrored functional differences between cells.

5.3.8 MSC subclone EV characterisations revealed notable differences in EV proteomes

Following functional assessment of MSC subclone-derived EVs, EV characterisation was conducted to see whether differences in EV function could be linked to differences in functional protein expression and to identify protein markers that could be used to identify EV populations with enhanced efficacy. LC-MS/MS proteomics analysis of three biological replicates of all MSC subclone-derived EVs and wild-type MSC EVs was performed. Data was analysed using MaxQuant Perseus v2 and PANTHER pathway analysis.

Firstly, principal component analysis was performed to assess overall differences in protein expression between MSC subclone EVs. As shown in Figure 5.20, profiles of each EV population were widely distributed, each appearing to be distinct from one another. Subclones E5 and G4 were the only subclones to closely cluster with one another, barring some similarity to their activity in functional assays. Therefore, PCA analysis presented heterogeneity among the proteomes of MSC subclone EVs.

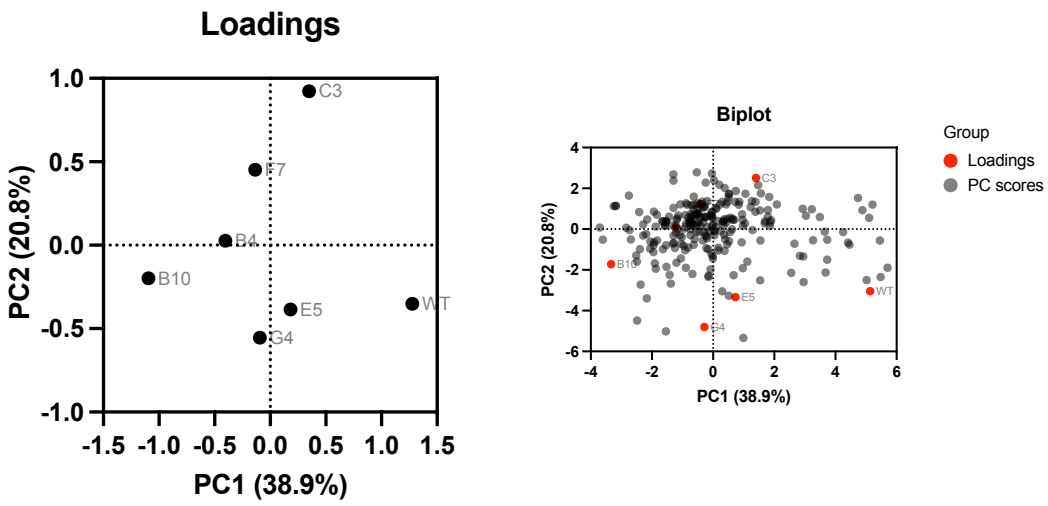

Figure 5.20 Principal component analysis revealed differences in proteomes of MSC subclone-derived EVs. The left plot shows mean PC scores for each MSC EV subclone. The right plot shows individual PC scores with respect to the expression of each protein common to all seven EV populations. Separation of mean PC scores presents proteomic differences in MSC EV subclone populations. Principal component 1 (PC1) and PC2 account for 38.9% and 20.8% of total variance, respectively. Mean ±SD; n = 3.

Volcano plots were also constructed to observe fold change in expression of all proteins common to all MSC subclone EV populations versus wild-type MSC EVs. As seen in Figure 5.20, the pattern in protein expression appeared similar across all MSC subclone EV populations; pronounced differences in protein expression were difficult to identify. Notably, a low number of proteins that were common to all samples were identified. This was surmised to be due to protein extraction and sample preparation problems that caused the number of proteins detected in some samples to be far lower than expected, thus reducing the number of proteins that could be included in comparisons. These errors also impacted the number of proteins shown to be significantly different in expression from the wild-type MSC EVs sample. Overall, a low number of proteins common to all EV

populations was identified, likely due to errors in sample preparations, and definition in EV proteomes were not visualised in volcano plots, requiring closer observations of protein expression among MSC subclone EVs to reveal any heterogeneous expression.

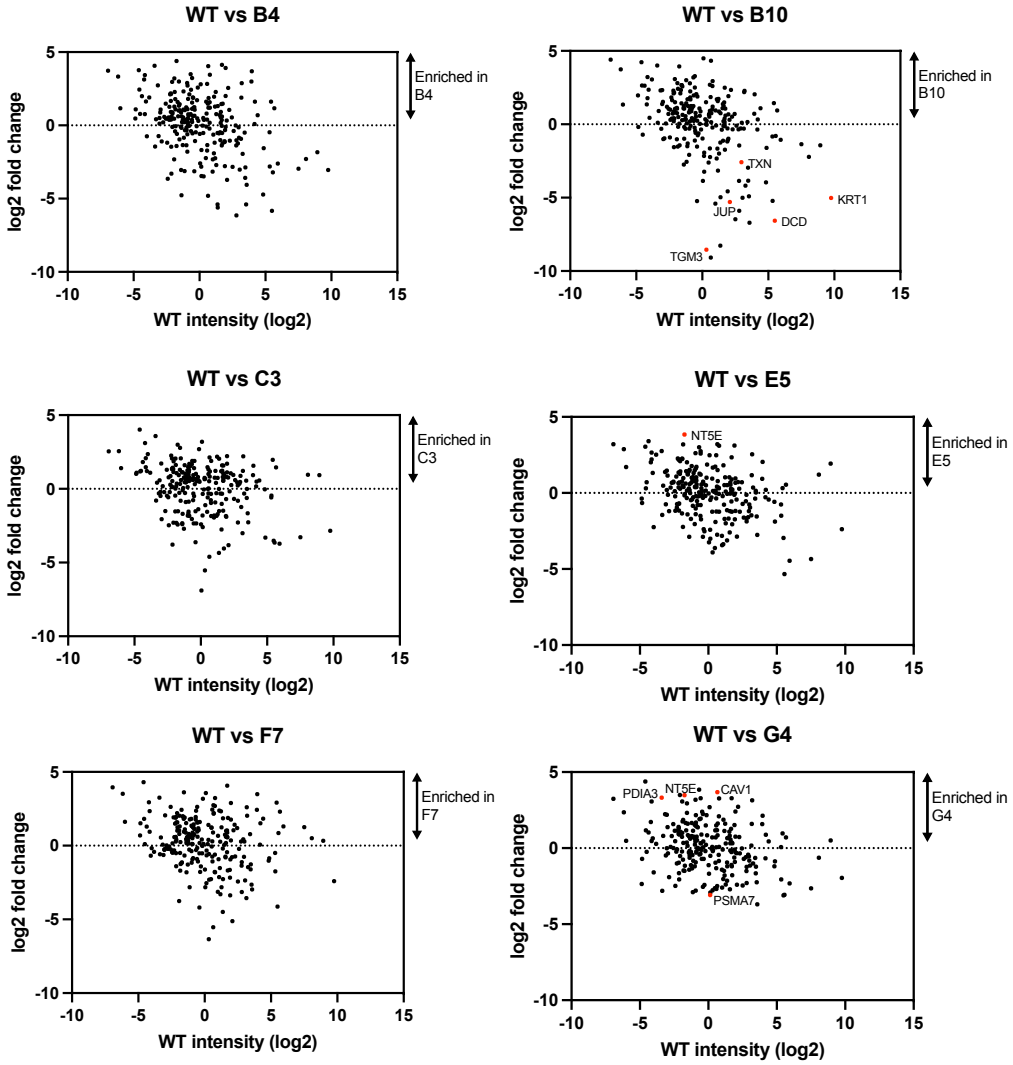

Figure 5.21 Volcano plots presenting fold change in protein expression in MSC subclone-derived EVs versus unfractionated controls. Raw intensity-based absolute quantification (iBAQ) scores filtered to remove protein duplicates, reverse variables, contaminants, and any protein hits included in only one of three n-numbers. Data was also transformed on a $\log_2$ scale, and width adjustment normalisation performed.

Comparisons between MSC subclone EVs and wild-type MSCs were made, and deviation determined by t-test with 250 randomisations where statistical significance is indicated by $P < 0.05$. Red colouration indicates statistically significant deviation. Mean ±SD; n = 3.

Next, the expression of typical EV marker proteins, as identified by MISEV2018, that were present across all MSC EVs populations were scrutinised to identify proteins which could serve as a marker of functional heterogeneity[18]. As seen in Figure 5.22, numerous EV markers were identified across all MSC EV populations. Some proteins, including the EV tetraspanins CD81 and CD63, the human leukocyte associated (HLA) protein subunits, heat shock proteins (HSPs) and GAPDH, were stably expressed. However, numerous proteins varied in expression between each subclone and wild-type MSC EVs. Most prominently, DPP4 variation was observed, with high expression in subclones B4, C3 and F7, which mirrored the EV-based DPP4 activity assay seen in 5.3.7.3. Additionally, high expression of some annexins was also seen in these same three subclones, which resembled the pattern in cell adhesion seen in 5.3.7.2. Varied expression was also seen in lysosome-associated membrane glycoprotein 1 (LAMP1) syntenin-1 (SDCBP), integrin beta-1 (ITGB1/CD29), CD59 and EHD2. In summary, heterogeneous expression of EV markers proteins was seen across all MSC EV populations and differences in DPP4 expression mirrored its activity in DPP4 activity assays.

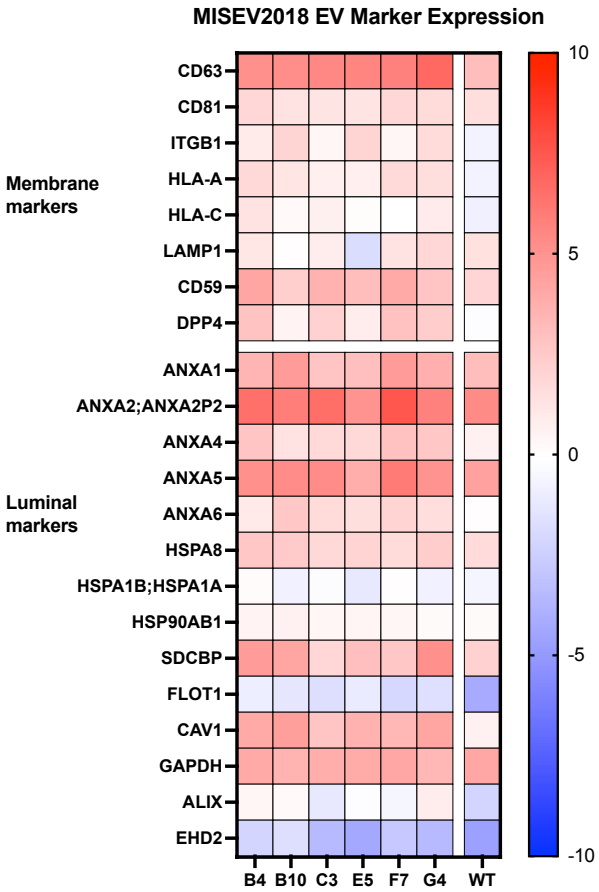

Figure 5.22 MISEV2018 EV marker expression among MSC subclones EVs and wild-type MSC EVs. iBAQ scores filtered to remove protein duplicates, reverse variables, contaminants, and any protein hits included in only one of three n-numbers. Data was also transformed on a $\log_2$ scale, and width adjustment normalisation performed. Red denotes high normalised expression, while blue denotes low normalised expression. Mean ±SD; n = 3.

Due to the differences in cell migration elicited by MSC subclone EVs, cell migration and wound healing proteins expressed among MSC EV populations were identified in the proteomics dataset by gene ontological biological process (GOBP) categorisation. This was performed to identify any proteins that could have been responsible for the heterogenous cell migration activity. As shown in Figure 5.23, the expression of

numerous EV-associated proteins, including annexin A2 (ANXA2), CD63, ITGB1, SDCBP, and caveolin-1 (CAV1), were identified among cell adhesion and wound healing proteins. The most pronounced differences were observed among extracellular matrix (ECM) proteins such as various collagens (COL5A1, COL1A2, COL1A1), keratin 1 (KRT1) and laminin A (LMNA). Overall, the only proteins that seemed to coordinate with EV function in migration assays seen in 5.3.7.1 were CAV1 and ITGB1. Altogether, various proteins involved in wound healing and cell migration were identified by GOBP analysis, most of which were similarly expressed among MSC EV populations, although fluctuations were seen among ECM proteins, ANXA2 and SDCBP.

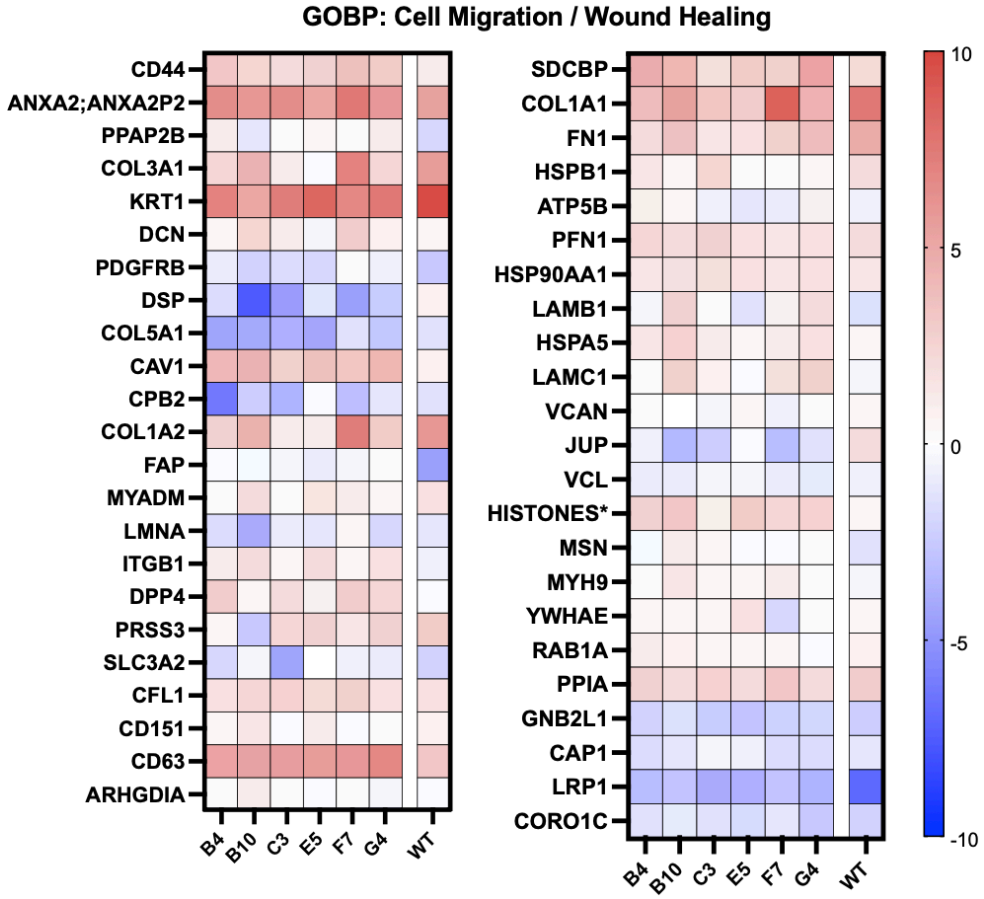

Figure 5.23 Expression of cell migration and wound healing proteins in MSC subclone EVs and wild-type MSC EVs. iBAQ scores filtered to remove protein

duplicates, reverse variables, contaminants, and any protein hits included in only one of three n-numbers. Data was also transformed on a log_2 scale, and width adjustment normalisation performed. Biological process classification is performed by PANTHER software. Red denotes high normalised expression, while blue denotes low normalised expression. Mean ±SD; n = 3.

Due to the differences in cell adhesion elicited by MSC subclone EVs, cell adhesion proteins expressed among MSC EV populations were identified in the proteomics dataset by gene ontological biological process (GOBP) categorisation. This was performed to identify any proteins that could have been responsible for the heterogenous cell adhesion activity. As presented in Figure 5.24, most proteins seemed to be consistently expressed among all EV populations. Once again, the only proteins that appeared to fluctuate in expression between populations were ECM proteins such as collagens. Collagen alpha-1(I) chain (COLA1) and COLA3 seemed to closely resemble the functions of EV subclones in the *in vitro* MSC cell adhesion assay seen in 5.3.7.2. Otherwise, some of the most highly expressed cell adhesion proteins were CD63, CD44, CAV1, fibronectin (FN1) and cytoplasmic actin 1 (ACTB). Unlike previous cell adhesion assays performed with SKOV3 cells, ITGB1 expression did not seem to correspond with cell adhesion. Overall, various cell adhesion proteins were identified by GOBP analysis among MSC subclone EVs, most of which were similarly expressed, except ECM proteins, which did seem to mirror cell adhesion activity.

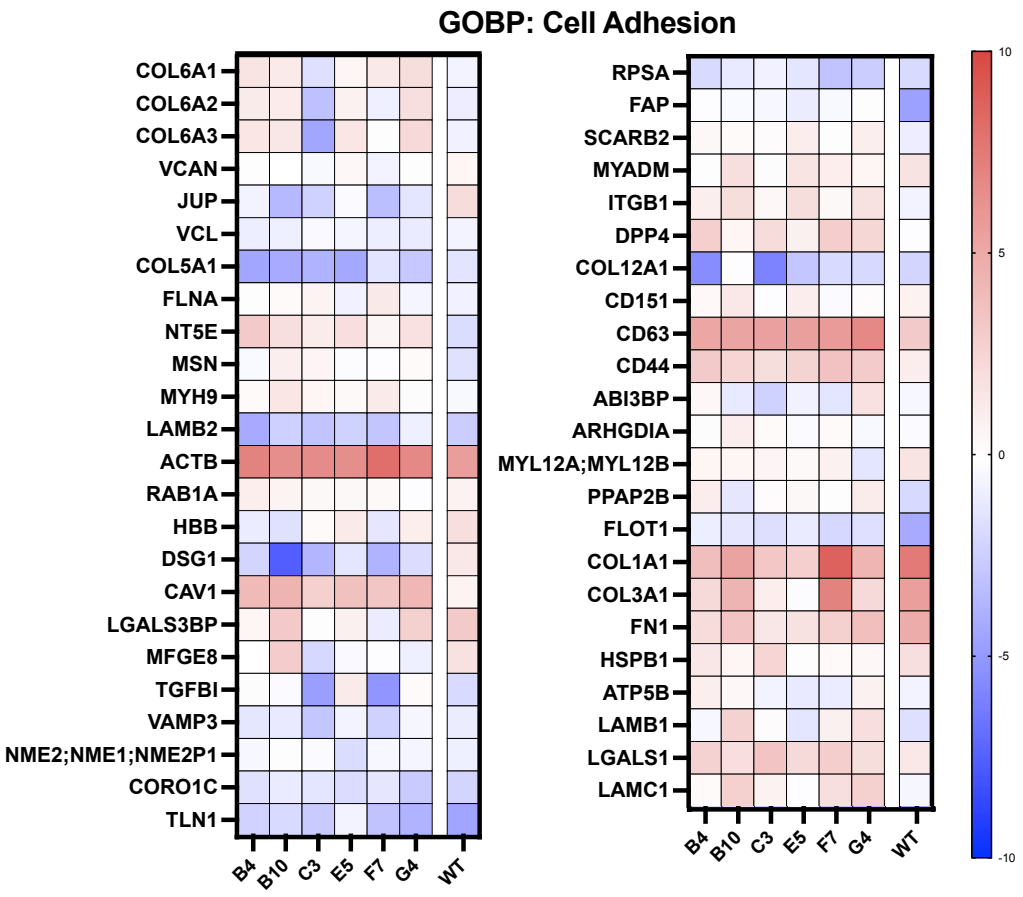

Figure 5.24 Expression of cell adhesion proteins in MSC subclone EVs and wild-type MSC EVs. iBAQ scores filtered to remove protein duplicates, reverse variables, contaminants, and any protein hits included in only one of three n-numbers. Data was also transformed on a $\log_2$ scale, and width adjustment normalisation performed. Biological process classification is performed by PANTHER software. Red denotes high normalised expression, while blue denotes low normalised expression. Mean ±SD; n = 3.

Finally, PANTHER protein class analysis was performed using a normalised list of proteins from each MSC EV population. PANTHER Overrepresentation Tests using Fisher's exact tests with Bonferroni corrections were performed to assess whether different protein classes were significantly over- or underrepresented versus their expected proportional representation within the entire human proteome. Fold enrichment

was calculated by dividing the proportional representation factor of protein classes observed within each sample list by the expected proportional representation factor from the human proteome. The negative inverse of results less than one were then found, while results more than one were left unchanged to express each protein class as fold over- or underrepresented on a linear scale. Figure 5.25 presents a heatmap of the PANTHER protein class analysis. Interestingly, multiple protein classes associated with nucleic acid interaction were among the most highly underrepresented in every MSC EV population, including gene-specific transcriptional regulators, DNA-binding transcription factors, chromatin/chromatin-binding or -regulatory proteins, helix-turn-helix transcription factors and homeodomain transcription factors. Chaperone proteins and chaperonins were the most overrepresented protein class in subclones C3 and E5. Structural proteins such as extracellular matrix proteins and actin or actin-binding cytoskeletal proteins were overrepresented in every EV population. However, other structural protein classes like tubulins were only overrepresented in subclones E5, F7 and G4. Vesicle coat proteins were overrepresented in every EV population aside from the wild-type MSC EVs, likely due to sample preparation issues previously surmised. Beyond this, accompanying the differential DPP4 activity observed among MSC subclones EVs, the protease protein class was also significantly overrepresented, although only slightly. However, interestingly there was little to no difference in the fold enrichment scores between each of the MSC EV subclones. Integrins were also significantly overrepresented in multiple subclone EVs but were not overrepresented in subclone B4, which elicited among the greatest cell adhesion responses. In conclusion, multiple protein classes were identified by PANTHER protein class analysis, some of which were exclusively or differentially expressed in different EV subclones, suggesting that some EV subclones were better at performing specific functions than others.

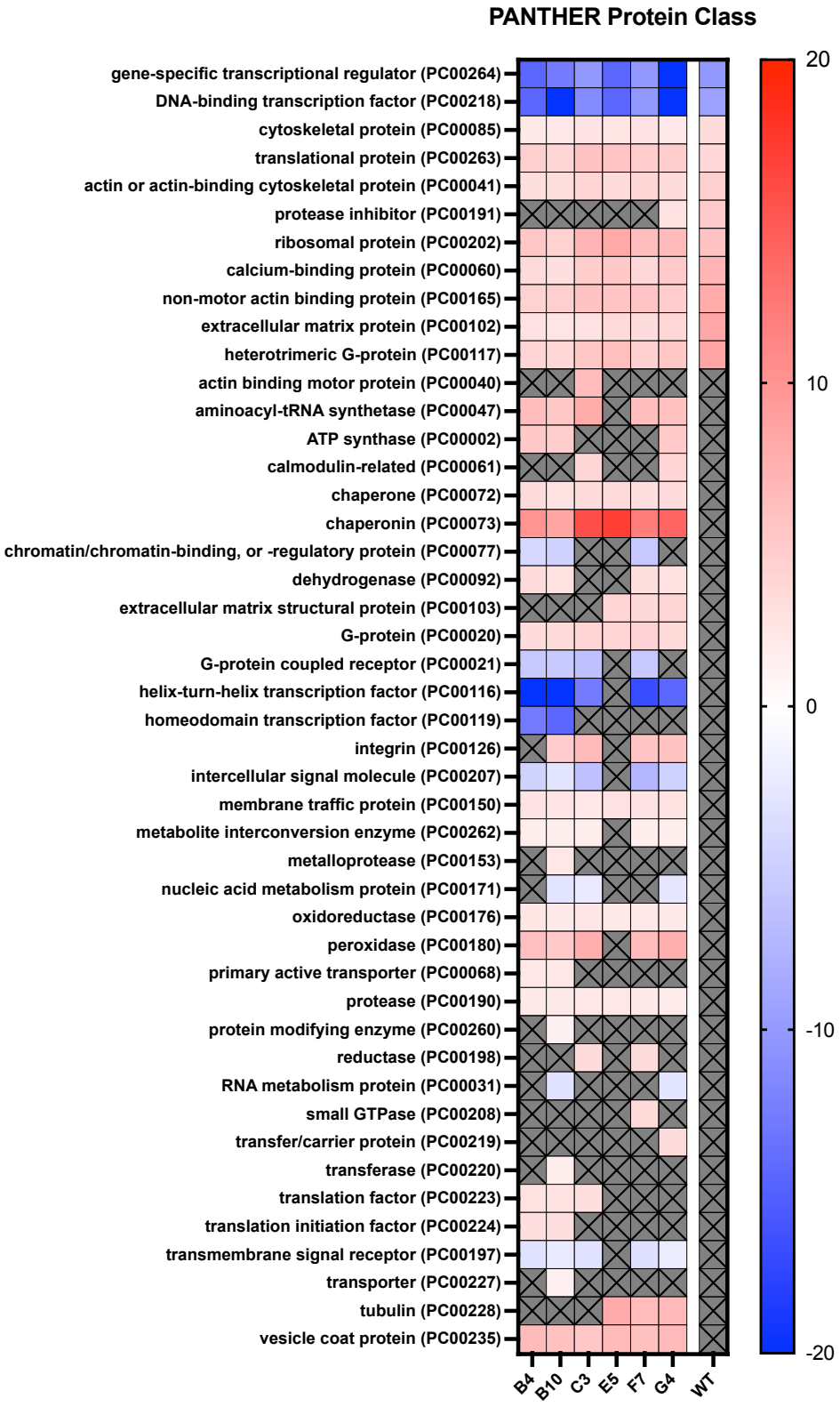

Figure 5.25 PANTHER protein class analysis presenting significantly over- or underrepresented protein classes versus expected representation in the human

proteome. After filtering, analysis was performed using a list of proteins remaining in each MSC EV population to remove protein duplicates, reverse variables, contaminants, and any protein hits included in only one of three n-numbers. PANTHER Overrepresentation Tests using Fisher's exact tests with Bonferroni corrections. Significance indicated by $P < 0.05$. Fold enrichment calculated by dividing proportional representation factor of protein classes observed within each sample list by expected proportional representation factor from the human proteome. Negative inverse of results less than one calculated and results more than one left unchanged to express each protein class as fold over or underrepresented on a linear scale. Red denotes overrepresentation, white denotes normal expression and blue denotes underrepresentation. Mean ±SD; n = 3.

After proteomics analysis, western blotting was performed in part to try and corroborate the expression of some of the highly expressed, potentially functional EV proteins reported within the proteomics data as well as to assess whether any differences in the EV proteomes were reflected in the cell proteomes as a potential source of heterogeneity within the EV proteomes. Figure 5.27 presents western blots of MSC subclone EVs, wild-type MSC EVs and their respective parent cells. Fibronectin, CD29 (integrin beta-1), laminin subunit beta-1, CD44, annexin a1 and a2, CD151 and caveolin-1 were assessed as all were highly expressed and identified by GOBP analysis as involved in cell migration/wound healing, cell adhesion or both. Fibronectin appeared to be more highly expressed in B4, B10 and F7 EV samples which seemed to coordinate with cell adhesion assay results, but aside from higher expression in B10, the signal did not match proteomics data. Fibronectin expression in cell lysate samples was not mirrored in EV samples. Similarly, a high expression of CD29 was seen in B10 and F7 EVs, though this

was not reflected in cell lysate or the proteomics data. As for laminin, CD44 and CAV1, a greater, more consistent expression was seen in cell lysate samples, and signal could not be detected among EV lysates. A high expression of ANXA1/A2 was seen in B4 and F7 EVs, aligning closely to cell adhesion assay results and CD151 with the addition of subclone B10, although no discernible differences in expression of these proteins were seen in cell lysate samples. Altogether, the expression of fibronectin, ANXA1/A2 and CD151 resembled the functional differences in cell adhesion assays, while laminin, CD44 and CAV1 could not be detected by western blot in EV samples. Western blotting was also unable to detect similarities between the expression of proteins in EVs and cell lysate, again suggesting that EV heterogeneity may be independent of cellular heterogeneity.

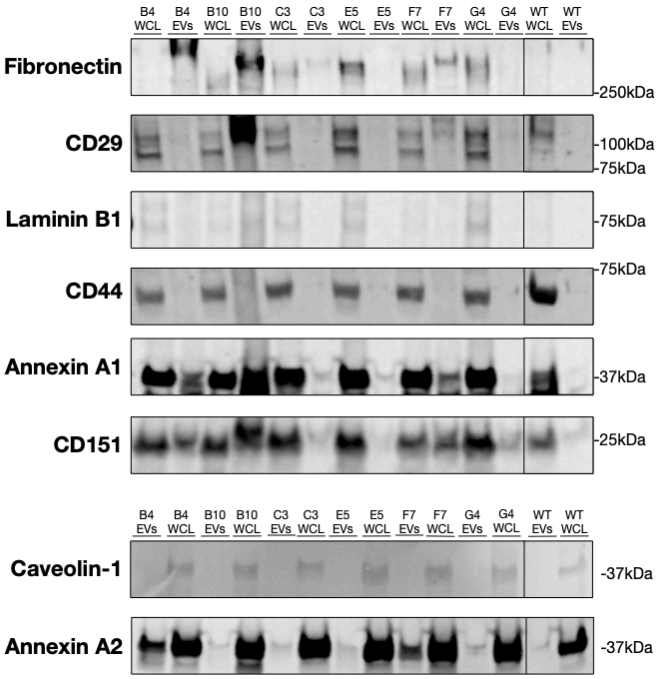

Figure 5.27 Western blot analysis of cell adhesion and cell migration proteins in MSC subclone-derived EVs. 10 µg of lysed EV and MSC whole cell lysate samples.

In addition to western blotting, nanoflow cytometry (NFC) of numerous EV surface proteins was also performed to validate protein expression in the proteomics data. The expression of all the common EV membrane markers identified in Figure 5.21 were assessed aside from HLA-A. As CD63 was identified as the most prominent EV membrane marker across all subpopulations during proteomics analysis, EV membrane marker antibodies were co-incubated with anti-CD63 antibodies to assess colocalisation and determine a true EV population within each sample. Figure 5.27 presents the results of NFC analysis for CD9, CD63 and CD81, along with correlation analysis between colocalised CD63 and CD81 detected in NFC and their expression in proteomics. Firstly, Figure 5.27A presents the percentage of particles that were mIgG1 positive, presenting a low percentage of positive particles in each MSC EV subclone in the FITC channel and low to no expression seen in the PE channel, indicating that the results seen in the other labelling conditions were accurate representations of protein expression. As seen in Figure 5.27B and D, EV tetraspanins followed a similar pattern in expression, with the highest expression of all three EV tetraspanins seen in subclones B4, followed by B10 and F7. Like proteomics data, CD63 appeared to be the most prominent EV tetraspanin, followed by CD81. CD9 was not observed within the proteomics data as CD9 expression was not detected in enough sample replicates to be considered part of the dataset, and the lower expression of CD9 seen in Figure 5.27B continued this trend. Unlike proteomics data, CD63 expression varied among MSC EV subpopulations. Consequently, in the correlation analysis in Figure 5.27C, no trend was seen between colocalised CD63 NFC data and CD63 proteomics data. Similarly, as seen in Figure 5.27D, unlike its expression seen in proteomics, CD81 expression also varied in NFC data. However, a significant ($P < 0.05$) positive correlation between CD81 expression in the two datasets was observed. In summary, NFC analysis of tetraspanins on MSC subclone EVs revealed a similar trend

in tetraspanin expression to proteomics analysis, with CD63 the most abundant, followed by CD81 and CD9, and a significant positive correlation between CD81 expression in NFC and proteomics, although no trend between CD63 expression seen in NFC and proteomics.

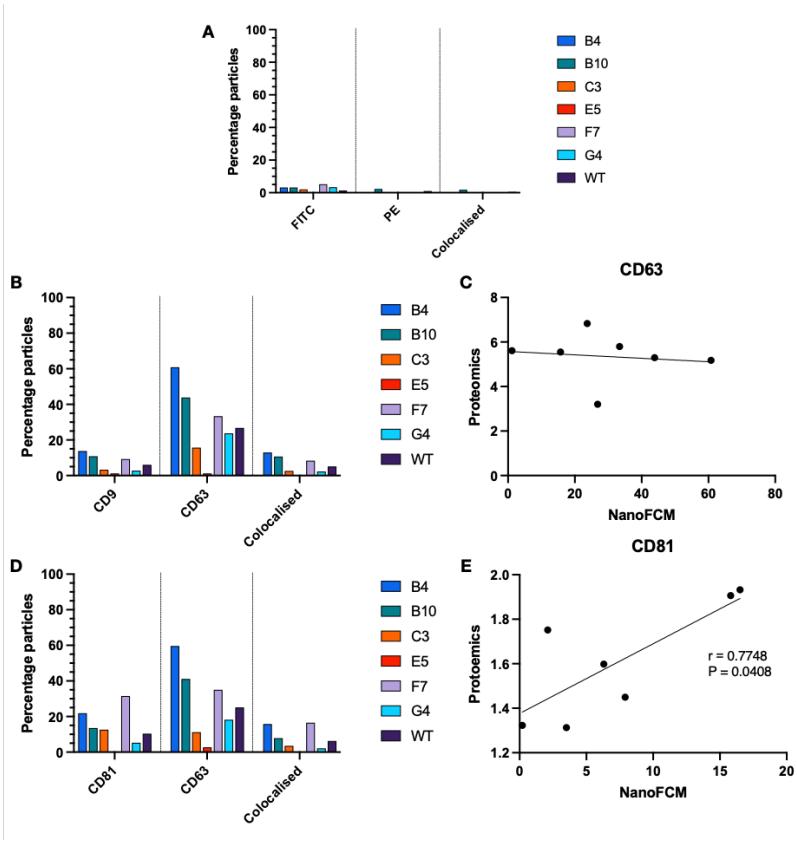

Figure 5.27 NanoFCM quantification of EV tetraspanins on MSC subclone-derived EVs. (A) Percentage of particles in FITC and PE channels stained with anti-mIgG1-PE and percentage colocalised signal. (B) Percentage of particles positive for anti-CD9-FITC or anti-CD63-PE and colocalised. (C) Two-tailed Pearson's correlation of CD63 positive particles in NanoFCM and CD63 expression in proteomics. (D) Percentage of particles positive for anti-CD63-FITC or anti-CD81-PE and colocalised. (E) Two-tailed Pearson's correlation of CD81 positive particles in NanoFCM and CD81 expression in proteomics

showing a significant positive correlation between the two datasets. Mean, n = 1 for NanoFCM data. Mean, n = 3 for proteomics data.

Subsequently, the remaining EV surface proteins were assessed by NFC to validate the protein expression seen in the proteomics data. As seen in Figure 5.28A, DPP4 (CD26) appeared modestly expressed across MSC subclone EVs with the highest expression seen in subclone F7 without CD63 colocalisation. However, when colocalisation was considered, subclone B4 had the highest DPP4 expression. Additionally, while not significant, a positive trend in DPP4 expression was seen, suggesting that the NFC data supported the proteomics data (Figure 5.28B). Aside from the CD63 expression demonstrated in Figure 5.27, CD59 presented the next highest average expression in NFC analysis (Figure 5.28C). This further supported the proteomics data as CD59 was also the second highest EV surface protein within that dataset. F7, C3 and B4 had the highest CD59 expression. Additionally, while not significant, a positive trend in CD59 expression between proteomics and NFC was again seen, further corroborating the proteomics data. CD107 and HLA-C (Figure 5.28E-H) were similarly differentially expressed, and both did not present a significant correlation, but positive trends were seen. HLA-C was weakly expressed, but a high percentage of HLA-C positive particles was observed in subclone B4. However, this was likely a false positive as correlation analysis showed a far lower percentage of particles. Overall, a positive trend between protein expression identified in proteomics and NFC was seen among all assessed EV surface proteins, as well as similar relative expression levels to those reported in proteomics, instilling confidence in the accuracy of the proteomics data.

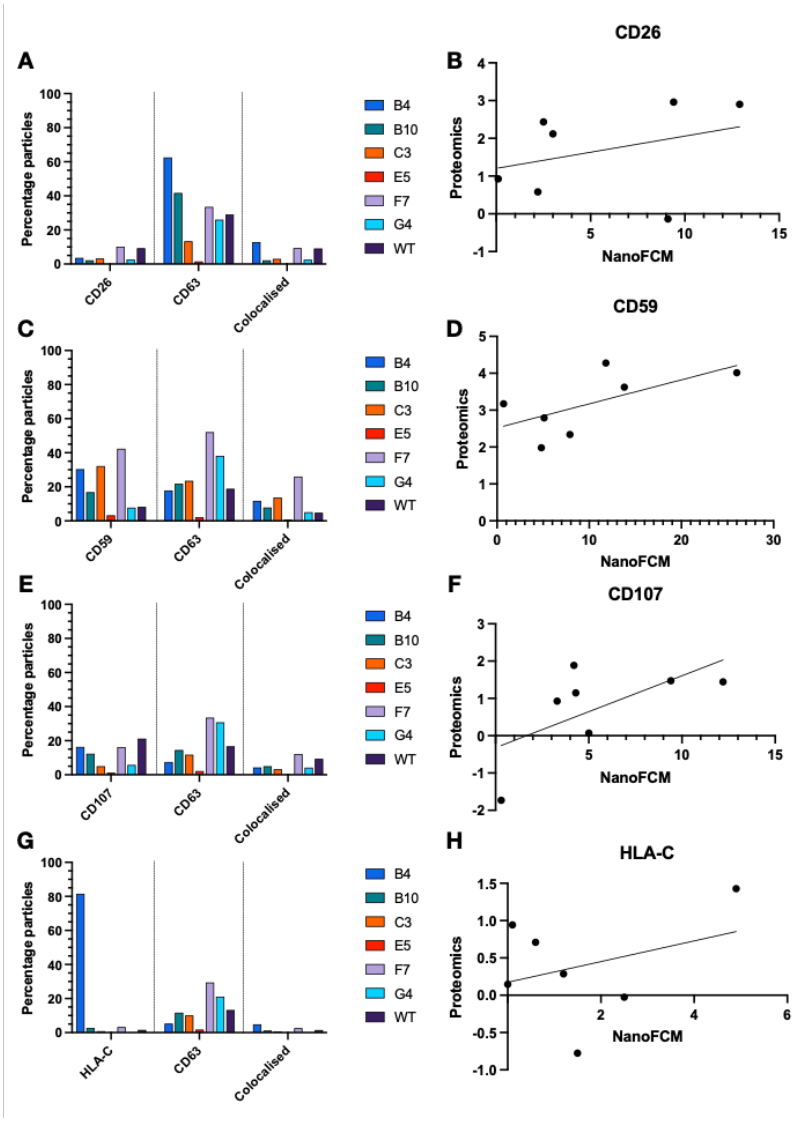

Figure 5.28 NanoFCM quantification of EV membrane proteins on MSC subclone-derived EVs. (A) Percentage of particles positive for anti-CD26-PE or anti-CD63-FITC and colocalised, (C) anti-CD59-FITC or anti-CD63-PE and colocalised, (E) anti-CD107-FITC or anti-CD63-PE and colocalised, and (G) anti-HLA-C-FITC or anti-CD63-PE and colocalised. (B) Two-tailed Pearson's correlation of CD26 positive particles, (D) CD59 positive particles, (F) CD107 positive particles, and (H) HLA-C positive particles in NanoFCM and expression in proteomics. Mean, n = 1 for NanoFCM data. Mean, n = 3 for proteomics data.

5.3.9 MSC EV subclone functions significantly correlated with proteins expression observed in proteomics

Finally, to aid identification of proteins responsible for functional differences observed in cell migration, cell adhesion and DPP4 activity assays, Pearson's correlation analysis was performed between MSC subclone EV functional assay data and proteins common to all MSC EV subclones identified in proteomics analysis. This analysis was also performed to identify markers of highly functional EV populations.

Firstly, correlation analysis was performed between cell migration assay data and proteomics data to identify proteins linked to functional differences and marker proteins among MSC subclone EVs. As shown in Figure 5.29, various proteins common to all seven MSC EV populations were significantly correlated with HMEC-1 wound healing assay results. The highest expressed protein presenting a significant positive correlation was annexin A2 (ANXA2) which is involved in cell adhesion and wound healing[325–328]. Other proteins involved in cell adhesion were also positively correlated, including plectin (PLEC) and caveolae-associated protein 1 (PTRF)[329–331]. Other proteins of note that were significantly positively correlated included peptidyl-prolyl cis-trans isomerase A (PPIA), which is involved in the proinflammatory activation of endothelial cells and inducing adhesion molecule expression[332], heat shock protein 70 1a/1b (HSPA1A/1B) involved in stress response[333], and calmodulin 2/3 (CALM2/3) which regulates cell growth and cycle progression[334]. Interestingly, despite its relatively high expression, integrin beta 1, which is also involved in cell adhesion, was significantly negatively correlated with wound healing function despite other cell adhesion proteins presenting positive correlations. Altogether, numerous proteins involved in cell migration and wound healing were significantly positively correlated with differential cell migration elicited by MSC subclone

EVs, including numerous EV surface proteins that could also serve as a marker of these populations.

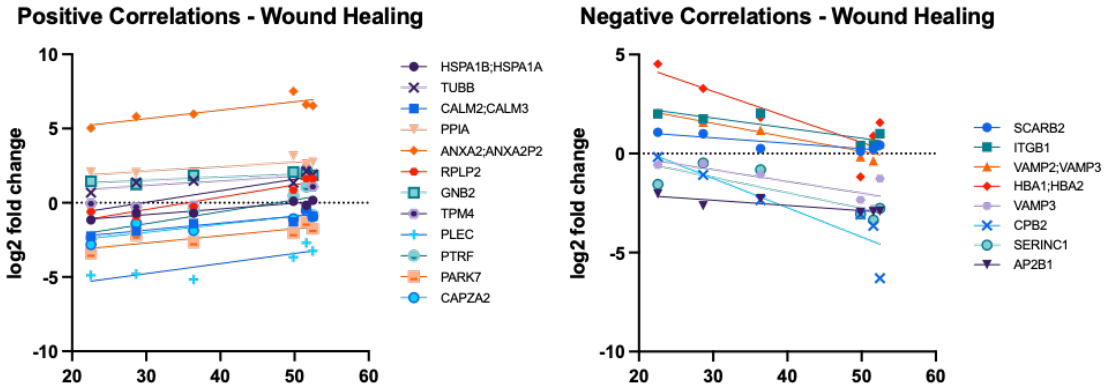

Figure 5.29 Significant positive and negative correlations of MSC subclone EV proteins and their activity in wound healing assays. Two-tailed Pearson's correlations where significance is indicated by $P < 0.05$. Log_2 protein expression versus wound closure after 24 hours. Mean ±SD; n = 3.

Next, correlation analysis was performed between cell adhesion assay data and proteomics data to identify proteins linked to functional differences and marker proteins among MSC subclone EVs. As shown in Figure 5.30, of the positively correlated proteins, annexin a1 was the highest expressed positively correlated protein which is also involved in cell adhesion[325,335]. Additionally, rho GDP-dissociation inhibitor 1 (ARHGDIA) was also positively correlated. This was curious as ARHGDIA may regulate cell motility and negatively regulates cell adhesion[336,337]. The EV marker protein EHD2 was also positively correlated with cell adhesion which could serve as a marker of enhanced cell adhesion among MSC subclone EVs[18]. Few proteins that were negatively correlated were associated with cell adhesion, although trypsin 3 (PRSS3) was negatively correlated,

which could be considered a negative regulator of cell adhesion, as trypsin cleaves cell attachments to tissue culture plastic. Overall, ANXA1 and ARHGDIA expressed in MSC subclone EVs, which are involved in cell adhesion, were significantly positively correlated with cell adhesion facilitated by MSC subclone EVs, and EV marker protein EHD2 also showed a positive correlation which could serve as a marker.

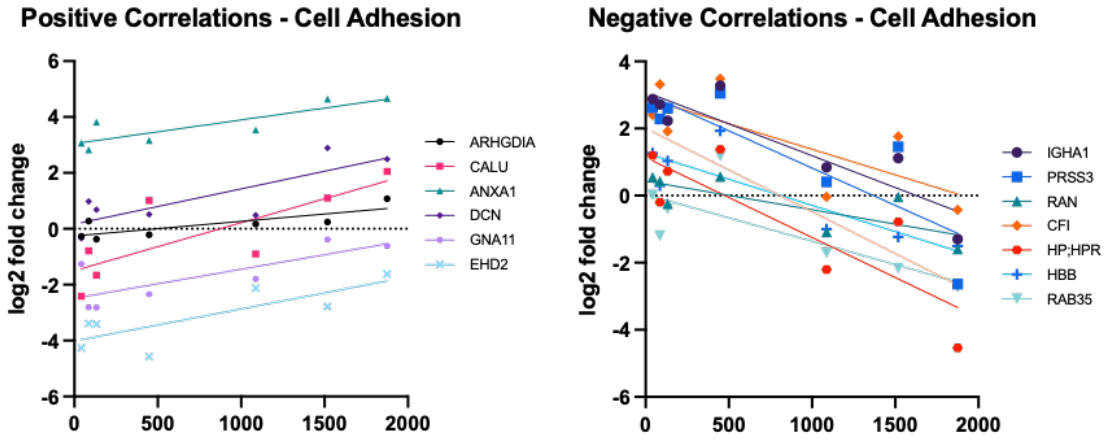

Figure 5.30 Significant positive and negative correlations of MSC subclone EV proteins and their activity in cell adhesion assays. Two-tailed Pearson's correlations where significance is indicated by $P < 0.05$. Log_2 protein expression versus mean raw MSC cell adhesion assay data. Mean ±SD; n = 3.

Finally, correlation analysis was performed between DPP4 activity assay data from MSC subclone EVs and proteomics data to identify proteins linked to differences in function and marker proteins among MSC subclone EVs. As seen in Figure 5.31, the most prominent of the significantly positively correlated proteins was DPP4. The significant positive correlation of DPP4 confirmed prior suggestions that the activity of DPP4 observed mimicked DPP4 expression from proteomics data. Additionally, numerous EV

membrane marker proteins were also positively correlated with EV DPP4 activity, including HSPA1B/A, CD59, CD81 and ANXA2[18]. In conclusion, correlation analysis confirmed that DPP4 activity seen in MSC subclone EVs was directly proportional to its expression in MSC EVs, and numerous EV surface proteins that also showed positive correlations may serve as markers of this function.

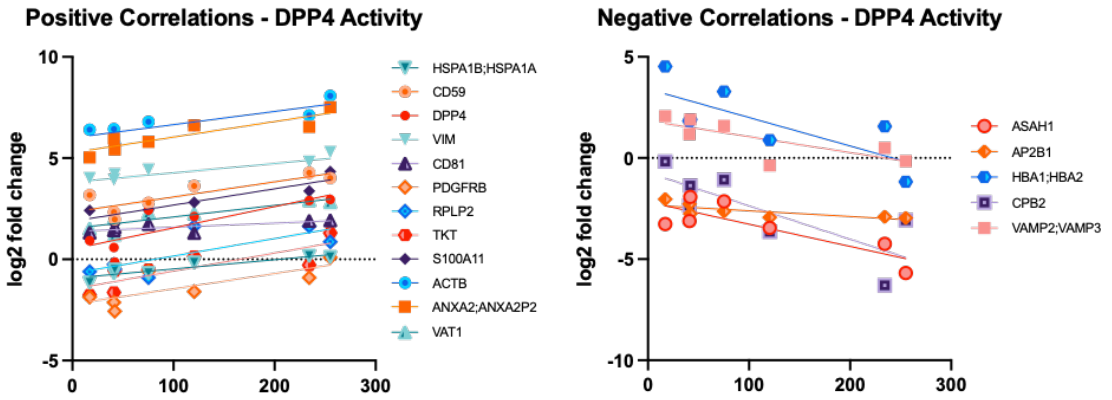

Figure 5.31 Significant positive and negative correlations of MSC subclone EV proteins and their activity in DPP4 activity assays. Two-tailed Pearson's correlations where significance is indicated by $P < 0.05$. Log_2 protein expression versus mean normalised DPP4 activity assay data. Mean ±SD; n = 3.

5.4 Discussion

Throughout this chapter, the heterogenous characteristics of EVs and the effects that different external factors had on EV heterogeneity were explored to attempt to identify the source of variability in EV populations. Furthermore, functional differences in EV subpopulations were assessed to further knowledge of EV heterogeneity and determine whether heterogeneity is linked to heterogeneity of EV producer cells or whether cells secrete a plethora of EVs that create heterogeneous effects in recipient cells.

5.4.1 Size-based heterogeneity

In sections 5.3.1 through 5.3.4 of this chapter, following the protocol outlined by Willms (2018), a Cytiva XK-16/70 column packed with Sephacryl S1000 resin was utilised to fractionate SKOV3 EVs into four different populations according to the XK-16/70 elution profile[51]. As described in section 5.1.2, numerous other studies have also successfully fractionated EVs and particles of different sizes. However, this study and Willms (2018) represent the first instances where SEC has been adapted and upscaled to increase resolution beyond the separation of EVs from contaminants and enable the separation of EVs into distinct subpopulations[51]. NTA analysis revealed heterogeneity in EV size distributions between each EV pool (Figure 5.1). EVs in pool 1 presented a much wider size distribution and larger modal size (demonstrated by the size distribution peaks), while EVs in pools 2 to 4 had incrementally narrower size distributions and modal sizes. Furthermore, direct measurement of EVs captured in TEM images presented highly significant differences between size distributions of EVs in each population, with size distributions and median sizes decreasing sequentially. Modal EV sizes seen in NTA analysis were very similar to medians reported in TEM analysis, although medians reported by NTA, while incrementally smaller in each population, were much larger than

those reported by TEM. This may highlight the drawbacks of NTA for size analysis, as a minimum detectable vesicle size by NTA has previously been reported as 50 nm[338], while TEM has been reported as low as 1 nm[339], therefore skewing NTA measurements towards larger sizes. Furthermore, differences in how different-sized particles scatter light and the effects temperature, viscosity, and vibration have on NTA analysis can also cause errors in size determination[147,339]. Interestingly, similar to those identified by Zhang *et al.* (2018), non-membranous sub-50 nm particles were also observed in pools 3 and 4, suggesting that the use of the XK-16/70 SEC column may be able to separate EVs from exomeres[50]. However, further work should be conducted to characterise these small particles to confirm they are not lipoprotein particles, as some low- and very low-density lipoproteins can be less than 50 nm in diameter and may present similar to exomeres in TEM imaging[153,205,282].

To assess functional heterogeneity among SKOV3 EV size-based subpopulations, *in vitro* cell adhesion assays were performed due to the effects of cancer-derived EVs on cell adhesion, including in establishing pre-metastatic niches to aid the adhesion of cancer cells to distant sites *in vivo* have been well documented[60,100,340–342]. As seen in Figure 5.3, unfractionated EVs elicited the greatest SKOV3 cell adhesion, while SKOV3 soluble protein that served as a control for EV function elicited the lowest influence. This was interesting as while higher cell adhesion in the unfractionated EV sample suggested that facilitation of cell adhesion was EV associated, all other size-based EV pools showed lower cell adhesion. This may suggest that cell adhesion is facilitated more strongly by larger vesicles or free protein in the unfractionated sample that is removed during XK-16/70 purification. Of the EV pools, pool 3 caused the greatest cell adhesion on average, concurrent with results observed by Willms (2018). However, while Willms (2018)

observed differential cell adhesion among all four SKOV3 EV pools, in this study, the remaining pools evoked lower levels of cell adhesion that were similar to one another[51]. Notable deviation among replicates in all samples resulted in only pool 4 and the soluble protein samples presenting a significant difference in cell adhesion. Although altogether, the data presented that size-based SKOV3 EV subpopulations elicit differential effects on cell adhesion.

Following functional assessment, SKOV3 EVs subpopulations were characterised to attempt to link differences in cell adhesion to functional or marker protein expression. ExoView R100 analysis revealed CD81 as the most abundant EV tetraspanin across all SKOV3 EV populations, followed by CD63 and CD9. Historically, CD81, CD63 and CD9 have served as exosomal markers due to their role in ESCRT-independent endosomal sorting and intraluminal vesicle biogenesis[32,33,293–295]. However, more recent evidence has shown that EVs expressing CD9 and CD81 with little CD63 are mainly plasma membrane-derived (microvesicles). In contrast, Mathieu *et al.* (2021) showed that EVs bearing CD63 with little CD9 but containing some late endosome proteins qualify as exosomes[152]. Given the similarities of these findings to the trend in tetraspanin expression seen in the ExoView analysis here and in other studies, the preferential or overproduction of microvesicles, as opposed to exosomes, may be a feature of SKOV3 cells. However, further research is necessary to corroborate the findings of Mathieu *et al.* (2021), and future studies may benefit from characterising microvesicles and exosomes produced by SKOV3 cells specifically due to the heterogeneity in EV characteristics seen between different cell lines. Due to the broadly similar pattern in expression of these markers observed across all four EV pools, based on this evidence alone, it is unlikely that the

difference in cell adhesion observed in response to pool 3 EVs is associated with tetraspanin expression.

Sizing data was also obtained using the ExoView by interferometry performed on each tetraspanin capture spot. In label-free mode, the ExoView is limited to measuring particles in the range of 50 to 200 nm. Unlike NTA and TEM data, little differences in mean size were seen between the four EV pools. A possible explanation for the differences in size may be the selective measurement of tetraspanin positive particles by ExoView, which may limit sizing to an exosomal population[18,152,236], driving down average sizes and narrowing size distributions compared to non-selective TEM and NTA analysis. Alternatively, as interferometry is also based on light scattering to measure particles, this data may further highlight the flaws in using light scatter-based techniques for measuring particle size, and concentration highlighted elsewere[147,338,339,343], and demonstrate the need for more sensitive and specific means of measuring these metrics on a nanoscale.

As ExoView analysis revealed a very high expression of CD81 among SKOV3-derived EVs, CD81 was used as an EV marker in structured illumination microscopy (SIM) analysis to assess the abundance of CD29 on SKOV3 EVs. Through antibody blockade of CD29 on SKOV3-derived EVs, Willms (2018) demonstrated complete inhibition of cell adhesion and showed that CD29 plays a role in SKOV3 EV-mediated cell adhesion *in vitro*[51]. Numerous other studies have also demonstrated the importance of CD29 in EV-mediated cell adhesion[313,344], including in the establishment of pre-metastatic niches[99,102,345]. However, surprisingly data from this investigation showed that CD29 and CD81 were completely anti-colocalised across all four SKOV3 EV subpopulations and unfractionated samples, despite the high expression of CD81. Previous evidence

regarding the colocalisation of CD81 and CD29 is mixed. Hierarchical clustering of MACSPlex analysis performed on EVs derived from breast cancer-positive lymphatic drain fluid has shown that CD81 and CD29 were closely associated with one another[346]. In contrast, studies of MSC-derived EVs have shown that CD81 and CD29 usually are not actively associated with one another unless MSCs are radioactively stimulated[347]. However, the complete anti-colocalisation of CD81 and CD29 seen here may be an artefact of structured illumination microscopy (SIM), as SIM lacks the spatial resolution to pinpoint the precise position of a fluorophore compared to an imaging technique such as single-molecule localisation microscopy which has a spatial resolution of 20-50 nm. Furthermore, due to point spread in SIM, the precise position of a fluorophore may be out by a few hundred nanometres[348]. Therefore, future colocalisation imaging studies with these EVs and others may benefit from a more sensitive technique, such as single-molecule localisation microscopy.

To further understand the characteristic differences of SKOV3 EV subpopulations that underpinned the differences in cell adhesion seen here and by Willms (2018)[51], LC-MS/MS proteomics analysis was performed. Principle component analysis and volcano plots (Figure 5.7) presented the heterogeneity in protein expression between each of the EV subpopulations. This was significant as previous EV subpopulation research has reported a homogenous exosomal population ranging from 30 to 120 nm in diameter[349]. PANTHER protein class analysis (Table 5.1) revealed universal upregulation of cell adhesion proteins across all four SKOV3 EV subpopulations, synonymous with the important role that SKOV3 EVs play in cell adhesion[102,340]. However, this did not provide insights into differential cell adhesion facilitated by the EV subpopulations. Numerous other protein classes were differentially upregulated among each EV subpopulation.

Upregulation of small GTPases in pools 2 and 3 was interesting as it coincided with the populations that elicited the greatest effect on cell adhesion both here and as observed by Willms (2018). GTPases regulate EV biogenesis and release and have also been suggested to play a role in assigning specific functions to EVs[350]. This suggested that GTPases may be responsible for assigning enhanced cell adhesion to EVs in pools 2 and 3 by loading certain cell adhesion proteins during EV biogenesis. Furthermore, protein classes upregulated in pool 4 EVs were highly similar to those identified by Zhang *et al.* (2018) that were upregulated in exomeres, including glycosidases, proteases, serine protease inhibitors and chaperonins[50]. This was particularly interesting due to the previous visualisations of the small, non-membranous particles previously visualised in pool 4 TEM images and the identification of the smallest particles in pool 4. However, further investigation is necessary to characterise EVs in pool 4 and confirm the identity of these particles.

After the apparent uniformity in high cell adhesion protein expression across all four SKOV3 EV subpopulations was identified by PANTHER protein class analysis, heterogeneous integrin expression was seen across all four EV pools (Figure 5.8). Most interestingly, CD29 (ITGB1) expression in each EV pool matched the trend in SKOV3 cell adhesion recorded by Willms (2018)[51] and was synonymous with the high cell adhesion elicited by pool 3 EVs in this investigation. Aside from CD29, integrin-alpha-3 (ITGA3) displayed a similar expression pattern. This was unsurprising as the pair form the alpha-3-beta-1 subunit [351]. The only integrin more abundantly expressed in pool 4 versus the unfractionated control was ITGAV. An upregulation in ITGAV expression was noted in pools 2 and 3, which matched the high SKOV3 cell adhesion seen in cell adhesion in this investigation and matched the trend of the *in vitro* SKOV3 adhesion assay observed by

Willms (2018)[51], more so than CD29. High ITGAV expression has been reported on cancer-derived EVs[352] and linked to prostate cancer cell adhesion and invasion[353] and liver metastasis[99]. ITGAV dimerises with ITGB3 and supports growth factor and immune modulation signalling pathways in cells[354–357]. Whether ITGAV on SKOV3 EVs and their subpopulations is also involved in these processes is undetermined but a potential subject of future investigations. Additionally, Hurwitz & Meckes (2019) investigated integrin expression on cancer-derived EVs and reported that while CD29/ITGB1 was the most highly expressed beta subunit, ITGB4 was the second most highly expressed among a variety of cancers, including ovarian cancers[352]. In contrast, this investigation showed a markedly lower representation of ITGB4, with a roughly two-fold higher expression of ITGB5 than B4. Additionally, an 18-fold decrease in ITGB4 enrichment versus the unfractionated control was observed in pool 4 EVs. Together with a large majority de-enrichment in integrin expression in pool 4, this further suggests a completely phenotypically and functionally distinct population of sEVs, particularly regarding cell adhesion.

However, despite integrin expression correlating with differences in cell adhesion mediated by size-based SKOV3 EV subpopulation, volcano plots in Figure 5.8 present differences in expression compared to unfractionated SKOV3 EVs, which evoked the highest cell adhesion seen in this investigation. This suggested that integrins may not be solely responsible for the high cell adhesion seen in unfractionated SKOV3 EVs. Instead, as seen in Table 5.2, numerous cell adhesion proteins not typically found in EVs were highly expressed in the unfractionated EV population than in all subpopulations, including fibronectin (FN1) and various collagen subunits, which could have enhanced the facilitation of cell adhesion by unfractionated SKOV3 EVs. These proteins associate with

EVs by interacting with EV surface receptors[18] and may have been removed during XK-16/70 SEC, evidenced by the downregulation of ECM proteins across EV subpopulations.

In summary, XK-16/70 Sephacryl S1000 size exclusion chromatography was capable of fractionating EVs into four distinct subpopulations. Highly significant differences in EV size were reported for each subpopulation, presenting XK-16/70 SEC as the first SEC-based technique to achieve size separation within an EV population. SKOV3 cell adhesion assays in this study and others presented that the fractionated SKOV3 EV subpopulations elicited heterogeneous adhesion. The heterogeneous effects were coupled with marked differences in protein expression and physical characteristics, including differential expression of highly expressed adhesion proteins, including CD29, which has previously been closely associated with EV-mediated cell adhesion. Altogether, data from this investigation showed that heterogeneity exists among size-based EV subpopulations and that size may be a determining factor in the assignment of EV functions.

5.4.2 Temporal effects on EV heterogeneity

In the last few decades, EV heterogeneity with respect to EV source, size and biogenesis has been rigorously studied[47,303]. However, whether EV heterogeneity changes over time has yet to be seen. In section 5.3.5 of this study, the possible role of temporal phenotypic drift on EV heterogeneity was investigated using a bead-based multiplexed flow cytometry assay to assess the surface proteome of EVs secreted from two different metastatic subclones of MDA-MB-231 breast cancer.

The conditioned medium was harvested from three independent cultures of lung and brain metastatic MDA-MB-231 over seven consecutive weeks. Three independent cultures were used for each subclone to monitor whether any changes in protein expression between the EVs samples were conserved or whether independent cell cultures were affected differently. Interestingly, protein expression changes appeared to be conserved among independent cultures (Supplementary Figure S5.5 and S5.6), suggesting that either a factor common to all three cultures affected change in protein expression or change in protein expression may be programmed and occur naturally over time. A factor common to all cultures of each cell type was the incubation of cells in serum-free OptiMEM for 72 hours to harvesting. This was necessary to ensure analysis of EVs secreted from MDA-MB-231 cells and prevent contamination with serum-derived EVs. However, Li *et al.* (2015) showed that culturing N2a cells in OptiMEM compared to culturing in EV-depleted DMEM for 48 hours yielded EVs with distinct protein expression profiles[302]. Alternatively, changes in environmental cell culture conditions such as temperature, culture nutrients or pH may induce stress and alter EV phenotype and functionality[300–302]. Therefore, any changes in protein expression seen in the MACSplex data may have occurred due to serum deprivation or environmental changes rather than by intrinsic cellular drift.

One of the most notable differences in the expression of proteins between both MDA subclone EVs (Figure 5.10) was the high expression of CD29 in the lung metastatic EVs. In addition to the function of CD29 and other integrins in cancer and EVs discussed in the previous section, CD29 expression is highly correlated with breast cancer metastasis[99,346,358]. The higher expression of CD29 in L-MDA EVs corroborates the findings of Hoshino *et al.* (2015) that CD29 was highly expressed in lung metastatic

cancer-derived EVs[99]. This may suggest that L-MDA EVs have an advantage over B-MDA EVs in facilitating cell adhesion. Furthermore, major histocompatibility complex (MHC) class I and II (HLA-ABC and HLA-DRDPDQ, respectively) were highly represented in L- and B-MDA EVs, although more so in L-MDA EVs. MHC class I expression remained mostly unchanged in both subclones over seven weeks, while MHC class II in L-MDA EVs fluctuated but was downregulated overall after seven weeks and remained unchanged in B-MDA EVs. Low MHC-I expression on breast cancer cells is correlated with immune system evasion by cancer cells[359], while high MHC-II expression on breast cancer cells has been shown to present antigens to CD4+ T-cells causing antitumor activity[360]. This was interesting as high expression of MHC class II in EVs may have a counter-productive effect on the immunosuppressive and evasive nature of tumours and tumour microenvironments needed to support tumour growth and metastasis[361]. Therefore, its downregulation over seven weeks may indicate a transition towards ensuring immunosuppression over time. Overall, changes in MHC class I and II expression in EVs derived L- and B-MDA EVs at different time points may have distinct immunological properties, which could have consequences for tumour growth, survival, and metastasis.

Other highly expressed proteins in both subclones were ROR1, SSEA-1, CD44, TF and CD146. ROR1 is overexpressed in several cancer types, is associated with enhanced tumour survival and growth, poor prognosis, and has been identified as essential for the activity of EMT-regulating proteins in breast cancer cells[362,363]. Therefore, increased ROR1 expression over time in both EVs populations may indicate favourable disease progression in derived cells and favour disease progression in recipient cells. Stage-specific embryonic antigen-1 (SSEA-1) is important in recognition between cells and

adhesion processes and is commonly overexpressed in breast cancer. Furthermore, SSEA-1 is thought to have a crucial role in breast cancer metastasis, explaining the relatively high expression of this protein in EVs secreted by lung metastatic MDA-MB-231 cells[364]. Although interestingly, SSEA1 was downregulated in lung metastatic EVs over time (Figure 5.12). Furthermore, while the role of CD146 is debated, both high and low expression of CD146 is found to be a predictive marker for tumour progression[365,366]. Notably, CD146 was the most highly upregulated protein in L-MDA EVs, suggesting that L-MDA cells may be progressing into a new phase of growth over time. Finally, CD44 has been shown to cause an increase in tumorigenicity and cell migration capacity[367]. Altogether, over time L- and B-MDA EVs transitioned further towards a pro-oncogenic and pro-metastatic phenotype, and this data presents the heterogeneity between EVs harvested at different time points.

Overall, the proteins that saw the greatest fluctuations in their expression over seven weeks were among the most highly represented proteins, which may cause changes in the functions of these EVs over time. Conversely, the expression of most lower represented proteins was consistent with negative controls for both subclone EVs. CD24, CD49e, MCSP and CD40 were exceptions to this trend in both L-MDA and B-MDA EVs. These proteins fluctuated in their expression over seven weeks but underwent an increase in expression overall. For most of these proteins, high expressions have been detected in various cancers and cancer-derived EVs and are associated with cancer progression, increased metastatic potential and poor prognosis[55,297,368]. However, the opposite is true for CD40, where higher expression in cancers is associated with susceptibility to immunotherapies[369]. Together the change in protein expression further

suggested that over time L- and B-MDA EVs transitioned towards a pro-oncogenic and pro-metastatic phenotype.

Altogether, temporal variation in EV surfaces proteomes was observed. These temporal changes may have been caused by variability in the cellular proteome over time, as many cell membrane proteins are represented in the EV surface proteome[311,370]. Alternatively, changes seen in breast cancer-derived EVs over time could be due to shared environmental or epigenetic factors. In this case, over time, L- and B-MDA EVs transitioned towards a pro-oncogenic and pro-metastatic phenotype over time. Furthermore, variation in temporal protein expression changes between each independent subclone highlights a previously unscrutinised problem when growing EV producer cells over extended periods; EVs purified at one time point may have different protein expression profiles to EVs purified at another time point which may impact EV function or therapeutic efficacy. Whether these changes lead to functional differences is yet to be determined; however, this may be pertinent to further investigations. Future investigations should also employ techniques to study luminal proteins to understand whether changes in protein expression over time are also seen there.

5.4.3 Identification of heterogeneity in EV function

Previously, numerous studies have documented differences in function between EVs with different sizes, protein expression and biogenesis origins derived from the same parent cell population[49,54–58]. This presents that a variety of EVs, some of which are better at performing specific functions than others, are included within a secreted EV population. Identification and characterisation of functionally heterogenous EV populations may aid EV therapeutic development by providing information to selectively purify EVs with

greater efficacy to use as therapeutics. Furthermore, whether heterogeneity in EV function is linked to heterogeneity in EV producer cell populations is yet to be determined. To investigate these questions, EVs from subclonal populations of MSCs generated by single-cell sorting were assessed for functional heterogeneity in numerous *in vitro* assays. This was followed by characterisation to identify functional proteins responsible for functional differences, and marker proteins to identify these EVs. Preliminary assessments of cellular heterogeneity were also made to investigate the association between EVs and cellular heterogeneity.

Eleven MSC populations were identified from single-cell sorting experiments. Following the expansion of each MSC subclone culture, the effects of MSC-derived EVs on T cell proliferation were analysed by quantifying extracellular lactate, which is released by T cells in proportion with T cell proliferation[312]. High and variable lactate concentrations were recorded in response to conditioned medium derived from each MSC subclone (Figure 5.13) and later recorded in response to incubation with purified MSC subclone EVs (Figure 5.15). This initially suggested that every MSC subclone EV sample appeared to induce T cell proliferation to some degree. This was surprising, as the immunosuppressive effects of MSCs and MSC EVs have been extensively documented in the literature[371–373]. However, repetition of the assay and assessing the lactate content of EV preparations alone identified the source of differential lactate as the EVs themselves rather than T cell proliferation (Figure 5.16). As MSCs have been shown to produce lactate to promote the polarisation of macrophages from a pro-inflammatory phenotype to an anti-inflammatory phenotype[374], lactate may be packaged into EVs. These high concentrations of lactate associated with EVs would likely have interfered with the assessment of EV-mediated immunosuppression using activated T cells in the same

assay. Therefore if this investigation were repeated, a new method of measuring T cell proliferation may be necessary. Additionally, differential lactate concentrations alone may suggest that MSC subclone EVs may have differential effects on macrophage immunosuppression[374].

MSC subclone-derived EVs were also assessed in numerous other assays. Firstly, research has shown that MSCs and MSC EVs have regenerative properties, and both have been used to aid wound closure both *in vitro* and *in vivo*[131,375–377]; thus, MSC subclone EVs were investigated for differential effects on cell migration *in vitro*. MSC subclone EVs evoked marked differences in cell migration, particularly among endothelial cells (Figure 5.17). In both MSC and HMEC-1 monolayers, subclones B10, E5, and G4 evoked faster wound closure than subclones B4, C3, and G4, presenting functional heterogeneity despite the subclonal nature of their parent cell lines. The difference in efficacy highlighted the importance of identifying EV heterogeneity during EV therapeutic development, as subpopulations of EVs may have lower efficacy or antagonistic effects on recipient cells, thus lowering overall efficacy of an EV therapy. While differences were observed, no statistically significant differences were detected, likely due to variability among biological repeats. Variability often arises in migration assays due to uneven wounds in cell monolayers, remnant cells following scratch wound application or damage to the tissue culture plastic[378]. Despite use of the Woundmaker 96 to provide uniformity in scratches, variability was still observed. Therefore, future analysis should attempt further biological repeats to produce concordant results.

Other studies have investigated heterogeneity in cell migration elicited by EV subpopulations. Hosseinkhani *et al.* (2020) reported that EVs isolated by 110,000 x *g*

ultracentrifugation compared to 10,000 x *g* evoked greater monocyte migration, and enhanced migration was seen among intercellular adhesion molecule 1-positive EVs[54]. Additionally, Shen *et al.* (2021) reported greater cell migration evoked by EVs derived from ovarian cancer cells with high metastatic potential as opposed to low metastatic potential, which was attributed to higher CD44 expression[379]. Similarities were seen in this investigation, as proteomics data revealed high expression of CD44 in MSC subclone EVs (Figure 5.23), although CD44 expression in MSC subclone EVs was not significantly positively correlated with cell migration (Figure 5.29). Enhanced cell migration has also been reported in response to MSC EVs enriched in chemotactic factors and growth factors such as fibroblast growth factor (FGF) and vascular endothelial growth factor (VEGF)[56,380]. Comparatively, growth factor expression was not detected in MSC subclone EVs and no growth factors known to be associated with cell migration were identified by GOBP annotation. YWHAE, PDGFR and HSPB1 were the only identified proteins involved in various growth factor signalling pathways [381–383], but these were not particularly highly expressed nor significantly positively correlated with cell migration activity (Figure 5.29). Elsewhere, correlation analysis revealed a positive correlation between cell migration activity and calmodulin 2/3 (CALM2/3), which modulates the activities of numerous physiological processes, including cell motility, cytoskeleton architecture and function, and cell proliferation, and has previously shown to significantly increase cell migration in wound healing assays[384,385]. PPIA expression in EVs was also significantly positively correlated with cell migration activity. PPIA is normally associated with leukocyte migration, although knockdown of PPIA has been shown to significantly impact wound healing and migration[386]. Alternatively, PPIA may be upregulated due to its pro-inflammatory activation of endothelial cells, which may have been induced following wound application[332]. ANXA2 was identified by GOBP annotation as involved in cell

migration and was the most highly expressed of all positively correlated proteins in MSC subclone EVs. This was interesting because ANXA2 expression in EVs and cells has been shown to significantly increase cell migration and wound healing[57,387], and because ANXA2 has been shown to increase internalisation of ITGB1 expressed on the cell surface during wound healing, enabling forward cell movement[387]. Therefore, this may explain the significant negative correlation between ITGB1 expression on MSC subclone EVs and cell migration. Altogether MSC subclone-derived EVs presented functional heterogeneity in cell migration assays. Differences in protein expression among EV subclones provided a possible explanation for the observed differences in EV function, particularly in cases where differences in function were significantly correlated with protein expression, such as for PPIA and ANXA2.

The facilitation of MSC cell adhesion by MSC subclone-derived EVs was also investigated to explore EV functional heterogeneity. Functional assessment and proteomic profiling of MSC EVs have previously shown that MSC-derived EVs are abundant in cell adhesion proteins and aid adhesion of MSCs to inert surfaces[388,389]. Notable differences in MSC cell adhesion were observed in 96-well plate wells coated with different MSC subclone EVs (Figure 5.18). However, in contrast to cell migration assays, different MSC subclones evoked cell adhesion to those that evoked cell migration. Subclones B4, B10, and F7 caused the greatest cell adhesion with significant differences between EVs derived from the parental wild-type (WT) MSC cells and MSC subclones B10 and F7, respectively. (Figure 5.18B). This provided further questions regarding what determines the differential functions of subclonal EV populations, as some MSC subclone-derived EVs highly affected both cell migration and cell adhesion (B10), some highly affected either cell migration (E5, G4) or cell adhesion (B4, F7), and

some affected neither (C3). Cell adhesion evoked by WT MSC EVs was roughly average that of the other subclones in both assays, which may suggest that EVs in the WT sample include EVs with the same phenotype as subclone-derived EVs due to the clonality of each of the cell lines. This may also necessitate identifying functional heterogeneity within EV populations to improve efficacy when developing EV therapeutics.

Similar to cell migration assays, numerous studies have demonstrated heterogeneity in EV-mediated cell adhesion by different EV populations based on size, cell line and protein expression[51,100,313,390,391]. In this study, GOBP cell adhesion annotation of proteomics data identified numerous extracellular matrix proteins, including collagen, laminin, and fibronectin (Figure 5.24). However, none of these proteins were significantly positively correlated with cell adhesion (Figure 5.30), suggesting that they were not responsible for the differences in cell adhesion observed. Additionally, the significant positive correlation of the EV-associated proteins annexin A1 (ANXA1) and EH-domain containing 2 (EHD) suggested that enhanced cell adhesion was associated with EVs and not a factor co-isolated with EVs[18]. More specifically, enhanced cell adhesion may be due to an abundance of microvesicles in some subclonal EV populations, as annexin A1 has been suggested as a marker of microvesicles[392]. Integrins have previously been shown to play a prominent in EV-mediated cell adhesion[99,352,353], although the only integrin common to MSC EV subclone populations was ITGB1, and its expression was not significantly positively correlated with elicited cell adhesion. Similarly, CD44, CAV1 and CD63 were all highly expressed among all MSC subclone EV populations and have previously shown to be involved in EV-mediated cell adhesion[58,390,393,394], although none of these proteins were shown to be significantly positively correlated with cell adhesion activity either. The only cell adhesion protein expressed in MSC subclone EVs identified by GOBP

annotation significantly positively correlated with cell adhesion was Rho GDP-dissociation inhibitor 1 (ARHGDIA). This was surprising as ARHGDIA is a negative regulator cell adhesion[395]. GOBP also annotated haemoglobin subunit β (HBB) as a cell adhesion protein, the expression of which was significantly negatively correlated with cell adhesion activity. However, the reason for its identification as a cell adhesion protein is linked to increased cell adhesion seen in sickle cell disease[396]. Altogether, while no proteins that positively impacted cell adhesion were positively correlated with cell adhesion elicited by MSC subclone EVs, the expression of ANXA1 and EHD2 suggested differences in cell adhesion were directly associated with EVs. Future investigation should further scrutinise the expression of cell adhesion proteins in MSC subclone EVs to identify a possible cause for the differences in cell adhesion observed.

The final functional assay used to assess functional differences between MSC subclone-derived EVs was the DPP4 activity assays (Figure 5.19B). Once again, heterogeneity between MSC subclone-derived EVs was seen from different MSC subclone EVs than observed in cell migration and cell adhesion assays. Subclones B4, C3, and F7 presented highly significant increases in DPP4 activity over the activity of WT MSC EVs, further provoking questions regarding what determines the functions of subpopulations. Like cell adhesion assays, DPP4 activity evoked by WT MSC EVs also seemed to be average that of the other subclones, further suggesting that the WT EV population included EVs with the same phenotype as in each subclone population due to the clonality of each of the cell lines. Heterogenous DPP4 activity has previously been observed in placental EVs from patients with and without gestational diabetes[321] and EVs derived from different leukaemia cell lines[322]. However, this is the first instance where heterogenous DPP4 activity has been observed in EVs derived from subclonal cells. As expected, DPP4

activity in MSC subclone EVs was positively correlated with its expression in proteomics analysis (Figure 5.31). Numerous EV membrane markers were also positively correlated, including HSPA1B/A, CD59, CD81 and ANXA2[18], providing strong evidence that DPP4 activity was directly associated with EVs. Aside from DPP4 itself, no other positively or negatively correlated proteins were directly associated with DPP4 activity. However, CD59, which also bared a positive correlation, is involved in signal transduction for T cell activation, which DPP4 also play a role in[397,398].

The DPP4 activity assay was repeated using MSC subclone cells to investigate whether the differences in DPP4 activity elicited by the MSC subclone EVs could be linked to differences in DPP4 activity in their parent cell line. As seen in Figure 5.19E, heterogeneous DPP4 activity was observed, although this did not mirror the DPP4 activity observed in EVs, and correlation analysis between the EV and cell-based assays confirmed this, revealing no correlation between the two datasets (Figure 5.19F). This presents that the heterogeneity in MSC subclone EVs may not be linked to heterogeneity in parent cell phenotypes. Historically, the function and content of EVs have been viewed as dependent on the function and content of parental cells[399]. However, in recent years, numerous studies have identified subpopulations of EVs with varying functionalities and proteomes originating from the same cell type[48–50,400,401]. Moreover, single vesicle analysis studies have identified EV populations with distinct protein, phospholipid and cholesterol markers and presented that EV characteristics and function may be influenced by other factors such as cellular physiological state[213,402,403]. Along with differential DPP4 activity in this study, cell phenotype is not the sole arbiter of EV function and phenotype. These observations were reaffirmed in western blot analysis of highly expressed cell adhesion and cell migration proteins, where little to no associations between EV and cell protein

expression were seen (Figure 5.27). However, further scrutinising cellular function and characteristics using more sensitive techniques such as flow cytometry or even proteomics to compare to the EV proteomics shown here is necessary to confirm these observations.

Aside from assessments of functional heterogeneity between MSC EVs, proteomics data displayed further heterogeneity in EV protein expression. Principle component analysis (Figure 5.20) revealed that protein expression in MSC EV populations was distinctly distributed. The only EV populations that were closely clustered with one another were subclones E5 and G4. This was interesting as both EV subclones had shown similar activity levels in every *in vitro* assay, including high function in migration assays, no influence on MSC cell adhesion, and low DPP4 activity. This may suggest that irrespective of correlation analyses, similarities between E5 and G4 EV proteomes may provide insights into the proteins responsible for the functions they elicit. Observing proteins involved in wound healing and cell migration (Figure 5.23), keratin 1 (KRT1), CAV1, ITGB1 and syntenin-1 (SDCBP) were all upregulated in E5 and G4 EVs. Aside from KRT1, EVs that have shown enhanced effects on cell migration have previously presented high expression of these proteins on their surface[58,313,344]. In contrast, differences in protein expression between MSC EV subclones were difficult to identify in volcano plots (Figure 5.21). Surmised sample losses during protein extraction and sample preparation resulted in the number of identified proteins common to all samples being far lower than expected. This may also have caused the number of proteins identified as significantly different from their expression in the WT MSC EVs to be very low[404].

PANTHER protein class analysis further highlighted the heterogeneity of MSC subclone-derived EVs and suggested various other functions that MSC EVs could influence and be tested to further evidence of functional heterogeneity between MSC subclone EVs. Chaperonins were the most highly upregulated protein class, particularly in subclone C3 and E5 EVs. Previous studies have shown chaperonin containing TCP1 subunit 2 (CCT2) to be highly upregulated in MSC-derived EVs and involved in the downregulation of CD154 expression in recipient T cells to prevent their activation[405], further highlighting the role of MSC-derived EVs in immunomodulation. Differential representation of the chaperonin protein class suggests that C3 and E5 EVs may be better at suppressing immune responses than other EVs. Among the most underrepresented protein across all MSC subclones were protein classes associated with nucleic acid transcription and binding, including gene-specific transcriptional regulators, DNA-binding transcription factors, chromatin/chromatin-binding or -regulatory proteins (also including histone proteins), helix-turn-helix transcription factors and homeodomain transcription factors. This suggested that EVs were not involved in the transfer of proteins involved with DNA handling, recognition, or utilisation and do not influence the regulation of protein expression at a genomic level[406,407]. Elsewhere, integrins were overrepresented in subclones B10, C3, F7, and G4, despite only ITGB1 being the only integrin common to all EVs and identified as involved in cell adhesion by GOBP annotation. This is likely due to filtering the data in previous analyses to remove proteins that were not common to all EV subclones. However, overrepresentation of the integrin protein class did not seem to correlate with MSC subclone EVs that significantly affected cell adhesion, further suggesting that different cell adhesion proteins may be responsible for their function. Otherwise, differential representation of various enzymes was observed among EV subclones, including protease inhibitors and proteases, dehydrogenases, peroxidases,

and reductases, suggesting differential enzymatic and metabolic activity of MSC subclone EVs.

5.5 Limitation, future work, and conclusions

5.5.1 Limitations

The lack of biological repeats for SKOV3 EV subpopulations proteomics is a limitation of the data presented in this chapter. While the implementation of technical replicates accounted for error in the implementations of proteomics protocols, if proteomics analysis were to be repeated, these experiments would benefit from biological replicates to ensure that differences in protein expression were not artefacts or affected by temporal variation as observed in MDA subclones in this chapter[404]. Biological repeats should also be implemented in MSC subclone NFC experiments seen later in section 5.3.8. Conversely, while three biological replicates were implemented in MSC subclone proteomics, only one technical replicate was used for each. As previously discussed, sample loss and pre-processing errors were surmised to cause a low number of proteins detected in MSC proteomics and high variation between biological replicates. Repetition of this analysis would be beneficial with the addition of technical replicates to reduce the variation.

Elsewhere, some *in vitro* functional assays lacked certain controls, including missing positive controls in MSC cell migration assays and positive controls in cell adhesion assay. This created a lack of scale and points of reference to understand the extent that MSC subclone-derived EVs influenced functional activity. Without positive controls, determining how strongly MSC subclone EVs facilitated cell migration or adhesion was

more difficult. If these assays were repeated, a positive control of complete culture medium should be implemented in MSC cell migration assays to match the positive controls in HMEC-1 migration assays, and coating assay wells with attachment factors such as collagen or fibronectin could serve as a positive control in cell adhesion assays[408]. Additionally, while established protocols were followed for cell migration and cell adhesion assays, dose-response assays were not performed to identify the most appropriate EV concentration at which to perform the assays to observe maximal functional differences.

5.5.2 Future work

Differences in cell adhesion were detected between size-based EV populations. However, unlike Willms (2018), the cell adhesion assay in section 5.3.7.2 did not assess the involvement of CD29 in EV-mediated cell adhesion.[51]. Subsequent investigations should block or knockout CD29 expression in EVs to determine whether the effects observed by Willms (2018) can be replicated. Furthermore, other highly expressed cell adhesion proteins identified in proteomics data could be blocked or knocked out to observe whether this also affects EV-mediated cell adhesion. Similarly, inhibition of proteins involved in EV biogenesis may provide insights into the origins of different size-based EV subpopulations.

Moreover, further functional assessments could be performed to determine whether SKOV3 EV subpopulations differentially affect other oncogenic processes such as angiogenesis or immunomodulation[92,94,95]. This may inform anti-cancer therapeutic strategies by developing therapies targeting pro-oncogenic EV subpopulations. Alternatively, the proteomics data could identify additional functional assays to link

differences in protein expression to other functions and further understand the impact of EV heterogeneity. For example, various metabolic activity assays could be explored due to differential expression of various metabolic protein classes identified by PANTHER protein class.

Additionally, further analysis of the small particles identified in pool 4 should be performed to confirm whether their identity is synonymous with exomeres[50], and may aid understanding of exomere proteome and function. Future work should also determine the extent of heterogeneity in size-based EVs derived from clinically relevant cell lines such as MSCs, which could help advance EV therapeutic development.

As for temporal EV heterogeneity experiments, further investigations should investigate how changes in cell culture environmental factors such as temperature, pH, nutrients, or other epigenetic factors affect EV protein expression over time. This may aid understanding of why changes in EV proteomes are observed over time. Furthermore, investigating whether changes in protein expression are translated into changes in functional effects of EVs may provide valuable insights into EV therapeutic development protocols regarding the conditions and how long EVs are harvested from cells. Analysis of changes in luminal protein expression will also provide insights into whether EV cargoes are affected over time. Finally, other cell lines should also be investigated to determine whether changes in expression may be due to the genomic instability of the cancer cell line[409].

Furthermore, numerous cell migration and cell adhesion proteins, including ANXA2, PPIA and ANXA1, were correlated with functional heterogeneity in MSC subclone EVs. Future

work should determine whether these proteins are, in fact, actively involved in these functions on EVs. This can be achieved by antibody blockade of proteins or inhibiting expression using siRNA. Additionally, future experiments should investigate whether EVs with the same functional activity can be selectively purified from parent cell MSC EV populations using proteins identified as positively correlated with subclone activity. If successful, this may influence EV therapeutic development strategy due to the possibility of selectively isolating functionally advantageous EVs, which can improve EV therapeutic efficacy. Similarly, MSC EV subclones that produce therapeutically advantageous EVs could also be grown and utilised for further EV production and therapeutic development.

Finally, further analysis is necessary to determine whether heterogeneity in subclonal EV populations is linked to heterogeneity of parent cell lines. As no association between cellular and EV activity or protein expression was seen in this study, proteomics analysis should also be performed on MSC subclone cells and analysis of similarities and differences between EV and cellular protein expression should be determined. In addition, assays for determining functional heterogeneity in both cells and EV should be sought.

5.5.3 Conclusions

Identifying EV heterogeneity and understanding the mechanisms that cause or control it is essential in determining EV effects on recipient cells and developing EV therapeutics. This chapter has linked numerous factors to EV heterogeneity, including EV size and temporal changes in protein expression. Additionally, functional heterogeneity among EVs derived from subclonal cell populations has been demonstrated, suggesting that

differences between cells in an assumed clonal population may give rise to EV heterogeneity.

SKOV3 EV subpopulations with significantly different sizes evoked significant differences in SKOV3 cell adhesion *in vitro*. Proteomics analysis revealed notable differences in protein expression, including cell adhesion proteins and integrins that presented similarities in expression to the cell adhesion functions elicited. Differences in functional protein classes suggested other functions of different size-based subpopulation EVs and identified proteins synonymous with an emerging class of EVs termed exomeres.

Temporal changes in EV protein expression were also observed over time. In addition, different proteins changed expression in two different subclonal MDA cell lines. However, changes in expression were conserved among biological repeats suggesting that changes in EV proteomes may be due to a common epigenetic or environmental influence or may be directed.

Lastly, heterogeneity in various functions was demonstrated among subclonal MSC-derived EVs. Furthermore, proteomics analysis demonstrated the protein expression of these EVs to be notably different from one another. Correlation analysis between the functions of MSC subclone EVs identified numerous proteins that were significantly correlated with differences in function, including ANXA2 and PPIA in migration, ANXA1 in adhesion and DPP4 itself in DPP4 activity assay, as well as numerous other correlations that could serve as potential markers of these functional EVs in other EV populations. Moreover, preliminary evidence presented in DPP4 assays and via western blotting analysis suggested heterogeneity in EV function and protein expression was not

linked to heterogeneity in the cellular proteome. Altogether, the data shown here highlights the existence of functional heterogeneity in EV populations and the potential benefits of its identification to improve EV efficacy.

5.6 Supplementary Figures

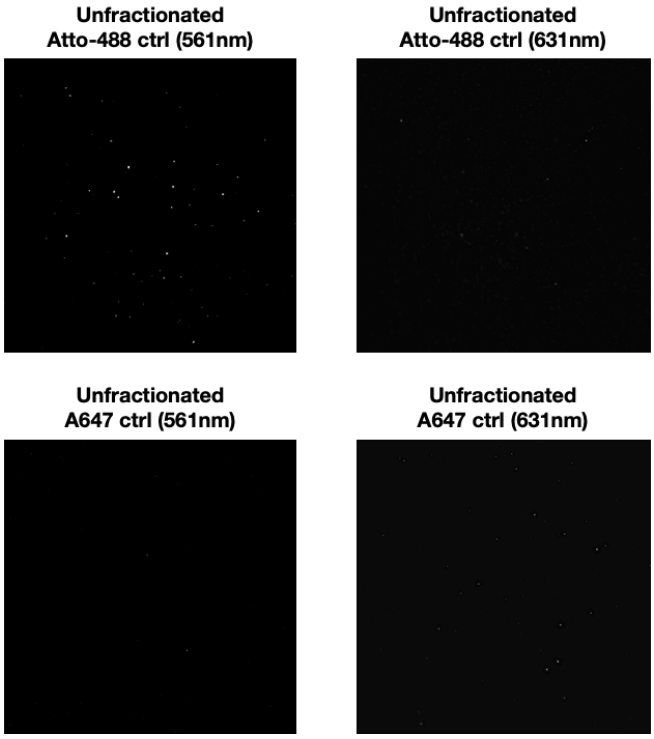

Supplementary Figure S5.1 Representative control SIM images of SKOV3 subpopulation EVs. EVs incubated with donkey anti-rabbit IgG Alexa Fluor® 647 and donkey anti-mouse IgG Atto-488 to check for non-specific binding. EVs incubated for one hour at room temperature and purified from excesses by SEC. Images were taken in both channels to check for bleed-through of fluorescent signal into either channel. Minimal fluorescent signal can be seen in the 561 nm channel for Atto-488 and 631 nm channel for Alexa647.

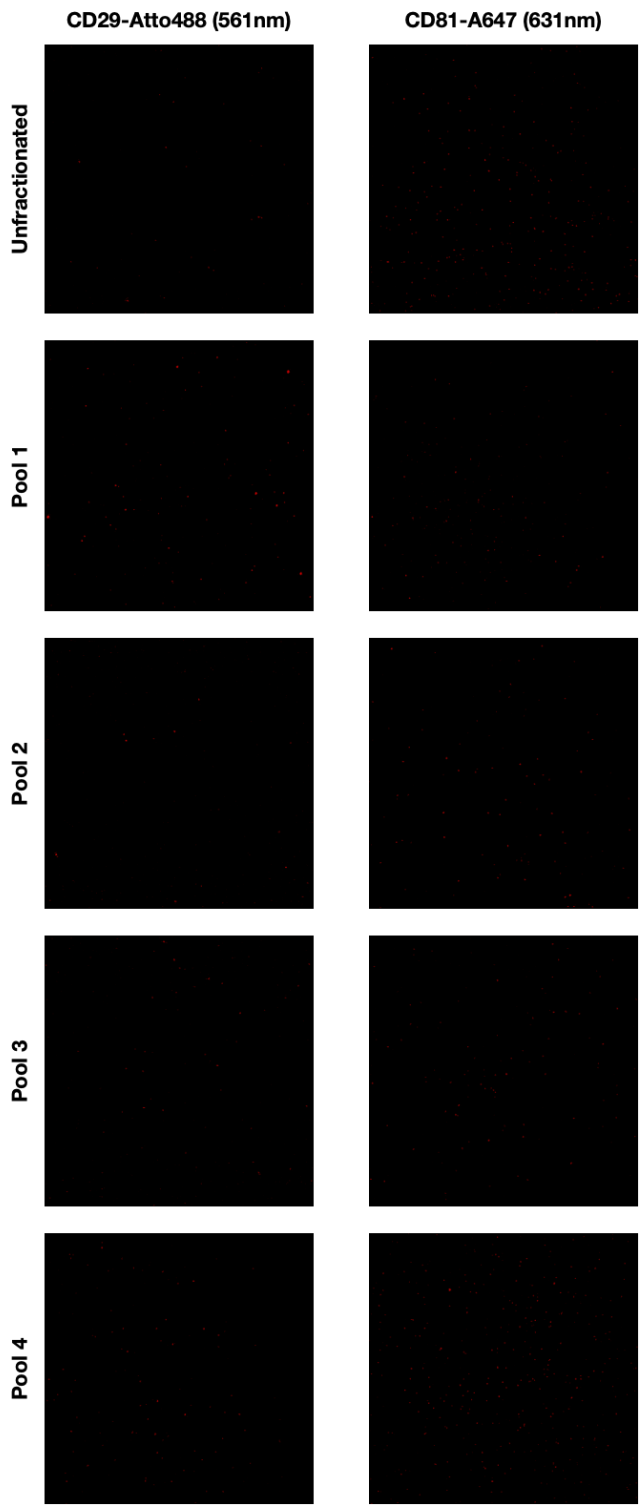

Supplementary Figure S5.2 Representative SIM CD29-CD81 colocalization images of SKOV3 subpopulation EVs. EVs incubated with mouse anti-CD29 with donkey anti-

mouse IgG Atto-488, and rabbit anti-CD81 with donkey anti-rabbit IgG Alexa Fluor® 647 for one hour at room temperature and purified from excesses by SEC.

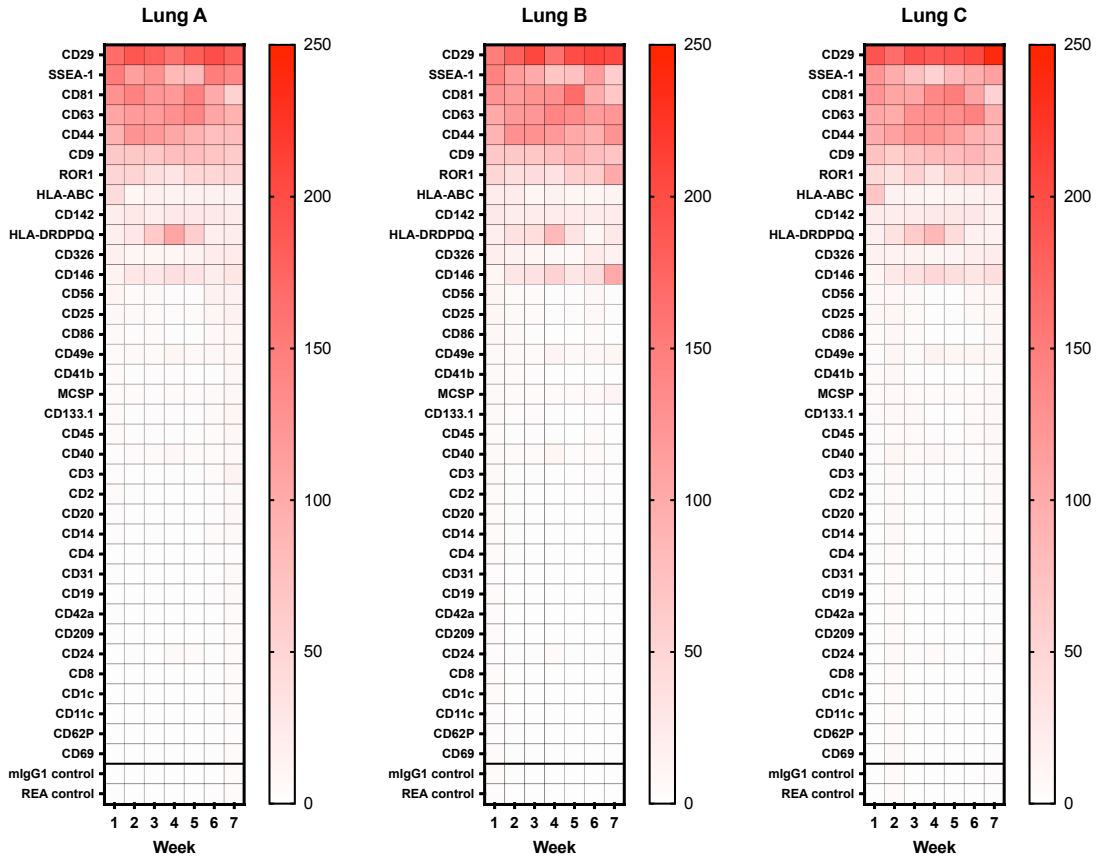

Supplementary Figure S5.3 MACSPlex analysis of EV surface proteins from each independent lung metastatic MDA culture. Variation can be seen on a week-by-week basis among highly expressed proteins. Red denotes high expression while white denotes low expression. Mean, background corrected data expressed as a factor of 1000 for protein expression each week.

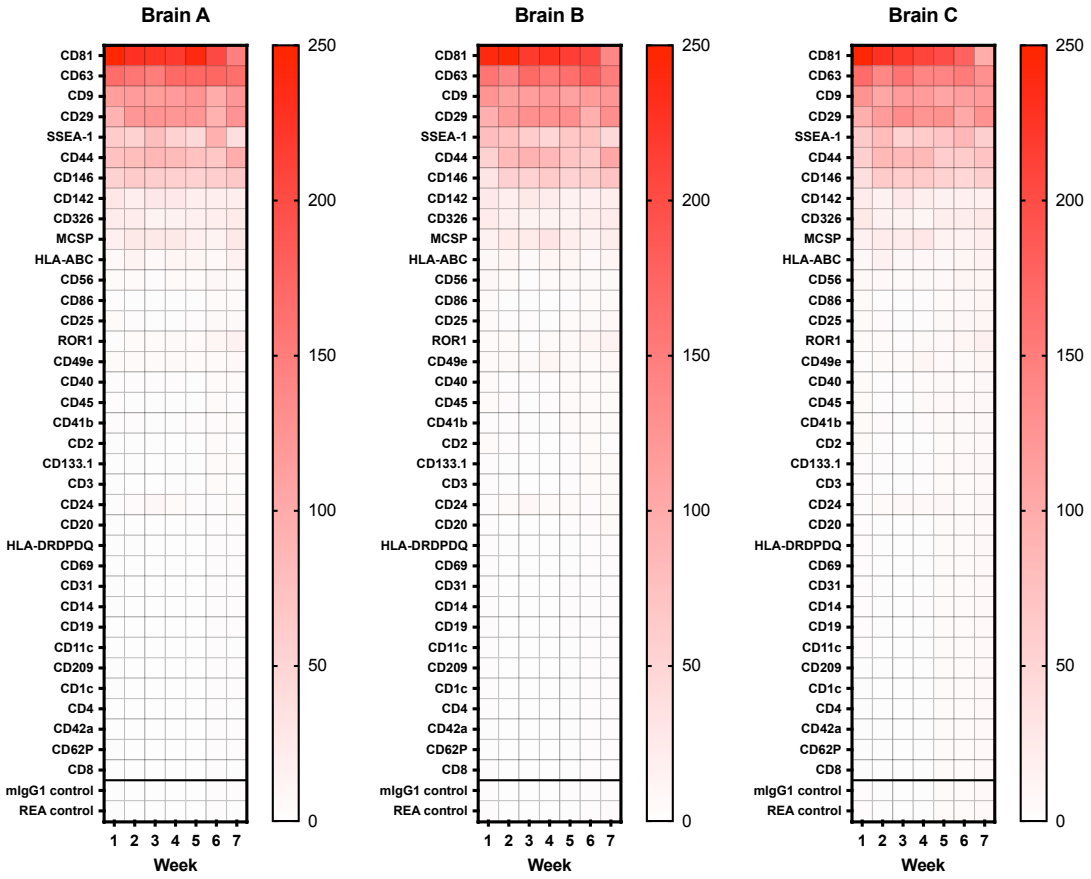

Supplementary Figure S5.4 MACSPlex analysis of EV surface proteins from each independent brain metastatic MDA culture. Variation can be seen on a week-by-week basis among highly expressed proteins. Red denotes high expression while white denotes low expression. Background corrected data expressed as a factor of 1000 for protein expression each week.

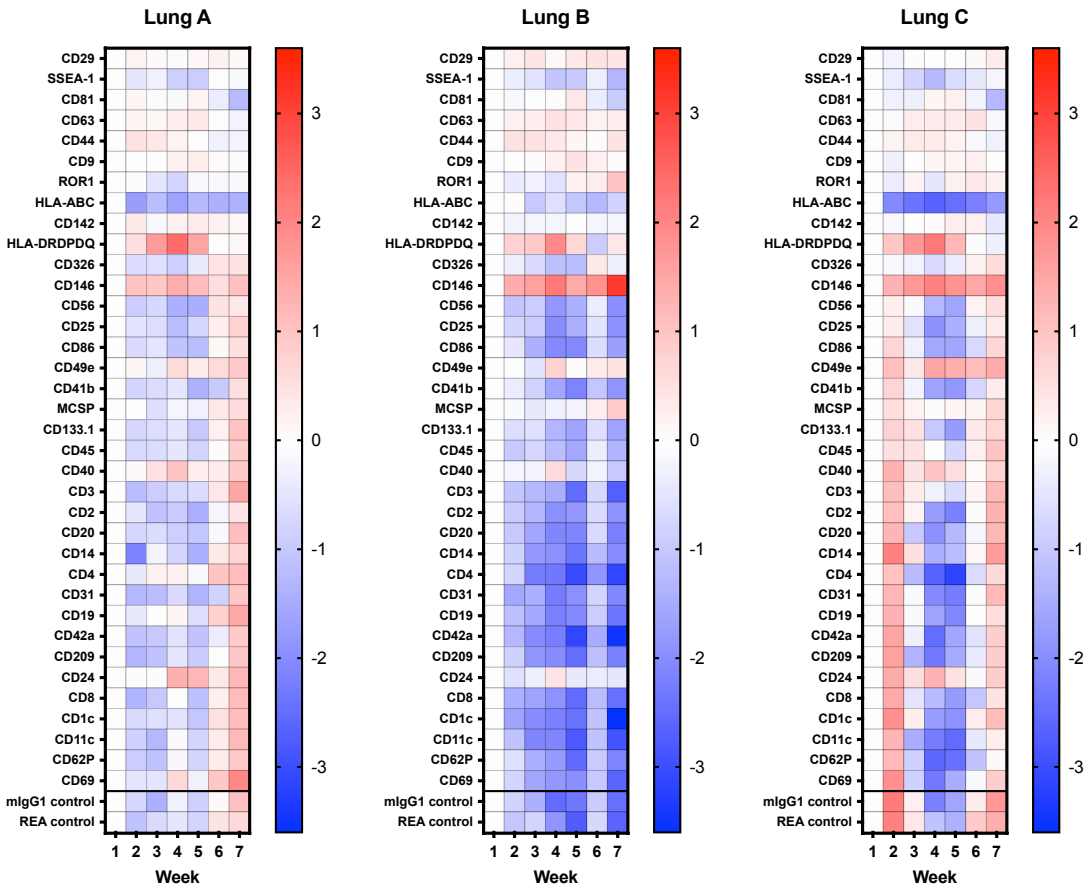

Supplementary Figure S5.5 Temporal variation of EV surface proteins from each independent lung metastatic MDA culture as shown by MACSPlex analysis. Blank corrected and scaled data normalised to respective expression in week one and expressed on a Log2 scale. Red denotes an increase in expression versus week, white indicates no change and blue indicates a decrease in expression.

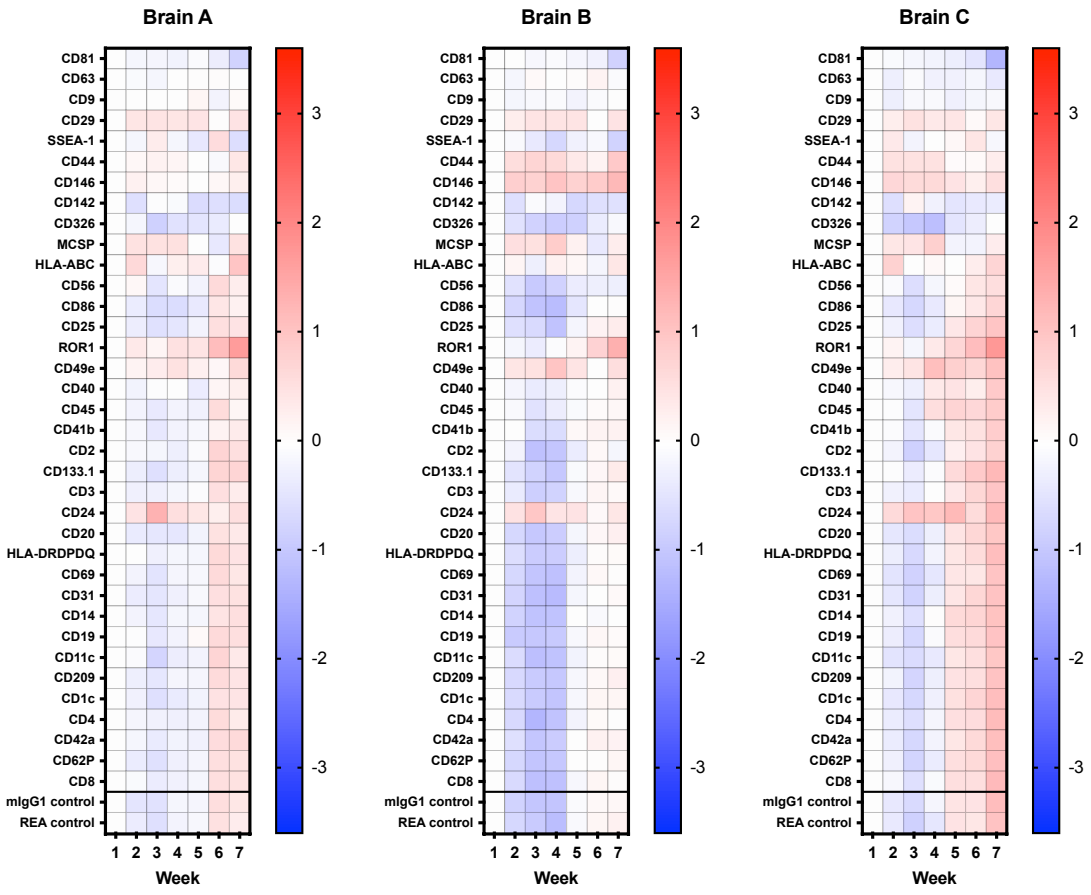

Supplementary Figure S5.6 Temporal variation of EV surface proteins from each independent brain metastatic MDA culture as shown by MACSPlex analysis. Blank corrected and scaled data normalised to respective expression in week one and expressed on a Log2 scale. Red denotes an increase in expression versus week, white indicates no change and blue indicates a decrease in expression.

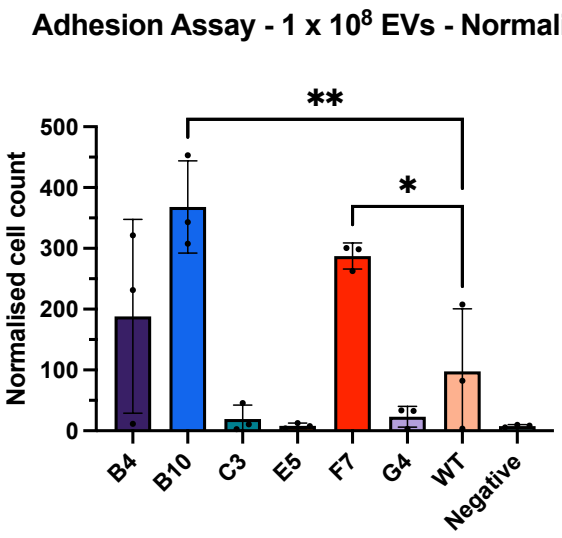

Supplementary Figure S5.7 MSC subclone cell adhesion assay coating with 1 x 10^8 EVs as opposed to 1 µg. Images analysed using FiJi – Analyze Particles. Raw results of each n-number were averaged and summed. Individual averages were divided by the sum and multiplied by 1000 to relativise results. One-way ANOVA with Tukey's multiple comparisons versus the wild type (WT) sample where significance is indicated by $P < 0.05$ (* = $P < 0.05$, ** = $P < 0.01$). Values are mean relativised values ±SD; n=3.

6.0 Discussion and conclusion

6.1 Summary of main findings

In this DPhil thesis, numerous technical challenges faced within the extracellular vesicles research space were addressed, including the limitations of methods currently used to assess EV biodistribution, the lack of suitable methods to purify EVs from high cell density cultures, and the existence of functional heterogeneity within EV populations.

Chapter 1 outlined the fundamentals of EVs, including their different biogenesis methods, their importance in intercellular communication, functions in healthy physiology and pathophysiological conditions, and the development of EVs as targeted therapeutic devices. Various problems facing the field of EV research were outlined, although these were more extensively introduced and addressed in subsequent chapters.

In chapter 3, current methods of EV biodistribution were outlined, including various fluorescent and bioluminescent labelling techniques, radiolabelling techniques, and imaging techniques. Each method presented pros and cons, though almost all suffered from sensitivity and specificity issues that warranted the development of a technique to overcome these limitations. Therefore, EV DNA barcoding was proposed and explored. However, while steps were made to optimise EV DNA barcoding, many challenges were faced, including low labelling efficiency, low EV yields and high background contamination. Furthermore, an assessment of labelling efficiency of NHS-functionalised DNA capture probes and complementary fluorescent barcodes by NFC revealed that at most, only 27.1% of particles in EV samples were successfully labelled, suggesting NHS is an inefficient method of labelling EV populations, synonymous with findings seen

elsewhere[141]. Altogether, further development is necessary to use EV DNA barcoding for EV labelling and biodistribution analysis, although the toolset showed promise after being repurposed for EV-mediated siRNA delivery *in vitro*.

In chapter 4, various methods of EV purification were introduced, along with the numerous applications, pros, and cons of each. Among all these methods, scalability was a significant issue which presented problems for the purification of EVs from preparations with high contaminant concentrations, such as those derived from high cell density bioreactor cultures. HiScreen Capto Core 700 kDa (CC700) binding chromatography was proposed as a novel solution to this problem due to the high contaminant binding capacity of CC700 resin. While CC700 had previously begun to be explored for EV purification from low cell density cultures[256,270,273,274,410], in this chapter, the use of binding chromatography to SEC for purification of EVs from high cell density cultures was compared. Results demonstrated significant differences in purity of EVs from free protein between SEC and CC700, although high levels of DNA and RNA remained in solution, which could have implications for the therapeutic use of CC700 purified EVs. Therefore, benzonase treatment and Capto Q anion exchange were explored to remove DNA and RNA. Capto Q showed excellent potential to remove DNA and RNA, although at the expense of particle yield. Later, in chapter 5, CC700 purified EVs in functional assays presented that the functionalities of EVs purified by CC700 are preserved. Overall, the superior purity of EVs purified by CC700 versus SEC presented CC700 as a new gold standard of EV purification and a viable tool for EV purification from high-density culture, though further work may be necessary to reduce DNA and RNA levels further while preserving EV yield.

Finally, in chapter 5, the extent of EV heterogeneity within EV populations associated with EV size and composition was introduced, along with the impact that this heterogeneity may have on EV function. Investigations to further characterise the association between EV size and both characteristic and functional heterogeneity were performed, as well as an investigation into temporal variation of protein expression in EV populations. Functional heterogeneity was observed among EVs derived from different size-based subpopulations, and these differences were linked to variations in integrin and cell adhesion protein expression in EV proteomes. Additionally, temporal heterogeneity was observed among EVs derived from subclonal breast cancer cell lines evoking further considerations for EV therapeutic development. Finally, following analysis of EVs derived from subclonal MSC populations, significant differences in EV function were identified in cell migration, cell adhesion and DPP4 activity assays. Once again, following proteomics analysis, these differences showed significant correlations to changes in expression of functional proteins such as ANXA2 and PPIA in migration assays, ANXA1 in adhesion assays and DPP4 itself in DPP4 activity assays. These results suggested that heterogeneity in EV populations was linked to heterogeneity in single-cell precursors of subclonal MSC populations and that heterogeneity between single cells in a larger population could be a source of EV heterogeneity. Altogether, prominent functional heterogeneity in EV populations associated with various factors has been extensively shown. Therefore, harnessing and attempting to mitigate the effects of EV heterogeneity is an important factor to consider in developing EV therapeutics. Moreover, selective purification of EV populations, such as those that express proteins significantly correlated with EV function, may provide novel avenues for improving EV therapeutic efficacy.

6.2 Future impact of findings

Overall, as the development of the therapeutic EV platform continues to grow, EV heterogeneity is a critical factor to understand and address if EV therapeutic efficacy is to be maximised[154]. The data and methods presented within this thesis offer an important addition to EV heterogeneity research by identifying factors associated with EV heterogeneity, establishing the functional impact of EV heterogeneity, and presenting the potential to harness EV heterogeneity to improve their therapeutic efficacy.

The EV purification and biodistribution tools explored in this thesis may enhance EV heterogeneity and therapeutic research. With further development, such as by implementing RCA as suggested in section 3.5.2, EV DNA barcoding could help ascertain heterogeneous EV activity *in vivo*. Identification of differential biodistribution, uptake and circulation half-life of EVs from different cell sources such as the MSC subclones utilised in chapter 5 or different EV subpopulations will enable the selection of a more efficacious EV population for therapeutic use. Furthermore, decorations of EV subpopulations with different barcodes and pooling labelled subpopulations into the same sample for administration could enable simultaneous detection of differences in the aforementioned factors. Elsewhere, CC700 represents an advancement in EV purification that is necessary to purify high, therapeutically appropriate EV concentrations. However, the precise amount of EVs needed for an EV therapy to be active *in vivo* remains unclear[156]. A combination of high EV concentrations achieved by CC700 with EV DNA barcoding offers the ability to investigate appropriate EV dosages.

Identifying functional heterogeneity within size-based and subclonal EV populations in this thesis highlights an important consideration for future EV therapeutic development

strategies. Determining and mitigating the presence of EV subpopulations within therapeutic EV populations that may hamper therapeutic efficacy will be as beneficial to maximising therapeutic efficacy as identifying and utilising therapeutically active EV subpopulations. Similarly, while differences in activity were detected between subclonal populations of MSC EVs, heterogeneity within subclonal EV populations should also be investigated. Altogether, future studies that implement the same methodologies described in this thesis for identifying subclonal cell populations that produce therapeutically beneficial EVs, followed by determining heterogeneity within EV populations, such as by size separation, offer a strategy to maximise the therapeutic potential of EVs. Additionally, the therapeutic potential of subclonal cell populations could also be investigated.

6.3 Concluding remarks

Over the last few decades, an abundance of evidence has demonstrated the importance of EVs in intercellular communication and their potential for targeted therapeutic delivery. However, EV heterogeneity presents a substantial challenge to EV therapeutic development. In this thesis, the impact of EV heterogeneity on their function was demonstrated among size-based and subclonal EV populations. Characterisation of functionally heterogeneous EV populations identified proteins that correlated with differences in EV function and may aid selective purification of functionally advantageous EV populations for future therapeutic EV development. Novel EV biodistribution and purification techniques explored in this thesis may also aid advancements in EV heterogeneity and therapeutic EV development studies. Overall, advancing understanding of EV heterogeneity and addressing the challenges associated with EV research is essential to ensure successful EV therapeutic development.

7.0 References

1. Schorey, J. S., Cheng, Y., Singh, P. P. & Smith, V. L. Exosomes and other extracellular vesicles in host-pathogen interactions. *EMBO Rep* **16**, 24–43 (2015).
2. Deatherage, B. L. & Cookson, B. T. Membrane vesicle release in bacteria, eukaryotes, and archaea: a conserved yet underappreciated aspect of microbial life. *Infect Immun* **80**, 1948–57 (2012).
3. Robinson, D. G., Ding, Y. & Jiang, L. Unconventional protein secretion in plants: a critical assessment. *Protoplasma* **253**, 31–43 (2016).
4. Witwer, K. W. *et al.* Standardization of sample collection, isolation and analysis methods in extracellular vesicle research. *J Extracell Vesicles* **2**, 20360 (2013).
5. Parolini, I. *et al.* Microenvironmental pH is a key factor for exosome traffic in tumor cells. *Journal of Biological Chemistry* **284**, 34211–34222 (2009).
6. Mittelbrunn, M. *et al.* Unidirectional transfer of microRNA-loaded exosomes from T cells to antigen-presenting cells. *Nat Commun* **2**, 1–10 (2011).
7. Kucharzewska, P. & Belting, M. Emerging roles of extracellular vesicles in the adaptive response of tumour cells to microenvironmental stress. *J Extracell Vesicles* **2**, 20304 (2013).
8. Patton, M. C., Zubair, H., Khan, M. A., Singh, S. & Singh, A. P. Hypoxia alters the release and size distribution of extracellular vesicles in pancreatic cancer cells to support their adaptive survival. *J Cell Biochem* **121**, 828–839 (2020).
9. Chargaff, E. & West, R. The biological significance of the thromboplastic protein of blood. *Journal of Biological Chemistry* **166**, 189–197 (1946).
10. Wolf, P. The nature and significance of platelet products in human plasma. *Br J Haematol* **13**, 269–288 (1967).
11. Pan, B. T. & Johnstone, R. M. Fate of the transferrin receptor during maturation of sheep reticulocytes in vitro: Selective externalization of the receptor. *Cell* **33**, 967–978 (1983).
12. Johnstone, R. M., Adam, M., Hammond, J. R., Orr, L. & Turbide, C. Vesicle formation during reticulocyte maturation. Association of plasma membrane activities with released vesicles (exosomes). *J Biol Chem* **262**, 9412–20 (1987).
13. Raposo, G. *et al.* B lymphocytes secrete antigen-presenting vesicles. *Journal of Experimental Medicine* **183**, 1161–1172 (1996).
14. Colombo, M., Raposo, G. & Théry, C. Biogenesis, Secretion, and Intercellular Interactions of Exosomes and Other Extracellular Vesicles. *Annu Rev Cell Dev Biol* **30**, 255–289 (2014).
15. Lo Cicero, A., Stahl, P. D. & Raposo, G. Extracellular vesicles shuffling intercellular messages: for good or for bad. *Curr Opin Cell Biol* **35**, 69–77 (2015).
16. Yáñez-Mó, M. *et al.* Biological properties of extracellular vesicles and their physiological functions. *J Extracell Vesicles* **4**, 27066 (2015).
17. Lee, Y., EL Andaloussi, S. & Wood, M. J. A. Exosomes and microvesicles: extracellular vesicles for genetic information transfer and gene therapy. *Hum Mol Genet* **21**, R125–R134 (2012).

18. Théry, C. *et al.* Minimal information for studies of extracellular vesicles 2018 (MISEV2018): a position statement of the International Society for Extracellular Vesicles and update of the MISEV2014 guidelines. *J Extracell Vesicles* **7**, 1535750 (2018).
19. Lötvall, J. *et al.* Minimal experimental requirements for definition of extracellular vesicles and their functions: a position statement from the International Society for Extracellular Vesicles. *J Extracell Vesicles* **3**, 26913 (2014).
20. Luzio, J. P., Gray, S. R. & Bright, N. A. Endosome-lysosome fusion. in *Biochemical Society Transactions* vol. 38 1413–1416 (2010).
21. Bucci, C., Thomsen, P., Nicoziani, P., McCarthy, J. & van Deurs, B. Rab7: A key to lysosome biogenesis. *Mol Biol Cell* **11**, 467–480 (2000).
22. Bonner, S. E. & Willms, E. Intercellular communication through extracellular vesicles in cancer and evolutionary biology. *Prog Biophys Mol Biol* **165**, 80–87 (2021).
23. Xu, R., Greening, D. W., Rai, A., Ji, H. & Simpson, R. J. Highly-purified exosomes and shed microvesicles isolated from the human colon cancer cell line LIM1863 by sequential centrifugal ultrafiltration are biochemically and functionally distinct. *Methods* **87**, 11–25 (2015).
24. Muralidharan-Chari, V. *et al.* ARF6-Regulated Shedding of Tumor Cell-Derived Plasma Membrane Microvesicles. *Current Biology* **19**, 1875–1885 (2009).
25. Piper, R. C. & Katzmann, D. J. Biogenesis and Function of Multivesicular Bodies. *Annu Rev Cell Dev Biol* **23**, 519–547 (2007).
26. Henne, W. M., Buchkovich, N. J. & Emr, S. D. The ESCRT Pathway. *Dev Cell* **21**, 77–91 (2011).
27. Stuffers, S., Sem Wegner, C., Stenmark, H. & Brech, A. Multivesicular Endosome Biogenesis in the Absence of ESCRTs. *Traffic* **10**, 925–937 (2009).
28. Tamai, K. *et al.* Exosome secretion of dendritic cells is regulated by Hrs, an ESCRT-0 protein. *Biochem Biophys Res Commun* **399**, 384–390 (2010).
29. Trajkovic, K. *et al.* Ceramide triggers budding of exosome vesicles into multivesicular endosomes. *Science* **319**, 1244–7 (2008).
30. Goñi, F. M. & Alonso, A. Effects of ceramide and other simple sphingolipids on membrane lateral structure. *Biochimica et Biophysica Acta (BBA) - Biomembranes* **1788**, 169–177 (2009).
31. Kajimoto, T., Okada, T., Miya, S., Zhang, L. & Nakamura, S. I. Ongoing activation of sphingosine 1-phosphate receptors mediates maturation of exosomal multivesicular endosomes. *Nat Commun* **4**, (2013).
32. Charrin, S., Jouannet, S., Boucheix, C. & Rubinstein, E. Tetraspanins at a glance. *J Cell Sci* **127**, 3641–3648 (2014).
33. Zimmerman, B. *et al.* Crystal Structure of a Full-Length Human Tetraspanin Reveals a Cholesterol-Binding Pocket. *Cell* **167**, 1041-1051.e11 (2016).
34. Baietti, M. F. *et al.* Syndecan-syntenin-ALIX regulates the biogenesis of exosomes. *Nat Cell Biol* **14**, 677–685 (2012).

35. Ghossoub, R. *et al.* Syntenin-ALIX exosome biogenesis and budding into multivesicular bodies are controlled by ARF6 and PLD2. *Nat Commun* **5**, 1–12 (2014).
36. Harding, C., Heuser, J. & Stahl, P. Endocytosis and intracellular processing of transferrin and colloidal gold-transferrin in rat reticulocytes: demonstration of a pathway for receptor shedding. *Eur J Cell Biol* **35**, 256–63 (1984).
37. Li, B., Antonyak, M. A., Zhang, J. & Cerione, R. A. RhoA triggers a specific signaling pathway that generates transforming microvesicles in cancer cells. *Oncogene* **31**, 4740–4749 (2012).
38. Nabhan, J. F., Hu, R., Oh, R. S., Cohen, S. N. & Lu, Q. Formation and release of arrestin domain-containing protein 1-mediated microvesicles (ARMMs) at plasma membrane by recruitment of TSG101 protein. *Proc Natl Acad Sci U S A* **109**, 4146–4151 (2012).
39. Bianco, F. *et al.* Acid sphingomyelinase activity triggers microparticle release from glial cells. *EMBO Journal* **28**, 1043–1054 (2009).
40. Hugel, B., Martínez, M. C., Kunzelmann, C. & Freyssinet, J.-M. Membrane Microparticles: Two Sides of the Coin. *Physiology* **20**, 22–27 (2005).
41. Bevers, E. M., Comfurius, P., Dekkers, D. W. C. & Zwaal, R. F. A. Lipid translocation across the plasma membrane of mammalian cells. *Biochimica et Biophysica Acta (BBA) - Molecular and Cell Biology of Lipids* **1439**, 317–330 (1999).
42. Hristov, M., Erl, W., Linder, S. & Weber, P. C. Apoptotic bodies from endothelial cells enhance the number and initiate the differentiation of human endothelial progenitor cells in vitro. *Blood* **104**, 2761–2766 (2004).
43. Halicka, H. D., Bedner, E. & Darzynkiewicz, Z. Segregation of RNA and Separate Packaging of DNA and RNA in Apoptotic Bodies during Apoptosis. *Exp Cell Res* **260**, 248–256 (2000).
44. Minciacchi, V. R. *et al.* Large oncosomes contain distinct protein cargo and represent a separate functional class of tumor-derived extracellular vesicles. *Oncotarget* **6**, 11327–11341 (2015).
45. di Vizio, D. *et al.* Oncosome Formation in Prostate Cancer: Association with a Region of Frequent Chromosomal Deletion in Metastatic Disease. *Cancer Res* **69**, 5601–5609 (2009).
46. Morello, M. *et al.* Large oncosomes mediate intercellular transfer of functional microRNA. *Cell Cycle* **12**, 3526–3536 (2013).
47. Willms, E., Cabañas, C., Mäger, I., Wood, M. J. A. & Vader, P. Extracellular vesicle heterogeneity: Subpopulations, isolation techniques, and diverse functions in cancer progression. *Front Immunol* **9**, 738 (2018).
48. Kowal, J. *et al.* Proteomic comparison defines novel markers to characterize heterogeneous populations of extracellular vesicle subtypes. *Proceedings of the National Academy of Sciences* **113**, E968–E977 (2016).
49. Willms, E. *et al.* Cells release subpopulations of exosomes with distinct molecular and biological properties. *Sci Rep* **6**, 22519 (2016).

50. Zhang, H. *et al.* Identification of distinct nanoparticles and subsets of extracellular vesicles by asymmetric flow field-flow fractionation. *Nat Cell Biol* **20**, 332–343 (2018).
51. Willms, E. Development of targeted exosomes for delivery of biotherapeutics. PhD Thesis. (University of Oxford, 2018).
52. Buzás, E. I., Tóth, E. Á., Sódar, B. W. & Szabó-Taylor, K. É. Molecular interactions at the surface of extracellular vesicles. *Semin Immunopathol* **40**, 453–464 (2018).
53. Mulcahy, L. A., Pink, R. C. & Carter, D. R. F. Routes and mechanisms of extracellular vesicle uptake. *J Extracell Vesicles* **3**, 24641 (2014).
54. Hosseinkhani, B., Akker, N. M. S., Molin, D. G. M. & Michiels, L. (Sub)populations of extracellular vesicles released by TNF-α –triggered human endothelial cells promote vascular inflammation and monocyte migration. *J Extracell Vesicles* **9**, 1801153 (2020).
55. Li, X.-Q., Zhang, R., Lu, H., Yue, X.-M. & Huang, Y.-F. Extracellular Vesicle–Packaged CDH11 and ITGA5 Induce the Premetastatic Niche for Bone Colonization of Breast Cancer Cells. *Cancer Res* **82**, 1560–1574 (2022).
56. Takov, K. *et al.* Small extracellular vesicles secreted from human amniotic fluid mesenchymal stromal cells possess cardioprotective and promigratory potential. *Basic Res Cardiol* **115**, 1–22 (2020).
57. Gao, L. *et al.* Exosomal ANXA2 derived from ovarian cancer cells regulates epithelial-mesenchymal plasticity of human peritoneal mesothelial cells. *J Cell Mol Med* **25**, 10916–10929 (2021).
58. Campos, A. *et al.* Caveolin-1-containing extracellular vesicles transport adhesion proteins and promote malignancy in breast cancer cell lines. *Nanomedicine* **13**, 2597–2609 (2018).
59. Morelli, A. E. *et al.* Endocytosis, intracellular sorting, and processing of exosomes by dendritic cells. *Blood* **104**, 3257–3266 (2004).
60. Sung, B. H., Ketova, T., Hoshino, D., Zijlstra, A. & Weaver, A. M. Directional cell movement through tissues is controlled by exosome secretion. *Nat Commun* **6**, 7164 (2015).
61. Leiss, M., Beckmann, K., Girós, A., Costell, M. & Fässler, R. The role of integrin binding sites in fibronectin matrix assembly in vivo. *Curr Opin Cell Biol* **20**, 502–507 (2008).
62. Purushothaman, A. *et al.* Fibronectin on the surface of myeloma cell-derived exosomes mediates exosome-cell interactions. *Journal of Biological Chemistry* **291**, 1652–1663 (2016).
63. Murphy, D. E. *et al.* Extracellular vesicle-based therapeutics: natural versus engineered targeting and trafficking. *Exp Mol Med* **51**, 32 (2019).
64. Rana, S., Yue, S., Stadel, D. & Zöller, M. Toward tailored exosomes: The exosomal tetraspanin web contributes to target cell selection. *International Journal of Biochemistry and Cell Biology* **44**, 1574–1584 (2012).

65. Nazarenko, I. *et al.* Cell surface tetraspanin Tspan8 contributes to molecular pathways of exosome-induced endothelial cell activation. *Cancer Res* **70**, 1668–1678 (2010).
66. Rana, S., Claas, C., Kretz, C. C., Nazarenko, I. & Zoeller, M. Activation-induced internalization differs for the tetraspanins CD9 and Tspan8: Impact on tumor cell motility. *International Journal of Biochemistry and Cell Biology* **43**, 106–119 (2011).
67. Melo, S. A. *et al.* Glypican-1 identifies cancer exosomes and detects early pancreatic cancer. *Nature* **523**, 177–182 (2015).
68. Bruno, S. *et al.* Mesenchymal stem cell-derived microvesicles protect against acute tubular injury. *Journal of the American Society of Nephrology* **20**, 1053–1067 (2009).
69. Barrès, C. *et al.* Galectin-5 is bound onto the surface of rat reticulocyte exosomes and modulates vesicle uptake by macrophages. *Blood* **115**, 696–705 (2010).
70. van Genderen, H. O., Kenis, H., Hofstra, L., Narula, J. & Reutelingsperger, C. P. M. Extracellular annexin A5: Functions of phosphatidylserine-binding and two-dimensional crystallization. *Biochimica et Biophysica Acta (BBA) - Molecular Cell Research* **1783**, 953–963 (2008).
71. Feng, D. *et al.* Cellular internalization of exosomes occurs through phagocytosis. *Traffic* **11**, 675–687 (2010).
72. Nakase, I., Kobayashi, N. B., Takatani-Nakase, T. & Yoshida, T. Active macropinocytosis induction by stimulation of epidermal growth factor receptor and oncogenic Ras expression potentiates cellular uptake efficacy of exosomes. *Sci Rep* **5**, 1–14 (2015).
73. Araki, N., Hamasaki, M., Egami, Y. & Hatae, T. Effect of 3-methyladenine on the Fusion Process of Macropinosomes in EGF-stimulated A431 Cells. *Cell Struct Funct* **31**, 145–157 (2006).
74. Dise, R. S., Frey, M. R., Whitehead, R. H. & Polk, D. B. Epidermal growth factor stimulates Rac activation through Src and phosphatidylinositol 3-kinase to promote colonic epithelial cell migration. *American Journal of Physiology-Gastrointestinal and Liver Physiology* **294**, G276–G285 (2008).
75. Conner, S. D. & Schmid, S. L. Regulated portals of entry into the cell. *Nature* **422**, 37–44 (2003).
76. Tian, T. *et al.* Exosome uptake through clathrin-mediated endocytosis and macropinocytosis and mediating miR-21 delivery. *Journal of Biological Chemistry* **289**, 22258–22267 (2014).
77. Costa Verdera, H., Gitz-Francois, J. J., Schiffelers, R. M. & Vader, P. Cellular uptake of extracellular vesicles is mediated by clathrin-independent endocytosis and macropinocytosis. *Journal of Controlled Release* **266**, 100–108 (2017).
78. Yates, A. G. *et al.* In sickness and in health: The functional role of extracellular vesicles in physiology and pathology in vivo. *J Extracell Vesicles* **11**, e12151 (2022).

79. Ramirez, M. I. *et al.* Technical challenges of working with extracellular vesicles. *Nanoscale* **10**, 881–906 (2018).
80. Lim, K. *et al.* Neutrophil trails guide influenza-specific CD8 $^{+}$ T cells in the airways. *Science (1979)* **349**, (2015).
81. Nolan, S., Dixon, R., Norman, K., Hellewell, P. & Ridger, V. Nitric Oxide Regulates Neutrophil Migration through Microparticle Formation. *Am J Pathol* **172**, 265–273 (2008).
82. Kolonics, F. *et al.* Neutrophils produce proinflammatory or anti-inflammatory extracellular vesicles depending on the environmental conditions. *J Leukoc Biol* **109**, 793–806 (2021).
83. Timár, C. I. *et al.* Antibacterial effect of microvesicles released from human neutrophilic granulocytes. *Blood* **121**, 510–518 (2013).
84. Lugini, L. *et al.* Immune Surveillance Properties of Human NK Cell-Derived Exosomes. *The Journal of Immunology* **189**, 2833–2842 (2012).
85. Pironti, G. *et al.* Circulating exosomes induced by cardiac pressure overload contain functional angiotensin II type 1 receptors. *Circulation* **131**, 2120–2130 (2015).
86. Street, J. M. *et al.* Exosomal transmission of functional aquaporin 2 in kidney cortical collecting duct cells. *J Physiol* **589**, 6119–6127 (2011).
87. Park, K.-H. *et al.* Ca $^{2+}$ Signaling Tools Acquired from Prostasomes Are Required for Progesterone-Induced Sperm Motility. *Sci Signal* **4**, (2011).
88. Rooney, I. A. *et al.* Physiologic relevance of the membrane attack complex inhibitory protein CD59 in human seminal plasma: CD59 is present on extracellular organelles (prostasomes), binds cell membranes, and inhibits complement-mediated lysis. *Journal of Experimental Medicine* **177**, 1409–1420 (1993).
89. Al-Dossary, A. A., Strehler, E. E. & Martin-DeLeon, P. A. Expression and Secretion of Plasma Membrane Ca2+-ATPase 4a (PMCA4a) during Murine Estrus: Association with Oviductal Exosomes and Uptake in Sperm. *PLoS One* **8**, e80181 (2013).
90. Choi, J. S. *et al.* Exosomes from differentiating human skeletal muscle cells trigger myogenesis of stem cells and provide biochemical cues for skeletal muscle regeneration. *Journal of Controlled Release* **222**, 107–115 (2016).
91. Chen, X. *et al.* Exosomes derived from hypoxic epithelial ovarian cancer deliver microRNA-940 to induce macrophage M2 polarization. *Oncol Rep* **38**, 522–528 (2017).
92. Chen, X. *et al.* Exosomes derived from hypoxic epithelial ovarian cancer cells deliver microRNAs to macrophages and elicit a tumor-promoted phenotype. *Cancer Lett* **435**, 80–91 (2018).
93. Chen, G. *et al.* Exosomal PD-L1 contributes to immunosuppression and is associated with anti-PD-1 response. *Nature* **560**, 382–386 (2018).

94. Wieckowski, E. U. *et al.* Tumor-Derived Microvesicles Promote Regulatory T Cell Expansion and Induce Apoptosis in Tumor-Reactive Activated CD8 $^{+}$ T Lymphocytes. *The Journal of Immunology* **183**, 3720–3730 (2009).
95. Ko, S. Y. & Naora, H. Extracellular Vesicle Membrane-Associated Proteins: Emerging Roles in Tumor Angiogenesis and Anti-Angiogenesis Therapy Resistance. *Int J Mol Sci* **21**, 5418 (2020).
96. Antonyak, M. A. *et al.* Cancer cell-derived microvesicles induce transformation by transferring tissue transglutaminase and fibronectin to recipient cells. *Proceedings of the National Academy of Sciences* **108**, 4852–4857 (2011).
97. Becker, A. *et al.* Extracellular Vesicles in Cancer: Cell-to-Cell Mediators of Metastasis. *Cancer Cell* **30**, 836–848 (2016).
98. Costa-Silva, B. *et al.* Pancreatic cancer exosomes initiate pre-metastatic niche formation in the liver. *Nat Cell Biol* **17**, 816–826 (2015).
99. Hoshino, A. *et al.* Tumour exosome integrins determine organotropic metastasis. *Nature* **527**, 329–335 (2015).
100. Jimenez, L. *et al.* Quantitative Proteomic Analysis of Small and Large Extracellular Vesicles (EVs) Reveals Enrichment of Adhesion Proteins in Small EVs. *J Proteome Res* **18**, 947–959 (2019).
101. Koumangoye, R. B., Sakwe, A. M., Goodwin, J. S., Patel, T. & Ochieng, J. Detachment of breast tumor cells induces rapid secretion of exosomes which subsequently mediate cellular adhesion and spreading. *PLoS One* **6**, (2011).
102. Nakamura, K. *et al.* Role of the Exosome in Ovarian Cancer Progression and Its Potential as a Therapeutic Target. *Cancers (Basel)* **11**, 1147 (2019).
103. Györffy, B. *et al.* Prediction of doxorubicin sensitivity in breast tumors based on gene expression profiles of drug-resistant cell lines correlates with patient survival. *Oncogene* **24**, 7542–51 (2005).
104. Muralidharan-Chari, V. *et al.* Microvesicle removal of anticancer drugs contributes to drug resistance in human pancreatic cancer cells. *Oncotarget* **7**, 50365–50379 (2016).
105. Ciravolo, V. *et al.* Potential role of HER2-overexpressing exosomes in countering trastuzumab-based therapy. *J Cell Physiol* **227**, 658–667 (2012).
106. Langui, D. *et al.* Subcellular topography of neuronal Aβ peptide in APPxPS1 transgenic mice. *American Journal of Pathology* **165**, 1465–1477 (2004).
107. Rajendran, L. *et al.* Alzheimer's disease β-amyloid peptides are released in association with exosomes. *Proc Natl Acad Sci U S A* **103**, 11172–11177 (2006).
108. Dinkins, M. B., Dasgupta, S., Wang, G., Zhu, G. & Bieberich, E. Exosome reduction invivo is associated with lower amyloid plaque load in the 5XFAD mouse model of Alzheimer's disease. *Neurobiol Aging* **35**, 1792–1800 (2014).
109. Lee, H. J., Patel, S. & Lee, S. J. Intravesicular localization and exocytosis of α-synuclein and its aggregates. *Journal of Neuroscience* **25**, 6016–6024 (2005).
110. Feneberg, E. *et al.* Limited role of free TDP-43 as a diagnostic tool in neurodegenerative diseases. *Amyotroph Lateral Scler Frontotemporal Degener* **15**, 351–356 (2014).

111. Münch, C., O'Brien, J. & Bertolotti, A. Prion-like propagation of mutant superoxide dismutase-1 misfolding in neuronal cells. *Proceedings of the National Academy of Sciences* **108**, 3548–3553 (2011).
112. Gomes, C., Keller, S., Altevogt, P. & Costa, J. Evidence for secretion of Cu,Zn superoxide dismutase via exosomes from a cell model of amyotrophic lateral sclerosis. *Neurosci Lett* **428**, 43–46 (2007).
113. Wheway, J., Latham, S. L., Combes, V. & Grau, G. E. R. Endothelial Microparticles Interact with and Support the Proliferation of T Cells. *The Journal of Immunology* **193**, 3378–3387 (2014).
114. Jy, W. *et al.* Endothelial microparticles (EMP) bind and activate monocytes: elevated EMP-monocyte conjugates in multiple sclerosis. *Front Biosci* **9**, 3137–3144 (2004).
115. Bellin, G. *et al.* Exosome in Cardiovascular Diseases: A Complex World Full of Hope. *Cells* **8**, 166 (2019).
116. Herrmann, M. *et al.* Extracellular Vesicles in Musculoskeletal Pathologies and Regeneration. *Front Bioeng Biotechnol* **8**, 1509 (2021).
117. Karpman, D., Ståhl, A. & Arvidsson, I. Extracellular vesicles in renal disease. *Nat Rev Nephrol* **13**, 545–562 (2017).
118. Simon, C. *et al.* Extracellular Vesicles in Human Reproduction in Health and Disease. *Endocr Rev* **39**, 292–332 (2018).
119. Chang, X. *et al.* Extracellular Vesicles with Possible Roles in Gut Intestinal Tract Homeostasis and IBD. *Mediators Inflamm* **2020**, 1–14 (2020).
120. Haas-Neill, S. & Forsythe, P. A Budding Relationship: Bacterial Extracellular Vesicles in the Microbiota-Gut-Brain Axis. *Int J Mol Sci* **21**, 8899 (2020).
121. Buzas, E. I., György, B., Nagy, G., Falus, A. & Gay, S. Emerging role of extracellular vesicles in inflammatory diseases. *Nat Rev Rheumatol* **10**, 356–364 (2014).
122. Lu, M. *et al.* The Role of Extracellular Vesicles in the Pathogenesis and Treatment of Autoimmune Disorders. *Front Immunol* **12**, (2021).
123. Schorey, J. S. & Harding, C. v. Extracellular vesicles and infectious diseases: new complexity to an old story. *Journal of Clinical Investigation* **126**, 1181–1189 (2016).
124. Martins, S. de T. & Alves, L. R. Extracellular Vesicles in Viral Infections: Two Sides of the Same Coin? *Front Cell Infect Microbiol* **10**, 737 (2020).
125. Alvarez-Erviti, L. *et al.* Delivery of siRNA to the mouse brain by systemic injection of targeted exosomes. *Nat Biotechnol* **29**, 341–345 (2011).
126. Rufino-Ramos, D. *et al.* Extracellular vesicles: Novel promising delivery systems for therapy of brain diseases. *Journal of Controlled Release* **262**, 247–258 (2017).
127. el Andaloussi, S., Lakhal, S., Mäger, I. & Wood, M. J. A. Exosomes for targeted siRNA delivery across biological barriers. *Adv Drug Deliv Rev* **65**, 391–397 (2013).
128. Wang, Q. *et al.* ARMMs as a versatile platform for intracellular delivery of macromolecules. *Nat Commun* **9**, 1–7 (2018).

129. Kamerkar, S. *et al.* Exosomes facilitate therapeutic targeting of oncogenic KRAS in pancreatic cancer. *Nature* **546**, 498–503 (2017).
130. Rodríguez-Fuentes, D. E. *et al.* Mesenchymal Stem Cells Current Clinical Applications: A Systematic Review. *Arch Med Res* **52**, 93–101 (2021).
131. Wiklander, O. P. B., Brennan, M. Á., Lötvall, J., Breakefield, X. O. & el Andaloussi, S. Advances in therapeutic applications of extracellular vesicles. *Sci Transl Med* **11**, eaav8521 (2019).
132. Nassar, W. *et al.* Umbilical cord mesenchymal stem cells derived extracellular vesicles can safely ameliorate the progression of chronic kidney diseases. *Biomater Res* **20**, 1–11 (2016).
133. Ohno, S. I. *et al.* Systemically injected exosomes targeted to EGFR deliver antitumor microrna to breast cancer cells. *Molecular Therapy* **21**, 185–191 (2013).
134. Tian, Y. *et al.* A doxorubicin delivery platform using engineered natural membrane vesicle exosomes for targeted tumor therapy. *Biomaterials* **35**, 2383–2390 (2014).
135. June, C. H., O'Connor, R. S., Kawalekar, O. U., Ghassemi, S. & Milone, M. C. CAR T cell immunotherapy for human cancer. *Science (1979)* **359**, 1361–1365 (2018).
136. Fu, W. *et al.* CAR exosomes derived from effector CAR-T cells have potent antitumour effects and low toxicity. *Nat Commun* **10**, 4355 (2019).
137. Zhang, X. *et al.* Engineered Extracellular Vesicles for Cancer Therapy. *Advanced Materials* **33**, 2005709 (2021).
138. Tian, T. *et al.* Surface functionalized exosomes as targeted drug delivery vehicles for cerebral ischemia therapy. *Biomaterials* **150**, 137–149 (2018).
139. Wu, P., Zhang, B., Ocansey, D. K. W., Xu, W. & Qian, H. Extracellular vesicles: A bright star of nanomedicine. *Biomaterials* **269**, 120467 (2021).
140. Li, Y.-J., Wu, J.-Y., Wang, J.-M., Hu, X.-B. & Xiang, D.-X. Emerging strategies for labeling and tracking of extracellular vesicles. *Journal of Controlled Release* **328**, 141–159 (2020).
141. Melling, G. E. *et al.* Confocal microscopy analysis reveals that only a small proportion of extracellular vesicles are successfully labelled with commonly utilised staining methods. *Sci Rep* **12**, 262 (2022).
142. Szabó-Taylor, K. É. *et al.* Monocyte activation drives preservation of membrane thiols by promoting release of oxidised membrane moieties via extracellular vesicles. *Free Radic Biol Med* **108**, 56–65 (2017).
143. Estelrich, J., Sánchez-Martín, M. J. & Busquets, M. A. Nanoparticles in magnetic resonance imaging: from simple to dual contrast agents. *Int J Nanomedicine* **10**, 1727–41 (2015).
144. Kang, M., Jordan, V., Blenkiron, C. & Chamley, L. W. Biodistribution of extracellular vesicles following administration into animals: A systematic review. *J Extracell Vesicles* **10**, e12085 (2021).
145. Sidhom, K., Obi, P. O. & Saleem, A. A Review of Exosomal Isolation Methods: Is Size Exclusion Chromatography the Best Option? *Int J Mol Sci* **21**, 6466 (2020).

146. Zhou, B. *et al.* Application of exosomes as liquid biopsy in clinical diagnosis. *Signal Transduct Target Ther* **5**, 144 (2020).
147. Gardiner, C., Ferreira, Y. J., Dragovic, R. A., Redman, C. W. G. & Sargent, I. L. Extracellular vesicle sizing and enumeration by nanoparticle tracking analysis. *J Extracell Vesicles* **2**, 19671 (2013).
148. Royo, F., Théry, C., Falcón-Pérez, J. M., Nieuwland, R. & Witwer, K. W. Methods for Separation and Characterization of Extracellular Vesicles: Results of a Worldwide Survey Performed by the ISEV Rigor and Standardization Subcommittee. *Cells* **9**, 1955 (2020).
149. Gobin, J. *et al.* Hollow-fiber bioreactor production of extracellular vesicles from human bone marrow mesenchymal stromal cells yields nanovesicles that mirrors the immuno-modulatory antigenic signature of the producer cell. *Stem Cell Res Ther* **12**, 1–20 (2021).
150. Paganini, C. *et al.* Scalable Production and Isolation of Extracellular Vesicles: Available Sources and Lessons from Current Industrial Bioprocesses. *Biotechnol J* **14**, 1800528 (2019).
151. de Almeida Fuzeta, M. *et al.* Scalable Production of Human Mesenchymal Stromal Cell-Derived Extracellular Vesicles Under Serum-/Xeno-Free Conditions in a Microcarrier-Based Bioreactor Culture System. *Front Cell Dev Biol* **8**, 1197 (2020).
152. Mathieu, M. *et al.* Specificities of exosome versus small ectosome secretion revealed by live intracellular tracking of CD63 and CD9. *Nat Commun* **12**, 4389 (2021).
153. Takov, K., Yellon, D. M. & Davidson, S. M. Confounding factors in vesicle uptake studies using fluorescent lipophilic membrane dyes. *J Extracell Vesicles* **6**, 1388731 (2017).
154. Tkach, M., Kowal, J. & Théry, C. Why the need and how to approach the functional diversity of extracellular vesicles. *Philosophical Transactions of the Royal Society B: Biological Sciences* **373**, (2018).
155. Mihara, K. *et al.* Development and functional characterization of human bone marrow mesenchymal cells immortalized by enforced expression of telomerase. *Br J Haematol* **120**, 846–849 (2003).
156. Gupta, D., Zickler, A. M. & el Andaloussi, S. Dosing extracellular vesicles. *Adv Drug Deliv Rev* **178**, 113961 (2021).
157. van Niel, G., D'Angelo, G. & Raposo, G. Shedding light on the cell biology of extracellular vesicles. *Nat Rev Mol Cell Biol* **19**, 213–228 (2018).
158. Wiklander, O. P. B. *et al.* Extracellular vesicle in vivo biodistribution is determined by cell source, route of administration and targeting. *J Extracell Vesicles* **4**, 1–13 (2015).
159. Kooijmans, S. A. A. *et al.* PEGylated and targeted extracellular vesicles display enhanced cell specificity and circulation time. *J Control Release* **224**, 77–85 (2016).

160. Matsumoto, A. *et al.* Role of Phosphatidylserine-Derived Negative Surface Charges in the Recognition and Uptake of Intravenously Injected B16BL6-Derived Exosomes by Macrophages. *J Pharm Sci* **106**, 168–175 (2017).
161. Mendt, M. *et al.* Generation and testing of clinical-grade exosomes for pancreatic cancer. *JCI Insight* **3**, 99263 (2018).
162. Kim, M. S. *et al.* Development of exosome-encapsulated paclitaxel to overcome MDR in cancer cells. *Nanomedicine* **12**, 655–664 (2016).
163. Munagala, R., Aqil, F., Jeyabalan, J. & Gupta, R. C. Bovine milk-derived exosomes for drug delivery. *Cancer Lett* **371**, 48–61 (2016).
164. Haney, M. J. *et al.* Exosomes as drug delivery vehicles for Parkinson's disease therapy. *Journal of Controlled Release* **207**, 18–30 (2015).
165. Lehmann, T. P. *et al.* Quantification of the asymmetric migration of the lipophilic dyes, DiO and DiD, in homotypic co-cultures of chondrosarcoma SW-1353 cells. *Mol Med Rep* **14**, 4529–4536 (2016).
166. Watson, D. C. *et al.* Efficient production and enhanced tumor delivery of engineered extracellular vesicles. *Biomaterials* **105**, 195–205 (2016).
167. Simonsen, J. B. Pitfalls associated with lipophilic fluorophore staining of extracellular vesicles for uptake studies. *J Extracell Vesicles* **8**, 1582237 (2019).
168. Xu, L. *et al.* Design of experiment (DoE)-driven *in vitro* and *in vivo* uptake studies of exosomes for pancreatic cancer delivery enabled by copper-free click chemistry-based labelling. *J Extracell Vesicles* **9**, 1779458 (2020).
169. Lee, T. S., Kim, Y., Zhang, W., Song, I. H. & Tung, C.-H. Facile metabolic glycan labeling strategy for exosome tracking. *Biochimica et Biophysica Acta (BBA) - General Subjects* **1862**, 1091–1100 (2018).
170. Wang, M., Altinoglu, S., Takeda, Y. S. & Xu, Q. Integrating Protein Engineering and Bioorthogonal Click Conjugation for Extracellular Vesicle Modulation and Intracellular Delivery. *PLoS One* **10**, e0141860 (2015).
171. Roberts-Dalton, H. D. *et al.* Fluorescence labelling of extracellular vesicles using a novel thiol-based strategy for quantitative analysis of cellular delivery and intracellular traffic. *Nanoscale* **9**, 13693–13706 (2017).
172. Headland, S. E., Jones, H. R., D'Sa, A. S. v., Perretti, M. & Norling, L. v. Cutting-Edge Analysis of Extracellular Microparticles using ImageStreamX Imaging Flow Cytometry. *Sci Rep* **4**, 5237 (2015).
173. Men, Y. *et al.* Exosome reporter mice reveal the involvement of exosomes in mediating neuron to astroglia communication in the CNS. *Nat Commun* **10**, 4136 (2019).
174. Piao, Y. J. *et al.* Breast cancer cell-derived exosomes and macrophage polarization are associated with lymph node metastasis. *Oncotarget* **9**, 7398–7410 (2018).
175. Verweij, F. J. *et al.* Live Tracking of Inter-organ Communication by Endogenous Exosomes In Vivo. *Dev Cell* **48**, 573-589.e4 (2019).
176. Sung, B. H. *et al.* A live cell reporter of exosome secretion and uptake reveals pathfinding behavior of migrating cells. *Nat Commun* **11**, 2092 (2020).

177. Hikita, T., Miyata, M., Watanabe, R. & Oneyama, C. Sensitive and rapid quantification of exosomes by fusing luciferase to exosome marker proteins. *Sci Rep* **8**, 14035 (2018).
178. Takahashi, Y. *et al.* Visualization and in vivo tracking of the exosomes of murine melanoma B16-BL6 cells in mice after intravenous injection. *J Biotechnol* **165**, 77–84 (2013).
179. Imai, T. *et al.* Macrophage-dependent clearance of systemically administered B16BL6-derived exosomes from the blood circulation in mice. *J Extracell Vesicles* **4**, 26238 (2015).
180. Charoenviriyakul, C. *et al.* Cell type-specific and common characteristics of exosomes derived from mouse cell lines: Yield, physicochemical properties, and pharmacokinetics. *European Journal of Pharmaceutical Sciences* **96**, 316–322 (2017).
181. Kanada, M. *et al.* Differential fates of biomolecules delivered to target cells via extracellular vesicles. *Proceedings of the National Academy of Sciences* **112**, E1433–E1442 (2015).
182. Gangadaran, P. *et al.* A new bioluminescent reporter system to study the biodistribution of systematically injected tumor-derived bioluminescent extracellular vesicles in mice. *Oncotarget* **8**, 109894–109914 (2017).
183. Hwang, D. W. *et al.* Noninvasive imaging of radiolabeled exosome-mimetic nanovesicle using 99mTc-HMPAO. *Sci Rep* **5**, 15636 (2015).
184. Busato, A. *et al.* Magnetic resonance imaging of ultrasmall superparamagnetic iron oxide-labeled exosomes from stem cells: a new method to obtain labeled exosomes. *Int J Nanomedicine* **11**, 2481–90 (2016).
185. Faruqu, F. N. *et al.* Membrane Radiolabelling of Exosomes for Comparative Biodistribution Analysis in Immunocompetent and Immunodeficient Mice - A Novel and Universal Approach. *Theranostics* **9**, 1666–1682 (2019).
186. Morishita, M. *et al.* Quantitative Analysis of Tissue Distribution of the B16BL6-Derived Exosomes Using a Streptavidin-Lactadherin Fusion Protein and Iodine-125-Labeled Biotin Derivative After Intravenous Injection in Mice. *J Pharm Sci* **104**, 705–713 (2015).
187. Betzer, O. *et al.* In Vivo Neuroimaging of Exosomes Using Gold Nanoparticles. *ACS Nano* **11**, 10883–10893 (2017).
188. Guo, S. *et al.* Intranasal Delivery of Mesenchymal Stem Cell Derived Exosomes Loaded with Phosphatase and Tensin Homolog siRNA Repairs Complete Spinal Cord Injury. *ACS Nano* **13**, 10015–10028 (2019).
189. Groot, M. & Lee, H. Sorting Mechanisms for MicroRNAs into Extracellular Vesicles and Their Associated Diseases. *Cells* **9**, 1044 (2020).
190. Sano, T., Smith, C. L. & Cantor, C. R. Immuno-PCR: Very Sensitive Antigen Detection by Means of Specific Antibody-DNA Conjugates. *Science (1979)* **258**, 120–122 (1992).

191. Tavoosidana, G. *et al.* Multiple recognition assay reveals prostasomes as promising plasma biomarkers for prostate cancer. *Proceedings of the National Academy of Sciences* **108**, 8809–8814 (2011).
192. Löf, L. *et al.* Detecting individual extracellular vesicles using a multicolor in situ proximity ligation assay with flow cytometric readout. *Sci Rep* **6**, 34358 (2016).
193. Wu, D. *et al.* Profiling surface proteins on individual exosomes using a proximity barcoding assay. *Nat Commun* **10**, 3854 (2019).
194. Forootan, A. *et al.* Methods to determine limit of detection and limit of quantification in quantitative real-time PCR (qPCR). *Biomol Detect Quantif* **12**, 1–6 (2017).
195. Getz, E. B., Xiao, M., Chakrabarty, T., Cooke, R. & Selvin, P. R. A Comparison between the Sulfhydryl Reductants Tris(2-carboxyethyl)phosphine and Dithiothreitol for Use in Protein Biochemistry. *Anal Biochem* **273**, 73–80 (1999).
196. Zwyssig, A. *et al.* Protein Reduction and Dialysis-Free Work-Up through Phosphines Immobilized on a Magnetic Support: TCEP-Functionalized Carbon-Coated Cobalt Nanoparticles. *Chemistry - A European Journal* **23**, 8585–8589 (2017).
197. Pretzer, E. & Wiktorowicz, J. E. Saturation fluorescence labeling of proteins for proteomic analyses. *Anal Biochem* **374**, 250–262 (2008).
198. Tyagarajan, K., Pretzer, E. & Wiktorowicz, J. E. Thiol-reactive dyes for fluorescence labeling of proteomic samples. *Electrophoresis* **24**, 2348–2358 (2003).
199. Salunkhe, S., Dheeraj, Basak, M., Chitkara, D. & Mittal, A. Surface functionalization of exosomes for target-specific delivery and in vivo imaging & tracking: Strategies and significance. *Journal of Controlled Release* **326**, 599–614 (2020).
200. Fredriksson, S. *et al.* Protein detection using proximity-dependent DNA ligation assays. *Nat Biotechnol* **20**, 473–477 (2002).
201. Söderberg, O. *et al.* Direct observation of individual endogenous protein complexes in situ by proximity ligation. *Nat Methods* **3**, 995–1000 (2006).
202. Sapra, P. & Allen, T. M. Ligand-targeted liposomal anticancer drugs. *Prog Lipid Res* **42**, 439–462 (2003).
203. Bannas, P., Hambach, J. & Koch-Nolte, F. Nanobodies and nanobody-based human heavy chain antibodies as antitumor therapeutics. *Front Immunol* **8**, 1603 (2017).
204. Zhang, L., Hurek, T. & Reinhold-Hurek, B. Position of the fluorescent label is a crucial factor determining signal intensity in microarray hybridizations. *Nucleic Acids Res* **33**, e166 (2005).
205. Veerman, R. E. *et al.* Molecular evaluation of five different isolation methods for extracellular vesicles reveals different clinical applicability and subcellular origin. *J Extracell Vesicles* **10**, e12128 (2021).

206. Silva, A. M. *et al.* Quantification of protein cargo loading into engineered extracellular vesicles at single-vesicle and single-molecule resolution. *J Extracell Vesicles* **10**, e12130 (2021).
207. Viveiros, A. *et al.* In-Cell Labeling Coupled to Direct Analysis of Extracellular Vesicles in the Conditioned Medium to Study Extracellular Vesicles Secretion with Minimum Sample Processing and Particle Loss. *Cells* **11**, 351 (2022).
208. Carrillo Sanchez, B., Hinchliffe, M. & Bracewell, D. G. GFP-tagging of extracellular vesicles for rapid process development. *Biotechnol J* **17**, 2100583 (2022).
209. Champlot, S. *et al.* An Efficient Multistrategy DNA Decontamination Procedure of PCR Reagents for Hypersensitive PCR Applications. *PLoS One* **5**, e13042 (2010).
210. O'Loughlin, A. J. *et al.* Functional Delivery of Lipid-Conjugated siRNA by Extracellular Vesicles. *Molecular Therapy* **25**, 1580–1587 (2017).
211. Dar, G. H. *et al.* GAPDH controls extracellular vesicle biogenesis and enhances therapeutic potential of EVs in silencing the Huntingtin gene in mice via siRNA delivery. *Nature* **12**, 1-15 (2020).
212. Busatto, S. *et al.* Considerations for extracellular vesicle and lipoprotein interactions in cell culture assays. *J Extracell Vesicles* **11**, e12202 (2022).
213. Bordanaba-Florit, G., Royo, F., Kruglik, S. G. & Falcón-Pérez, J. M. Using single-vesicle technologies to unravel the heterogeneity of extracellular vesicles. *Nat Protoc* **16**, 3163–3185 (2021).
214. Ali, M. M. *et al.* Rolling circle amplification: a versatile tool for chemical biology, materials science and medicine. *Chem Soc Rev* **43**, 3324 (2014).
215. Gardiner, C. *et al.* Techniques used for the isolation and characterization of extracellular vesicles: Results of a worldwide survey. *J Extracell Vesicles* **5**, (2016).
216. Doyle, L. & Wang, M. Overview of Extracellular Vesicles, Their Origin, Composition, Purpose, and Methods for Exosome Isolation and Analysis. *Cells* **8**, 727 (2019).
217. Livshits, M. A. *et al.* Isolation of exosomes by differential centrifugation: Theoretical analysis of a commonly used protocol. *Sci Rep* **5**, 17319 (2015).
218. Momen-Heravi, F. Isolation of Extracellular Vesicles by Ultracentrifugation. *Methods Mol Biol* **1660**, 25–32 (2017).
219. Théry, C., Amigorena, S., Raposo, G. & Clayton, A. Isolation and Characterization of Exosomes from Cell Culture Supernatants and Biological Fluids. *Curr Protoc Cell Biol* **30**, 3.22.1-3.22.29 (2006).
220. Baranyai, T. *et al.* Isolation of Exosomes from Blood Plasma: Qualitative and Quantitative Comparison of Ultracentrifugation and Size Exclusion Chromatography Methods. *PLoS One* **10**, e0145686 (2015).
221. Momen-Heravi, F. *et al.* Impact of biofluid viscosity on size and sedimentation efficiency of the isolated microvesicles. *Front Physiol* **3**, 162 (2012).

222. Linares, R., Tan, S., Gounou, C., Arraud, N. & Brisson, A. R. High-speed centrifugation induces aggregation of extracellular vesicles. *J Extracell Vesicles* **4**, 29509 (2015).
223. Li, P., Kaslan, M., Lee, S. H., Yao, J. & Gao, Z. Progress in Exosome Isolation Techniques. *Theranostics* **7**, 789–804 (2017).
224. Konadu, K. A. *et al.* Isolation of Exosomes from the Plasma of HIV-1 Positive Individuals. *Journal of Visualized Experiments* **107**, 53495 (2016).
225. van Deun, J. *et al.* The impact of disparate isolation methods for extracellular vesicles on downstream RNA profiling. *J Extracell Vesicles* **3**, 24858 (2014).
226. Brennan, K. *et al.* A comparison of methods for the isolation and separation of extracellular vesicles from protein and lipid particles in human serum. *Sci Rep* **10**, 1039 (2020).
227. Lane, R. E., Korbie, D., Trau, M. & Hill, M. M. Purification Protocols for Extracellular Vesicles. in *Methods in molecular biology (Clifton, N.J.)* **1660**, 111–130 (Methods Mol Biol, 2017).
228. Zhang, X., Borg, E. G. F., Liaci, A. M., Vos, H. R. & Stoorvogel, W. A novel three step protocol to isolate extracellular vesicles from plasma or cell culture medium with both high yield and purity. *J Extracell Vesicles* **9**, 1791450 (2020).
229. Patel, G. K. *et al.* Comparative analysis of exosome isolation methods using culture supernatant for optimum yield, purity and downstream applications. *Sci Rep* **9**, 5335 (2019).
230. Carnino, J. M., Lee, H. & Jin, Y. Isolation and characterization of extracellular vesicles from Broncho-Alveolar lavage fluid: A review and comparison of different methods. *Respir Res* **20**, 1–11 (2019).
231. Samsonov, R. *et al.* Lectin-induced agglutination method of urinary exosomes isolation followed by mi-RNA analysis: Application for prostate cancer diagnostic. *Prostate* **76**, 68–79 (2016).
232. Tauro, B. J. *et al.* Comparison of ultracentrifugation, density gradient separation, and immunoaffinity capture methods for isolating human colon cancer cell line LIM1863-derived exosomes. *Methods* **56**, 293–304 (2012).
233. Greening, D. W., Xu, R., Ji, H., Tauro, B. J. & Simpson, R. J. A protocol for exosome isolation and characterization: Evaluation of ultracentrifugation, density-gradient separation, and immunoaffinity capture methods. *Methods in Molecular Biology* **1295**, 179–209 (2015).
234. Mor-Vaknin, N. *et al.* DEK in the synovium of patients with juvenile idiopathic arthritis: Characterization of DEK antibodies and posttranslational modification of the DEK autoantigen. *Arthritis Rheum* **63**, 556–567 (2011).
235. Boriachek, K. *et al.* Avoiding Pre-Isolation Step in Exosome Analysis: Direct Isolation and Sensitive Detection of Exosomes Using Gold-Loaded Nanoporous Ferric Oxide Nanozymes. *Anal Chem* **91**, 3827–3834 (2019).
236. Campos-Silva, C. *et al.* High sensitivity detection of extracellular vesicles immune-captured from urine by conventional flow cytometry. *Sci Rep* **9**, 2042 (2019).

237. Mathivanan, S. *et al.* Proteomics Analysis of A33 Immunoaffinity-purified Exosomes Released from the Human Colon Tumor Cell Line LIM1215 Reveals a Tissue-specific Protein Signature. *Molecular & Cellular Proteomics* **9**, 197–208 (2010).
238. Song, Z. *et al.* Development of a CD63 Aptamer for Efficient Cancer Immunochemistry and Immunoaffinity-Based Exosome Isolation. *Molecules* **25**, 5585 (2020).
239. Liang, L.-G. *et al.* An integrated double-filtration microfluidic device for isolation, enrichment and quantification of urinary extracellular vesicles for detection of bladder cancer. *Sci Rep* **7**, 46224 (2017).
240. Dudani, J. S. *et al.* Rapid inertial solution exchange for enrichment and flow cytometric detection of microvesicles. *Biomicrofluidics* **9**, 014112 (2015).
241. Liu, C. *et al.* Field-Free Isolation of Exosomes from Extracellular Vesicles by Microfluidic Viscoelastic Flows. *ACS Nano* **11**, 6968–6976 (2017).
242. Wu, M. *et al.* Isolation of exosomes from whole blood by integrating acoustics and microfluidics. *Proceedings of the National Academy of Sciences* **114**, 10584–10589 (2017).
243. Ibsen, S. D. *et al.* Rapid Isolation and Detection of Exosomes and Associated Biomarkers from Plasma. *ACS Nano* **11**, 6641–6651 (2017).
244. Wunsch, B. H. *et al.* Nanoscale lateral displacement arrays for the separation of exosomes and colloids down to 20 nm. *Nat Nanotechnol* **11**, 936–940 (2016).
245. Park, J., Han, D. H. & Park, J.-K. Towards practical sample preparation in point-of-care testing: user-friendly microfluidic devices. *Lab Chip* **20**, 1191–1203 (2020).
246. Marzano, G. *et al.* Sperm selection in assisted reproduction: A review of established methods and cutting-edge possibilities. *Biotechnol Adv* **40**, 107498 (2020).
247. Mani, V. *et al.* Microchip-based ultrafast serodiagnostic assay for tuberculosis. *Sci Rep* **6**, 35845 (2016).
248. Guo, S.-C., Tao, S.-C. & Dawn, H. Microfluidics-based on-a-chip systems for isolating and analysing extracellular vesicles. *J Extracell Vesicles* **7**, 1508271 (2018).
249. Salafi, T., Zeming, K. K. & Zhang, Y. Advancements in microfluidics for nanoparticle separation. *Lab Chip* **17**, 11–33 (2017).
250. Cheruvanky, A. *et al.* Rapid isolation of urinary exosomal biomarkers using a nanomembrane ultrafiltration concentrator. *Am J Physiol Renal Physiol* **292**, 1657–1661 (2007).
251. Vergauwen, G. *et al.* Confounding factors of ultrafiltration and protein analysis in extracellular vesicle research. *Sci Rep* **7**, 2704 (2017).
252. Heinemann, M. L. & Vykoukal, J. Sequential Filtration: A Gentle Method for the Isolation of Functional Extracellular Vesicles. *Methods Mol Biol* **1660**, 33–41 (2017).

253. Kim, K. *et al.* Cyclic tangential flow filtration system for isolation of extracellular vesicles. *APL Bioeng* **5**, 016103 (2021).
254. Busatto, S. *et al.* Tangential Flow Filtration for Highly Efficient Concentration of Extracellular Vesicles from Large Volumes of Fluid. *Cells* **7**, 273 (2018).
255. Heath, N. *et al.* Rapid isolation and enrichment of extracellular vesicle preparations using anion exchange chromatography. *Sci Rep* **8**, 5730 (2018).
256. Nordin, J. Z., Bostancioglu, R. B., Corso, G. & el Andaloussi, S. Tangential Flow Filtration with or Without Subsequent Bind-Elute Size Exclusion Chromatography for Purification of Extracellular Vesicles. *Methods in Molecular Biology* **1953**, 287–299 (2019).
257. Lindqvist, B. & Storgårds, T. Molecular-sieving Properties of Starch. *Nature* **175**, 511–512 (1955).
258. Hong, P., Koza, S. & Bouvier, E. S. P. Size-Exclusion Chromatography for the Analysis of Protein Biotherapeutics and their Aggregates. *J Liq Chromatogr Relat Technol* **35**, 2923–2950 (2012).
259. la Verde, V., Dominici, P. & Astegno, A. Determination of Hydrodynamic Radius of Proteins by Size Exclusion Chromatography. *Bio Protoc* **7**, (2017).
260. Kaddour, H., Tranquille, M. & Okeoma, C. M. The Past, the Present, and the Future of the Size Exclusion Chromatography in Extracellular Vesicles Separation. *Viruses* **13**, 2272 (2021).
261. Nordin, J. Z. *et al.* Ultrafiltration with size-exclusion liquid chromatography for high yield isolation of extracellular vesicles preserving intact biophysical and functional properties. *Nanomedicine* **11**, 879–883 (2015).
262. Dissanayake, K., Godakumara, K. & Fazeli, A. Isolation of Extracellular Vesicles (EVs) Using Size-Exclusion High-Performance Liquid Chromatography (SE-HPLC). *Methods in Molecular Biology* **2273**, 189–200 (2021).
263. Vogel, R. *et al.* A standardized method to determine the concentration of extracellular vesicles using tunable resistive pulse sensing. *J Extracell Vesicles* **5**, 31242 (2016).
264. Benedikter, B. J. *et al.* Ultrafiltration combined with size exclusion chromatography efficiently isolates extracellular vesicles from cell culture media for compositional and functional studies. *Sci Rep* **7**, 15297 (2017).
265. Böing, A. N. *et al.* Single-step isolation of extracellular vesicles by size-exclusion chromatography. *J Extracell Vesicles* **3**, (2014).
266. Tzaridis, T. *et al.* Extracellular Vesicle Separation Techniques Impact Results from Human Blood Samples: Considerations for Diagnostic Applications. *Int J Mol Sci* **22**, 9211 (2021).
267. Saludas, L. *et al.* Isolation methods of large and small extracellular vesicles derived from cardiovascular progenitors: A comparative study. *European Journal of Pharmaceutics and Biopharmaceutics* **170**, 187–196 (2022).
268. Coumans, F. A. W. *et al.* Methodological Guidelines to Study Extracellular Vesicles. *Circ Res* **120**, 1632–1648 (2017).

269. Huang, T. & He, J. Characterization of Extracellular Vesicles by Size-Exclusion High-Performance Liquid Chromatography (HPLC). in *Methods in molecular biology (Clifton, N.J.)* vol. 1660 191–199 (NIH Public Access, 2017).
270. Corso, G. *et al.* Reproducible and scalable purification of extracellular vesicles using combined bind-elute and size exclusion chromatography. *Sci Rep* **7**, 11561 (2017).
271. Mertz, M., Golombek, F., Boye, S., Moreno, S. & Castiglione, K. Fast and effective chromatographic separation of polymersomes from proteins by multimodal chromatography. *Journal of Chromatography B* **1162**, 122459 (2021).
272. Lothert, K. *et al.* A scalable downstream process for the purification of the cell culture-derived Orf virus for human or veterinary applications. *J Biotechnol* **323**, 221–230 (2020).
273. Onódi, Z. *et al.* Isolation of high-purity extracellular vesicles by the combination of iodixanol density gradient ultracentrifugation and bind-elute chromatography from blood plasma. *Front Physiol* **9**, 1479 (2018).
274. Reiter, K. *et al.* Separation of virus-like particles and extracellular vesicles by flow-through and heparin affinity chromatography. *J Chromatogr A* **1588**, 77–84 (2019).
275. Sánchez-Trasviña, C. *et al.* Structure and functional properties of Capto™ Core 700 core-shell particles. *J Chromatogr A* **1621**, 461079 (2020).
276. McNamara, R. P. *et al.* Large-scale, cross-flow based isolation of highly pure and endocytosis-competent extracellular vesicles. *J Extracell Vesicles* **7**, 1541396 (2018).
277. Rikkert, L. G., Nieuwland, R., Terstappen, L. W. M. M. & Coumans, F. A. W. Quality of extracellular vesicle images by transmission electron microscopy is operator and protocol dependent. *J Extracell Vesicles* **8**, 1555419 (2019).
278. Hong, C. S., Muller, L., Boyiadzis, M. & Whiteside, T. L. Isolation and Characterization of CD34+ Blast-Derived Exosomes in Acute Myeloid Leukemia. *PLoS One* **9**, e103310 (2014).
279. Povero, D. *et al.* Human induced pluripotent stem cell–derived extracellular vesicles reduce hepatic stellate cell activation and liver fibrosis. *JCI Insight* **4**, (2019).
280. Nikishin, I. *et al.* ScanEV – A neural network-based tool for the automated detection of extracellular vesicles in TEM images. *Micron* **145**, 103044 (2021).
281. Huang, S. *et al.* Rapid separation of blood plasma exosomes from low-density lipoproteins via a hydrophobic interaction chromatography method on a polyester capillary-channeled polymer fiber phase. *Anal Chim Acta* **1167**, 338578 (2021).
282. Sódar, B. W. *et al.* Low-density lipoprotein mimics blood plasma-derived exosomes and microvesicles during isolation and detection. *Sci Rep* **6**, 24316 (2016).
283. Vader, P., Mol, E. A., Pasterkamp, G. & Schiffelers, R. M. Extracellular vesicles for drug delivery. *Adv Drug Deliv Rev* **106**, 148–156 (2016).

284. di Liegro, C. M., Schiera, G. & di Liegro, I. Extracellular Vesicle-Associated RNA as a Carrier of Epigenetic Information. *Genes (Basel)* **8**, 240 (2017).
285. Galbiati, S. *et al.* Small EVs-Associated DNA as Complementary Biomarker to Circulating Tumor DNA in Plasma of Metastatic Colorectal Cancer Patients. *Pharmaceuticals* **14**, 128 (2021).
286. Liu, H. *et al.* Analysis of extracellular vesicle DNA at the single-vesicle level by nano-flow cytometry. *J Extracell Vesicles* **11**, e12206 (2022).
287. Fang, S. *et al.* Small extracellular vesicles derived from human mesenchymal stromal cells prevent group 2 innate lymphoid cell-dominant allergic airway inflammation through delivery of miR-146a-5p. *J Extracell Vesicles* **9**, 1723260 (2020).
288. Rautaniemi, K. *et al.* Addressing challenges in the removal of unbound dye from passively labelled extracellular vesicles. *Nanoscale Adv* **4**, 226–240 (2022).
289. Deregibus, M. C. *et al.* Charge-based precipitation of extracellular vesicles. *Int J Mol Med* **38**, 1359–1366 (2016).
290. Chen, P. *et al.* Extraction and identification of synovial tissue-derived exosomes by different separation techniques. *J Orthop Surg Res* **15**, 1–8 (2020).
291. Foers, A. D. *et al.* Enrichment of extracellular vesicles from human synovial fluid using size exclusion chromatography. *J Extracell Vesicles* **7**, 1490145 (2018).
292. Panagopoulou, M. S., Wark, A. W., Birch, D. J. S. & Gregory, C. D. Phenotypic analysis of extracellular vesicles: a review on the applications of fluorescence. *J Extracell Vesicles* **9**, 1710020 (2020).
293. van Niel, G. *et al.* The Tetraspanin CD63 Regulates ESCRT-Independent and -Dependent Endosomal Sorting during Melanogenesis. *Dev Cell* **21**, 708–721 (2011).
294. Buschow, S. I. *et al.* MHC II in Dendritic Cells is Targeted to Lysosomes or T Cell-Induced Exosomes Via Distinct Multivesicular Body Pathways. *Traffic* **10**, 1528–1542 (2009).
295. Chairoungdua, A., Smith, D. L., Pochard, P., Hull, M. & Caplan, M. J. Exosome release of β-catenin: a novel mechanism that antagonizes Wnt signaling. *Journal of Cell Biology* **190**, 1079–1091 (2010).
296. Zhang, H. & Lyden, D. Asymmetric-flow field-flow fractionation technology for exomere and small extracellular vesicle separation and characterization. *Nat Protoc* **14**, 1027–1053 (2019).
297. Pietrowska, M. *et al.* Proteomic profile of melanoma cell-derived small extracellular vesicles in patients' plasma: a potential correlate of melanoma progression. *J Extracell Vesicles* **10**, (2021).
298. Mustapic, M. *et al.* Plasma extracellular vesicles enriched for neuronal origin: A potential window into brain pathologic processes. *Front Neurosci* **11**, 278 (2017).
299. Hurwitz, S. N. *et al.* Proteomic profiling of NCI-60 extracellular vesicles uncovers common protein cargo and cancer type-specific biomarkers. *Oncotarget* **7**, 86999–87015 (2016).

300. Bewicke-Copley, F. *et al.* Extracellular vesicles released following heat stress induce bystander effect in unstressed populations. *J Extracell Vesicles* **6**, 1340746 (2017).
301. de Jong, O. G. *et al.* Cellular stress conditions are reflected in the protein and RNA content of endothelial cell-derived exosomes. *J Extracell Vesicles* **1**, (2012).
302. Li, J. *et al.* Serum-free culture alters the quantity and protein composition of neuroblastoma-derived extracellular vesicles. *J Extracell Vesicles* **4**, 26883 (2015).
303. Vagner, T. *et al.* Protein Composition Reflects Extracellular Vesicle Heterogeneity. *Proteomics* **19**, 1800167 (2019).
304. Fathi, M. *et al.* Single-cell cloning of breast cancer cells secreting specific subsets of extracellular vesicles. *Cancers (Basel)* **13**, 4397 (2021).
305. Miwa, H., Dimatteo, R., de Rutte, J., Ghosh, R. & di Carlo, D. Single-cell sorting based on secreted products for functionally defined cell therapies. *Microsyst Nanoeng* **8**, 84 (2022).
306. Hanlon, K. *et al.* Single-cell cloning of human T-cell lines reveals clonal variation in cell death responses to chemotherapeutics. *Cancer Genet* **237**, 69–77 (2019).
307. Miao, X. *et al.* A promising iPS-based single-cell cloning strategy revealing signatures of somatic mutations in heterogeneous normal cells. *Comput Struct Biotechnol J* **18**, 2326–2335 (2020).
308. Huang, S. Non-genetic heterogeneity of cells in development: more than just noise. *Development* **136**, 3853–3862 (2009).
309. Sork, H. *et al.* Heterogeneity and interplay of the extracellular vesicle small RNA transcriptome and proteome. *Sci Rep* **8**, 10813 (2018).
310. Stauffer, W., Sheng, H. & Lim, H. N. EzColocalization: An ImageJ plugin for visualizing and measuring colocalization in cells and organisms. *Sci Rep* **8**, 15764 (2018).
311. Wiklander, O. P. B. *et al.* Systematic Methodological Evaluation of a Multiplex Bead-Based Flow Cytometry Assay for Detection of Extracellular Vesicle Surface Signatures. *Front Immunol* **9**, 1326 (2018).
312. Grist, J. T. *et al.* Extracellular Lactate: A Novel Measure of T Cell Proliferation. *The Journal of Immunology* **200**, 1220–1226 (2018).
313. Guo, Q. *et al.* Integrin β1-enriched extracellular vesicles mediate monocyte adhesion and promote liver inflammation in murine NASH. *J Hepatol* **71**, 1193–1205 (2019).
314. Tauro, B. J. *et al.* Oncogenic H-Ras Reprograms Madin-Darby Canine Kidney (MDCK) Cell-derived Exosomal Proteins Following Epithelial-Mesenchymal Transition. *Molecular & Cellular Proteomics* **12**, 2148–2159 (2013).
315. Klemann, C., Wagner, L., Stephan, M. & von Hörsten, S. Cut to the chase: a review of CD26/dipeptidyl peptidase-4's (DPP4) entanglement in the immune system. *Clin Exp Immunol* **185**, 1–21 (2016).
316. Mulvihill, E. E. & Drucker, D. J. Pharmacology, Physiology, and Mechanisms of Action of Dipeptidyl Peptidase-4 Inhibitors. *Endocr Rev* **35**, 992–1019 (2014).

317. Kim, W. & Egan, J. M. The Role of Incretins in Glucose Homeostasis and Diabetes Treatment. *Pharmacol Rev* **60**, 470–512 (2008).
318. Deacon, C. F. Physiology and Pharmacology of DPP-4 in Glucose Homeostasis and the Treatment of Type 2 Diabetes. *Front Endocrinol (Lausanne)* **10**, 80 (2019).
319. Gallwitz, B. Clinical use of DPP-4 inhibitors. *Front Endocrinol (Lausanne)* **10**, 389 (2019).
320. van Niel, G. *et al.* Intestinal epithelial cells secrete exosome–like vesicles. *Gastroenterology* **121**, 337–349 (2001).
321. Kandzija, N. *et al.* Placental extracellular vesicles express active dipeptidyl peptidase IV; levels are increased in gestational diabetes mellitus. *J Extracell Vesicles* **8**, 1617000 (2019).
322. Namburi, S., Broxmeyer, H. E., Hong, C.-S., Whiteside, T. L. & Boyiadzis, M. DPP4+ exosomes in AML patients' plasma suppress proliferation of hematopoietic progenitor cells. *Leukemia* **35**, 1925–1932 (2021).
323. Du, J. *et al.* Tubular epithelial cells derived-exosomes containing CD26 protects mice against renal ischemia/reperfusion injury by maintaining proliferation and dissipating inflammation. *Biochem Biophys Res Commun* **553**, 134–140 (2021).
324. Tang, M., Wang, Q., Wang, K. & Wang, F. Mesenchymal stem cells-originated exosomal microRNA-152 impairs proliferation, invasion and migration of thyroid carcinoma cells by interacting with DPP4. *J Endocrinol Invest* **43**, 1787–1796 (2020).
325. Guo, Z. *et al.* E-cadherin interactome complexity and robustness resolved by quantitative proteomics. *Sci Signal* **7**, rs7 (2014).
326. Babbin, B. A. *et al.* Annexin 2 Regulates Intestinal Epithelial Cell Spreading and Wound Closure through Rho-Related Signaling. *Am J Pathol* **170**, 951–966 (2007).
327. Barwe, S. P. *et al.* Novel Role for Na,K-ATPase in Phosphatidylinositol 3-Kinase Signaling and Suppression of Cell Motility. *Mol Biol Cell* **16**, 1082–1094 (2005).
328. Ma, Y. & Wang, H. Clinical significance of Annexin A2 expression in oral squamous cell carcinoma and its influence on cell proliferation, migration and invasion. *Sci Rep* **11**, 5033 (2021).
329. Boczonadi, V., McInroy, L. & Määttä, A. Cytolinker cross-talk: Periplakin N-terminus interacts with plectin to regulate keratin organisation and epithelial migration. *Exp Cell Res* **313**, 3579–3591 (2007).
330. Yoon, S. & Leube, R. E. Keratin intermediate filaments: intermediaries of epithelial cell migration. *Essays Biochem* **63**, 521–533 (2019).
331. Hill, M. M. *et al.* Co-Regulation of Cell Polarization and Migration by Caveolar Proteins PTRF/Cavin-1 and Caveolin-1. *PLoS One* **7**, e43041 (2012).
332. Jin, Z.-G. *et al.* Cyclophilin A Is a Proinflammatory Cytokine that Activates Endothelial Cells. *Arterioscler Thromb Vasc Biol* **24**, 1186–1191 (2004).
333. Seo, J. H. *et al.* ARD1-mediated Hsp70 acetylation balances stress-induced protein refolding and degradation. *Nat Commun* **7**, 12882 (2016).

334. Tsang, W. Y. *et al.* CP110 Cooperates with Two Calcium-binding Proteins to Regulate Cytokinesis and Genome Stability. *Mol Biol Cell* **17**, 3423–3434 (2006).
335. Drechsler, M. *et al.* Annexin A1 Counteracts Chemokine-Induced Arterial Myeloid Cell Recruitment. *Circ Res* **116**, 827–835 (2015).
336. Leffers, H. *et al.* Identification of Two Human Rho GDP Dissociation Inhibitor Proteins Whose Overexpression Leads to Disruption of the Actin Cytoskeleton. *Exp Cell Res* **209**, 165–174 (1993).
337. Boulter, E. *et al.* Regulation of Rho GTPase crosstalk, degradation and activity by RhoGDI1. *Nat Cell Biol* **12**, 477–483 (2010).
338. Dragovic, R. A. *et al.* Sizing and phenotyping of cellular vesicles using Nanoparticle Tracking Analysis. *Nanomedicine* **7**, 780–788 (2011).
339. van der Pol, E. *et al.* Particle size distribution of exosomes and microvesicles determined by transmission electron microscopy, flow cytometry, nanoparticle tracking analysis, and resistive pulse sensing. *Journal of Thrombosis and Haemostasis* **12**, 1182–1192 (2014).
340. Cardeñes, B. *et al.* ALCAM/CD166 Is Involved in the Binding and Uptake of Cancer-Derived Extracellular Vesicles. *Int J Mol Sci* **23**, 5753 (2022).
341. Fu, Q. *et al.* Primary tumor-derived exosomes facilitate metastasis by regulating adhesion of circulating tumor cells via SMAD3 in liver cancer. *Oncogene* **37**, 6105–6118 (2018).
342. Yu, Z. *et al.* Pancreatic cancer-derived exosomes promote tumor metastasis and liver pre-metastatic niche formation. *Oncotarget* **8**, 63461–63483 (2017).
343. Mitra, A., Deutsch, B., Ignatovich, F., Dykes, C. & Novotny, L. Nano-optofluidic Detection of Single Viruses and Nanoparticles. *ACS Nano* **4**, 1305–1312 (2010).
344. Wang, R. *et al.* Exosome Adherence and Internalization by Hepatic Stellate Cells Triggers Sphingosine 1-Phosphate-dependent Migration. *Journal of Biological Chemistry* **290**, 30684–30696 (2015).
345. Huang, R. & Rofstad, E. K. Integrins as therapeutic targets in the organ-specific metastasis of human malignant melanoma. *Journal of Experimental & Clinical Cancer Research* **37**, 92 (2018).
346. Ekström, K. *et al.* Characterization of surface markers on extracellular vesicles isolated from lymphatic exudate from patients with breast cancer. *BMC Cancer* **22**, 1–17 (2022).
347. Hazawa, M. *et al.* Radiation increases the cellular uptake of exosomes through CD29/CD81 complex formation. *Biochem Biophys Res Commun* **446**, 1165–1171 (2014).
348. Lelek, M. *et al.* Single-molecule localization microscopy. *Nature Reviews Methods Primers* **1**, 39 (2021).
349. Keerthikumar, S. *et al.* Proteogenomic analysis reveals exosomes are more oncogenic than ectosomes. *Oncotarget* **6**, 15375–15396 (2015).
350. Blanc, L. & Vidal, M. New insights into the function of Rab GTPases in the context of exosomal secretion. *Small GTPases* **9**, 95–106 (2018).

351. Kreidberg, J. A. Functions of α3β1 integrin. *Curr Opin Cell Biol* **12**, 548–553 (2000).
352. Hurwitz, S. N. & Meckes, D. G. Extracellular Vesicle Integrins Distinguish Unique Cancers. *Proteomes* **7**, 14 (2019).
353. Ciardiello, C. *et al.* Large oncosomes overexpressing integrin alpha-V promote prostate cancer adhesion and invasion via AKT activation. *Journal of Experimental & Clinical Cancer Research* **38**, 317 (2019).
354. Ieguchi, K. *et al.* Direct Binding of the EGF-like Domain of Neuregulin-1 to Integrins (αvβ3 and α6β4) Is Involved in Neuregulin-1/ErbB Signaling. *Journal of Biological Chemistry* **285**, 31388–31398 (2010).
355. Saegusa, J. *et al.* The Direct Binding of Insulin-like Growth Factor-1 (IGF-1) to Integrin αvβ3 Is Involved in IGF-1 Signaling. *Journal of Biological Chemistry* **284**, 24106–24114 (2009).
356. Mori, S. *et al.* Direct Binding of Integrin αvβ3 to FGF1 Plays a Role in FGF1 Signaling. *Journal of Biological Chemistry* **283**, 18066–18075 (2008).
357. Bax, Daniel. V. *et al.* Cell Adhesion to Fibrillin-1 Molecules and Microfibrils Is Mediated by α5β1 and αvβ3 Integrins. *Journal of Biological Chemistry* **278**, 34605–34616 (2003).
358. Barnawi, R. *et al.* β1 Integrin is essential for fascin-mediated breast cancer stem cell function and disease progression. *Int J Cancer* **145**, 830–841 (2019).
359. Wang, M. *et al.* Mechanism of immune evasion in breast cancer. *Onco Targets Ther* **10**, 1561–1573 (2017).
360. Forero, A. *et al.* Expression of the MHC Class II Pathway in Triple-Negative Breast Cancer Tumor Cells Is Associated with a Good Prognosis and Infiltrating Lymphocytes. *Cancer Immunol Res* **4**, 390–9 (2016).
361. Tang, Z., Li, D., Hou, S. & Zhu, X. The cancer exosomes: Clinical implications, applications and challenges. *Int J Cancer* **146**, 2946–2959 (2020).
362. Zhang, S. *et al.* ROR1 Is Expressed in Human Breast Cancer and Associated with Enhanced Tumor-Cell Growth. *PLoS One* **7**, e31127 (2012).
363. Cui, B. *et al.* Targeting ROR1 Inhibits Epithelial–Mesenchymal Transition and Metastasis. *Cancer Res* **73**, 3649–3660 (2013).
364. Blanas, A., Sahasrabudhe, N. M., Rodríguez, E., van Kooyk, Y. & van Vliet, S. J. Fucosylated Antigens in Cancer: An Alliance toward Tumor Progression, Metastasis, and Resistance to Chemotherapy. *Front Oncol* **8**, 39 (2018).
365. Ouhtit, A., Abdraboh, M. E., Hollenbach, A. D., Zayed, H. & Raj, M. H. G. CD146, a novel target of CD44-signaling, suppresses breast tumor cell invasion. *Cell Communication and Signaling* **15**, 45 (2017).
366. Zabouo, G. *et al.* CD146 expression is associated with a poor prognosis in human breast tumors and with enhanced motility in breast cancer cell lines. *Breast Cancer Research* **11**, 1–14 (2009).
367. Li, W. *et al.* Unraveling the roles of CD44/CD24 and ALDH1 as cancer stem cell markers in tumorigenesis and metastasis. *Sci Rep* **7**, 13856 (2017).

368. Jing, X. *et al.* CD24 is a Potential Biomarker for Prognosis in Human Breast Carcinoma. *Cellular Physiology and Biochemistry* **48**, 111–119 (2018).
369. Yan, C. & Richmond, A. Hiding in the dark: pan-cancer characterization of expression and clinical relevance of CD40 to immune checkpoint blockade therapy. *Mol Cancer* **20**, 146 (2021).
370. Garnier, D., Magnus, N., Meehan, B., Kislinger, T. & Rak, J. Qualitative changes in the proteome of extracellular vesicles accompanying cancer cell transition to mesenchymal state. *Exp Cell Res* **319**, 2747–2757 (2013).
371. di Trapani, M. *et al.* Differential and transferable modulatory effects of mesenchymal stromal cell-derived extracellular vesicles on T, B and NK cell functions. *Sci Rep* **6**, 24120 (2016).
372. Qian, X. *et al.* Immunosuppressive Effects of Mesenchymal Stem Cells-derived Exosomes. *Stem Cell Rev Rep* **17**, 411–427 (2021).
373. Cosenza, S. *et al.* Mesenchymal stem cells-derived exosomes are more immunosuppressive than microparticles in inflammatory arthritis. *Theranostics* **8**, 1399–1410 (2018).
374. Selleri, S. *et al.* Human mesenchymal stromal cell-secreted lactate induces M2-macrophage differentiation by metabolic reprogramming. *Oncotarget* **7**, 30193–30210 (2016).
375. Shabbir, A., Cox, A., Rodriguez-Menocal, L., Salgado, M. & Badiavas, E. van. Mesenchymal Stem Cell Exosomes Induce Proliferation and Migration of Normal and Chronic Wound Fibroblasts, and Enhance Angiogenesis In Vitro. *Stem Cells Dev* **24**, 1635–1647 (2015).
376. Pittenger, M. F. *et al.* Mesenchymal stem cell perspective: cell biology to clinical progress. *NPJ Regen Med* **4**, 22 (2019).
377. Tsiapalis, D. & O'Driscoll, L. Mesenchymal Stem Cell Derived Extracellular Vesicles for Tissue Engineering and Regenerative Medicine Applications. *Cells* **9**, 991 (2020).
378. Kramer, N. *et al.* In vitro cell migration and invasion assays. *Mutation Research/Reviews in Mutation Research* **752**, 10–24 (2013).
379. Shen, X. *et al.* Exosome-mediated transfer of CD44 from high-metastatic ovarian cancer cells promotes migration and invasion of low-metastatic ovarian cancer cells. *J Ovarian Res* **14**, 1–11 (2021).
380. Salomon, C. *et al.* Exosomal Signaling during Hypoxia Mediates Microvascular Endothelial Cell Migration and Vasculogenesis. *PLoS One* **8**, e68451 (2013).
381. Lee, Y. J. *et al.* Soluble HSPB1 regulates VEGF-mediated angiogenesis through their direct interaction. *Angiogenesis* **15**, 229–242 (2012).
382. Geraghty, K. M. *et al.* Regulation of multisite phosphorylation and 14-3-3 binding of AS160 in response to IGF-1, EGF, PMA and AICAR. *Biochemical Journal* **407**, 231–241 (2007).
383. Andrae, J., Gallini, R. & Betsholtz, C. Role of platelet-derived growth factors in physiology and medicine. *Genes Dev* **22**, 1276–1312 (2008).

384. Mu, G. *et al.* Calmodulin 2 Facilitates Angiogenesis and Metastasis of Gastric Cancer via STAT3/HIF-1A/VEGF-A Mediated Macrophage Polarization. *Front Oncol* **11**, 3713 (2021).
385. Berchtold, M. W. & Villalobo, A. The many faces of calmodulin in cell proliferation, programmed cell death, autophagy, and cancer. *Biochimica et Biophysica Acta (BBA) - Molecular Cell Research* **1843**, 398–435 (2014).
386. Qian, Z. *et al.* Downregulation of Cyclophilin A by siRNA diminishes non-small cell lung cancer cell growth and metastasis via the regulation of matrix metallopeptidase 9. *BMC Cancer* **12**, 1–11 (2012).
387. Rankin, C. R. *et al.* Annexin A2 Regulates β1 Integrin Internalization and Intestinal Epithelial Cell Migration. *Journal of Biological Chemistry* **288**, 15229–15239 (2013).
388. Wang, X. *et al.* Exosomes influence the behavior of human mesenchymal stem cells on titanium surfaces. *Biomaterials* **230**, 119571 (2020).
389. Haraszti, R. A. *et al.* High-resolution proteomic and lipidomic analysis of exosomes and microvesicles from different cell sources. *J Extracell Vesicles* **5**, 32570 (2016).
390. Altei, W. F. *et al.* Inhibition of αvβ3 integrin impairs adhesion and uptake of tumor-derived small extracellular vesicles. *Cell Communication and Signaling* **18**, 1–15 (2020).
391. Hosseinkhani, B., Kuypers, S., van den Akker, N. M. S., Molin, D. G. M. & Michiels, L. Extracellular vesicles work as a functional inflammatory mediator between vascular endothelial cells and immune cells. *Front Immunol* **9**, 1789 (2018).
392. Jeppesen, D. K. *et al.* Reassessment of Exosome Composition. *Cell* **177**, 428-445.e18 (2019).
393. Nakamura, K. *et al.* Exosomes promote ovarian cancer cell invasion through transfer of CD44 to peritoneal mesothelial cells. *Molecular Cancer Research* **15**, 78–92 (2017).
394. Mu, W. *et al.* Exosomal CD44 Cooperates with Integrin α6β4 to Support Organotropic Metastasis via Regulating Tumor Cell Motility and Target Host Cell Activation. *Engineering* **7**, 1413–1423 (2021).
395. Fukata, M. & Kaibuchi, K. Rho-family GTPases in cadherin-mediated cell — cell adhesion. *Nat Rev Mol Cell Biol* **2**, 887–897 (2001).
396. Tebbi, C. K. Sickle Cell Disease, a Review. *Hemato* **3**, 341–366 (2022).
397. Korty, P. E., Brando, C. & Shevach, E. M. CD59 functions as a signal-transducing molecule for human T cell activation. *J Immunol* **146**, 4092–8 (1991).
398. Dang, N. H. *et al.* Cell surface modulation of CD26 by anti-1F7 monoclonal antibody. Analysis of surface expression and human T cell activation. *J Immunol* **145**, 3963–71 (1990).
399. Raposo, G. & Stoorvogel, W. Extracellular vesicles: Exosomes, microvesicles, and friends. *Journal of Cell Biology* **200**, 373–383 (2013).

400. Paolini, L. *et al.* Fourier-transform Infrared (FT-IR) spectroscopy fingerprints subpopulations of extracellular vesicles of different sizes and cellular origin. *J Extracell Vesicles* **9**, 1741174 (2020).
401. Kim, S. Y., Khanal, D., Kalionis, B. & Chrzanowski, W. High-fidelity probing of the structure and heterogeneity of extracellular vesicles by resonance-enhanced atomic force microscopy infrared spectroscopy. *Nat Protoc* **14**, 576–593 (2019).
402. Tatischeff, I., Larquet, E., Falcón-Pérez, J. M., Turpin, P.-Y. & Kruglik, S. G. Fast characterisation of cell-derived extracellular vesicles by nanoparticles tracking analysis, cryo-electron microscopy, and Raman tweezers microspectroscopy. *J Extracell Vesicles* **1**, 19179 (2012).
403. Smith, Z. J. *et al.* Single exosome study reveals subpopulations distributed among cell lines with variability related to membrane content. *J Extracell Vesicles* **4**, 28533 (2015).
404. Baldwin, M. A. Protein Identification by Mass Spectrometry. *Molecular & Cellular Proteomics* **3**, 1–9 (2004).
405. Zheng, J. *et al.* Extracellular Vesicles Derived from Human Umbilical Cord Mesenchymal Stem Cells Protect Liver Ischemia/Reperfusion Injury by Reducing CD154 Expression on CD4+ T Cells via CCT2. *Advanced Science* **7**, 1903746 (2020).
406. Lambert, S. A. *et al.* The Human Transcription Factors. *Cell* **172**, 650–665 (2018).
407. Klemm, S. L., Shipony, Z. & Greenleaf, W. J. Chromatin accessibility and the regulatory epigenome. *Nat Rev Genet* **20**, 207–220 (2019).
408. Khalili, A. A. & Ahmad, M. R. A Review of Cell Adhesion Studies for Biomedical and Biological Applications. *Int J Mol Sci* **16**, 18149 (2015).
409. Hanahan, D. & Weinberg, R. A. Hallmarks of cancer: The next generation. *Cell* **144**, 646–674 (2011).
410. Barnes, B. *et al.* Investigating heparin affinity chromatography for extracellular vesicle purification and fractionation. *J Chromatogr A* **1670**, 462987 (2022).

8.0 Appendix

8.1 Manuscripts accepted for publication

Mäger, I., Willms, E., Bonner, S., Hill, A. F. & Wood, M. J. A. Chapter 12 - Extracellular vesicles in neurodegenerative disorders. in *Exosomes: A Clinical Compendium*. (eds. Edelstein, L. R., Smythies, J. R., Quesenberry, P. J., Noble, D.) 285–305 (Academic Press, 2020).

Zanetti-Domingues, L. C., Bonner, S. E., Iyer, R. S., Martin-Fernandez, M. L. & Huber, V. Cooperation and Interplay between EGFR Signalling and Extracellular Vesicle Biogenesis in Cancer. *Cells* **9**, 2639 (2020).

Zanetti-Domingues, L. C., Bonner, S. E., Martin-Fernandez, M. L. & Huber, V. Mechanisms of Action of EGFR Tyrosine Kinase Receptor Incorporated in Extracellular Vesicles. *Cells* **9**, 2505 (2020).

Bonner, S. E. & Willms, E. Intercellular communication through extracellular vesicles in cancer and evolutionary biology. *Prog Biophys Mol Biol* **165**, 80–87 (2021).

Jainarayanan, A. K., Capera, J., Cespedes, P., Conceição, M., Elanchezhian, M., Thomas, T., Bonner, S., Valvo, S., Kruz, E., Berridge, G., Hester, S., Fischer, R., Wood, M., Dustin, M. Comparison of different methods for isolating CD8 T lymphocyte derived extracellular vesicles and supramolecular attack particles. *Journal of Extracellular Biology*. **In review**.

8.2 Attended conferences

October 2019
Oxosome Meeting (The Oxford Extracellular Vesicle Group), Oxford, UK. Oral Presentation: Characterisation of tumour derived extracellular vesicles and their involvement in cancer development.

December 2019
UKEV (United Kingdom Extracellular Vesicles) Forum, Francis Crick Institute, London.

May 2020
ISEV (International Society for Extracellular Vesicles) Annual Meeting, online. Poster presentation with oral summary: Extracellular vesicle heterogeneity and the impact of cellular phenotypic drift on the vesicular proteome.

September 2020

3rd GSEV Autumn Meeting, organised jointly with UK Society for Extracellular Vesicles, online.

Wired Health: Tech, online.

October 2020
Inaugural Cancer and Evolution Symposium, online. Oral presentation: Extracellular vesicles in metastasis and their evolutionary aspects.

November 2020
University of Tartu EV Symposium, Online Oral presentation: Extracellular vesicle heterogeneity and the impact of cellular phenotypic drift on the vesicular proteome.

December 2020
UKEV Forum, online.

March 2021
Wired Health: Tech, online.

May 2021
ISEV Annual Meeting, online. Poster presentation with oral summary: High purity extracellular vesicles isolated from high-density cultures using novel Capto Core bind-elute chromatography.